HAL open science

Structural analysis of heterogeneous multi-phased compounds : application to carbon-based black pigments from Antiquity

Pierre-Olivier Autran

▶ To cite this version:

Pierre-Olivier Autran. Structural analysis of heterogeneous multi-phased compounds : application to carbon-based black pigments from Antiquity. Material chemistry. Université Grenoble Alpes [2020-..], 2021. English. NNT : 2021GRALY048 . tel-03525945

HAL Id: tel-03525945

https://theses.hal.science/tel-03525945v1

Submitted on 14 Jan 2022

HAL is a multi-disciplinary open access archive for the deposit and dissemination of scientific research documents, whether they are published or not. The documents may come from teaching and research institutions in France or abroad, or from public or private research centers.

L'archive ouverte pluridisciplinaire **HAL**, est destinée au dépôt et à la diffusion de documents scientifiques de niveau recherche, publiés ou non, émanant des établissements d'enseignement et de recherche français ou étrangers, des laboratoires publics ou privés.

THÈSE

Pour obtenir le grade de

DOCTEUR DE L'UNIVERSITÉ GRENOBLE ALPES

Spécialité : **Physique des matériaux**

Arrêtée ministériel : 25 mai 2016

Présentée par

Pierre-Olivier AUTRAN

Thèse dirigée par **Pauline MARTINETTO**
et codirigéee par **Catherine DEJOIE**

préparée au sein de **l'European Synchrotron Radiation Facility**
et de **l'Institut Néel - CNRS - UGA**
dans **l'École Doctorale de Physique**

Structural analysis of heterogeneous multi-phased compounds: application to carbon-based black pigments from Antiquity

Thèse soutenue publiquement le **27 juillet 2021**,
devant le jury composé de :

Madame Isabelle GAUTIER-LUNEAU
PROFESSEUR DES UNIVERSITES, UNIVERSITE GRENOBLE ALPES, Présidente

Madame Laurence DE VIGUERIE
CHARGEE DE RECHERCHE HDR, CNRS DELEGATION PARIS CENTRE, Rapporteure

Monsieur Gilles WALLEZ
PROFESSEUR DES UNIVERSITES, SORBONNE UNIVERSITE, Rapporteur

Monsieur Andrew KING
DOCTEUR EN SCIENCES, SYNCHROTRON SOLEIL, Examinateur

Monsieur Philippe SCIAU
DIRECTEUR DE RECHERCHE, CNRS DELEGATION OCCITANIE OUEST, Examinateur

à Marius Autran, mon grand-père.

Acknowledgements

First, I would like to deeply thank my two thesis directors Dr. Pauline Martinetto and Dr. Catherine Dejoie for their consistent support and guidance during the running of this thesis project. Pauline and Catherine were the foundation of my expertise in both material science as well as Cultural Heritage Materials. Their commitment as well as a persistent pursuit of accuracy and excellence developed a perfect environment for the growth of this research project.

I would like to thank Dr. Pierre Bordet and Dr. Jean-Louis Hodeau for guiding me during this project and for the stimulating remarks and questions on crystalline and amorphous materials as well as diffraction-based techniques. The meetings and conversations were vital for me in the understanding of these materials and techniques.

I address my thanks to Dr. Laurence De Viguerie and to Pr. Gilles Wallez for having accepted to be the rapporteurs of this work. I also thank Pr. Isabelle Gautier-Luneau for presiding the thesis jury as well as Dr. Andrew King and Dr. Philippe Sciau for honouring with their presence.

I would like to thank Dr. Andy Fitch, for welcoming me during this 3 years at the ID22 beamline. His advices and answers to my questions were particularly helpful during this project.

I would like to thank Mrs. Caroline Dugand and Mrs. Maëva Gervason for their trust and their involvement in the collaboration between ESRF, Institut Néel - CNRS - UGA and the Musée Champollion for the papyrus fragment study.

I would like to thank Mr. Sebastien Pairis for his contribution to the SEM measurement done at the Néel Institute as well as Mrs. Valérie Reita for her help and expertise carrying Raman spectroscopy measurements done at the Néel Institute.

I would like to thank Dr. Jonathan Wright for his help particularly on diffraction data analysis.

I would like to thank Dr. Michel Anne and Dr. Philippe Walter for their presence during beamtimes and meeting and for their precious advices.

I would like to thank Mrs. Rebecca Erbanni and Mr. Flavien Cottin, trainees that contributed actively to this project.

I would like to thank the ESRF for financial support and the provision of synchrotron beamtime.

Finally, I would like to thank my parents, my family and my friends.

Analyse structurale de composés hétéreogènes multiphasés : applications aux pigments noirs à base de carbone de l'Antiquité

Introduction

L'étude des matériaux du patrimoine culturel est souvent un défi en raison de leur hétérogénéité mais aussi des possibles transformations et dégradations survenant sur plusieurs centaines voire milliers d'années. Ce projet va se focaliser sur la détermination de la nature des pigments noirs à base de carbone d'Egypte ancienne et de la période gréco-romaine. Ces pigments ont été utilisés dans différents contextes (encres, peintures, cosmétiques,...), et résultent d'un mélange de plusieurs composés dans des proportions variées. Si l'on parvient à caractériser ces matériaux multiphasés, une meilleure compréhension du processus de fabrication des pigments pourra être obtenue, et certains marqueurs spécifiques d'une période donnée ou sous-produits dus à une dégradation pourront être identifiés.

Il existe trois types de pigments à base de carbone dans l'Antiquité définis par J. Winter en 1983 [1] : les noirs de flamme, les cokes et les charbons. Le groupe des noirs de flamme représente les résidus de carbone formés par une flamme sur une surface (noir de fumée formé par la combustion d'huile et la suie formée par la combustion du bois). La catégorie des cokes désigne l'ensemble des matériaux carbonés produits par carbonisation de précurseurs à l'état liquide ou plastique (sucres, gélatines, huiles ainsi que les os). Le groupe des charbons inclut tous les précurseurs solides qui conservent leur morphologie après carbonisation. Cette catégorie contient principalement les charbons à base de végétaux.

Les pigments noirs à base de carbone ont été utilisés par les Romains des centaines d'années avant J.C. et l'une de leurs toutes premières mentions se trouve dans une lettre de Cicéron à son frère [2]. Selon les textes anciens, les pigments sont composés de noir de flamme (suie ou noir de fumée), drêches de vin séchées, ou de charbons. Le noir de fumée était obtenu en brûlant de la résine ou des graisses dans des fours empêchant le dégagement de fumée. Puis l'encre était produite en mélangeant le résidu noir collecté sur les parois du four, avec un liant et de l'eau. Des études récentes mentionnent les différentes phases qui composent les poudres noires collectées dans des récipients trouvés sur les sites de Pompéi et d'Herculanum. Dans deux de ces études [**?**] [4], la nature des pigments noirs à base de carbone a été également étudiée en relation avec l'utilisation de poudres noires dans l'Antiquité. Avec une même approche, nous avons regardé treize échantillons provenant des sites archéologiques de Pompéi et d'Herculanum (Coll. M.-C. Gamberini, Univ. Modène). Les échantillons ont été prélevés dans des récipients de différents types, avec une incertitude quant à leur utilisation à l'époque (encre, cosmétiques, peinture,...). Notre premier objectif sera d'identifier la nature de ces poudres. Sur la base de cette identification, le deuxième objectif sera de vérifier un lien éventuel entre le type de contenant dans lequel les poudres ont été trouvées et leur utilisation.

Dès le quatrième millénaire avant notre ère, les écrits égyptiens sur papyrus ont permis la diffusion de la connaissance tout autour de la mer Méditerranée. Les pigments noirs à base de carbone de la période égyptienne étaient notamment utilisés comme base pour la fabrication des encres. Bien qu'une grande quantité de papyrus ait été préservée, aucun des textes traduits n'ont mentionné la recette de l'encre noire jusqu'à présent. La complexité résultant de la nature non-cristalline des pigments à base de carbone et du papyrus lui-même, explique également notre compréhension limitée des techniques d'écriture égyptienne. Des études récentes sur des fragments de papyrus d'Herculanum et d'Égypte ancienne ont montré la présence d'éléments

métalliques tels que le cuivre et le plomb dans l'encre, leur origine restant sans réponse. Malgré leur origine inconnue, ces éléments ont été utilisés comme agents de contraste pour pratiquement "lire" des papyrus hautement dégradés ou enroulés [3]. Nous avons établi une collaboration avec C. Dugand, conservatrice au Musée Champollion (Vif, Département de l'Isère, France) qui nous a permis d'accéder à douze fragments de papyrus écrits et/ou peints. Si notre premier objectif est de caractériser l'encre noire trouvée à la surface des papyrus de cette collection, la seconde, est de proposer une manière de lire "virtuellement" les papyrus anciens en utilisant le contraste structural donné par le pigment noir lui-même, une alternative intéressante en l'absence de contraste chimique.

Dans ce projet, les échantillons sont des matériaux très hétérogènes, avec la présence de phases cristallines et non cristallines présentant des tailles de cristallites variées. Afin d'étudier ces échantillons, une méthodologie dédiée a été mise en œuvre dans laquelle la microscopie électronique à balayage, la spectroscopie Raman, la fluorescence des rayons X et les données de diffraction des rayons X / PDF sont combinées. Nous nous concentrerons en particulier sur les études structurales basées sur les techniques impliquant le rayonnement X synchrotron avec le développement d'outils dédiés. Notre approche méthodologique tiendra compte des spécificités des échantillons sur le plan de leur préciosité et de leur fragilité.

Le premier chapitre de cette thèse posera les bases de notre étude. Nous discuterons du contexte historique autour des pigments à base de noir de carbone, de leur utilisation dans les encres de l'Antiquité et de l'évolution des encres au carbone vers les encres mixtes et métallo-galliques. Nous résumerons également les résultats d'analyses récentes réalisées sur des pigments à base de carbone anciens. Ensuite, nous verrons les techniques de caractérisation que nous avons utilisées tout au long de ce projet et leur spécificité ainsi que les développements que nous avons faits pour les adapter à notre type d'échantillon. Dans la dernière partie du chapitre seront montrés les résultats de la caractérisation d'échantillons de carbone de référence (commerciaux et synthétisés).

Le deuxième chapitre sera consacré à l'analyse des poudres noires de Pompéi et d'Herculanum. Nous combinerons les techniques de spectroscopie et de diffraction pour identifier les phases qui composent les poudres. Nous utiliserons les informations fournies par la diffraction des rayons X sur poudre haute-résolution (HR-XRD) pour quantifier les phases cristallines. Pour la partie amorphe, qui renferme notamment les phases carbonées, la fonction de distribution de paires sera calculée pour récupérer des informations sur l'ordre structural à courte et moyenne distance. Les poudres noires étant hétérogènes, l'une des parties difficiles de ce chapitre sera la séparation des contributions des phases poudre et monocristalline du signal de diffraction. À la fin, nous discuterons de la nature des pigments noirs à base de carbone et de leurs utilisations en tenant compte du type de récipients dans lesquels ils ont été trouvés.

Le dernier chapitre se concentrera sur l'étude des pigments noirs et colorés de douze fragments de papyrus. La chronologie des différents types de pigments colorés utilisés dans l'Égypte ancienne est assez bien établie, l'étude de ces pigments colorés nous aidera à préciser l'époque à laquelle les fragments de la collection Champollion ont été réalisés. Notre étude a été menée en utilisant la fluorescence X (XRF) et la DRX pour identifier et quantifier les phases cristallines. Nous discuterons de la superposition des couches picturales, ainsi que les processus d'altération de certains pigments. La présence d'un pigment noir à base de carbone sera vérifiée par spectroscopie Raman. Par rapport aux poudres libres étudiées dans le chapitre précédent, la caractérisation des pigments à base de carbone sur un support en papyrus (cellulose), est plus difficile. En effet, étant donné que le support et les pigments sont tous les deux à base de carbone, il est plus complexe d'extraire des informations seulement sur le pigment. Pour ce faire, nous avons combiné la diffraction des rayons X et la fluorescence X en tomographie (XRD/F-CT) pour séparer virtuellement le signal de l'encre de son support. Un contraste entre l'encre et le support de papyrus a été extrait en se basant uniquement sur le signal de diffusion du pigment à base de carbone. L'identification des différents éléments chimiques, phases cristallines et phases

désordonnées présents dans les pigments noirs à base de carbone de l'Antiquité donne de nouvelles perspectives sur les processus de fabrication développés à l'époque romaine et dans l'Égypte ancienne, ainsi que sur l'effet possible du vieillissement de ces matériaux historiques. Ce travail montre également que l'étude des matériaux du patrimoine culturel permet de relever de nouveaux défis méthodologiques qui peuvent profiter à d'autres domaines de la science des matériaux.

Poudres noires de Pompéi et d'Herculanum

Cette partie du projet est consacrée à l'étude des poudres noires de l'époque romaine. Treize échantillons de Pompéi et d'Herculanum ont été sélectionnés. Les échantillons ont été prélevés dans différents types de contenants, avec une incertitude quant à leur utilisation dans l'Antiquité (ex: encre, cosmétiques, peinture,...)(Cersoy *et al.* [4], Canevali *et al.* [5]). Le premier objectif de cette étude est d'identifier la nature du pigment noir et le composé d'origine qui a été carbonisé. Sur la base de ces connaissances, le deuxième objectif sera de vérifier s'il existe un lien éventuel entre le type de contenant dans lequel les poudres ont été trouvées et leur utilisation quotidienne.

Comme la morphologie de la matière première utilisée pour produire le pigment noir peut être préservée après le processus de carbonisation, les échantillons ont été observés au MEB. Pour deux échantillons, la présence de noir de fumée a été attestée en comparant la morphologie des grains avec la morphologie de références de composé à base de carbone. Les caractéristiques morphologiques du noir de pêche et du bois carbonisé ont été identifiées dans l'échantillon P3897 (Figure 1). Pour le deuxième échantillon (P12458), la présence de particules sphériques de taille nanométrique a été attribuée au noir de fumée en comparant avec la référence correspondante (Figure 1). Néanmoins, dans le cas des autres échantillons, les observations MEB sont restées non concluantes et une stratégie basée sur la diffraction des rayons X a été mise en œuvre.

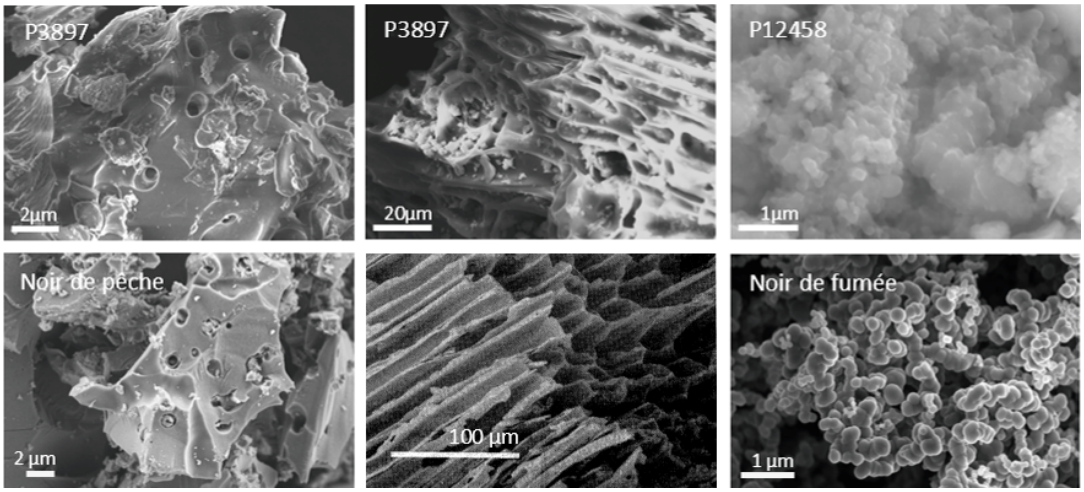

Figure 1: Images MEB (électrons secondaires, Institut Néel) obtenues sur deux poudres noires d'un contenant du site archéologique de Pompéi, et sur des références. Les morphologies du noir de pêche, du bois carbonisé (Winter, 1983 [1]) et du noir de fumée sont clairement visibles.

Les échantillons sont des poudres contenant un ou des pigments noirs à base de carbone mal cristallisés associés à des phases cristallines, voire des liants. Des capillaires contenant les échantillons de poudre ont été analysés sur la ligne de lumière ID22 (ESRF) par la diffraction des rayons X de poudre à haute résolution angulaire pour l'identification de phase et la quantification des phases cristallines. L'acquisition des données a été réalisée grâce a un multi-analyseur comprenant neuf cristaux de silicium 111 couplé à neuf scintillateurs. Un exemple d'affinement de Rietveld est donné sur la Figure 2A. Des phases telles que l'analcime, la sanidine, la leucite et

l'augite ont été trouvées dans la plupart des échantillons et sont très probablement liées à l'éruption du volcan. Quelques phases supplémentaires telles que la malachite et la cassitérite pourraient résulter de la dégradation respectivement des récipients en bronze et en étain [4]. Enfin, la présence d'une grande quantité de gypse et de calcite dans certains des échantillons pourrait être liée à l'utilisation de ces composés comme agents desséchants [5].

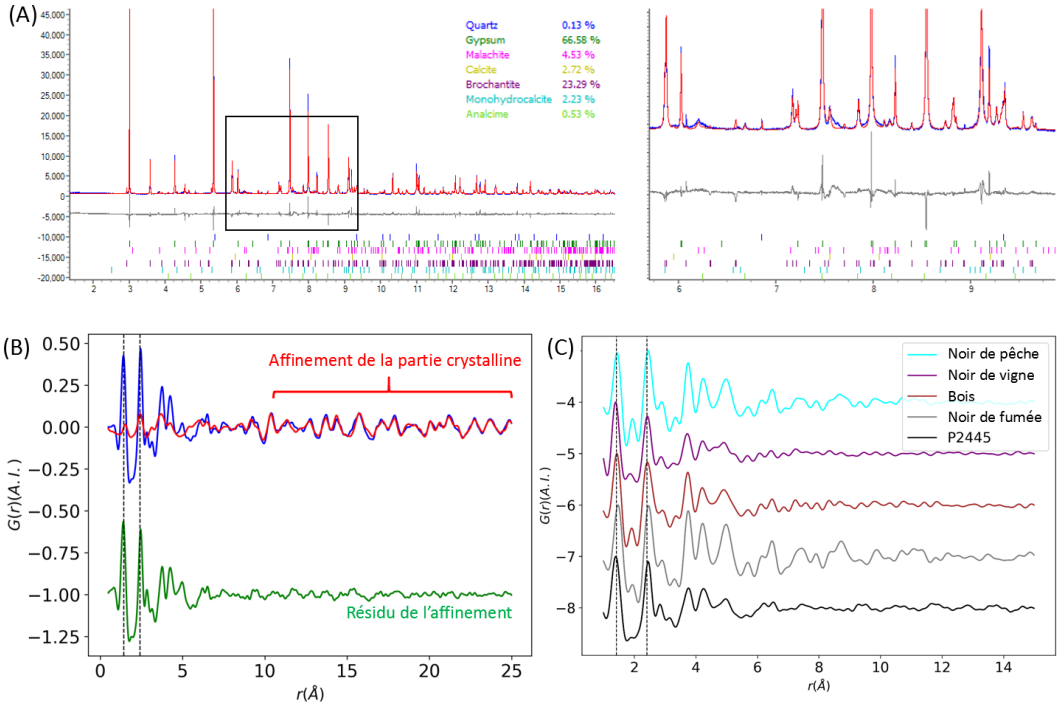

Figure 2: (A) Exemple d'affinement de Rietveld d'une poudre noire (HE03) prélevée dans un récipient découvert sur le site de Herculanum (bleu: données expérimentales, rouge: modèle calculé, gris : différence). Sept phases cristallines ont été identifiées. (Rwp = 10.29, Rexp = 3.95, Rp = 7.62) (B) Affinement de la PDF à grande distance (échantillon P2445) après identification et quantification des phases cristallines (bleu: données expérimentales, rouge: modèle calculé, vert: résidu, qui correspond à la PDF de la phase amorphe à identifier). (C) Comparaison de la PDF de la phase amorphe obtenue en B avec les PDFs des échantillons de référence.

Des informations sur la partie amorphe des échantillons ont été obtenues en utilisant l'analyse de la fonction de distribution de paires (PDF). Expérimentalement, la PDF étant obtenue par transformée de Fourier d'un diagramme de diffraction sur poudre, il faut arriver à enregistrer des données de diffraction à grands Q ($Q = 4\pi sin(\theta)/\lambda$) avec une statistique de comptage élevée, pour limiter à la fois les effets de coupure et le niveau de bruit dans la transformée de Fourier. Ici, nous avons travaillé sur la ligne de lumière ID22 et utilisé un détecteur 2D de grande dimension (Perkin-Elmer), positionné relativement près de l'échantillon (380mm), et une énergie incidente de 60 keV, afin de maximiser la valeur de Q. Pour certains des échantillons, en raison de la présence de cristaux de taille comparable à la taille du faisceau, des taches de diffraction monocristallines coexistent avec des anneaux de poudre sur les images 2D. Nous avons vérifié que la présence de ces monocristaux entraine une erreur sur la quantification qui reste inférieure à 5%. L'analyse quantitative, conduite à partir des données de haute résolution (HR), donc non corrigées de la contribution monocristalline, reste donc valable. La présence d'un signal de diffraction monocristallin pouvant empêcher une interprétation correcte de la PDF, les images de diffraction 2D ont été pré-traitées à l'aide de la fonction separate de la bibliothèque python pyFAI (Ashiotis et al. [6]), avant l'intégration 2D vers 1D et le calcul de la

transformée de Fourier. Suite au développement de ce pré-traitement, des images 2D ont été obtenues, exemptes de toute contribution monocristalline (Figure 3), et ces données corrigées ont été utilisées pour calculer la PDF.

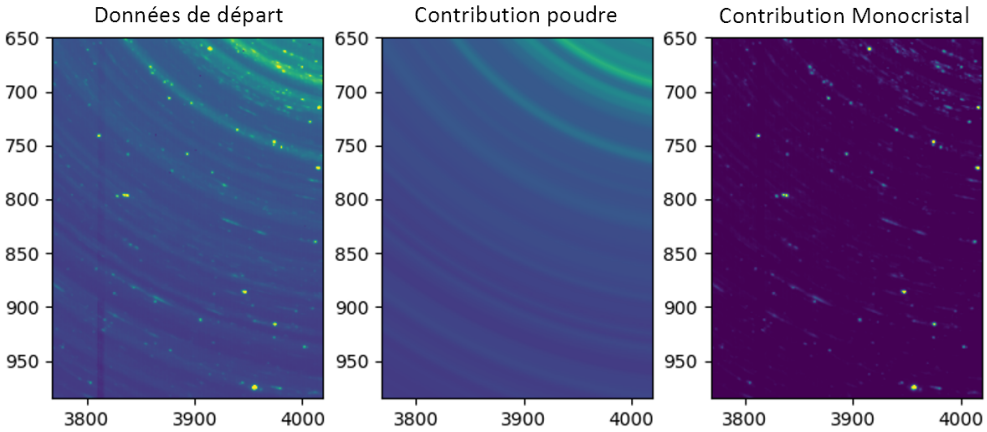

Figure 3: Illustration de la procédure de pré-traitement des données de diffraction 2D avec pyFAI. Sur l'image brute, les anneaux de poudre et les taches des monocristaux coexistent. Les contributions poudre et monocristalline peuvent être séparées, ce qui permet d'intégrer l'image de la contribution poudre puis de calculer la PDF.

Nous avons ensuite utilisé la procédure initialement développée par Cersoy *et al.* [4], et décrite ci-après :

- Affinement de la PDF à grande distance r entre 10 et 25 Å (possible car les phases cristallines ont été identifiées et quantifiées grâce aux affinements de Rietveld effectués sur les données HR). Le résidu obtenu correspond à la PDF de la partie amorphe (Figure 3B).
- Comparaison qualitative de la PDF de la partie amorphe avec les PDFs mesurées dune série de références de pigments carbonés non-graphitiques : noir de fumée et noir de pêche commerciaux, pigments noirs obtenus après carbonisation de sarments de vigne, de coquilles de noix, de noisettes et d'amandes (ces pigments ont été choisis car ils sont décrits dans les recettes anciennes d'époque gréco-romaine de préparation de pigments noirs).
- Identification de la phase amorphe par calcul d'un facteur de corrélation (facteur de corrélation de Pearson) [4] entre PDF de la partie amorphe et PDFs de référence.

Dans huit des échantillons archéologiques, les distances caractéristiques carbone-carbone dans le plan de graphite (1.4 Å et 2.4 Å) étaient présentes, et la PDF montre des caractéristiques similaires à celles trouvées dans les références (Figure 2C), confirmant ainsi l'origine carbonée du pigment noir pour ces huit échantillons. Pour trois échantillons, une phase amorphe différente a été trouvée, qui pourrait être une phase lipidique correspondant à un liant. De plus, pour quatre échantillons, la PDF de la phase carbonée est très similaire à celles mesurées pour les charbons de référence (végétaux carbonisés). Pour l'échantillon P3897, ce résultat est en accord avec l'identification faite par MEB à partir de critères morphologiques (Figure 1).

En rassemblant toutes les informations obtenues à partir des études de morphologie, des affinements de Rietveld et des analyses PDF, une utilisation possible pour chacun des échantillons noirs de la période gréco-romaine est proposée (Tableau 1). Quatre catégories ont été extraites, conformément aux résultats obtenus dans les études précédentes [4] [5].

Table 1: Tableau 1 : Résumé des principaux résultats obtenus sur les échantillons noirs de Pompéi (P) et d'Herculanum (H). Les phases "volcaniques" sont traduites par la présence d'analcime, de sanidine, de leucite ou d'augite. Phases de dégradation (malachite, cassitérite); Charbon veg. = charbons végétaux; Cosm. = cosmétiques; Ox. de fer = oxyde de fer (magnétite). Les quatre catégories d'échantillons ont été mises en évidence avec des couleurs différentes.

Échant.	**Phases Volcan**	**Phases de Dégradat**	**Gypse**	**Lipide**	**Pigment noir**	**Source de carbone**	**Utilisat**	**Récipient**
P2445					Carbone	Charbon veg.	Encre/ Cosm.	Unguentarium en verre
P3897	X				Carbone	Charbon veg.	Encre/ Cosm.	Unguentarium en verre
P9253					Carbone	Charbon veg.	Encre/ Cosm.	Petite nochoé
P11432					Carbone	Charbon veg.	Encre/ Cosm.	Unguentarium en verre
P12458	X	X	X		Carbone	Noir de fumée	Encre	Theca~ atramentaria
P18109	X		X		Carbone	?	Encre	Coupe d'argile
HE03	X	X	X		Carbone	?	Encre	-
HE02	X	X		X	?		Cosm.	-
H75430	X			X	Carbone	?	Cosm.	Ampoule en verre
H76238	X			X	?		Cosm.	Oya d'argile
HE08		X			?		?	-
HE11	X				Ox. de Fer		?	-
P9505	X	X			?		?	Fritillo

La première catégorie (quatre échantillons de Pompéi) correspond à des échantillons dans lesquels des charbons végétaux ont été identifiés comme étant la source probable du pigment noir. Ces échantillons ont été trouvés dans de petits contenants, comme des unguentariums en verre (vase) et œnochoé (pichet), et correspondent très probablement à de l'encre ou des cosmétiques. Les trois échantillons appartenant à la deuxième catégorie contiennent du gypse, en plus du pigment noir identifié dans un échantillon comme étant du noir de fumée. Comme mentionné précédemment, la présence d'un agent de séchage comme le gypse pourrait être en accord avec l'utilisation de ces échantillons en tant qu'encre. La troisième catégorie est composée de trois échantillons d'Herculanum dans lesquels une phase lipidique amorphe a été identifiée. Même si le carbone amorphe a été identifié dans un seul de ces échantillons, la présence d'une phase lipidique est compatible avec leur utilisation en tant que cosmétiques. Enfin, la dernière catégorie contient trois échantillons pour lesquels aucune phase carbonée n'a

été trouvée. En l'absence de tout autre élément, leur utilisation éventuelle reste une question ouverte.

Faire le lien entre l'utilisation des poudres noires et le type de récipient n'est pas simple, et une conclusion n'a été obtenue que pour la première catégorie d'échantillons. Dans le cas des trois autres catégories, plusieurs types de conteneurs ont été utilisés (dans chaque cas, d'un seul type), et des échantillons/conteneurs supplémentaires seraient nécessaires pour préciser notre conclusion.

Papyrus de la collection Champollion

La deuxième partie du projet est consacrée à l'étude de l'encre noire déposée sur des papyrus de l'Égypte ancienne. Les encres noires de l'Égypte ancienne étaient principalement obtenues après avoir mélangé un pigment à base de carbone avec un liant (gomme arabique) et de l'eau [7]. Plusieurs auteurs ont signalé la présence supplémentaire d'éléments chimiques tels que le plomb, le fer ou le cuivre, dont l'origine reste à déterminer (Mocella *et al.* [8], Christiansen *et al.* [9]). Malgré leur origine inconnue, ces éléments ont été utilisés comme agents de contraste pour déchiffrer les inscriptions de papyrus hautement dégradés ou enroulés (Brun *et al.* [3]). Si notre principal objectif est de caractériser l'encre noire trouvée à la surface de 12 fragments de papyrus de la collection du musée Champollion (Figure 4A), le second est de trouver un moyen de lire virtuellement le papyrus ancien en utilisant le contraste structural donné par le pigment noir lui-même, une alternative intéressante en l'absence de contraste chimique.

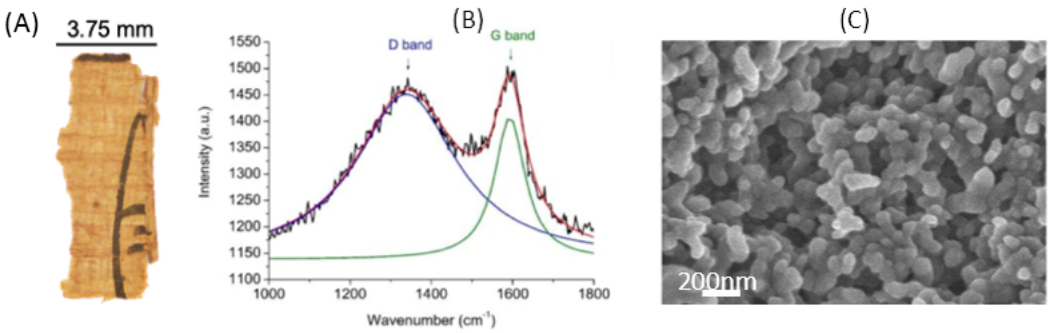

Figure 4: (A) Exemple du fragment de papyrus PAP-1 de la collection du Musée Champollion (Vif, département de l'Isère) montrant des hiéroglyphes écrits à l'encre noire et rouge. (B) Spectre Raman (Institut Néel, Grenoble) enregistré sur l'encre noire du fragment PAP-1. La largeur et l'intensité relative des deux bandes D et G sont caractéristiques d'un composé carboné désordonné. (C) Photo MEB de l'encre noire à la surface du fragment de papyrus PAP-1, correspondant au noir de fumée (Institut Néel, Grenoble).

La présence de carbone amorphe dans l'encre noire utilisée sur les papyrus de la collection Champollion a été confirmée par spectroscopie Raman (Figure 4B). Les matériaux carbonés présentent des bandes dans la région de 1000 à 1800 cm^{-1} dont leur intensité et leur largeur sont fonction du degré de désordre (Jawhari *et al.* [10]). La bande G à 1580 cm^{-1} du graphite s'élargit lorsque le désordre des carbones sp^2 augmente, et de nouvelles bandes apparaissent autour de 1340 cm^{-1} (bandes D). Les bandes G et D ont été identifiées sur les spectres Raman collectés sur l'encre noire de nos fragments de papyrus (Figure 4B), en accord avec la présence d'un pigment à base de carbone à l'état désordonné. L'identification du type de carbone (charbon, noir de fumée ou cokes) a été réalisée en utilisant le MEB et en comparant les morphologies (Figure 4C). La présence de particules sphéroïdales d'environ 85 nm (+/- 10 nm) de diamètre dans les régions comportant de l'encre est en accord avec l'utilisation de noir de fumée (la morphologie d'une référence de noir de fumée est montrée sur la Figure 1).

Le support de papyrus et l'encre déposée sur celui-ci ont également été analysés par diffraction des rayons X. L'encre et le papyrus étant composés respectivement de noir de fumée et de cellulose peu ou pas cristallins, la qualité statistique (au lieu de la résolution angulaire) a été favorisée lors de l'acquisition des données de diffraction recueillies sur ID22 (ESRF) en utilisant le détecteur 2D Perkin-Elmer. Les échantillons de papyrus ont été montés dans des supports imprimés en 3D que j'ai conçus, adaptés à chaque fragment et positionnés dans le faisceau à l'aide d'une platine de translation (Figure 5A). L'affinement de Rietveld d'un diagramme caractéristique du papyrus vierge est montré Figure 5B. Le diffractogramme est dominé par les raies larges de la cellulose, le principal composant du papyrus. En plus de la cellulose, deux phases bien cristallisées d'oxalate de calcium hydratés, la weddellite et la whewellite, ont été identifiées. La présence de ces deux phases résulte de la réaction entre l'acide oxalique présent dans les plantes à croissance rapide comme le papyrus avec le calcium extrait par la plante du sol mais aussi possiblement de la présence de micro organismes sécrétant de l'acide oxalique.

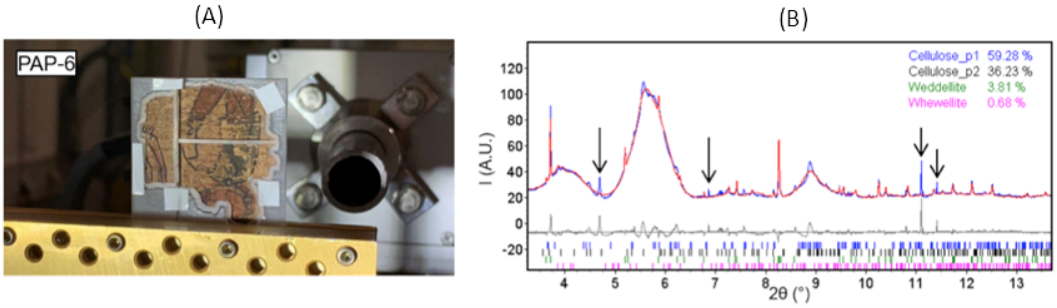

Figure 5: (A) Vue d'un fragment de papyrus (Musée Champollion) monté dans un porte-échantillon dédié imprimé en 3D sur le setup expérimental de la ligne de lumière ID22. (B) Affinement de Rietveld d'un diffractogramme de poudre enregistré sur le papyrus vierge (bleu: données expérimentales, rouge: diagramme calculé, gris: différence). Les flèches noires indiquent des pics de diffraction non indexés.

La forme des principaux pics de cellulose peuvent indiquer la présence de deux phases cellulosiques. Afin de vérifier ceci, deux phases de cellulose basées sur la structure I_β(monoclinique, $P2_1$) de paramètres de mailles différents, ont été introduites dans l'affinement (Cellulose_p1 et Cellulose_p2 sur la Figure 5B). Les pics de Bragg de la cellulose 2 ont une largeur à mi-hauteur (FWHM) plus faible que ceux de la cellulose 1, indiquant une meilleure cristallinité.

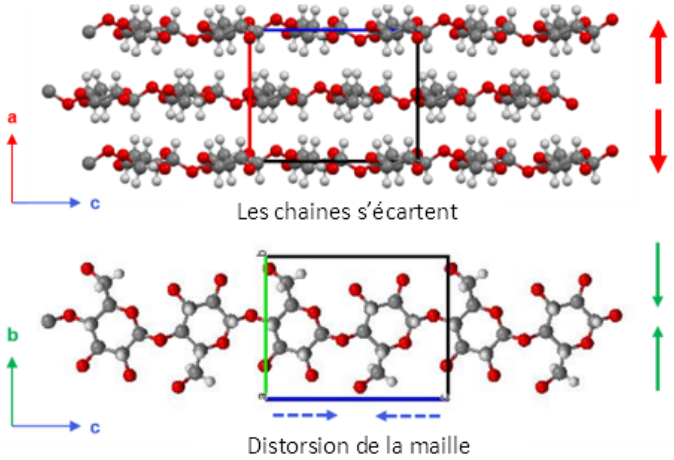

Figure 6: Modifications de la structure cristalline de la cellulose dans le cas du papyrus ancien.

Les paramètres de maille obtenus après affinement sont donnés dans le Tableau 2. Comparé à la cellulose "moderne" (Nishiyama *et al.* [11]), le paramètre *a* des deux phases de cellulose constituant le papyrus est plus grand. En revanche, les paramètres *b* et *c* sont tous deux plus faibles. Cela suggère une modification de la structure cristalline de la cellulose dans le cas du papyrus ancien, illustrée sur la Figure 6. L'augmentation du paramètre *a* indique que les chaînes cellulosiques s'écartent alors que le rétrécissement dans les directions **b** et **c** peut être corrélé à une distorsion ou un réarrangement de la molécule de base. Nous interprétons la présence des deux phases de cellulose et l'augmentation de la distance entre les différentes chaînes comme une indication possible d'un processus de vieillissement. Des investigations supplémentaires sont encore nécessaires pour le confirmer.

Table 2: Tableau 2 : Paramètres de maille des deux phases de cellulose (papyrus ancien) après affinement. Les valeurs de Nishiyama et al. *[11], correspondant à la cellulose "moderne", sont également données à titre de comparaison.*

Paramètres de maille	**Nishiyama *et al.***	**Ce travail Phase 1**	**Ce travail Phase 2**
a (Å)	7.784(8)	7.9582(1)	8.2631(3)
b (Å)	8.201(8)	8.0188(2)	7.7890(1)
c (Å)	10.380(10)	10.2876(4)	10.3337(2)
γ(°)	96.5	98.311(3)	93.694(8)

Afin de rechercher un éventuel contraste structural entre le pigment noir et la cellulose, un diagramme de diffraction collecté sur le sceptre Ouas du dieu Rê (Figure 7) a été comparé à celui collecté sur le papyrus vierge. Le signal du noir de fumée, caractérisé par un pic sur la même plage de Q (1.15Å et 1.64Å), est également représenté sur la Figure 7. Comme attendu, les diagrammes de diffraction sont très proches : d'abord en raison du faible volume diffractant de l'encre noire par rapport au volume du papyrus, mais aussi en raison des principales caractéristiques à la fois du pigment noir et du papyrus : deux composés peu ou pas cristallins.

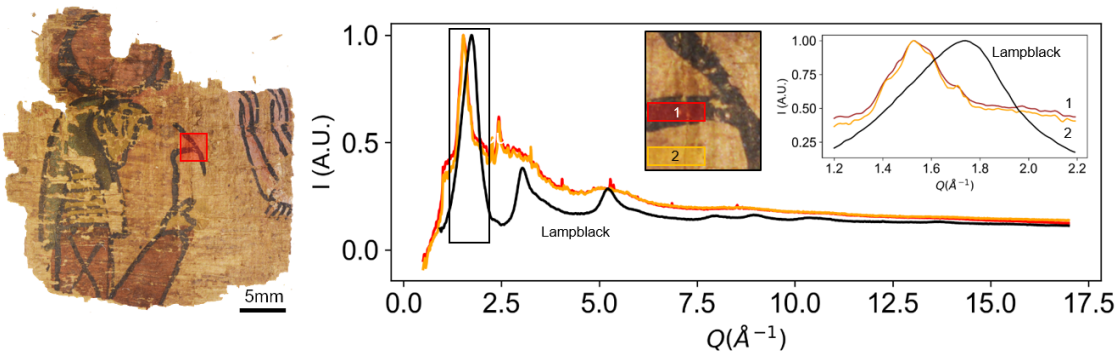

Figure 7: Diagrammes de diffraction de poudre enregistrés sur une zone couverte d'encre et une zone vierge autour du sceptre Ouas du Dieu Rê (Musée Champollion). Le diagramme de diffraction du noir de fumée est également montré pour comparaison.

Un moyen d'améliorer la sensibilité des techniques de diffraction consiste à utiliser la diffraction des rayons X couplée à la tomographie assistée par ordinateur (XRD-CT) (Bleuet *et al.* [12]). Cette technique permet d'obtenir une image de coupe d'un échantillon avec un contraste structural mais aussi de quantifier les phases. Une telle approche s'est avérée efficace pour détecter des phases mineures (jusqu'à 0.1% en volume) et peut être appliquée à l'étude des matériaux cristallins et non-cristallins (Alvarez-Murga *et al.* [13]). Un fragment de papyrus a été

analysé sur la station 3D-XRD de ID11 (ESRF) (Figure 8A), et les deux diagrammes de diffraction de poudre et les spectres de fluorescence-X (XRF) ont été collectés simultanément. Une coupe virtuelle a été reconstruite (Figure 8B), et montre la section de deux cellules parenchymateuses (en forme de tube) du papyrus, prises en sandwich dans deux parois.

L'utilisation du signal de diffraction global de l'ensemble du fragment n'a conduit à aucun contraste entre la zone d'encre et la zone vierge (support). Le signal de diffraction moyen du support a été calculé et, après normalisation avec l'intensité prise sur une plage à grand Q, soustrait du signal de diffraction global. Un contraste est alors apparu et la position de l'encre dans la coupe a été révélée. Ce signal est affiché en orange sur la Figure 8B. Le diagramme de diffraction correspondant à la région de l'encre a été extrait par analyse inverse et comparé au signal de diffraction du noir de fumée de référence (Figure 8B). Un bon accord a été obtenu, confirmant que le contraste entre l'encre et le support de papyrus peut être extrait en se basant uniquement sur le signal de diffraction du pigment à base de carbone. À notre connaissance, c'est la première fois qu'un tel contraste structural est révélé.

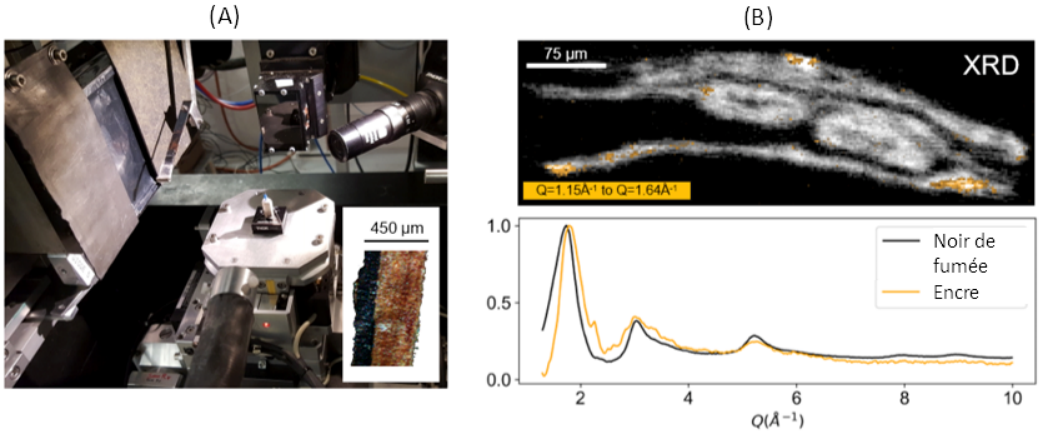

Figure 8: (A) Vue du setup de ID11 pour enregistrer les données XRD-CT sur un petit fragment de papyrus (Champollion Museum). (B) Section reconstruite par XRD-CT. La couleur blanche représente le signal de diffraction sommé et la couleur orange la contribution du signal entre Q = 1.15 Å et 1.64 Å (position du pic de diffraction principal noir de fumée). Le diffractogramme de la zone d'encre obtenue par analyse inverse correspond à celui du noir de fumée.

Un contraste similaire entre le support et l'encre a également été obtenu par XRF-CT en suivant la raie d'émission Lα du plomb, validant le résultat obtenu à partir de XRD-CT. Cela peut ouvrir une nouvelle façon d'enquêter sur les anciens papyrus endommagés ou carbonisés, et utiliser à la fois le contraste structural et chimique provenant du pigment à base de carbone lui-même en l'absence de tout autre contraste chimique. Ces travaux sont publiés dans Autran *et al.* [117].

Conclusion

L'objectif de cette thèse était de comprendre l'origine des pigments noirs à base de carbone utilisés dans l'Antiquité. Pour ce faire, nous avons étudié des poudres noires de Pompéi et d'Herculanum ainsi que des fragments de papyrus de l'Égypte ancienne du musée Champollion. Dans notre approche méthodologique, nous avons employé une combinaison de techniques de microscopie, de spectroscopie et de diffraction. Ces techniques ont été choisies pour résoudre la principale difficulté de nos échantillons : leur hétérogénéité. En effet, du fait de la large gamme de tailles de cristallites et des phases de cristallinité différentes qu'ils renferment, les échantillons archéologiques sont souvent des matériaux complexes. Acquérir de nouvelles connaissances sur

ces matériaux nécessite souvent une méthodologie dédiée comme démontré dans cette thèse.

En étudiant les poudres noires provenant de récipients des sites de Pompéi et Herculanum à l'aide d'affinements de Rietveld, nous avons identifié et quantifié leurs principales phases cristallines. Certaines d'entre elles sont liées à l'éruption volcanique et d'autres résultent de la dégradation d'un composé présent dans la poudre ou provenant du récipient. Ensuite, après une transformée de Fourier du diagramme de diffraction de poudre, une analyse PDF a été réalisée pour obtenir des informations sur la partie amorphe de l'échantillon, en particulier les phases carbonées. L'un des défis auxquels nous avons dû faire face est lié à la présence de gros cristaux dans nos échantillons. Si la quantification de phase n'est pas trop affectée par leur présence, c'est un problème majeur pour mener une analyse PDF pertinente. En collectant des données de diffraction en 2D, nous avons pu séparer la partie poudre des contributions monocristallines, et cette partie poudre sans monocristal a ensuite été utilisée pour calculer la PDF. Connaissant le contenu cristallin de l'échantillon, le comportement à longue distance de la PDF a pu être modélisé quantitativement, et la courbe de différence entre la PDF observée et la PDF calculée fournit la PDF de la partie amorphe. La PDF de la partie amorphe a été comparé à celle des références carbonées. En combinant ces résultats avec les observations réalisées au MEB, nous avons conclu que la plupart des échantillons contiennent des pigments à base de carbone provenant de végétaux brûlés (charbons). Les résultats obtenus sur les phases cristallines et amorphes nous permettent de suggérer les types d'utilisation les plus probables de ces poudres noires dans l'Antiquité. La présence de gypse indique que la plupart de nos poudres sont des encres ou entre dans la composition d'encres tandis que plusieurs poudres contenant des traces de matière huileuse indiquent qu'elles sont davantage liées à des cosmétiques.

Des fragments de papyrus du musée Champollion, écrits et/ou peints, ont ensuite été étudiés. Par rapport à l'étude des poudres noires de Pompéi et d'Herculanum, l'enjeu supplémentaire est de séparer le signal de diffraction du pigment noir de celui du support. Le papyrus est fait de cellulose, et deux oxalates de calcium ont été également identifiés. L'étude du diagramme de diffraction de la cellulose laisse penser à un possible effet de vieillissement, mais des études complémentaires sont nécessaires pour le confirmer.

La plupart des pigments colorés trouvés sur les fragments sont cohérents avec la palette égyptienne classique. Cependant, les couleurs blanche et verte contenaient des phases que nous avons attribuées à une dégradation chimique due à l'interaction entre différents composés ayant évolué au fil du temps. D'autres analyses seront nécessaires pour clarifier les réactions de dégradation mises en jeu. Ces transformations peuvent nous aider à comprendre l'évolution des mélanges avec le temps, et donc, à plus long terme, une aide afin de mieux préserver les fragments de papyrus. Enfin, la présence d'un pigment blanc à base de plomb dans plusieurs fragments nous permet de proposer une datation approximative au plus tôt autour de la période ptolémaïque (lorsque le blanc de plomb a commencé à être utilisé), une période plus tardive que celle que nous avions supposé initialement.

Dans tous les fragments de papyrus qui présentent des traces d'encre noire, le pigment noir utilisé dans l'encre est exclusivement du noir de flamme. Même si des éléments supplémentaires ont été détectés, aucune phase cristalline n'a pu leur être associé, ce qui est conforme à l'utilisation d'encres purement à base de carbone. En comparant le signal DRX du support et celui de l'encre noire (plus support), nous avons montré que la contribution du support en papyrus représente la quasi-totalité du signal. Dans le but d'obtenir une sélectivité spatiale, nous avons utilisé la technique de XRD/XRF-CT. Nous avons été en mesure d'extraire la contribution du pigment noir à base de carbone, ce qui constitue une première. L'utilisation de la XRD-CT ouvre de nouvelles perspectives d'étude des papyrus anciens. L'utilisation du contraste structurel provenant du pigment noir nous permettrait d'être en mesure de "lire" les écrits ou illustrations de déroulé papyrus ou endommagés, en l'absence de contraste chimique.

Pour conclure sur les deux périodes et types d'échantillons que nous avons étudiés, nous observons que les encres noires de la période égyptienne sont exclusivement constituées de noir

de flamme, tandis que les échantillons identifiés comme des encres de Pompéi proviennent de végétaux carbonisés. Si cette tendance peut être un artefact du fait du nombre limité d'échantillons que nous avons analysés, cela pourrait aussi être une indication d'un changement de pratique avec le temps, ou de pratiques différentes en fonction de la zone géographique.

Pour continuer ce projet, plusieurs pistes pourraient être envisagées. La première concerne la possibilité d'analyser un plus grand nombre d'échantillons de pigments noirs à base de carbone, à la fois poudres libres de l'époque romaine et encres sur papyrus de l'époque égyptienne. En particulier, accéder à des papyrus d'une période bien référencée aiderait à mieux comprendre l'évolution des recettes d'encre dans l'Égypte ancienne. Concernant les poudres noires de Pompéi, les échantillons analysés dans cette thèse complètent le premier lot analysé par Cersoy et al. Néanmoins, conclure sur le type de récipients par rapport à l'utilisation de la poudre dans l'Antiquité reste difficile, et regarder un corpus plus grand aiderait à clarifier ce point.

Une deuxième voie à explorer concerne la couleur noire elle-même. Nous avons examiné les pigments noirs à base de carbone de différentes époques et pour différents usages, et il serait intéressant de mieux quantifier la nuance noire de chacun d'eux. Nous pouvons proposer l'utilisation de la colorimétrie, ou de la photographie calibrée sur des surfaces peintes avec une encre préparée contenant différentes concentrations de chaque pigment de référence, et les comparer avec les pigments anciens. Ce serait une façon d'essayer de répondre à la question de savoir pourquoi certains types de sources de carbone ont été utilisés plutôt que d'autres. On suppose que certains pigments apporteraient une teinte spécifique ou une meilleure adhérence au support.

Enfin, il serait également intéressant de se pencher sur les composés organiques contenus dans les encres, peintures et cosmétiques. Cela nécessite une méthodologie orientée sur l'utilisation de la spectroscopie infrarouge, ou d'autres techniques telles que la chromatographie en phase gazeuse - techniques de spectroscopie de masse (même si destructives dans le dernier cas). Cela pourrait donner des informations sur l'évolution possible de la recette dans le temps du point de vue du liant, ainsi que sur la différence de recette en fonction du type d'utilisation de la poudre noire. Une autre piste à explorer concerne la partie méthodologique. En effet, un protocole d'analyse de données a été implémenté dans cette thèse pour analyser les données XRD-CT, collectées en 2018 sur la ligne ID11. Depuis, la machine de l'ESRF a été reconstruite (EBS, Extremely Brilliant Source), offrant un faisceau d'une brillance sans précédent. En conséquence, les collectes de données sont désormais plus rapides, ce qui implique la possibilité de mesurer plus d'échantillons (ou des échantillons plus grands) dans le même laps de temps. En outre, plusieurs lignes de lumière ont été équipées de détecteurs à comptage de photons plus rapides. En utilisant l'ensemble des programmes développés dans cette thèse, l'intégration 2D à 1D seule a pris environ 4 heures pour chaque scan. En utilisant maintenant les données collectées à 500 Hz pendant cinq heures avec le détecteur Eiger2 4M CdTe (Dectris) récemment mis en service sur ID11, 40 heures seraient nécessaires pour effectuer la reconstruction. Les outils d'analyse des données doivent être optimisés et/ou de nouvelles stratégies doivent être développées pour traiter cette nouvelle quantité de données. La librairie PyXRDCT devrait évoluer dans un futur proche, notamment pour profiter d'une éventuelle parallélisation via CPU ou GPU et fonctionner sur plusieurs curs.

En combinant plusieurs techniques, nous avons amélioré nos connaissances sur les encres noires utilisées dans l'Égypte ancienne et les périodes romaines, une étape supplémentaire vers le déchiffrement des messages du passé encore cachés dans les matériaux du patrimoine culturel.

Contents

Acknowledgements i

Résumé de la thèse en français i

Summary xv

General Introduction **1**

1 Carbon-based black pigments: history, techniques of characterization and physicochemical analysis of references **3**

1 Introduction 4

2 Carbon-based pigments in history and recent studies 4

2.1 History of uses of the carbon-based black pigments 4

2.1.1 Carbon-based inks 5

2.1.2 Iron-gall inks 5

2.1.3 Mixed inks 5

2.2 Ancient texts on carbon-based inks 6

2.3 Recent analysis 6

2.3.1 Black powders from the Greco-Roman period 6

2.3.2 Black pigments found on papyrus 7

2.4 Main objectives of the project 7

3 Techniques of characterization 8

3.1 Imaging 8

3.1.1 Optical microscopy 8

3.1.2 Scanning electron microscopy 9

3.2 Spectroscopy 9

3.2.1 Raman spectroscopy 9

3.2.2 X-ray fluorescence 10

3.3 Structural analysis – Diffraction 11

3.3.1 X-ray powder diffraction 11

3.3.2 Crystalline phase identification 13

3.3.3 Whole pattern fitting methods 13

3.3.4 Agreement factors 15

3.3.5 Refinement strategy 15

3.3.6 Fourier transform: the pair distribution function 16

3.3.7 Data acquisition: the ID22 beamline at the ESRF 17

3.4 X-ray diffraction computed tomography 21

3.4.1 About X-ray tomography 21

3.4.2 XRD-CT principle 21

3.4.3 About XRF-CT 22

3.4.4 XRD/XRF-CT on ID11 22

3.4.5 Reconstructing data from an XRD-CT experiment 23

3.4.6 PyXRDCT 24

4 Carbon-based pigments: references and reproductions . . . 24
4.1 References . . . 25
4.1.1 Commercial references . . . 25
4.1.2 Synthesized references . . . 25
4.2 Characterization . . . 27
4.2.1 XRD . . . 27
4.2.2 PDF . . . 29
4.2.3 SEM . . . 30
4.2.4 The case of bone and ivory . . . 32
5 Conclusion . . . 35

2 Study of black powders from Roman archaeological sites 37
1 Introduction . . . 38
2 Powders from Italian Antique containers . . . 38
2.1 Use of black powders in Roman times . . . 38
2.2 Samples from Pompeii and Herculaneum . . . 39
3 Observation by SEM . . . 41
3.1 Sample preparation . . . 41
3.2 Observation and results . . . 41
4 Heterogeneous powders: separating amorphous and crystalline contributions . . . 43
4.1 Introduction . . . 43
4.2 Exploiting the crystalline part . . . 43
4.2.1 Separating the single-crystal and powder contributions . . . 43
4.2.2 Phase identification . . . 49
4.2.3 Rietveld refinements of HR-XRPD data . . . 51
4.2.4 Conclusions, limits, and improvements . . . 53
4.3 Exploiting the amorphous contribution to the signal with PDF fitting . . . 54
4.3.1 Methodology . . . 54
4.3.2 Example . . . 55
4.3.3 Results . . . 56
5 Discussion . . . 58
6 Conclusion of the chapter . . . 61

3 Investigation of pigments found on Ancient Egyptian papyrus 63
1 Introduction . . . 65
1.1 About colored pigments . . . 65
1.2 Carbon-based black pigments . . . 65
1.3 Corpus and objectives . . . 66
2 Writing and painting on papyrus in Ancient Egypt . . . 67
2.1 Papyrus, support of communication . . . 67
2.1.1 The first uses of papyrus . . . 67
2.1.2 Biology of the papyrus plant . . . 67
2.1.3 Manufacturing papyrus writing support and writing techniques 68
2.1.4 Papyrus illustration in Ancient Egypt . . . 69
2.2 The Egyptian pigment palette . . . 70
2.2.1 Minerals used for inks and paints . . . 70
2.2.1.a Copper-based minerals . . . 70
2.2.1.b Iron oxide-based minerals . . . 71
2.2.1.c Calcium-based minerals . . . 71
2.2.1.d Arsenic-based minerals . . . 71
2.2.1.e Lead-based minerals . . . 71

2.2.1.f Carbon-based pigments 72
2.2.1.g Summary 72
2.2.2 Recent studies carried out on pigments from Egyptian papyrus 72
2.3 Methodological approach 74
3 Handling and measuring fragile archeological samples 74
3.1 Finding a suitable support 74
3.1.1 Support adapted for manipulation, transport, and X-ray measurements 74
3.1.2 Specific sample mounting for SEM and EDX 76
3.2 Potential effects from the measurements 77
3.2.1 Scanning electron microscopy 77
3.2.2 X-ray measurements 77
3.2.3 Raman spectroscopy 78
4 Analysis results of the papyrus support 78
4.1 Visual observations 78
4.2 SEM and EDX analyses 78
4.3 XRF of papyrus support 80
4.4 XRD of the papyrus support 81
4.4.1 Phase identification 81
4.4.2 Structure of cellulose 82
5 Analysis of colored pigments on papyrus from Champollion collection 84
5.1 Fragments and analytical techniques 84
5.2 Identification of colored pigments by XRD and XRF 85
5.2.1 PAP-6 – Re 85
5.2.2 PAP-11 – Black and yellow stripes 92
5.2.3 PAP-12 – Cobra and column 95
5.2.4 PAP-7 – Writings 99
5.2.5 The art of papyrus painting 99
5.3 Intentional and non-intentional phases 101
5.3.1 The case of blue 101
5.3.2 The case of red 102
5.3.3 The case of yellow 104
5.3.4 The case of white 104
5.3.5 The case of green 106
5.4 Conclusion 107
6 Analysis of black pigment on papyrus from Champollion collection 109
6.1 The fragments 109
6.2 Identification of the black pigment 110
6.2.1 Raman spectroscopy 110
6.2.2 Morphology of black pigment 111
6.3 Elemental and structural analysis of the ink 112
6.4 Looking for structural contrast using XRD 115
6.5 Retrieving contrast using X-ray diffraction and fluorescence tomography 116
6.5.1 Sample mounting 118
6.5.2 Data optimization 119
6.5.3 Specific data reduction and corrections for XRD 120
6.5.4 Separating pigment from papyrus contributions 121
6.5.5 Results 122
6.6 Discussion 123
6.6.1 Ink recipe 123
6.6.2 Writing on papyrus 123

6.6.3 Contrast in XRD-CT 124
7 Conclusion of the chapter 124

General conclusion **127**

Bibliography **I**

List of Figures **XI**

List of Tables **XIX**

A Physico-chemical analysis data **XXII**
1 Pompei and Herculaneum samples XXIII
1.1 P2445 XXIII
1.1.1 Diffraction patterns phase identification XXIII
1.1.2 Diffraction patterns Pawley fit XXIII
1.1.3 Diffraction patterns 2D and PDF XXIV
1.2 P3897 XXVI
1.2.1 Diffraction patterns phase identification XXVI
1.2.2 Diffraction patterns 2D and PDF XXVII
1.3 P9505 XXVIII
1.3.1 Diffraction patterns phase identification XXVIII
1.3.2 Diffraction patterns Pawley fit XXVIII
1.3.3 Diffraction patterns 2D and PDF XXIX
1.4 P11432 XXXI
1.4.1 Diffraction patterns phase identification XXXI
1.4.2 Diffraction patterns Pawley fit XXXII
1.4.3 Diffraction patterns 2D and PDF XXXIII
1.5 P12458 XXXIV
1.5.1 Diffraction patterns phase identification XXXIV
1.5.2 Diffraction patterns Pawley fit XXXV
1.5.3 Diffraction patterns 2D and PDF XXXVI
1.6 P18109 XXXVII
1.6.1 Diffraction patterns phase identification XXXVII
1.6.2 Diffraction patterns Pawley fit XXXVII
1.6.3 Diffraction patterns 2D and PDF XXXVIII
1.7 HE02 XL
1.7.1 Diffraction patterns phase identification XL
1.7.2 Diffraction patterns Pawley fit XL
1.7.3 Diffraction patterns 2D and PDF XLI
1.8 HE03 XLIII
1.8.1 Diffraction patterns phase identification XLIII
1.8.2 Diffraction patterns Pawley fit XLIII
1.8.3 Diffraction patterns 2D and PDF XLIV
1.9 HE08 XLVI
1.9.1 Diffraction patterns phase identification XLVI
1.9.2 Diffraction patterns Pawley fit XLVI
1.9.3 Diffraction patterns 2D and PDF XLVII
1.10 HE11 XLIX
1.10.1 Diffraction patterns phase identification XLIX

1.10.2 Diffraction patterns Pawley fit XLIX
1.10.3 Diffraction patterns 2D and PDF L
1.11 H75430 LII
1.11.1 Diffraction patterns phase identification LII
1.11.2 Diffraction patterns Pawley fit LII
1.11.3 Diffraction patterns 2D and PDF LIII
1.12 H76238 LV
1.12.1 Diffraction patterns phase identification LV
1.12.2 Diffraction patterns Pawley fit LV
1.12.3 Diffraction patterns 2D and PDF LVI

General Introduction

The study of Cultural Heritage materials is often a challenge, mostly because of their intrinsic heterogeneity but also because of possible transformations and degradation over several hundred or thousand years. Among Cultural Heritage materials, this project will shed light on the nature of carbon-based black pigments from ancient Egypt and Roman times. These pigments were used in various contexts (ink, paintings, cosmetics,...), and resulted from a mix of several components in various proportions. If the multiphase composition can be established, it may be possible to gain a new understanding of the manufacturing process of the pigments, identify some specific markers depending on the period, or identify by-products due to long-term degradation.

From historical recall, several categories of carbon-based pigments can be distinguished. There are three types of carbon pigments in Antiquity defined by J. Winter in 1983 [1]: flame carbons, cokes, and chars. Flame carbons group represents the carbon residues formed by a flame on a surface (lampblack formed by burning oil and soot formed by burning wood). The cokes category designate all the carbon materials produces by carbonizing liquid or plastic state precursors (sugars, gelatins, oils as well as bones). The chars are including any solid precursors that keep their morphology after carbonization. This category holds all the wood-based chars.

Carbon-based pigments were used by Romans hundreds of years B.C. and one of their very first occurrence in Roman texts was in a letter from Cicero to his brother [2]. According to ancient texts, the pigments were composed of flame carbons (soot or lampblack), dregs of wine, or chars. The flame carbon was obtained by burning resin or fats in furnaces preventing the release of smoke. Then ink was produced by mixing the carbon collected on the walls of the furnace, with gum. In recent studies, the different phases composing black powders collected in vessels from Pompeii and Herculaneum sites were identified. In two of these studies, the nature of the carbon-based pigments was also investigated in relation to the use of black powders in ancient times. With a similar approach, we have looked at thirteen additional samples from Pompeii and Herculaneum sites (Coll. M.-C. Gamberini, Univ. Modena). The samples were found in different types of containers, with uncertainty concerning their use in ancient times (e.g. ink, cosmetics, paint,...). Our first objective is to identify the nature of the black pigment, and to identify its type. Based on this knowledge, the second objective is to check for a possible link between the type of container in which the powders were found and their everyday use.

Starting as early as the fourth millennium B.C., Egyptian writings on papyrus spread the knowledge all around the Mediterranean Sea. Carbon-based pigments from the Egyptian period were used in particular as a base for ink manufacturing. Although a large amount of papyri has been preserved, the translated texts do not mention the black ink recipe (to our knowledge yet). The complexity resulting from the non-crystalline nature of carbon-based pigments and the papyrus support, also explains our limited understanding of Egyptian writing techniques. Recent studies on papyri fragments from both Herculaneum and ancient Egypt showed the presence of metallic elements such as copper and lead in the ink, their origin remaining unanswered. Despite their unknown origin, these elements have been used as contrast agents to virtually "read" highly degraded or rolled papyrus [3]. We have established a collaboration with C. Dugand, curator at the Champollion Museum (Vif, Département de l'Isère, France) who provided twelve written and/or painted papyrus fragments. If our first objective is to characterize the black ink found at the surface of the papyrus from this collection, the second one, at the longer term, is to propose a way to virtually read ancient papyrus using structural contrast given by the black pigment itself, an attractive alternative in the absence of chemical contrast.

In this project, the samples are highly heterogeneous materials with the presence of

crystalline and non-crystalline phases under different crystallite sizes. In order to study these samples, a dedicated methodology was implemented in which scanning electron microscopy, Raman spectroscopy, X-ray fluorescence, and X-ray diffraction/PDF data are combined. We will focus in particular on structural studies based on synchrotron X-ray techniques (XRD-CT) with the development of dedicated tools. Our methodological approach will also take care of specificities of the samples for both their preciousness and fragility.

The first chapter of this thesis will set the basis of our study. We will discuss the historical context around black carbon-based pigments, their use in ancient times in ink, and the evolution of the carbon inks into mixed inks and iron-gall inks. We will also summarize the results of recent analyses performed on ancient carbon-based pigments. Then we will see the characterization techniques that we used across this project and their specificity as well as the development we made to adapt them to our type of sample. In the last part of the chapter, the characterization of carbon-based reference samples (commercial and in-house-synthetized), will be given. All reference samples were characterized using the same techniques used on the archaeological samples.

The second chapter will be dedicated to the analysis of black powders from Pompeii and Herculaneum. We will combine spectroscopy and diffraction techniques to identify the phases that compose the powders. We will use the information given by high-resolution X-ray powder diffraction (HR-XRD) to quantify the crystalline phases. For the amorphous part, the pair distribution function will be calculated, to retrieve information about the short-to-medium range structural order of the carbonaceous phases. The black powders being heterogeneous, one of the challenging parts of this chapter will be the separation of the powder and single-crystal contributions in the diffraction signal. In the end, we will discuss the nature of the carbon-based black pigments and their uses taking into account the type of containers they were found in.

The last chapter will be focused on the study of both black and colored pigments from 12 papyrus fragments. The chronology of the different pigments used in ancient Egypt is quite well established, the study of colored pigments will help us to set a context and a period around the fragments from the Champollion collection. The study was carried on using X-ray fluorescence (XRF) and XRD to identify and quantify the crystalline phases. The superposition of the pictural layers, as well as the alteration processes of some pigments, will be discussed. The presence of carbon-based black pigment will be first attested using Raman spectroscopy. Compared to the loose powders studied in the previous chapter, the characterization of carbon-based pigments on a papyrus support, made of cellulose, is more challenging. Indeed, since the support and the pigments are both carbon-based, it will be more complex to extract information about the pigment only. To do so, we used a combination of X-ray diffraction computed tomography (XRD-CT) and X-ray fluorescence computed tomography (XRF-CT) to virtually separate the signal of the ink from its support. A contrast between the ink and the papyrus support has been extracted by relying only on the diffusion signal of the carbon-based pigment.

Identifying the different chemical elements, crystalline and ill-ordered phases present in ancient carbon-based black pigments gives new insights into the manufacturing processes developed in the Roman period and ancient Egypt, as well as the possible aging effect on such historical materials. This work also shows that the study of Cultural Heritage materials allows tackling new methodological challenges that can benefit other areas of materials science.

1

Carbon-based black pigments: history, techniques of characterization and physicochemical analysis of references

Contents

1 Introduction 4

2 Carbon-based pigments in history and recent studies 4

2.1 History of uses of the carbon-based black pigments 4

2.2 Ancient texts on carbon-based inks 6

2.3 Recent analysis 6

2.4 Main objectives of the project 7

3 Techniques of characterization 8

3.1 Imaging 8

3.2 Spectroscopy 9

3.3 Structural analysis – Diffraction 11

3.4 X-ray diffraction computed tomography 21

4 Carbon-based pigments: references and reproductions 24

4.1 References 25

4.2 Characterization 27

5 Conclusion 35

1 Introduction

In this first chapter, we will set the context around this Ph.D. project. We will provide essential information about the development of our scientific approach on the study of ancient carbon-based black pigments but also more generally on heterogeneous materials.

In this project, we are mostly dealing with the physicochemical analysis of cultural heritage materials. The first step to understand is: what do we have in front of our eyes? This question has many sub-questions such as: what is the sample made of, in which context, at which period? Is the object that I see supposed to be like it is currently, or did it degrade over time? Then, the following questions appear: How can I probe it without damaging it and get the information I need?

All these questions are already present before any experimental approach and this is the objective of this chapter to answer them.

We propose in this chapter to start with a review of ancient texts describing black pigments, especially based on carbon. These texts are mostly dealing with the manufacture of black pigment and its preparation combined with different additives to produce inks, paints, or make-up. Then we will show some of the recent studies that were performed on ancient carbon-based black pigments, especially focusing on ancient Egypt and the Roman periods.

The next part will be on the characterization techniques that will be used in the project. We will focus on the technique itself, the data processing, and the information we can obtain from them.

Finally, we will apply those techniques to a set of reference samples. These references were carefully chosen based on ancient texts and from what we expect to find in the archaeological samples. This will help us to set a comparison when we will deal with our archaeological samples.

2 Carbon-based pigments in history and recent studies

2.1 History of uses of the carbon-based black pigments

In this manuscript, we will focus our attention on objects from Antiquity. Most of the knowledge about ancient carbon-based black pigments is described either by ancient texts from the Greco-Roman period or by observations and studies made on artifacts in the last two centuries. Black pigments were traditionally used for three purposes, inks, paint and cosmetics. In the following part, we will assume that inks and paints are not distinguishable from one another in ancient times. Since the pigments responsible for the color are the same, only remain the binder that could be different especially when looking at inks and paints compared to cosmetics. In the next part, we will use only the term ink to describe either inks or paints.

During Antiquity, we can distinguish three categories of black ink: inks exclusively made of carbon, iron-gall inks, and mixed inks made of carbon and metallic elements. The earliest black pigments for inks were made of carbon only and evolved toward the use of metallic elements. This could have been the result of the nature of a change in the support used for writing or painting [14]. It started with papyrus where carbon ink easily adheres, and the shift toward the use of parchment made the transition toward the use of iron-gall inks.

A book describing exhaustively the history of these black inks in Antiquity up to 1600 AD written by Monique Zerdoun Bat-Yehouda [7] summarizes the manufacturing and uses of inks over the ages. The author managed to translate and interpret a large number of ancient texts, and this with the main problem of interpreting correctly the words in their context. This book from which we will focus on the periods before the Roman ages and around the Mediterranean will help us to understand the ink manufacturing processes in the next part.

2.1.1 Carbon-based inks

The first attested black writings in ancient Egypt, dating from the fourth millennium BC, have been found on a series of gesso objects [15] from tomb group 1466 in the cemetery of Armant [16]. Manufacturing a carbon-based black ink resides in mixing the black pigment with a binder and water.

There are three types of carbon pigments in Antiquity: flame carbons, cokes, and chars. These categories were defined by J. Winter in 1983 [1] [17] and E. Tomasini [17]. Flame carbons group represents the carbon residues formed by a flame that produces soot (i.e. not complete combustion). From this group there is lampblack, the residue formed by burning oil, and soot, the residue formed by burning wood. The cokes category designates all the carbon materials residue produced by carbonizing liquid or plastic state precursors, from which the morphology is irregular. In our case, it includes sugars, gelatins, oils as well as bones. The chars include any solid precursors that keep its morphology after carbonization. This category holds all the wood-based chars.

Concerning the binder, its role is to both stabilize the mixture and thickens the preparation. The grains of finely grounded carbon are not soluble in water, they aggregate because of Van der Waals interactions. To stabilize the carbon particles in water, the binder is added to the solution of water plus carbon. This binder can be either glucosidic-based (gum Arabic, honey), protein-based (skin glue, egg white), or lipid-based (oils). In the example of gum arabic, the binder dissolves in the water, one side of the molecule "sticks" to the carbon grains and coat it surface while the other side behaves like a tail. This surface covered in binder molecules tails make the grains repelling each other because of the hydrophilic nature of their tails lowering the importance of grain-to-grain van der Waals interaction. This is disabling the flocculation process and makes a stable colloidal solution [18].

2.1.2 Iron-gall inks

The ingredients for the base of an iron-gall type ink (involving tannins and a metallic salt) were firstly described by Philo of Byzantium in the late second century BCE in *Belopoeica* [19]. Philo of Byzantium described the reactions to produce sympathetic inks (also known as invisible inks) [**?**]. The process was inspired by the leather black dyeing, in which the vitriol reacts with the leather tannins darkening its color.

Specifically, the iron-gall ink production relies on the reaction of two compounds, tannins, and sulfate salts. The first attested recipe is written in the Papyrus Y of Leiden [20]. Tannins are obtained after the maceration of vegetables (oak galls) in water for a long period (months). Then after filtration, a sulfate salt is added, most of the time iron or copper sulfate. Iron sulfate which comes from vitriol reacts with gallic acid contained in tannins and oxidizes in presence of air. This reaction was not deeply studied and remains to be sorted out. In the end, before use, a binder is also added to thicken the mixture. This type of ink used mainly for parchment writing, appeared to be corrosive, compared to the carbon ink which is rather neutral to the support. This property makes the preservation of the support not often ideal, leading to major degradation over time [7].

2.1.3 Mixed inks

Carbon-based inks are known to be the very first uses of black inks. Between the apparition and the use of iron-gall inks, there is an uncertain period where a range of preparation may have been hybrid. Those types of inks are called mixed inks. Those are carbon-based inks containing metallic elements or iron gall inks in which carbon was added.

2.2 Ancient texts on carbon-based inks

Three main ancient texts refer to black carbon-based pigments. All of them are belonging to the Greco-Roman period, and sadly there is no text older than them (up to our knowledge) that could attest to the eldest uses of black pigments, especially in ancient Egypt.

Written by Roman architect Marcus Vitruvius Polio between 30 and 15 BC, *De architectura* is the only treatise about antique architecture. Even if the main topic is architecture, Vitruvius explains (Book VII, Chapter X) that to produce a black pigment, we can burn a resin, collect the soot, on a wooden vault that had to be polished [21]. He specifies that if you don't have enough time, you can also burn branches or pine shavings, or even dried wine lees, and mix the charcoal obtained with gum (typically gum Arabic) to produce ink and skin glue to make paint.

The second text was written by Dioscorides. Pedanius Dioscorides wrote *De Materia Medica* between 50 and 70 AD. In this book (Book V, 62) [22], he gives similar explanations and another recipe where this time you still have to add two binders of different kinds of gum, but also bull's glue, as well as the use of metallic salt. He thus already describes a mixed carbon ink. As Dioscorides was mainly interested in medicine, he specifies that this mixture is also suitable for making plasters and treating both wounds and burns.

Finally, Pliny the Elder wrote *Naturalis Historia* from 77 to 79 AD. In the book XXXV, 41 written in 77 AD about the description of the ink manufacturing, Pliny was largely inspired by Vitruvius from which he copies almost the same recipe, just adding a mention specifying that vinegar must be added a priori to make the ink more tenacious. Otherwise, it is easily erased. He adds that you can also put absinthe to keep rodents away [23].

To conclude on these three texts, none of them was originally about inks or pigments but on other topics. These texts mostly describe the pigment itself and tell less about the binder used for inks. None of them describe the state in which the ink was during the manufacturing process, or during use. No other elder text was found so far, and we rely on these as starting recipes for more ancient manufacturing processes such as the one used by ancient Egyptians.

2.3 Recent analysis

2.3.1 Black powders from the Greco-Roman period

A set of black powders from Pompeii were analyzed by Gamberini *et al.* [24]. This set was part of a series of 1300 small containers found in Casa Bacci House from which around 30% were containing traces of powder. These powders may have been used as pigments, inks, paints or cosmetics. This study relies on the use of Raman spectroscopy, Fourier-transform infrared spectroscopy (FTIR), and gas chromatography mass-spectrometry (CG-MS) techniques applied to 133 black to grey samples.

From this set, black powders were found to be containing amorphous carbon particularly soot (author mention fuligo) and in several cases, apatite. On the other hand, the presence of fatty acids and beeswax indicated that some of the powders may have been used as cosmetics. Authors precise that the distinction between cosmetics and painting materials is loose.

Following this study, Canevali *et al.* [5] analyzed nine black powders from this set from different types of bronze vessels. This set was part of a series of 1300 small containers found in Casa Bacci House from which around 30% were containing traces of powder. The carbon found in the sample is associated with a vegetable char. From this, the analyses of the powders enabled to correlate the use of cylindrical *theca atramentaria* as a container for writing inks whereas *unguentarium* and *aryballos* containers may have contained inks as well as cosmetics.

To go further, Cersoy *et al.* [4] set up a new methodological approach to identify the different types of carbon origins that could be used to produce these powders. This study was focused on five samples from the same collection. The authors used XRD to identify and quantify the crystalline powder contribution. Pair distribution function (PDF) was also used to extract

information from the amorphous part of the samples, in this case, most of the time organic compound and carbon. They managed to identify three types of powders: charred vegetables with calcium phosphates, metallic phases with lipids, as well as a mixture of charred vegetables and gypsum.

2.3.2 Black pigments found on papyrus

Concerning black pigments found on papyrus, Mocella *et al.* [8] were the first to reveal writings from rolled papyrus from Herculaneum that were carbonized due to the Vesuvius eruption in 79 A.D. These rolls of carbonized papyrus are impossible to unwrap because of their extreme fragility. With X-ray phase-contrast tomography (XPCT) performed on ID17 at the ESRF, the authors were able to virtually unwrap the roll to identify several written characters.

Following this study, Brun *et al.* [3] thanks to X-ray fluorescence microscopy (XRF, ID21 ESRF) and FTIR were able to read letters from papyrus fragments from Villa dei Papiri. XRF revealed the presence of lead in the ink used to write. The contrast obtained with XRF revealed the letters that were hardly optically visible.

On the same corpus, Tack *et al.* [25] used XRF and X-ray absorption fine structure (XAFS, ID21 ESRF) to identify the origin of the lead present in the ink. They conclude that the presence of lead is not accidental. However, they were not able to explain the origin of the lead.

Delange *et al.* [26] carried out an extensive study on the Louvre museum papyrus collection. The analyzes were carried out with the AGLAE accelerator using the particle-induced X-ray emission (PIXE) method. It showed the existence of a relationship between the nature of the ink, the language, and the scribe instruments that were used. She worked on papyrus dated to the 3rd century B.C., written in both Demotic and Greek, and showed that demotic writing always corresponded to carbon-based ink and that many metallic elements (copper, lead, zinc, and iron) were present in the ink of Greek writing. The presence of metallic elements may be correlated to iron-gall inks but the hypothesis remains to be confirmed.

The Carlsberg papyrus collection was studied by Christiansen *et al.* [27]. A corpus of twelve papyrus from 1st to 3rd century B.C. were analyzed with XRF, SEM-EDX and XANES. By tracking the presence of copper in the fragments, the authors were able to show that the black ink contained copper. They argue that the copper comes from residues of metallurgy processes that were employed to manufacture the carbon pigment.

Finally, Ghigo et *al.* [28] studied a corpus of 133 papyrus, parchment, and paper from a 3rd century CE up to the 11th century CE. Their goal was to track the evolution of the carbon ink into the iron-gall ink using Raman spectroscopy, FTIR, and XRF. They conclude that the transition from carbon to iron-gall ink was not a function of time according to their corpus, but rather relying on the environment in which the ink was produced. Some economical factors could also have been the reason for the choice of the expensive iron-gall ink for more valuable documents and the cheap carbon-ink for ephemeral manuscripts.

2.4 Main objectives of the project

The previous parts helped us to understand different aspects of carbon-based black pigments, either looking at ancient recipes or descriptive texts or from recent studies that try to match ancient recipes to archaeological samples. These studies revealed that carbon-based pigments can potentially be of different origins (flame black, chars...). In addition, the presence of metallic elements in certain inks was shown, the origin of these still under debate.

Most of the previous studies are based on spectroscopic techniques. In our project, we want to focus rather on the structural nature of the compound present in the carbon black inks. This analysis would allow identifying more precisely the source of the carbon in the pigment. We keep in mind that spectroscopy techniques are still valuable information and we will also consider them as previous authors did.

Our study will aim to understand if the use of a specific carbon precursor was used at a specific time, based on the analysis of two different types of samples, powders from Pompeii and papyrus fragments from ancient Egypt. From the ancient texts and recent studies, we expect to find carbon-only pigments in ancient Egyptian papyrus while possibly a testimony of the evolution of the ink towards the iron-gall inks in the Roman period powders. We will aim at confirming or not the presence of metallic elements in the carbon-based black powders to add information on the quest to understand the evolution of the use of metallic elements in black inks through the ages.

In practice, we will face complex situations because of the nature of the samples. Since we have archaeological samples we can only perform non-destructive characterization techniques on them. Moreover, the heterogeneous nature of those samples will add a level of complexity to the analysis of the data. We will have to develop a series of sample-specific data corrections, involving analyses to separate the contributions from heterogeneous samples. All of these techniques will be detailed in the next part.

3 Techniques of characterization

In the next part, we will cover what type of experimental techniques we can perform to try to track down the origin of the carbon, from samples both from Roman and Egyptian times. These non-destructive techniques will be set up for the analyses of both powder samples as well as papyrus fragments.

3.1 Imaging

3.1.1 Optical microscopy

The optical microscopy analysis was done on Nikon Eclipse LV100ND optical microscope, located at the Néel Institute in Grenoble, France. The microscope has three objective lenses of x5, x10, and x20 coupled with an x10 ocular lens. The sample stage can handle 150x150mm samples with coarse and fine adjustment knobs. The microscope has a built-in camera of 2558x1920 pixel resolution.

The main advantage of this microscope compared to a classic one is its capability to record composite images taken at different focal lengths. This is particularly helpful when the observed sample is not perfectly flat. On one side we lose the depth of view, but we gain sharpness on out-of-focus parts of the sample. This allows us to produce better images of our samples, particularly on the papyrus fragments that had rough surfaces because of the presence of large grains. One example of a picture taken on a papyrus fragment shows the problem of out of focus areas in an extreme case even with the use of such correction (Figure 1.1).

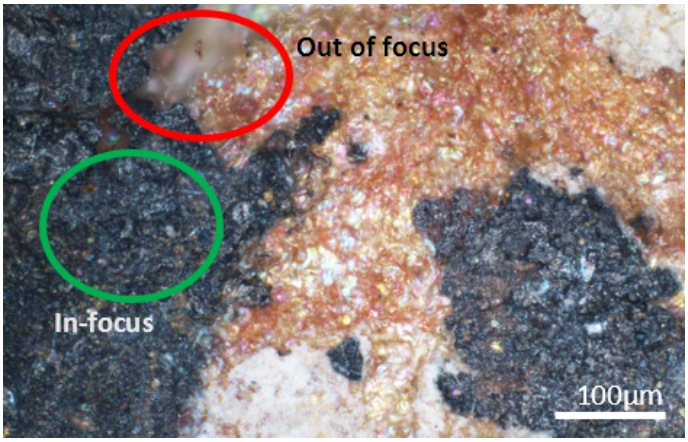

Figure 1.1: PAP-6 fragment surface observed at a black part to white ink junction. The picture is recorded with x20 objective lens.

3.1.2 Scanning electron microscopy

To perform the SEM observations we used a Zeiss Ultra Plus microscope located at the Néel Institute in Grenoble, France. The SEM is a Field Emission-Scanning Electron Microscope (FE-SEM) which provides an extremely focused electron beam with the possibility of being used at a low voltage. The Zeiss Ultra Plus has In-lens and Type II Secondary Electron (SE2) detectors to provide topographic images while Energy Backscatter Detector (EsB) and Annular Backscatter Detector (AsB) give element contrast images. Besides, the microscope can perform energy dispersive X-ray (EDX) analysis thanks to a Silicon Drift Detector (SDD) from Bruker. The EDX analysis gives the elemental composition of the sample both point to point or by mapping an area.

3.1.2.1 Basic principles and uses

The SEM technique is mainly used to image objects with a magnification almost a thousand times higher than optical microscopy. This will be particularly helpful for us to track down the microstructure of our samples.

An electron beam is produced in a gun and focalized on the sample with electromagnetic lenses. This beam is scanned across the sample and electrons interact with matter. These interactions result in signals that are captured by specific detectors. For every step in the scan, the signal is then amplified and displayed on an image as a pixel. The result is an image where the contrast is attributed to an effect of the interaction between the beam and the surface of the sample.

3.1.2.2 Electron-matter interactions in SEM

The interactions can be divided into two types, the elastic interaction, and the inelastic interactions. The elastic interactions are happening when no energy from the incident electron is lost when encountering the sample. In practice, the electron undergoes attraction forces from the nucleus of the atom. The electron is then scattered in a different direction from its incident angle. The closer the electron is approaching the nucleus, the higher the deflection will be. Electrons can undergo a sufficient deflection to be scattered back out of the specimen, they are called backscattered electrons (BSE). The probability of elastic scattering and, thus the possibility of BSE presence, increases with the atomic number squared Z^2, but decreases as the energy is higher, with a $1/E^2$ ratio.

Inelastic interactions correspond to a loss of energy because of the interaction of the incident electron with an electron from an atom of the sample. The incident electron is scattered and a secondary electron is emitted. This energy loss increases with the traveled distance of the electron in the sample. Both of these electron interaction types lead to a distribution of electron paths in the sample called the interaction volume. The shape and size of the interaction volume depend on the amount of elastic and inelastic scattering in the sample, which relies on the sample nature and beam parameters. Since the beam parameters are known and can be adjusted, the operator can tweak these parameters to probe the sample to have different information.

Most of the observations were carried out with the secondary electron detector to obtain a greater contrast based on the sample topography. The experimental conditions for each type of sample as well as specific mounting mechanisms will be detailed in the part dedicated to the results.

3.2 Spectroscopy

3.2.1 Raman spectroscopy

Raman spectroscopy is a method for characterizing the molecular composition and structure of a material. Raman scattering arises from the light-matter interaction and results from molecular

and crystalline vibrations. It is non-destructive, fast, and above all very sensitive to short-range ordering, which makes it possible to obtain different and complementary information from diffraction techniques. When a sample is subjected to a monochromatic electromagnetic wave, most of the incident beam is transmitted, but a small part of the light is scattered. The analysis of the scattered light then reveals a component of the same wavelength as the incident beam called the elastic scattering, and a component of a different wavelength called the inelastic scattering or Raman scattering. The measurement is taken directly on the sample placed on a glass slide. Our samples were investigated using two different radiations with the aim to confirm the presence of amorphous carbon on papyrus samples:

- the 633nm radiation wavelength on a WITec Alpha 500 Raman spectrometer coupled with an iDus 401 CCD camera. The spectrometer was coupled to a 600T/cm filter. The spectra were corrected and assembled with the WITec software suite.
- the 785nm radiation wavelength on a HORIBA T64000 Raman spectrometer coupled with a 1200T/cm filter.

In both cases, the measurement area is around $1\mu m$ and several points per sample are made to obtain better statistical values. All measurement points were restrained to 1mW power and between 20 and 60 seconds of acquisition time per point to avoid beam damage. An average of five points per sample was taken. Most of the measurements were oriented around the D and G bands of the carbon, between 1000 and 1800cm^{-1}. A 2-band model was used to fit the position and the width of the two bands.

3.2.2 X-ray fluorescence

X-ray fluorescence (XRF) delivers elemental composition information that can help to identify compounds present in our samples. By exposing the sample to an X-ray beam, the X-ray photons interact with the core electrons of atoms and eject them as photoelectrons. Electrons from an outer shell move to the inner shell to fill the vacancies. The energy of these electrons is becoming lower and so the energy difference is liberated as X-ray photons. These photons have specific energies that are characteristics of emissions lines of certain energy transition states.

In an experiment, we expose the sample to the X-ray beam (i.e. the synchrotron X-rays in our case, at the ID22 and the ID11 beamlines, ESRF) and by the reaction to that, the sample emits (among others) fluorescence X-rays. They are collected by a silicon drift detector (SDD) which measures the energy of an incoming photon based on the ionization of silicon. The signal obtained is a spectrum of the count per energy channel (usually 4096 channels). The energy of the X-ray beam is chosen based on the potential presence of certain elements. We use an incident energy 1.2 to 1.5 times higher than the emission line of the element we target to be sure that the energy is sufficient to reach this emission line.

In this project, we use two different ways of obtaining fluorescence information.

The first way is simply to put the sample and illuminate it with an X-ray beam which has a size relatively close to the sample size. This method is the basic way to obtain the elemental composition of the sample. This is suitable for samples in capillaries or to average the fluorescence signal from an area.

The measured fluorescence signal is analyzed using the PyMca software [29]. The software allows to import the fluorescence spectrum, and associates the peak position to an element emission line. To do so, we start the experiment by putting reference elements that have one or several emissions lines in the energy range we will use. Then we calibrate the detector channels with a simple linear equation based on the emission line of the reference. The software can also fit the fluorescence spectrum to obtain a semi-quantification of the elements. The peak fitting model is based on a Gaussian distribution. The user has to input a matrix that provides

information about the estimated chemical nature of the samples, as well as sample-detector distance and beam energy. Then the program deconvolutes the contribution of each element in the spectrum. The result serves two purposes, first confirming the nature of the elements thus (and revealing maybe unidentified elements), and secondly quantifying elements relative to each other.

Secondly, there is the mapping technique. It is particularly helpful in our case for two reasons. If the sample can be assimilated as a quasi 2-dimensional sheet at the measurement scale, then the cartography of the elemental distribution is quite easy. Such a possibility will be used in the third chapter, in the case of superimposed pigment layers on papyrus fragments.

The maps are built also with PyMca software, using the ROI Imaging tool on a ".hdf5" file containing the dataset. A dataset is built from assembling a 3D matrix with XYZ dimensions. X and Y are the positions of the steps of the scan and Z, the third dimension contains the data collected from the detector.

In practice, the principal elements from the spectrum are isolated using the Roi Imaging Tool, with ROI (Regions of Interest) define by selecting minimum and maximum energies around a peak. The peaks used corresponds to the signal of Kα, Lα or Mα lines. The displayed images are obtained by the extraction of the contribution to the signal after background subtraction. This subtraction corresponds to the removal of the signal below a straight line between the minimum and the maximum of the defined ROI. The mapping analysis remains a qualitative analysis and allows localizing the elements. We can note that the semi-quantification procedure is the same as described for point measurement.

The main drawback of the XRF technique is the energy range. The setup we used was optimized for an energy range between 4 to 30keV in energy. Because of this, it was not possible to get information on light elements. The light elements (Z<18) will emit X-ray photons that can easily be absorbed by the environment leading to low to no signal on the detector.

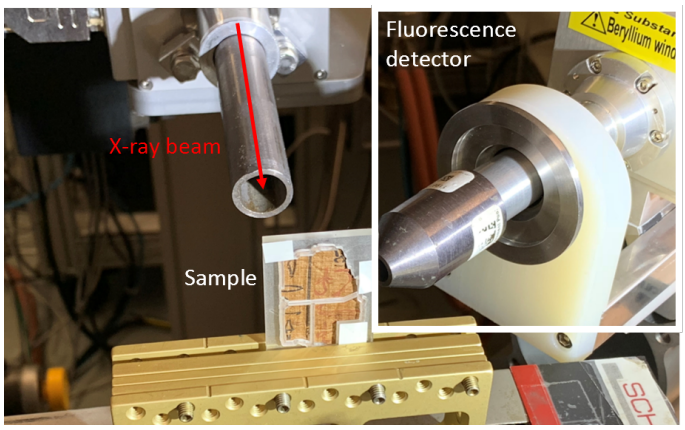

Figure 1.2: XRF setup on ID22 beamline with SDD fluorescence detector. The sample is on XYZ stage to acquire 2D maps.

3.3 Structural analysis – Diffraction

3.3.1 X-ray powder diffraction

3.3.1.1 What is XRPD?

The diffraction phenomenon corresponds to the bending of a wave encountering an obstacle. When a coherent wave encounters an object that has a size comparable to the wavelength of the wave, it can result in interferences.

In the case of X-ray diffraction, the wavelength of X-ray beam is in the range of the Ångström unit (10^{-10}m). This distance corresponds to the distance between atoms in a lattice of a crystal. Each atom, each molecule is a diffusing center for incident radiation of such a short wavelength.

When the X-ray beam is scattered by a crystal, interference occurs between the waves scattered by each scatterer (atom, molecule). Due to the periodicity of the crystal, intense diffusion is observed in discrete directions. This phenomenon is called crystal diffraction.

When the X-ray beam encounters a large number of crystals randomly oriented, the discrete directions that were a set of dots appear now as rings on the detector plane. This is due to the infinite number of planes diffracting in a different direction for each crystal. An infinite number of small randomly oriented crystals corresponds to an ideal powder. On the other side, a finite number of diffracting crystals will move the case towards single-crystal diffraction where each crystal produces a discrete set of diffraction spots on the detector plane.

3.3.1.2 What information holds XRPD?

The raw data collected in an X-ray or neutron powder diffraction experiment consists of a set of intensities recorded at regular intervals in a given angular domain. They constitute a diffraction pattern, which will then be analyzed according to the theory of diffraction. Three types of information can be obtained from a diffraction pattern.

The position of the peaks. In a polycrystalline powder, the grains are made up of monocrystalline domains, also called crystallites, which coherently scatter the X-rays. From a geometric point of view, the diffraction of an incident beam by a family of reticular planes hkl occurs only if Bragg's law is satisfied (Equation 1.1):

$$2d_{hkl}sin(\theta_B) = n\lambda \tag{1.1}$$

where:

- d_{hkl}d is the interreticular spacing,
- θ_B is the angle of the incident beam,
- n is the order of the reflection,
- λ is the beam wavelength.

The profile shape. It describes the intensity distribution around the Bragg position $2\theta_B$. Indeed, a diffraction line is never built from a single Dirac peak but the profile of the diffraction lines is broadened. Two components responsible for this enlargement can be distinguished:

- the first is the instrumental contribution to the profile of the lines. It is linked to the intrinsic characteristics of the diffractometer and the wavelength dispersion of the primary radiation (beam optics, monochromator, detector, etc.)
- the second corresponds to the contribution of the sample to the diffraction profile, which one generally separates into two effects: the size effect, which appears when the dimensions of the crystallites are very small, and the effect of micro-deformations. The latter corresponds to local variations of the local displacements of the atoms with respect to the ideal positions, which can come from residual or applied stresses, from a chemical composition gradient, or from any other crystalline defect such as dislocations or vacancies.

The intensity of the diffraction peaks. The intensity of the diffraction peaks is obtained by integrating the diffraction profile for each reflection (hkl). When line overlap becomes important, profile modeling techniques must be used to separate them. It can be noted that the intensity of the continuous background can also be rich in information. It is made up of contributions due to both the processes of interaction of the incident beam with the sample

(fluorescence and Compton scattering for X-rays, incoherent scattering for neutron diffraction, diffuse thermal scattering, scattering of an amorphous phase, or disordered within the powder ...) and instrumental effects (air scattering, sample holder, electronic noise, ...). While most of these processes generate a continuous background, which is often modeled by a polynomial when analyzing diffraction patterns, the diffusion of an amorphous or disordered phase within the powder may be due to the origin of a more or less structured signal.

3.3.2 Crystalline phase identification

Based on the information that holds each XRPD pattern, we can identify the phases that are responsible for the peaks in the pattern. The set of peaks for each phase will have different peak positions, peak intensities, and peak widths. So each powder will have its own set of peaks corresponding to its crystal structure. This means that if we can compare our diffraction pattern to a set of other diffraction patterns, we can identify the phases present. In practice, the comparison will be based on peak positions, and peak intensities. The phase identification theory is based on the minimization of the difference between peak position and intensities of the experimental data and a database. We define a number called the Figure of Merit (FoM) that is calculated for each phase of the database compared to the experimental data. The FoM is expressed with the formula (Equation 1.2):

$$FoM = \sqrt{\frac{FoM_{db} \cdot (w_\theta \cdot FoM_\theta + w_I \cdot FoM_I + w_{ph} \cdot FoM_{ph})}{w_\theta + w_I + w_{ph}}} \tag{1.2}$$

where,

- FoM$_{db}$ is the contribution from intensities of the database,
- FoM$_\theta$ is the contribution from the difference of the 2θ,
- FoM$_I$ is the contribution from the difference of the intensities,
- FoM$_{ph}$ is the contribution from intensities of the experimental data.

In practice, we used the software DIFFRAC.EVA v5.0 from Bruker to compare the experimental dataset to the database PDF2-2003.

3.3.3 Whole pattern fitting methods

Modeling techniques consist of fitting a calculated model to an observed diffraction pattern and extracting from a group of lines, the parameters defining each individual component. The modeling of a diffraction diagram can be done according to two whole pattern approaches. The Pawley fit consists in refining the calculation of the diffraction peaks position based on the lattice parameters and unit cells. The second approach is the Rietveld refinement. In this case, the position and intensity of diffraction peaks are calculated from the crystal structure (i.e. atoms positions). In both cases, the calculated diffraction pattern is compared to experimental data and the difference between the calculated pattern and experimental data is minimized.

3.3.3.1 Full pattern matching: Pawley fit

In this approach, the total profile is analyzed without reference to a structural model. The observed intensity y_{obs_i} at each step i is modeled by a calculated intensity. The formula expressing y_{calc} is given by (Equation 1.3):

$$y_{calc} = y_{b_i} + \sum_{k=k_1}^{k_2} I_k \Omega_{ki} \tag{1.3}$$

where,

- y_{b_i} represents the background noise at step i,
- $\Omega_{ki} = \Omega(2\theta_i - 2\theta_k)$ describes the shape of the peak k at the Bragg angle $2\theta_k$,
- I_k is the intensity of the $k^t h$ peak of the diagram contributing to the measurement step i.

The position of the lines is constrained by the lattice parameters and their intensity is deduced from the experimental profile.

3.3.3.2 Structure fitting: Rietveld refinement

Rietveld refinement is a profile refinement technique proposed by H. Rietveld [30]. It is the most common procedure for analyzing powder X-ray diffraction patterns when the crystal structures of the phases present in the sample are known. Rather than considering the individual integrated intensities of the Bragg peaks for structural refinement, the Rietveld algorithm makes it possible to directly adjust the overall profile of the experimental diffraction pattern. It is using the profile parameters (instrumental characteristics, profile function) and structural (atomic positions, site occupation, atomic displacement parameters). In the case of a sample corresponding to a mixture of n crystallized phases, the intensity calculated at the point i takes the following general expression (Equation 1.4):

$$y_{calc} = y_{b_i} + \sum_{\phi=1}^{n} S_\phi \sum_{k=k_1}^{k_2} J_{\phi,k} L_k P_{\phi,k} O_{\phi,k} M_k \left|F_{\phi,k}\right|^2 \Omega_{i,\phi,k} \tag{1.4}$$

where,

- S_ϕ is the scale factor of the phase ϕ
- $J_{\phi,k}$ is the multiplicity factor of the kth reflection
- L_k is the Lorentz polarization factors
- $O_{\phi,k}$ is the effects of preferential orientation
- M_k is the absorption correction function
- $F_{\phi,k}$ is the structure factor of phase ϕ for reflection k.
- $\Omega_{i,\phi,k}$ is the profile function of line k

The structure factor $F_{\phi,k}$ also noted F_{hkl} is expressed by the formula (Equation 1.5):

$$F_{hkl} = \sum j = 1 b_j e^{2\pi i[hx_j + ky_j + lz_j]} \tag{1.5}$$

where,

- b_j is the diffusion factor of atom j
- $[hx_j + ky_j + lz_j]$ is the term corresponding to atom j coordinates

The refinement procedure is minimized by the method of least squares to match the calculated pattern with the observed intensities. This function is represented byEquation 1.6:

$$S = \sum_i w_i \left|y_{obs_i} - y_{calc_i}\right|^2 \tag{1.6}$$

where,

- w_i is the weighting factor assigned to the observable
- y_{obs_i} and y_{calc_i} the observed and calculated intensities.

In practice, the Rietveld refinement allows the quantification of each phase based on the value of the S_ϕ scale factor. The refinement can serve another purpose such as refining atoms' positions in the lattice, finding the grain sizes, the strain, and stress, or identifying a preferred orientation. In our case, we will use this type of refinement to both confirm the identification of the crystalline phases and quantify them (meaning one in relation to each other).

3.3.4 Agreement factors

The validation of the quality of a refinement is carried out by several residual measures, expressed in terms of agreement factors R, which make it possible to quantify the convergence of a refinement.

There are two profile agreement factors R_p and R_{wp}, they represent the square root of the quantity minimized, scaled by the weighted (R_{wp}), or not weighted (R_p) intensities. The best theoretical value of R_{wp} is R_{exp}.

From these agreement factors, we can assess the goodness of fit χ^2 which provides an index on the quality of the refinement. This value should be as close as possible to 1 (Equation 1.7).

$$\chi^2 = \frac{R_{wp}^2}{R_{exp}^2} \tag{1.7}$$

These agreement factors are calculated directly by the refinement software. In this project we mainly used TOPAS 6 program [31] as our main refinement software.

3.3.5 Refinement strategy

Our XRPD pattern refinement strategy will have two goals, to match the phases identified with phase identification software to existing structures, and quantify these phases. As seen in subsubsection 3.3.3, we have two refinements possible: Pawley fit and Rietveld refinement. When possible, a Rietveld refinement will be carried out in order to obtain crystalline phases quantification, one of our objectives in this project. The downside is that Rietveld refinements by definition work on diffraction patterns of materials behaving as powders. In our case, the heterogeneous samples we are studying present various degrees of grain sizes, and may include phases that have a single-crystal behavior. The presence of single-crystal peaks in the diffraction patterns is problematic. Indeed, to some extent, the quantification cannot be accurate if peaks are not properly modeled by the refinement. When the Rietveld refinement presents agreement factors that are not good enough to validate a model, we may have to use the Pawley fit. The Pawley fit will handle the presence of single-crystal-like phases in a better way, as the intensities are not constrained. This will be a way to validate the presence of phases but the quantification will be lost. If only minor phases are present as single-crystals we will still use the Rietveld refinement on all other phases while just fitting those in Pawley, considering that their quantification is meaningless.

In any cases, during the course of the refinement, the zero point, the lattice parameters, the peak profile, and the scale factor in the case of Rietveld will be allowed to vary. Each of the phases will be imported in Topas 6 from a .cif file taken from Mindat, CoD, or ICDD databases. The background is defined prior to the refinement and is picked point by point by hand. Then the first parameters to be refined are the lattice parameters, then the scale, and finally the peak shape. In the end, we try to obtain a value of χ^2 as close to one as possible. The final result is a set of crystalline phases parameters such as their scale factor (from which quantification is deduced) and refined cell parameters with corresponding errors.

3.3.6 Fourier transform: the pair distribution function

3.3.6.1 Principle

The Fourier transform of an XRPD pattern shifts the information from the reciprocal space to the real space. This obtained signal is called the Pair Distribution Function (PDF), formulated through the function G(r). This function G(r) describes the probability of finding a pair of atoms at a given interatomic distance r. It is expressed with the formula:

$$G(r) = 4\pi r[\rho(r) - \rho_0] = \int_0^\infty Q[S(Q) - 1]sin(Qr)dQ \tag{1.8}$$

where,

- r is the interatomic distance
- $\rho(r)$ is the pair intensity and ρ_0 the average numerical density
- $S(Q)$ is the normalized coherent scattered intensity
- Q is defined by $Q = \frac{4\pi sin(\theta)}{\lambda}$

It gives information about the presence of certain atom pairs distances that are present in the structure. This is not only characterizing long-range ordering with the periodicity of a lattice, but also the short-range ordering.

The exploitation of the Fourier transform of the signal is particularly helpful to study amorphous or ill-ordered compounds. These compounds will present peaks only at low values of r, since the probability of getting a pair decreases proportionally with the crystallite size.

We can illustrate the shape of the PDF signal with two examples: graphite, a well-crystallized form of carbon and, lampblack (a type of flame carbon), an amorphous form of carbon (Figure 1.3). The graphite PDF signal is present up to very high r values. The reason for this is that the crystal structure keeps a coherence between atoms at long distance. On the other hand, the PDF signal of lampblack drops much faster to zero because of its amorphous nature that reduces the coherence between the atoms at a distance of a few carbon-carbon bonds.

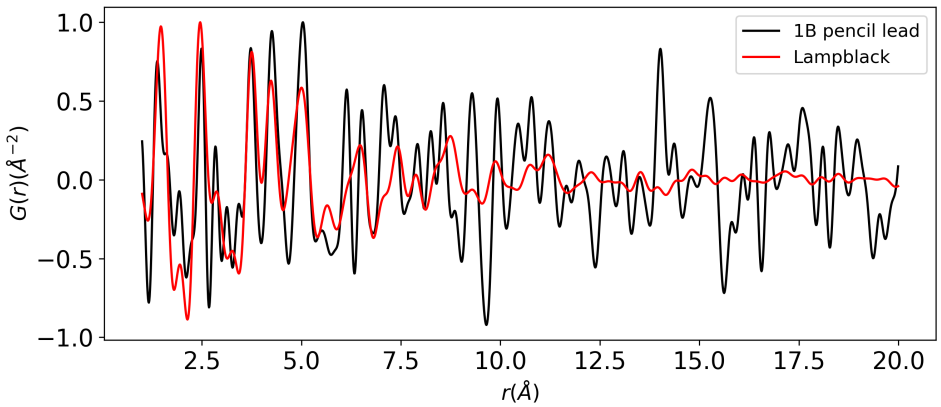

Figure 1.3: Examples of PDF signals of two carbon phases: 9B pencil lead composed mostly of crystalline graphite, and an amorphous compound: lampblack.

3.3.6.2 Data acquisition strategy

In practice, the PDF analysis starts with the acquisition of a diffraction pattern. Since we will perform a transformation from the reciprocal space to the real space, the most valuable information of our diffraction patterns is held in the highest values of Q (i.e. of 2θ). So the data acquisition would be optimized to get high statistical data at high values of Q. To do so, we would increase the energy to measure a larger range of angles as well as putting the detector closer to the sample (when using a 2D detector to acquire the data).

Once the data are recorded, the XRPD data are transformed with the pdfgetx3 software [32]. The process consists of giving the software a diffraction pattern in Q-space, then subtracting background acquired by measuring an empty container. Corrections for polarization, absorption effects and Compton and inelastic contributions were applied before Fourier transforming the data using a maximum Q-value of 50 $^{-1}$. We can note that in the case of the use of a 2D detector, the azimuthal integration from a 2D diffraction pattern to a 1D diffraction pattern will require a carefully made mask to avoid any hot or dead pixels at high scattering angles that would result in a massive spike in the PDF.

3.3.6.3 Refinements

The refinement of PDF data is based on the same principle as for the reciprocal space data, a minimization between the data and a model through a least-square fitting. In our case, the variables will be the lattice parameters and a scale factor.

To perform the refinement we will use PDFgui [33], a software containing a graphical interface based on the PDFfit2 engine [33]. The engine uses the small-box model where we assume periodic boundary conditions with a small number of atoms. The symmetry constraints are equal or usually lower than the average crystal symmetry. The starting point of the refinement is always a known structure to reduce the number of parameters.

In practice, we input the PDF data in the software as well as the structure (in the case of crystalline samples) we identified beforehand. Then we refine the lattice parameters and the phase scale factors up to convergence. We note the success of such a procedure resides in good quality data, meaning, a high value of Q-range (>20Å), a careful mask on the 2D diffraction pattern, and a sufficient counting time to get better high-Q values statistics.

We will use this technique specifically to identify the presence of amorphous carbon in our samples. The objective would be to correlate the PDF signal of our archaeological samples to measured references.

3.3.7 Data acquisition: the ID22 beamline at the ESRF

The ID22 beamline is an experimental station of the European Synchrotron Radiation Facility (ESRF). It is built on an undulator source at a 6 GeV storage ring and combines a wide continuous range of incident energy (6–80 keV) with high brightness. The beamline is specialized in High-Resolution powder diffraction (HR-XRPD) but can also produce data for XRPD with a 2D detector for total scattering (PDF) experiments.

3.3.7.1 Synchrotron radiation

The main advantage of the synchrotron X-rays compared to lab sources is the higher flux, the coherence of the beam, and the possibility to tune the wavelength depending on the measurement and the type of sample. If coherence is not a criterion in our case, the two other parameters play an important role.

Synchrotron provides a much higher flux that allows in our case quicker acquisitions. This implies the possibility to measure a larger number of samples per experiment or also increase drastically the statistics of our XRPD patterns.

Furthermore, synchrotron beamline provides a wide range of sample environment tools such as robots to load samples automatically (Figure 1.4), cryostats or cryostream devices for low-temperature measurements, or hot-air blowers. Measurement can also be made under vacuum, high pressures, or in the presence of different gases.

Figure 1.4: ID22 Robot setup with a cryostream (left)

The wavelength of the X-ray beam can be tuned easily to almost any value in a synchrotron source whereas lab sources rely on the emission line of a specific element.

A downside of using a synchrotron source is to be able to access it. This is done through the proposal submission process. Once the beamtime is allocated, the user will have a number of eight hours shifts to measure samples, and measurements will be made any time of the day or night. In the case of this project, twenty-seven shifts were allocated on ID22 and twelve on ID11. Around 20 shifts were also obtained through the in-house time available on ID22 and several hours on ID11.

3.3.7.2 HR-XRPD

High-resolution powder diffraction at a synchrotron facility relies on the natural high collimation of the incident radiation, and a highly monochromated beam. The highest resolution is attained with an analyzer crystal (e.g. a perfect Si 111 crystal) intercepting the diffracted beam before the detector. A diffracted X-ray must strike the analyzer crystal at precisely the correct Bragg angle to be diffracted into the detector (Figure 1.5A). Since the acceptance of the Si 111 crystal is very small (a few arcseconds), an analyzer crystal stringently defines the 2θ angle of diffraction yielding very narrow diffraction peaks (Figure 1.5B).

At ID22, a set of nine LaBr3 scintillator detectors are scanned vertically to measure the diffracted intensity as a function of 2θ. Each detector is preceded by an Si 111 analyzer crystal and the detector channels are nominally 2° apart (Figure 1.6). This concept was first set up by Hodeau *et al.* [34].

Each scintillator outputs a set of intensities that are associated with the diffractometer angle. Each of these nine series of intensities is binned (e.g. 0.002° steps) and re-assembled into one diffraction pattern through the program called *id31sum* [35] (ID31 is the former ID22 beamline).

3.3.7.3 XRPD with a 2D detector

It is also possible to use a 2D detector to obtain XRPD data from our samples. Instead of using the high-resolution setup, we can use a 2-dimensional detector that will record the powder rings. ID22 beamline has a PerkinElmer XRD 1611CP3 2D detector, used to acquire XRPD 2D diffraction patterns (Figure 1.7). Compared to the HR-XRPD setup, the use of the 2D detector implies a quicker measurement because of the absence of the scanning step. On the other hand, the angular

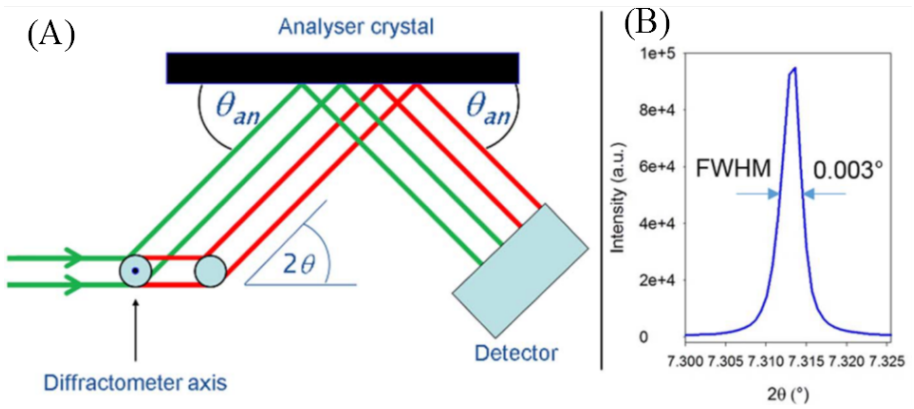

Figure 1.5: (A) X-ray beam path on HR-XRPD setup. (B) Silicon 111 reflection recorded at 31 keV from ID22 beamline setup.

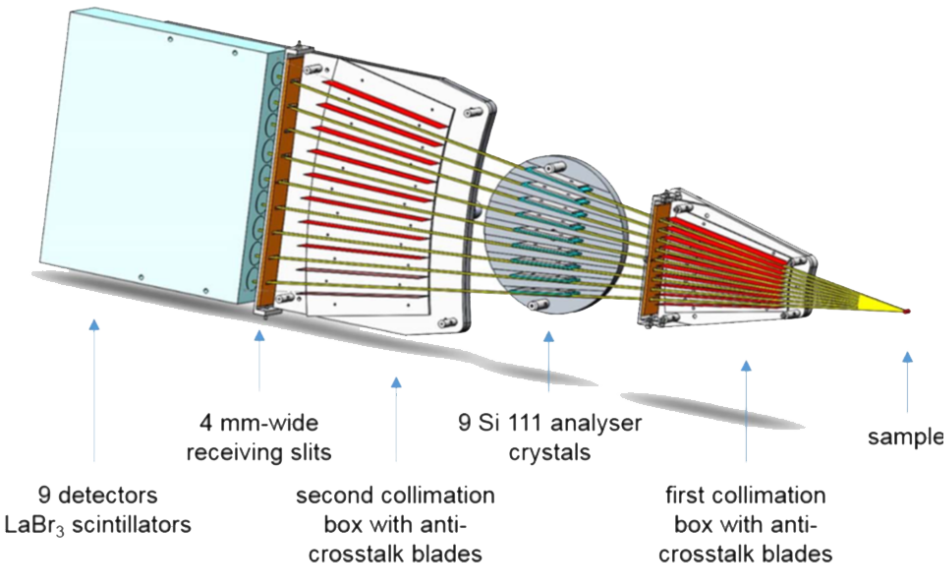

Figure 1.6: Schematic representation of ID22 beamline multi-analyzer stage.

resolution is worse, but the statistical information is better thanks to the higher number of photons that are directly intercepted by the detector.

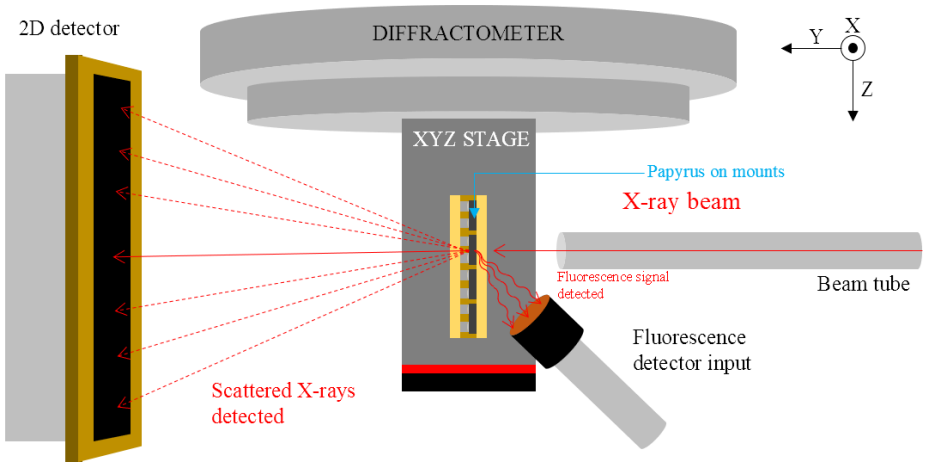

Figure 1.7: ID22 setup for 2D detector experiment

The detector outputs 2D diffraction patterns that require converting into 1-dimensional diffraction patterns (Figure 1.8). This conversion step is called the azimuthal integration. The integration requires a preliminary calibration with a standard reference (Si NIST) that takes parameters such as the wavelength, the peak positions, and a mask. Then the sample-detector distance and the detector parameters are calculated to be processed by the azimuthal integrator. This integration step was done with the PyFAI-integrate package using data calibrated with the PyFAI-calib2 GUI tool [6].

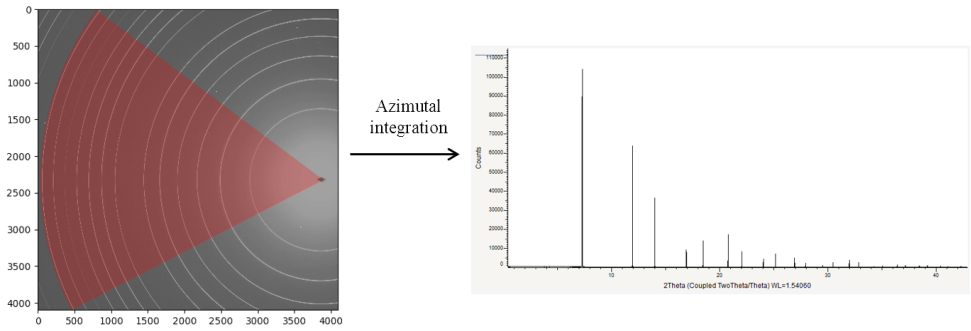

Figure 1.8: Example of the azimuthal integration of a 2D diffraction pattern (Silicon)

3.3.7.4 PDF measurement

With the same data acquisition routine, we can perform the PDF analysis. It has to be noted that to obtain good data, it is highly preferable to maximize the Qmax value, the maximal value of Q defined as (Equation 1.9):

$$Q = \frac{4\pi sin(\theta)}{\lambda} \tag{1.9}$$

To maximize this value, there are several options. We can lower the wavelength, which is the same as increasing energy. We can also increase the 2θ range at which we acquire the data, which implies scanning up to a higher diffractometer angle (HR setup) or moving the 2D detector closer to the sample (2D detector setup).

In our case, we chose to use the 2D detector setup to maximize the statistics of the diffraction patterns while still keeping a reasonable measurement time (scanning the diffractometer takes more time).

3.4 X-ray diffraction computed tomography

3.4.1 About X-ray tomography

The X-ray computed tomography (based on X-ray absorption) technique is the easiest example to illustrate the tomography principle. The sample is entirely illuminated by an X-ray beam. A detector is placed behind the sample which records so-called projections. A set of projections is recorded at different angles of rotation of the sample. This set of projections is stacked in a 3D volume in a series of sinograms. Then, a computed transformation is applied to back project each projection to its angle (Filtered Back Projection: FBP) (Figure 1.9). Each reconstructed projection represents a cut of a 3-dimensional volume. Stacking these projections in a 3D matrix allows us to observe the entire sample in 3D where the contrast of the volume is based on the absorption coefficient of each voxel of the sample.

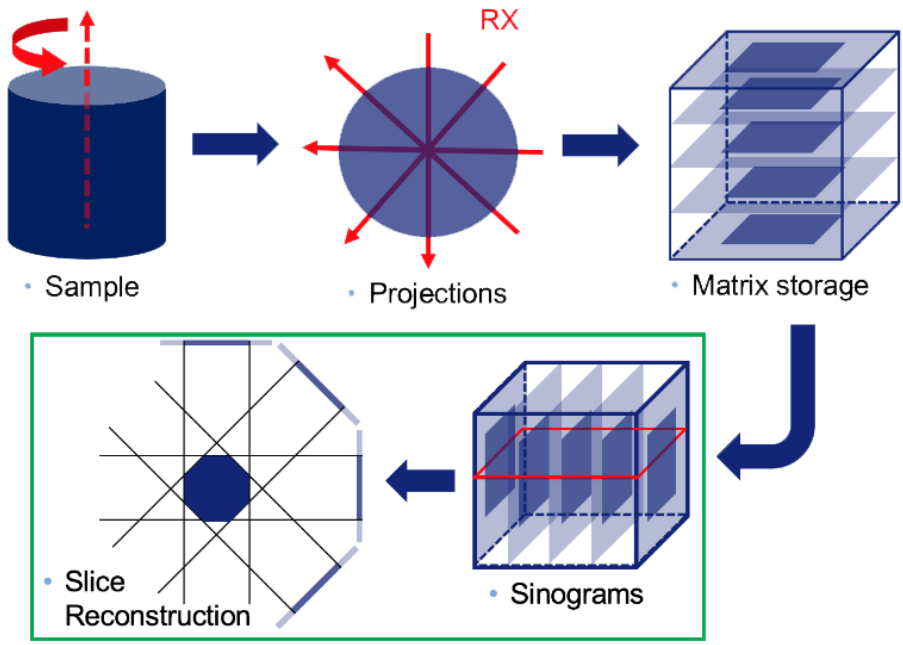

Figure 1.9: Example of the pipeline of an X-ray tomography experiment

3.4.2 XRD-CT principle

Compared to the previously described technique, X-ray diffraction - computed tomography is not based on the illumination of the entire sample at once, but only on a local portion defined by the size of the X-ray. The first experiment of XRD-CT at a synchrotron facility was detailed by Kleuker *et al.* [36] and the data acquisition and reduction process was explained by Bleuet *et al.* [12]. The acquisition relies on the repetition of a line scan on the sample and a rotation (or the complete rotation and then a translation). The detector record a 2D diffraction pattern for each point in the line scan. We end up with N_y number of points in the line scan times N_ω rotation positions, which correspond to the total number of diffraction patterns collected.

After the data reduction process, we built the 3D sinogram, which is a matrix containing N_y columns, N_ω lines, and N_θ the number of points in the diffraction patterns. For each θ angle in the diffraction pattern, we have a sinogram which is the projection of the sample at the diffraction angle θ.

All the XRD patterns are recombined in sinograms according to the scan geometry. A realignment of each line in the sinograms to account for beam drifts during the measurements is implemented prior to the reconstruction using a center of mass correction described by the

following formula (Equation 1.10):

$$CoM_i = \frac{\sum_{j=1}^{n} x_j S_{i,j} B_{i,j}}{\sum_{j=1}^{n} x_j} \tag{1.10}$$

where CoM_i is the center of mass of the line i in the sinogram, x_j is the position of jth pixel in the line, $S_{i,j}$ is the intensity of the jth pixel in the ith line of the sinogram, and $B_{i,j}$ the intensity of the jth pixel in the ith line of a mask where pixels of air are imposed to 0 and pixels of sample to 1. Finally, the FBP algorithm [37] was run to reconstruct the final image. This image corresponds to a structural contrast of our sample.

3.4.3 About XRF-CT

With the same acquisition methods as XRD-CT it is also possible to obtain some elemental information of the sample. The only difference between the data analysis of XRF-CT is that the signal does not require much data reduction and correction. Each acquisition point gives one XRF spectrum that is stack in the exact same way as XRD patterns. At the end, we obtain a 3D volume of our slices where the third dimension is the intensity of the signal at certain energy giving the contrast in the image.

3.4.4 XRD/XRF-CT on ID11

The ID11 beamline has a dedicated setup to perform XRD/XRF-CT experiments. The setup that we used in this project is articulated around a sample stage that has two XYZ translation stages with a rotation stage in between. This configuration allows putting the sample in the center of rotation. This placement in the center of rotation is a key step for any tomography experiment. It ensures that the center of mass of the sample is always at the same place whatever the rotation angle is. To do so, we rotate the sample 90, back and forth while acting on the top translation stage to align the sample. Once the sample is correctly placed in the center of rotation, the beamline is set up with a CCD camera (FReLoN) and a fluorescence detector (Figure 1.10).

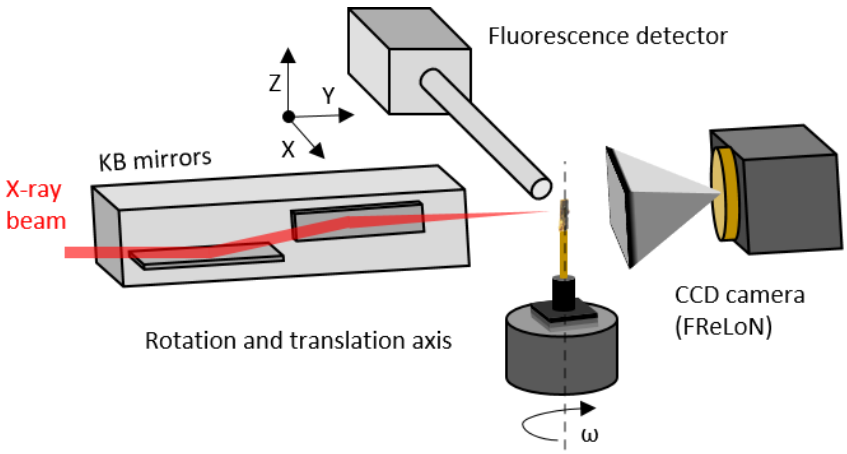

Figure 1.10: XRD-CT experimental setup on the ID11 beamline

Then the scan is set to a certain number of steps and rotation angles and an image on the CCD is collected as well as a fluorescence spectrum for each point. The beam size was around 2x2 μm. The sample size, in our case some fragment of papyrus, was roughly 1 mm in diameter. Each point takes around one second to be acquired and it takes 500 translation times 180 rotation angles to do an entire slice. This leads to 90,000 images which corresponds to about 25 hours of acquisition. We will see in the last chapter how can we reduce this time in the case of a flat sample.

3.4.5 Reconstructing data from an XRD-CT experiment

From this experiment, we obtained a series of .edf images (now a single .hdf5 file). These images are similar to a .tiff image with the addition of a header. The very first step is to transform them from the 2D space to a 1D diffraction pattern. To do so, we used pyFAI API, the Fast Azimuthal Integration python library. We embedded this library in a python script that takes as input the .edf (or .hdf5) images and outputs a 3D matrix containing the data in translation, rotations, and intensities.

To build the 3D matrix, we create an empty matrix based on the size of the scan and the number of 2θ (or Q). The size is found directly by the numbering of the .edf images files contained in the input. Then we iterate on each .edf file and the result of the integration is put in the correct rotation and translation position in the matrix.

At the end of the process, the 3D matrix is filled. Each 2D image taken from the matrix at a fixed value of 2θ (or Q) is a sinogram (Figure 1.11).

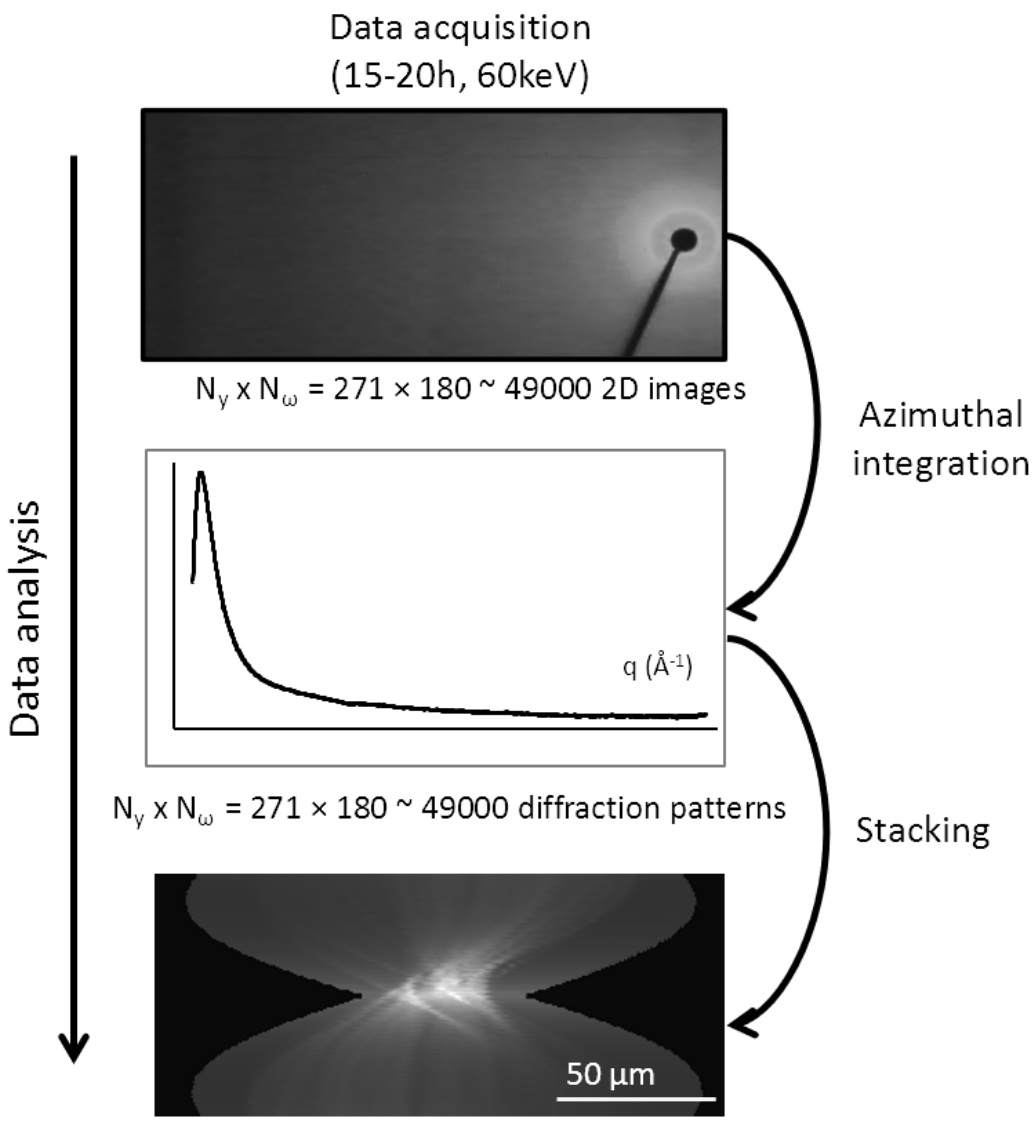

Figure 1.11: Data analysis pipeline for an XRD-CT experiment. The numbers are based on a sample size of 100x400µm size with a beam size of 2x2µm

With the sinogram build the last step is to reconstruct the image of the sample for each sinogram (Figure 1.12). The reconstruction relies only on the Filtered Back Projection (FBP) step, which is simply applied to each of the sinograms. The function is built in the *skimage.transform* library as *iradon*. The function takes the list of ω acquisition angles and the sinogram. Then we end up with the reconstructed signal.

We have to note that in most cases it is mandatory to subtract to each diffraction pattern a background, usually just the signal of air. If forgotten, this will lead to a very poor contrast in the final image from which the back-projected signal would mostly be due to air.

We can also mention the existence of alternatives to the FBP reconstruction which involves iterative reconstruction methods such as the Algebraic Reconstruction technique [38] (ART) or the Conjugate Gradient Least Squares (CG-LS) [39]. The reconstructed data is also a stack that is saved as an hdf5 file. This file can be opened by ImageJ to be processed. This last process will be detailed in the last chapter.

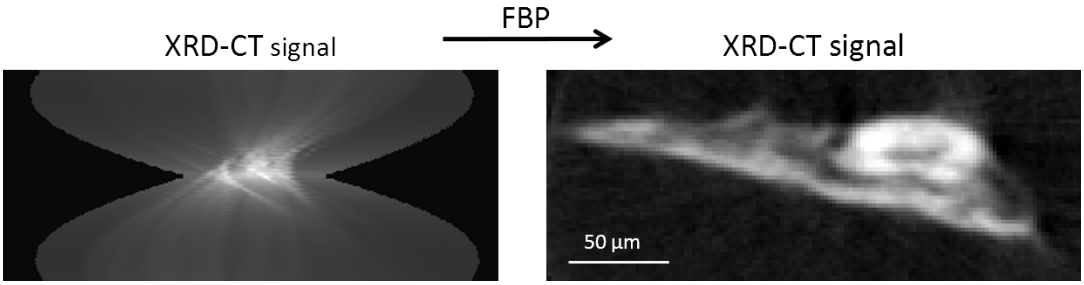

Figure 1.12: Reconstruction of XRD-CT signal using the filtered back-projection algorithm (FBP)

3.4.6 PyXRDCT

I developed an entire data processing pipeline for this project under the name of PyXRDCT. The method is implemented in a python library available on Github. It contains all the functions required to integrate the data from pyFAI, the stacking functions, and the reconstruction functions. The package is evolving towards the use of statistical tools such as principal component analysis to extract meaningful full data and a graphical interface to view the reconstruction in real-time.

4 Carbon-based pigments: references and reproductions

The approach consists of collecting several pigment references from commercial pigments. To extend our reference corpus, we also tried to elaborate a set of carbonized compounds in a controlled environment. These references will be analyzed with all characterization techniques that can also be performed on archeological samples. Then, the data obtained will be used later for comparison with archeological samples. The characterization techniques will be based on morphological studies with scanning electron microscopy that will be performed to isolate different types of morphology that could be a characteristic of a certain type of carbon. Then, structural analyses such XRD, PDF, and Raman spectroscopy will be used. These data will provide an accurate example of the structure we can expect to retrieve from the analysis of archeological samples as well as a strong comparison point.

4.1 References

4.1.1 Commercial references

4.1.1.1 9B pencil lead

Used to be called Plumbago, and thought to be made from lead, the pencil lead is commonly made of graphite and clay (most of the time kaolinite). Graphite is one of the crystalline forms of carbon that can be found naturally or manufactured by the heavy heating of hydrocarbons. This reference will allow us to track if any crystalline carbon is present in our samples.

4.1.1.2 Vegetable-based

This category groups two references, peach black and vine black. The peach black comes from Kremer Pigmente manufacturer (Ref: 12010). The manufacturer is writing that the pigment comes from the carbonization of peach kernels. The vine black pigments come from Ôkhra manufacturer (Ref: T2000040A). It is said to be made of carbonized vine branches.

4.1.1.3 Animal-based

Two pigments from Kremer are animal-based. The first is ivory black, made from carbonized ivory by Kremer Pigmente (Ref: 12000). The manufacturer says that the pigment is made out of ivory powder that was carbonized to 800°C in iron pots. Even if it is surprising that ivory black is legally sold, indeed the pigment is still available based on the remaining stock that exists. Manufacturing is now forbidden for obvious species protection legislation.

The second pigment is bone black manufactured also by Kremer (Ref: 47100). It is produced by the carbonization of animal bones between 400 and 800°C. The animal from which bones are collected is not mentioned.

4.1.1.4 Lampblack

The manufacturing process of lampblack consists of the incomplete combustion of a particular combustible in a chamber [40]. The combustible can be oil, fat, wood, coal, or nowadays more frequently hydrocarbons. Our lampblack reference comes from the Dousselin manufacturer (Figure 1.13).

4.1.2 Synthesized references

To complete our set of references we manufactured four carbon-based pigments from vegetables. Based on ancient texts, we chose, almond, hazelnut, and walnut shells, and also vine tree branches. With the help of literature [41], we carbonized our vegetables into an oven for 1h at 100°C and then at 300°C for 4 hours in porcelain crucibles (Figure 1.14). The first attempts were not success full because of the presence of oxygen in the oven which favored the combustion process and left only a few ashes during the first tries. To solve that we simply covered the top of our crucibles with porcelain plates to keep the level of oxygen as low as possible.

The result of good carbonization is the preservation of the original shape of the samples, with almost no visual change except for the color (Figure 1.15). Then the last test is to crush the char in pieces to see if we obtain a black powder, which was the case in this process.

The conclusion of this experiment is not to benchmark which conditions are suitable to carbonize vegetables but rather to get an extra set of reference materials to compare to our archaeological samples.

Figure 1.13: Buckets containing commercial black pigments.

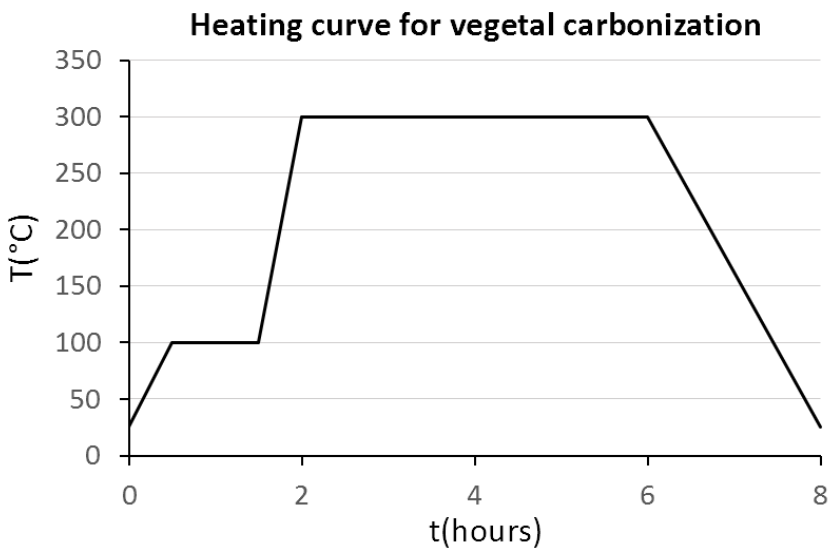

Figure 1.14: Evolution of the oven temperature in function of time to carbonize vegetable sample.

Figure 1.15: Vegetables before and after carbonization: hazelnut shells (top-left), vine branches (top-right), almond shells (bottom-left), and walnut shells (bottom-right).

4.2 Characterization

4.2.1 XRD

4.2.1.1 Phase identification

The first step of the characterization is to identify the crystalline phases present in our reference powders if any. The XRPD technique will allow separating the samples that contain identifiable crystalline phases from the purely amorphous ones. We expect that such a distinction could also be present in our archeological samples. The references were prepared in capillaries and measured at the ID22 beamline. The samples were measured firstly using the 2D detector and then the HR-XRPD stage at 65keV and 27,5keV respectively, with a beam size of 1x1μm. Only samples containing crystalline phases were recorded in HR with the objective of facilitating peak identification (because narrower peaks in HR are deconvoluted more easily).

By plotting the diffraction patterns, we already have two groups, crystalline samples and amorphous samples (Figure 1.16, Figure 1.17):

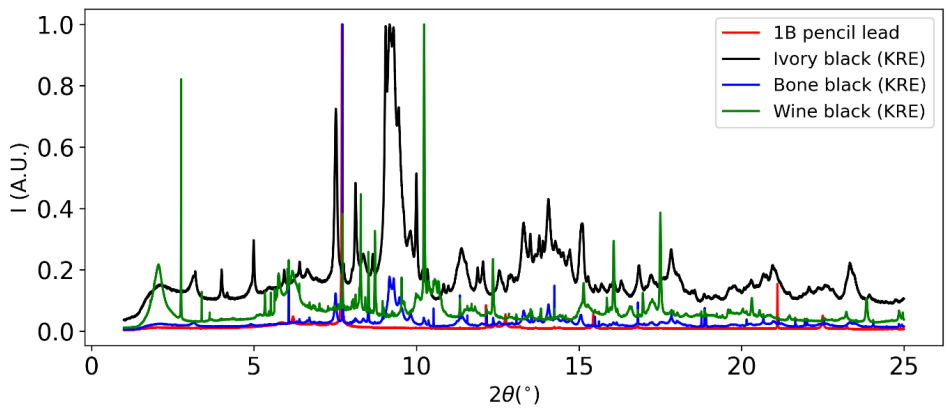

Figure 1.16: HR-XRPD diffraction patterns from ID22 beamline of the reference containing mostly crystalline phases. (KRE = Kremer pigmente)

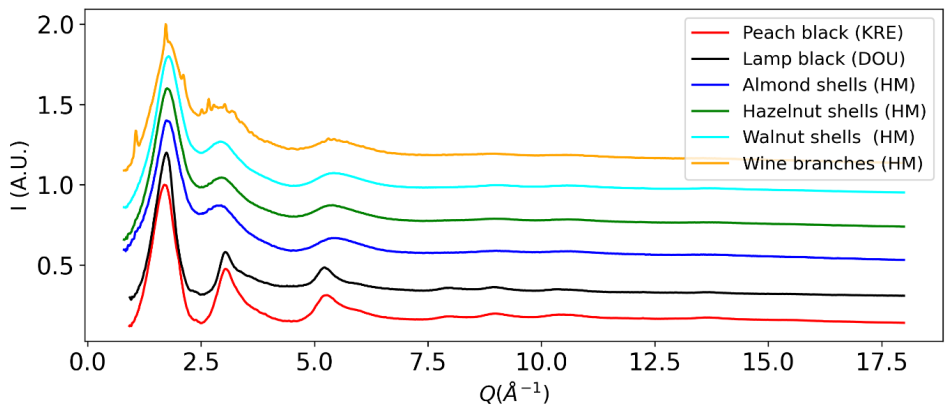

Figure 1.17: Diffraction pattern from ID22 2D detector of the mostly amorphous references (the air was subtracted from the signal). (KRE = Kremer Pigmente, DOU = Dousselin, HM = Home Made)

From this, we identified the phases in the samples containing crystalline phases with the DIFFRAC.EVA V5.0 software (Table 1.1).

Table 1.1: Phase identification of the crystalline phases contained in the set of reference samples from ID22 HR-XRPD setup (and 2D detector for amorphous samples)

Category	**Reference**	**Crystalline phases**
Contain crystalline phases	9B pencil lead	Graphite (C), Anatase (TiO_2), Quartz (SiO_2)
	Ivory black (KRE)	Hydroxylapatite ($Ca_5(PO_4)_3(OH)$), Whitlockite ($Ca_3(PO_4)_2$)
	Bone black (KRE)	Hydroxylapatite ($Ca_5(PO_4)_3(OH)$), Quartz (SiO_2), Calcite ($CaCO_3$)
	Vine black (KRE)	Montmorillonite ($(Na,Ca)_{0.33}(Al,Mg)_2(Si_4O_{10})$), Goethite ($FeO(OH)$), Chromite ($FeCr_2O_4$), Calcite ($CaCO_3$), Talc ($Mg_3Si_4O_{10}(OH)_2$), Gypsum ($CaSO_4,2H_2O$)
Amorphous	Peach black (KRE)	Ø
	Lampblack (DOU)	Ø
	Almond shells (HM)	Ø
	Hazelnut shells (HM)	Ø
	Walnut shells (HM)	Ø
	Vine branches (HM)	Minor phase(s) not identified

From these results, we will exclude the vine black (Kremer) reference from the next characterization step. Indeed, as shown in Table 1.1, this reference sample surprisingly contains a series of oxides and Ca-based phases. Although the pigment name is vine black, the naming clearly does not designate the composition but most probably the shade of black. This pigment was most likely reproduced by the manufacturer with several oxides (goethite and chromite) giving the black color and clay to match the shade of the original pigment.

The 9B pencil lead contains graphite, anatase, and quartz. No traces of crystalline compounds corresponding to clay (used as a charge) have been found. There is a possibility that the industrials would use a type of clay that contains a mix of anatase, quartz, and other amorphous compounds that are not identifiable with this technique.

For the two bone-based references we obtain the presence of hydroxylapatite (HAP) and in the case of ivory the whitlockite (WH) phase. HAP is the major crystalline phase found in bone tissues. WH may coexist with HAP but with a lower amount and/or in a more amorphous form and is found at a higher concentration in ivory [42]. Calcite is not a component of bone, however, the heating process can explain its formation from either HAP or WH [43] [44]. Concerning quartz, we do not explain its presence except for pollution or manufacturing process. Ivory black appears to not contain any calcium or quartz.

The rest of the references are amorphous, which is expected for our homemade chars, and tells us that the two last industrial references (peach black and lampblack) most likely used vegetables as raw materials as well. Only the homemade vine branches sample comports a minor crystalline phase. This could be explained maybe from the chemical treatment of the vine while the plan was growing. Even if the vine we used was organic, treatments such as copper sulfates are allowed, but we could not correlate the diffraction peaks to such a compound.

4.2.1.2 Refinement

To validate the nature of the phases present we decided to do a Pawley fit of the phases. We tried to perform a Rietveld refinement of the diffraction pattern but we were not successful, even if the samples do not appear to contain single-crystal. This is probably because of the intensities of several peaks being wrong as well as a bad crystallinity.

The refinements were performed with the TOPAS 6 software. We used a Pseudo Voigt function as our peak shape. The structure of the hydroxylapatite chosen was published by Wilson *et al.* [45] and the structure of whitlockite is from C. Calvo *et al.* [46]. Background was defined by a 6-coefficient equation. We refined the background points as well as the lattice parameters, peak shape and peak intensities.

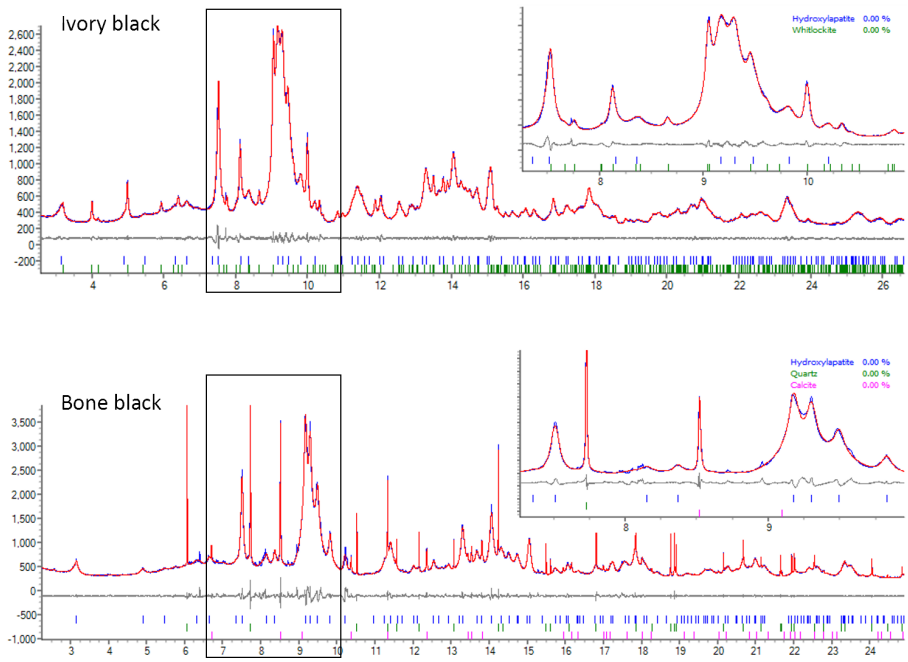

Figure 1.18: HR-XRPD diffraction patterns from ID22 beamline of bone and ivory blacks. Pawley fits are shown in red, with Rwp_{bone} = 3.11 and Rwp_{ivory} = 1.93

The result is that we validate the presence of hydroxylapatite in our bone and ivory blacks (Figure 1.18) as well as the presence of whitlockite in ivory black. This is in agreement with previous studies that showed that burned bones are almost exclusively made of hydroxylapatite [47].

4.2.2 PDF

With the phases identified for the crystalline samples, we can focus on the amorphous references. To do so, we will perform the PDF analysis of the samples containing only amorphous materials. Even if the samples containing crystalline phases may contain also amorphous phases, we consider that any crystalline phase identified in both references and archaeological samples would orient us on the nature of the archaeological sample. For example, if we find hydroxylapatite in our archaeological samples, we have already strong evidence to think that bone or ivory was involved in pigment manufacturing.

We obtained our set of PDF references (Figure 1.19) that we will try to match later to our archeological samples. The PDFs have in common the first peaks at 1.4Å and 2.4Å that correspond to the carbon-carbon and the nearest carbon neighbor distances (Figure 1.19), respectively. This atomic pair distribution of carbon was measured and interpreted for the first time by Rosalind

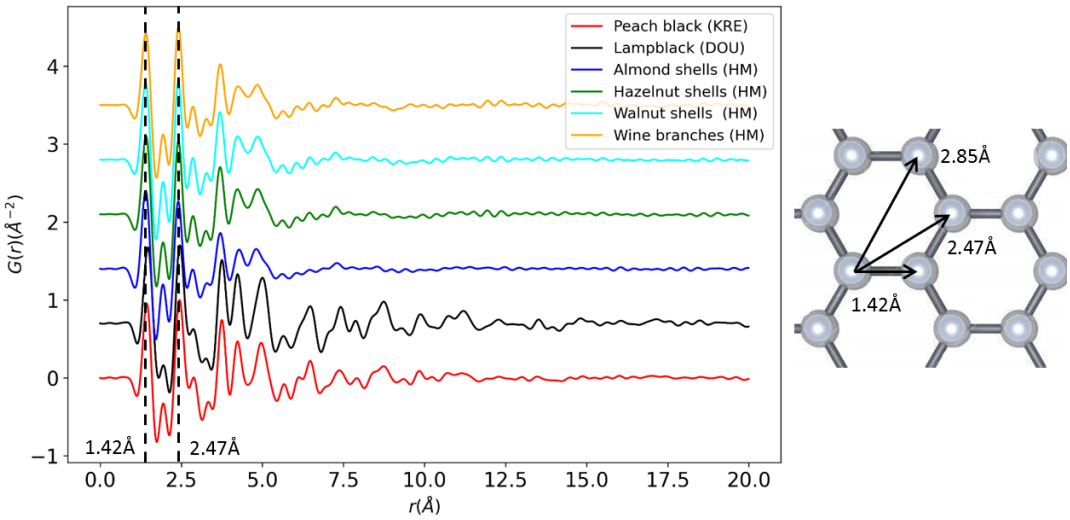

Figure 1.19: PDF signals of the amorphous references with the graphene structural model and carbon atom distances.

Franklin in 1950 [48].

The homemade references have similar PDF profiles while the two industrial references present a much higher signal at higher values of r. This indicates that either the coherence between the carbon atoms is greater (i.e. order at a longer distance between 5 and 12Å) or that the particle size is larger. For the lampblack reference, the carbon particles have nothing to do with vegetables, which could explain the difference. On the other hand, the industrial peach black which should be close to our reference chars may have had a different heat treatment procedure compared to ours. This difference between homemade and industrial references remains to be understood.

4.2.3 SEM

The scanning electron microscopy technique was applied to seven reference samples. Hazelnut chars images could not be recorded because of charging effect while graphite is already a known morphology [49](industrial vine black is irrelevant because of its metal oxides nature). The samples were prepared on a multi-samples stage that can hold up to nine sample holders. Each sample holder is a little stainless-steel disk with a rod at the bottom that can slide into the sample stage holes. The sample holder is then tightened to the sample stage with a screw.

Each sample holder is covered with a piece of carbon tape. The carbon tape piece is cut to a unique shape in order to recognize it easily once it is in the microscope. Then a small quantity of powder is put on the carbon tape and the excess of powder that did not stick to the tape is removed. No other preparation was required (Figure 1.20).

The observation of each reference allows the categorization of the samples into three groups based on their morphology (Figure 1.21).

Concerning our vegetable homemade references, we do not have similar morphologies as what J. Winter presented [1]. Our samples have distinctly angular shapes with holes (almond shells, peach black) or more undetermined morphologies (walnut shells, vine branches) compared to the channel-like morphologies that is obtained when observing wood chars. In general, the result of the observation made on carbon from vegetable sources is that the microstructure of the raw material is kept through the carbonization process.

From Winter study we have to bear in mind the possibility of finding another type of morphologies in our archaeological sample batch. Wood is one of the additional morphology that

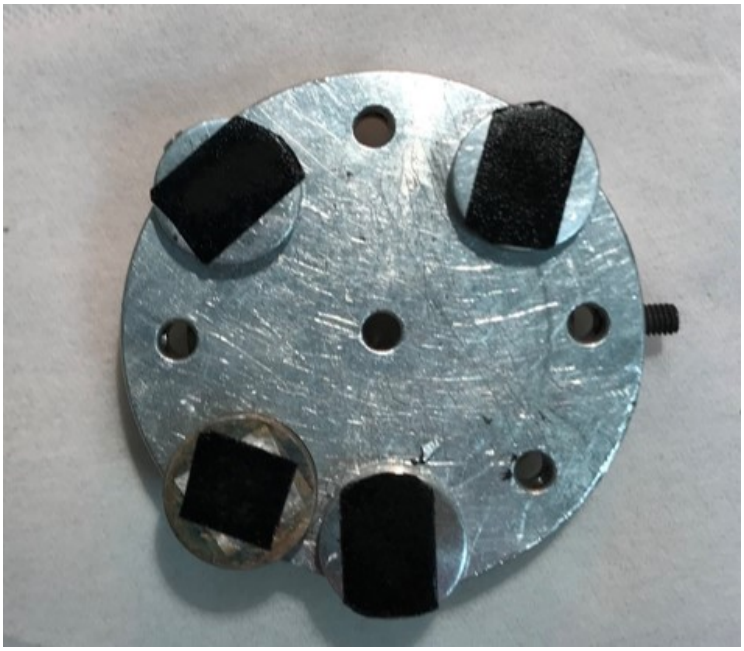

Figure 1.20: Sample stage with four samples put on carbon tape. These pieces of carbon tape were not carefully cut to be easily identifiable.

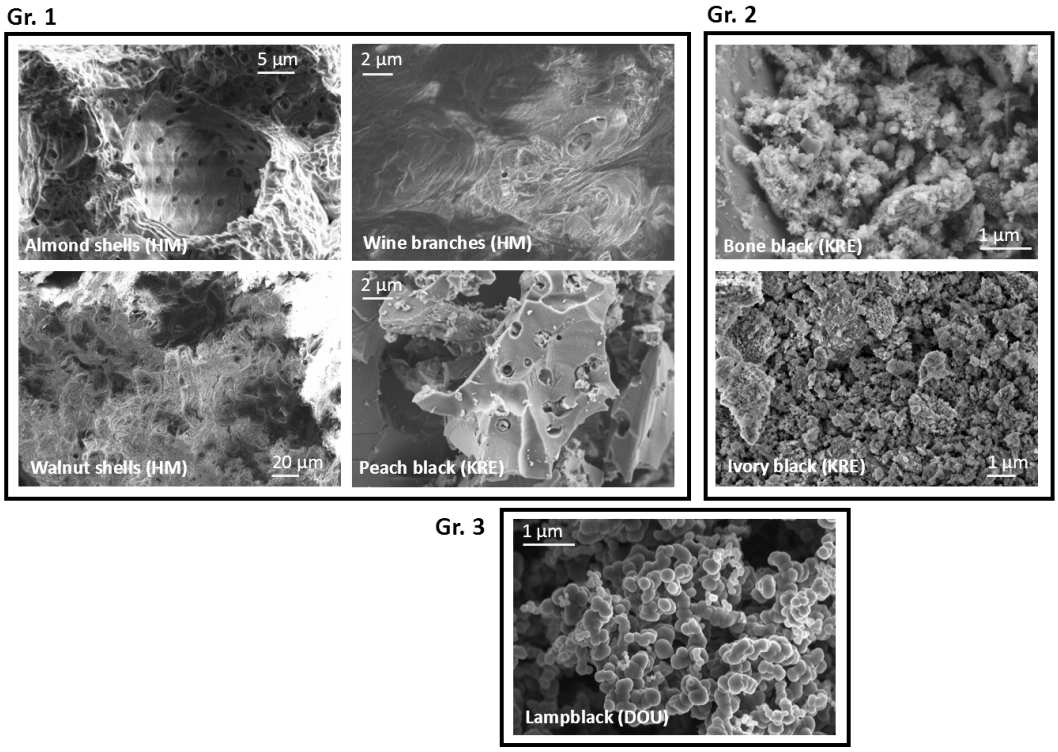

Figure 1.21: SEM images of references black pigments. Group 1 corresponds to vegetal-based morphologies with holes, big angular chunks, or wave-like patterns. Group2 is the bone or ivory-based pigments with small angular chunks. Group 3 is the flame carbon with spheroidal particles of 200nm size.

is not present in our reference set (vine branches seem to have a different morphology as wood would) are shown in Figure 1.22.

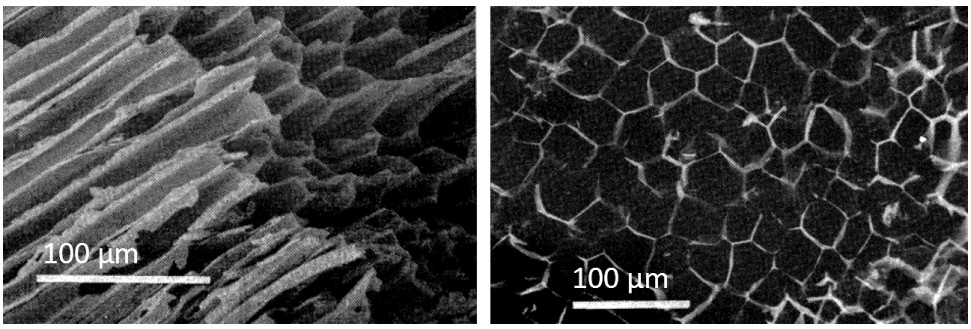

Figure 1.22: Scanning electron micrograph of sugar-pine char (left), Scanning electron micrographs of cork char (right) [1].

With these observations, we have four groups from which we intend to categorize the carbon morphology of our archaeological samples.

- flame carbons: spherical particles
- bone or ivory blacks: irregular sharp chunks of various sizes
- fruit kernels or shells: larger chunks with holes
- wood: channel-like structure

4.2.4 The case of bone and ivory

The composition of ivory and bone black commercial references were identified with HR-XRPD (Table 1.1). Ivory and bones contain hydroxylapatite (HAP), and whitlockite (WH) only in the case of ivory. To get a better understanding of the conditions in which ivory and bone black pigments could have been produced in Antiquity, we set up a series of in-situ experiments in which we tried to reproduce ivory and bone black by heating raw ivory and bone (Figure 1.23).

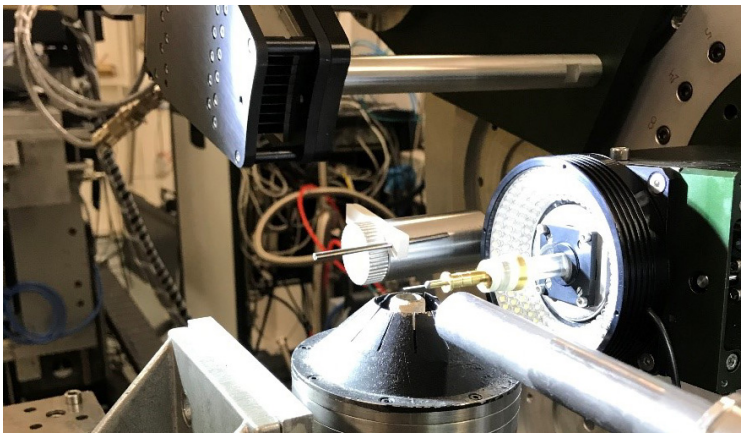

Figure 1.23: HR-XRPD setup with hot air blower for the in-situ experiment on ID22.

The samples chosen for this series of experiment were powders taken from two objects from a personal collection. The ivory powder was extracted after drilling a 0.5mm hole in the bottom part of the cap of a propeller pencil. This propeller pencil originates most probably from the beginning of the XXth century (Figure 1.24). Bone was extracted in the same way from a knife.

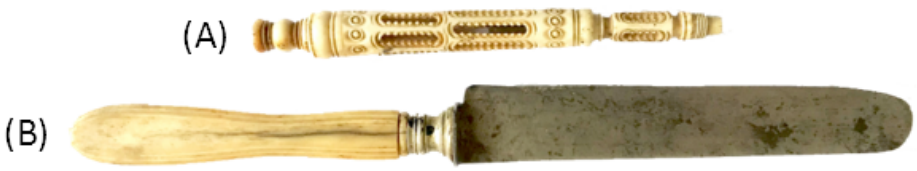

Figure 1.24: (A) XXth ivory century propeller pencil (B) XXth century bone handle knife.

The powders were then encapsulated into capillaries for HR-XRPD analysis. The objective is to trace the evolution of the crystalline part while the powder is being heated and assess at which temperature the transformation of bone and ivory produces corresponding black pigments. Those tests will be performed with and without sealing the capillary to compare the differences with the effect of oxygen.

We recorded diffraction patterns at intervals of 50°C (heat from a hot-air blower) on four samples, one per material and one sealed and not sealed. We obtain the following data curves in the case of an open capillary of ivory (Figure 1.25).

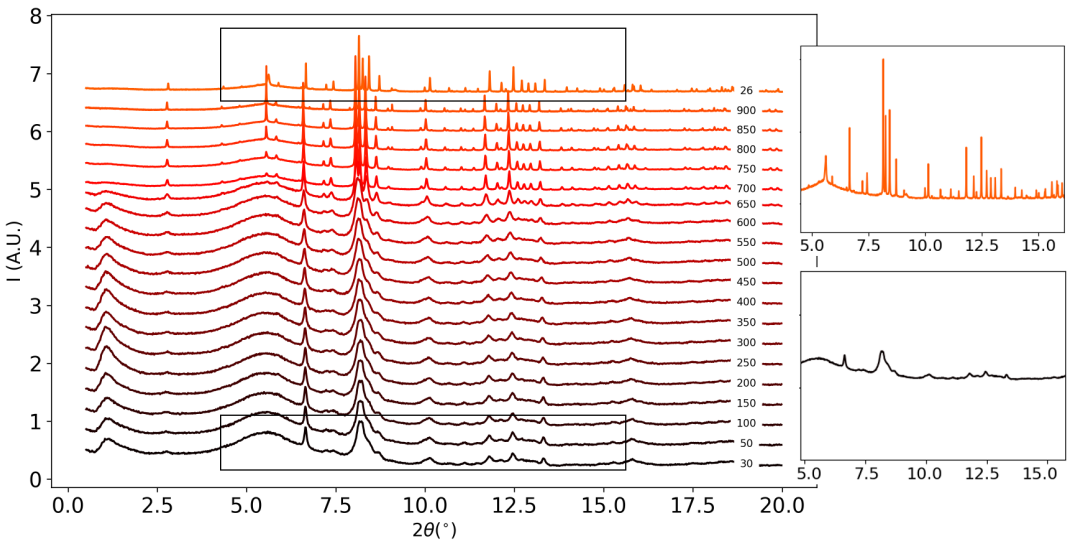

Figure 1.25: Evolution of the diffraction pattern of ivory with temperature (exposed to oxygen). The top diffraction pattern was recorded at RT after the experiment (temperatures are displayed on each curve in °C).

With this test, we are able to track down the evolution of the crystalline structure of HAP. We clearly see re-crystallization happening around 650°C (Figure 1.25). Even if we observed the presence of WH in ivory black commercial reference, we do not have any traces of it in the in-situ diffraction patterns. We show in Figure 1.26 the comparison between commercial ivory and bone black, and our bone and ivory patterns of the in-situ experiments. Only the commercial ivory black contains WH. The presence of this noticeable quantity can have multiple reasons:

- the manufacturing process involves a step that creates WH (temperature effect or other compounds)
- the raw materials are taken from a specific part of raw ivory (e.g. exposed to weathering)

Since some authors [50] found small quantities of WH in heated ivory, there is a chance that the industrial process involves the degradation of HAP into WH. Such type of reaction was described by Jang *et al.* [51]. This reaction involves the transformation of HAP in WH with the effect of

acidic (below pH = 4.2) conditions in presence of Mg^{2+} ions at 70°C. In our reaction we use only pure ivory, but in the process of making ivory black, industrials could have added extra compounds to the ivory that could lead to the transformation of HAP in WH.

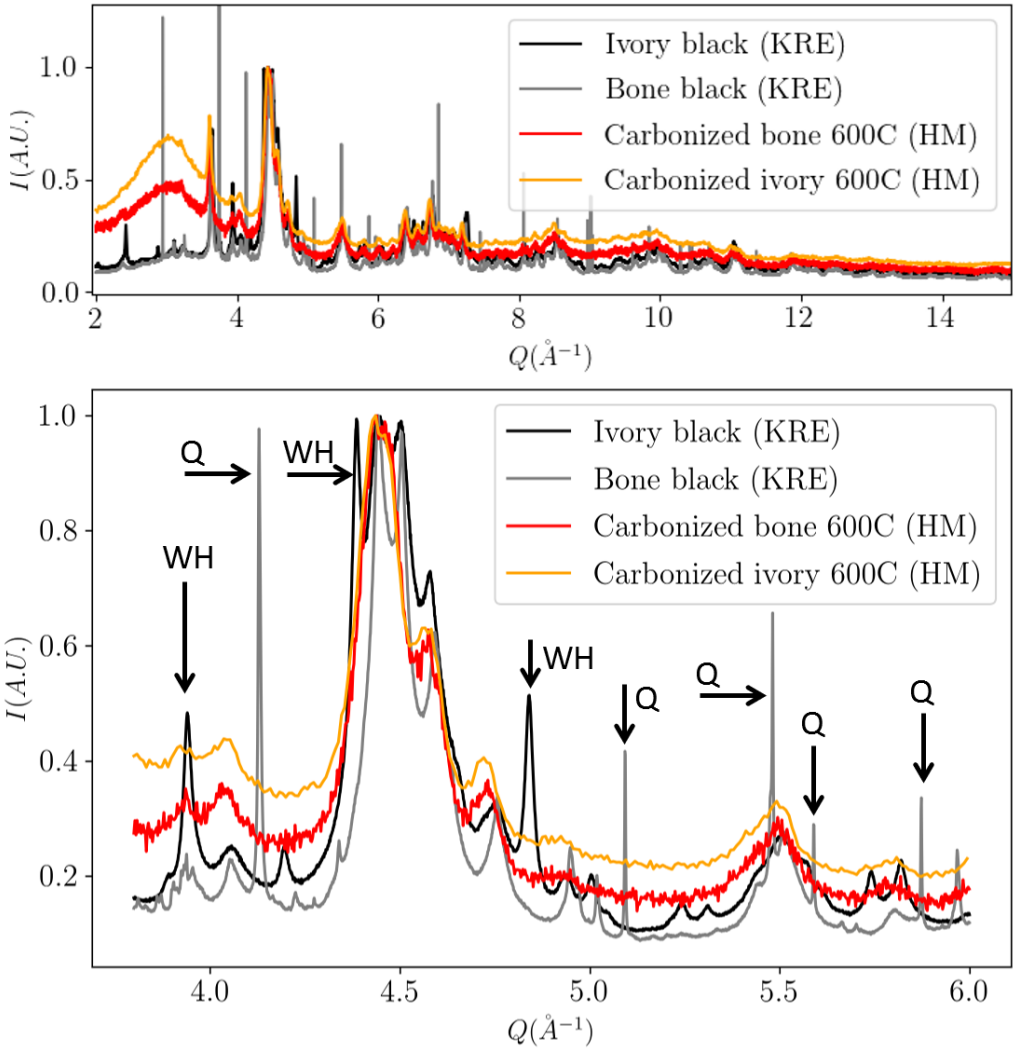

Figure 1.26: XRPD patterns of bone black and ivory black references with results of in-situ carbonization of bone and ivory. We observe WH only on the industrial ivory black. The carbonized ivory and bones patterns were taken at 600°C which is the reason for the offset. WH = Whitlockite, Q = Quartz

We can compare the diffraction patterns of the industrial reference with the one from the in-situ experiment. By comparing the peak shapes of the heated reference we are able to determine the temperature at which the industrials baked the raw materials. Figure 1.26 shows that the measurement made at 600°C matches well the peak shape of the reference. Passed 650°C the recrystallisation process of HAP narrows down the peaks and below these temperatures, the peaks are too wide. Also, it seems that commercial bone black may have been heated slightly more than the ivory.

By doing the same in-situ experiment on the other powders we obtain relatively the same result in terms of the evolution of the diffraction signal. However, the obtained final color varies depending on if we are in a sealed or not environment.

The presence of a sufficient amount of oxygen in the near environment causes the reaction of transformation of carbon in CO_2, rendering the sample firstly black and after all carbon is

consumed completely white instead of conserving the black color.

5 Conclusion

In this chapter, we wrote a review on the manufacturing and uses of carbon-based pigments in Antiquity. We discussed the three types of black pigments (coke, char, flame carbon) that were present in Antiquity. Only several ancient texts are talking about black inks and always out of context compared to the original purpose of the books the author wrote. We have characterized one type of each and they are all predominantly amorphous. Only apatite mineral phases are present as crystalline compounds. The morphologies observed with SEM are characteristics to distinguish chars and flame carbons.

The chosen characterization techniques enabled us to establish a small database containing structural and chemical information of our reference samples. This will be particularly helpful for the next chapter where the powder nature of our sample is already scalable to the exact same techniques shown previously.

In the next chapter, we will analyze a set of thirteen of these black powders from ancient Roman sites. Then, we will focus on written and painted papyrus from ancient Egypt. This investigation has two aspects, historical and scientific. The historical aspect will be focused on the understanding of the ancient black pigment manufacturing process, the raw materials used, the origin of metallic elements, and the origin of the carbon. On the other side, this type of sample is particularly complex. Because of their heterogeneous nature (amorphous, crystalline, single crystal, powder, all at the same time) as well as their fragility, we will have to develop some strategies to get as much information as possible from each signal contribution.

2

Study of black powders from Roman archaeological sites

Contents

1 Introduction 38

2 Powders from Italian Antique containers 38

2.1 Use of black powders in Roman times 38

2.2 Samples from Pompeii and Herculaneum 39

3 Observation by SEM 41

3.1 Sample preparation 41

3.2 Observation and results 41

4 Heterogeneous powders: separating amorphous and crystalline contributions 43

4.1 Introduction 43

4.2 Exploiting the crystalline part 43

4.3 Exploiting the amorphous contribution to the signal with PDF fitting . . 54

5 Discussion 58

6 Conclusion of the chapter 61

1 Introduction

In the previous chapter, we analyzed reference black pigments that we chose based on ancient text and recent studies. We are now going to analyze archeological black powders. These powders are expected to not only be composed of amorphous carbons but also crystalline phases or other amorphous phases.

The black powders corpus is a set of thirteen black powders from two Roman archeological sites, Pompeii and Herculaneum. They were provided by Pr. Maria-Christina Gamberini from the University of Modena and were collected during campaigns of excavations during the XVIIIth century carried out in those two sites. Since both excavations result from the discoveries of these two famous cities preserved after the eruption of the Vesuvius Volcano, we can accurately date those from 79 A.D.

These powders were found in different types of containers, and their uses remain unknown. Identifying each of the phases that compose these powders is a first step to understand their use and possibly correlate it to a special type of container. However, we may also face potential degradation of these compounds, as a result of exposure to both eruption and time degradation.

This mixture of phases makes these powders extremely heterogeneous compounds and induces complex analysis. With the addition of the archeological value they hold, it is then extremely important to avoid any alteration or destruction during analysis.

So why do we study those? It is a challenge to analyze mixtures of amorphous and crystalline phases that have several degrees of grain size, coupled to the presence of possible alteration. Pompeii and Herculaneum both hold secrets not only about the daily life of ancient society but also about the technologies and knowledge during the Roman period. We will try to focus on the uses of black pigments at this epoch and reveal their nature to further understand the evolution of black pigment uses through the ages.

What protocol are we going to use? After observation of the samples using SEM, we will implement a dedicated X-ray-based methodology, as first started by Cersoy *et al.* [4]. This methodology is based on the use of diffraction techniques in both reciprocal and direct spaces to identify and quantify the amorphous and crystalline phases. Our main goal is to apply such a method to a larger corpus of samples. In addition, as a consequence of their heterogeneity, large and smaller crystals co-exist in the archaeological powder. This aspect, which may prevent meaningful quantitative analyses, will be taken care of as part of an upgrade to the dedicated methodology.

2 Powders from Italian Antique containers

2.1 Use of black powders in Roman times

Black pigment uses in Antiquity in Roman times were various. The most common use was mixing these pigments with various organic compounds to produce black inks, dyes, or cosmetics. Depending on the use, the excipients were carefully chosen to suit the purpose. One of the most described example is the use of black pigments in inks. As seen in the historical part of the previous chapter, three recipes were described by Vitruvius [21], Dioscorides [22], and Pliny the Elder [23]. These three recipes involve the preparation of the ink by mixing black pigment under the form of flame carbon (soot or lampblack), also chars of wood (pinewood), or charred bone (bone black) with a binder, most probably a glucosidic binder (gum) or a proteic binder (animal skin glue). The resulting mixture was intended for writing or painting, the difference most probably coming from the type of binder used [7]. On the other side, during the Roman period, black pigments were also used in the manufacturing of cosmetics. At that time, Romans and Greeks were producing black make-up by mixing these black pigment powders (chars, flame carbon) with excipients (vegetable oils, animal fats, or saliva). These excipients

were destined to make the mixture adhere to the skin [24]. The final product was used to mark eyebrows and the contour of eyelashes.

2.2 Samples from Pompeii and Herculaneum

The eruption of Vesuvius that buried a few ancient cities in 79 A.D. is a dramatic event but opened new possibilities to better understand the daily life of Romans at that period. The effect of the eruption preserved not only the shapes of the body at the instant of their last breath but also many objects of daily life with unprecedented conservation states.

Taking this opportunity, it was possible to find very well preserved containers of various shapes, sizes, and matter that retained various types of powders Figure 2.1. Focusing on the black powders, our collaborator Maria-Christina Gamberini from the Department of Life Sciences of the University of Modena started an extensive study on these [24]. These powders are coming from a set of 1300 containers discovered in Casa di Bacco House in Pompeii. From these 1300 containers, around 30% of them contained traces of substances.

As a result, several studies were made on these black powders from Pompeii vessels, as described in Table 2.1. The first two studies are based on FT-IR and Raman spectroscopy and showed the presence of amorphous carbon and several organic compounds uses as excipients or binders. The third study, using X-ray-based techniques, was more oriented towards the identification of the black carbon-based compounds.

Table 2.1: The three studies based on Pompeii black powders from Casa di Bacco House with the techniques used, the identified phases, and the containers. (FT-IR = Fourier-transform infrared spectroscopy, RS = Raman spectroscopy, EPR = Electron paramagnetic resonance spectroscopy, CG/MS = Gas chromatography-mass spectrometry)

Authors	**Samples and Techniques**	**Identified phases**	**Containers**
Gamberini *et al.* (2008) [24]	113 samples from Pompei FT-IR, RS	Amorphous carbon associated with beeswax, also apatite, cerussite.	No correlation with container type
Canevali *et al.* (2011) [5]	9 samples from Pompeii SEM, FT-IR, RS, XRD, EPR, CG-MS	Charred vegetable material with gypsum	*Theca Atramentaria*
		Variable composition, Calcite, and gypsum	*Unguentarium*
		Organic and inorganic compounds, vegetable oil, copper carbonates	*Aryballos*
Cersoy *et al.* (2016) [4]	5 samples from Pompeii EDX, XRD, PDF, XRD-CT	Charred vegetable material with CaP mineral	*Unguentarium*
		Metallic phases (from the degradation of the bronze vessel)	*Balsamarium*
		Charred vegetable material with gypsum	*Theca Atramentaria*

In the last two studies [4] [5], one of the objectives was to correlate the container and the use of the powder in Roman times. Indeed, the powders intended for use as ink, dyes, or cosmetics may have been stored in specific containers.

One of the authors showed that the most commons vessels are glass, bronze, or *fictile unguentaries* (Figure 2.1) (tear shape vessel) [24]. Regarding the link between the specific use of the powder and the recipient in which it was found, it was demonstrated that cylindrical *theca atramentaria* were mostly used as writing ink containers [5]. On the other hand, *unguentary* and *aryballos* (small spherical flask) were not attributed to a specific powder use [5].

To perform additional analysis, we obtained from M.-C. Gamberini thirteen samples of black powders Table 2.2. These samples are represented in two sets, one from Pompeii with seven samples, and another from Herculaneum with six samples. We also present the type of container in which the powders were collected. Three of these containers are shown in Figure 2.1.

Table 2.2: 7 samples from Pompeii (P) and six samples from Herculaneum (HE))

Sample N	**P2445**	**P3897**	**P9253**	**P9505**	**P11432**	**P12458**	**P18109**
Container	*Glass unguentary*	*Glass unguentary*	*Miniatur-istic olpe*	*Fictile fritillo* on foot	*Glass unguentary*	Bronze *theca cilindrica atramentaria* with lid	Globose clay cup
Sample N	**HE02**	**HE03**	**HE08**	**HE11**	**H75430**	**H76238**	
Container	/	/	/	/	Glass ampoule	Clay olla	

Figure 2.1: Examples of vessels found on Pompeii site with their corresponding inventory numbers. From left to right: glass unguentary, fictile fritillo *on foot, and bronze* theca cilindrica atramentaria con coperchio

In this project, we will first have a look at the morphology of the grains constituting the powders. The observed microstructure can be a characteristic of a specific type of carbon based-pigment as we saw in the first chapter. By using SEM, we will try to identify the morphology of the phases of each sample by comparing it to the set of references shown in the first chapter.

In the next step, we have stored the powders in capillaries (0.7 or 1 mm) and collected XRD data at ID22 in both setups (HR-XRPD : crystal analyzer, 31keV and PDF : 2D detector, 60 keV). We started to record datasets with a 2D detector. This is a way to check for large grains in the diffraction volume, and if necessary, implement specific image processing to separate the single-crystal and the powder contributions prior to quantification.

Then the data analysis will involve Rietveld refinement of datasets recorded at ID22 using the high-resolution setup. In a second time, they will be used to obtain the PDF signal. The PDF approach will be based on the methodology developed by Cersoy *et al.* [4]. This approach involves the comparison of the archaeological signal with a series of reference signals by calculating a correlation factor, the objective being to match the ancient carbon pigment with the references.

3 Observation by SEM

The first step in our methodological approach will be to use the SEM technique to first try to sort out the different types of powder samples. Based on previous studies, we can expect to observe characteristic morphologies from carbon-based compounds. We will then divide our observation into three categories, morphology that can be associated with chars, flames carbons, or non-identifiable.

3.1 Sample preparation

Samples were prepared by microsampling each powder to deposit it on a piece of carbon tape. Then each micro-sample is put on an SEM stage and is numbered. Each piece of tape has a different shape and is placed in a recognizable orientation so that it is easier to proceed with several measurements on the same batch at different times (Figure 2.2).

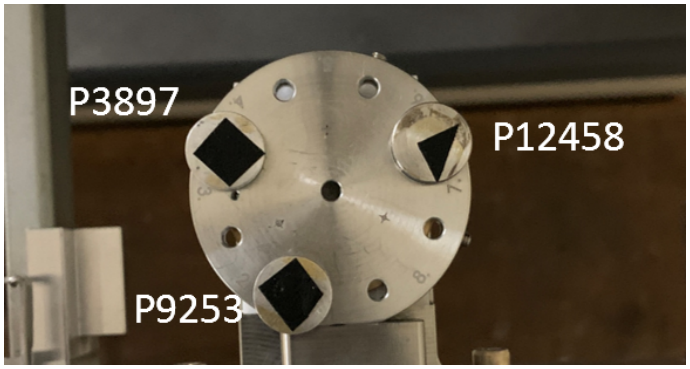

Figure 2.2: Samples on carbon tape, mounted on the SEM nine-holes stage.

3.2 Observation and results

From our thirteen samples, meaningful images from only seven samples were captured. The morphology of the last six samples could not be observed because of strong charging. Each observed sample was observed at different magnifications (100x, 1kx, 10kx) when possible. We recorded images from a secondary electron sensor, with an acceleration voltage of 20kV and a working distance of around 8mm.

From these images, we can recognize three types of morphologies. The flame carbon morphology seen in our commercial lampblack belongs to sample P12458. Sample P3897 has two morphologies: carbonized vegetable with wood cells (Figure 2.3 middle left) and peach black-like morphology (Figure 2.3 bottom left). We assume that even if a morphology can be associated with a type of carbon that corresponds to a measured reference, we will still have to confront these results to the identification of the phases (see XRD part). As a result of the SEM observations, we obtain three categories of sample: flame carbon-based samples, chars-based samples, and samples with undetermined morphologies, as shown in the table(Table 2.3).

These observations show us that in most cases it is complex to identify the origin of the carbon. However, in two cases, the microstructure observed is easily identifiable. This is encouraging in our ability to identify the carbon provenance (chars, flame carbon,...). However, the charging effect

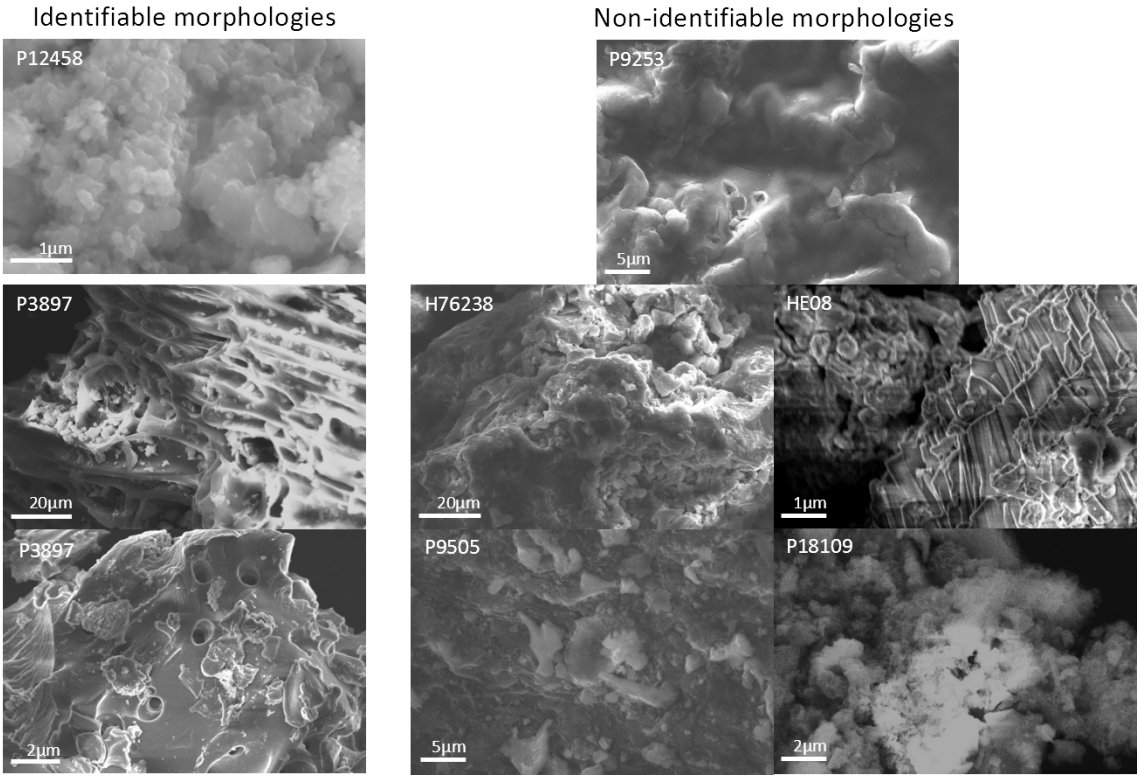

Figure 2.3: SEM secondary electrons image of the seven samples (P3897 has two distinct morphologies) (20kV, WD=7.4mm)

Table 2.3: Observations of seven powder samples. The type corresponds to the aspect of the powder at 100x, either in big chunks or spreads particles.

Sample	**Type and observation**	**Closest reference**	**Category**
P3897	Powder, wood-like structure with cells, 1m pores	Charred wood, peach black	Chars
P9253	Chunk, no image under 2kx	/	Undetermined
P9505	Powder, angular microstructure	/	Undetermined
P12458	Chunk, mixture of angular shapes, 100nm spheroidal particles	Lampblack	Flame carbons
P18109	Powder, angular microstructure	/	Undetermined
HE08	Chunk, scale-like microstructure	/	Undetermined
H76238	Chunk, scale-like microstructure	/	Undetermined

that happens sometimes prevents us from recording good quality pictures at high magnification, which would allow the identification of flame carbon for example. We tried to tackle this by varying the pressure in the chamber of the microscope, but with no success. The only step that would sort this would be to coat the sample with carbon, or gold, but this was not envisaged at this point to avoid sample alteration.

Since observing the microstructure is only qualitative information, we will focus on turning the diffraction signal to our advantage to obtain information about the structure as a part of our multi-analytical approach.

4 Heterogeneous powders: separating amorphous and crystalline contributions

4.1 Introduction

With XRPD we are going to first identify the crystalline phases present in the sample. This will be done with the comparison of the measured d_{hkl} positions with a database through the Search-Match algorithm based on data collected on ID22 using the HR-XRPD technique at 31keV. The use of HR-XRPD is a massive asset because the resolution of the instrument narrows the diffraction peaks increasing the chance of deconvoluting each phase in the patterns.

To help us out, we will also use the fluorescence signal to verify if the elements present in each sample match the identified phases. With the identification done, we will perform Rietveld refinement to obtain quantitative information regarding the powder-like crystalline phases. However, knowing the highly heterogeneous nature of our sample, we can expect to face the situation where the sample does not only behave as a powder (i.e. present diffraction rings) but also can contain larger grains that will behave as single-crystals. It may be complicated to integrate their signal contribution to the quantitative analysis, thus increasing the complexity of the analysis.

To tackle this we have exploited the 2D diffraction images initially collected at 60 keV to perform PDF analysis: we set up a method to separate single-crystal and powder contribution to enable quantification of the powder phase even if there is presence of single-crystals.

Once all the crystalline contribution to the signal is sorted out, we will focus on the amorphous part, which completes the story around our sample. After fitting the crystalline part of each PDF signal, we will be able to isolate the amorphous contribution, and then compare it to the measured references with the Pearson Correlation Coefficient (PCC).

4.2 Exploiting the crystalline part

4.2.1 Separating the single-crystal and powder contributions

Prior to crystalline phase identification, knowing the heterogeneous nature of the samples, we have tried to categorize each sample based on its microstructure (presence of large grains or not). We will use 2D diffraction pattern data to visualize the presence of grains behaving like single-crystals. Since the presence of single-crystals signals in our diffraction is our major concern in the quantification step, it will be important to evaluate if their contribution is significant or not prior to the Rietveld refinement.

To assess the presence of single-crystal, we will first have a look at the diffraction images, looking for diffraction spots. If the presence of single-crystal is important we will use a workaround that consists of removing their contribution with an image processing algorithm directly on the 2D diffraction patterns collected, before their azimuthal integration. To do so, we are using a function already built in the pyFAI python library [6], called *separate*. We created a

program that runs this function followed by azimuthal integration. This code is freely available on Github as a part of PyXRDCT library: poautran/PyXRDCT.

4.2.1.1 Microstructures of the samples

We collected 2D diffraction patterns for each sample on ID22 at 60keV to be able to both categorize the samples and later perform PDF analysis. The data collection aimed to have a first understanding of the heterogeneity of the samples. Figure 2.4 shows the diffraction signals close to the position of the direct beam. Based on the observation of these thirteen images we can divide the samples in three categories: mostly-amorphous powders, mostly-powder powders, and single-crystal-rich.

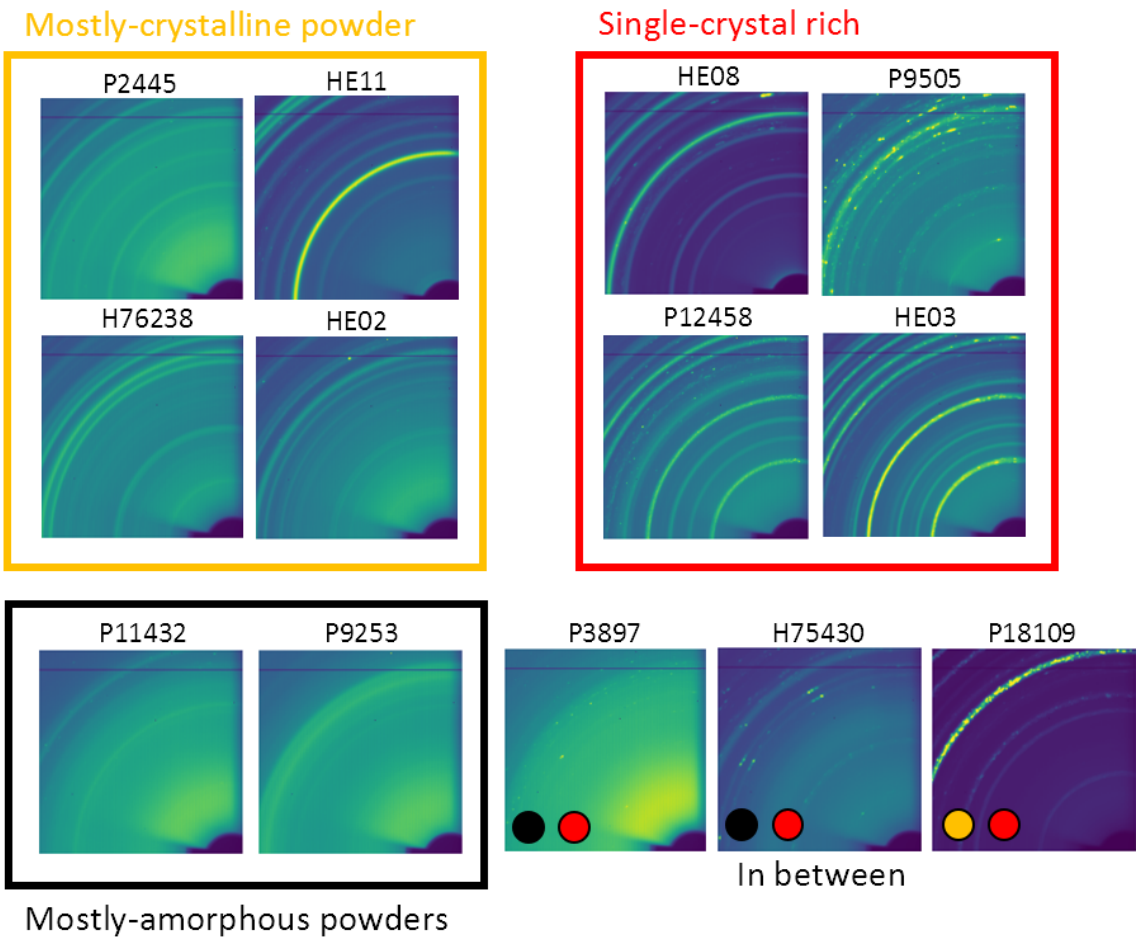

Figure 2.4: 2D diffractions patterns of Pompeii and Herulaneum black powders (60keV, PerkinElmer detector, ID22–ESRF). The pictures are 512x512 pixels out of 4096x4096 to obtain a better view of the single-crystal signal. The direct beam position is corresponding to the bottom corner of each image (Black dot = mostly-amorphous powders, red dot = single-crystal-rich, orange dot = single-crystal-rich).

From this classification, we can already tell on which samples we will focus our attention. Regarding the quantification of the phases, the "mostly-powder" samples are the most adequate samples to perform Rietveld refinements (even if a few single-crystal spots can still be spotted, coming from phases such as quartz, as for HE02). On the other hand, the most complex samples to get information from will be the single-crystal-rich ones. And in between, we have two cases where either a minor single-crystal contribution is present or the single crystal contribution seems

to behave almost like a powder (P18109).

Knowing that the presence of a single-crystals may prevent meaningful quantitative analysis, we decided to correct the 2D diffraction images, and compare the Rietveld refinement carried out on corrected data to the one on uncorrected data. In the next part, we will use the P18109 sample as a proof of concept to show the process of single-crystal and powder contributions separation.

4.2.1.2 Example of powder and single-crystal contributions separation

The goal of this correction is to separate the single-crystal contribution from the powder contribution on 2D diffraction data to be able to fit the powder contribution alone. Figure 2.5 shows the result we want to obtain.

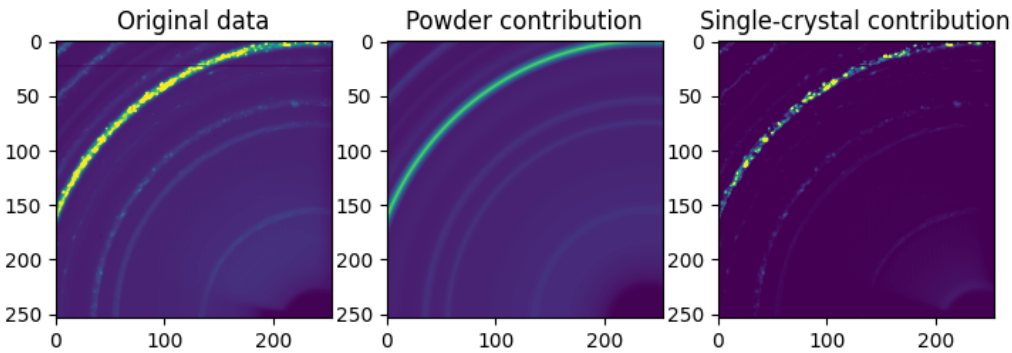

Figure 2.5: Separation of single-crystal and powder contribution from a 2D diffraction pattern portion of sample P18109.

This represents the perfect case where all the single-crystals appearing as dots from variable sizes are separated from the powder contribution.

The separate function works with median filtering on the azimuthal integrated 2D image, also called cake. This filtering is controlled by a percentile value used to set the cutoff depending on the different cases. After applying this median filter, the image is then back-projected to obtain the 2D powder contribution (Figure 2.5). The single-crystal contribution is obtained by subtracting the 2D powder contribution from the original data.

To carefully set the percentile parameter, it is important to assess the quality of the process by observing the result of the single-crystal contribution. Either the value is too high and no single-crystals are found, or the value is too low and we overshoot and remove also part of the powder contribution from the image. This parameter is currently set step-by-step empirically and would require a dedicated algorithm for a more appropriate guess. The two extreme cases of the percentile parameter choice are presented in Figure 2.6A-B.

The perfect choice of P is achieved when the single-crystals appear on the corresponding extracted image while the single-crystal contribution signal is not negative. If the single crystal signal becomes negative, the subtracted signal over compensates the signal associated with a single-crystal contribution and creates a spike (Figure 2.6C).

4.2.1.3 Application to the data:

With the use of this tool to separate the single-crystal contribution from the powder, we can apply it to our 2D diffraction patterns recorded on our powders from Roman archeological sites. Since a few of them presents various degrees of single-crystals, we will present two different cases: an ideal case and an extreme case.

Ideal case: This case represents the entire family of diffraction patterns that have a few single-crystals that can be either related or non-related to a powder-phase (mostly powder and

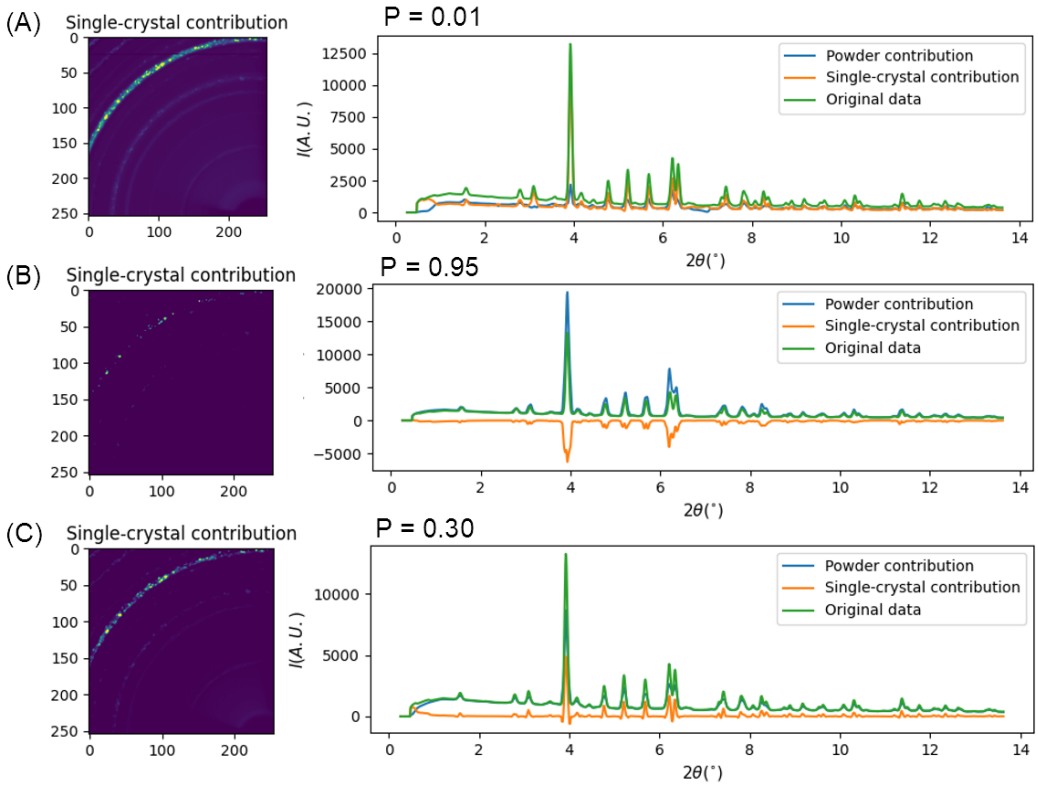

Figure 2.6: Influence of the percentile on the single-crystal/powder contribution separations. (A) P=0.01, the percentile is too low and powder rings are assimilated as single-crystals, the obtained powder pattern lacks some powder data. (B) P=0.95, the percentile is too high, some single crystals are not detected and the algorithm compensates with a negative signal, (C) P=0.30, the percentile is correctly chosen and the single-crystal signal remains positive. The single-crystal contribution is correctly removed.

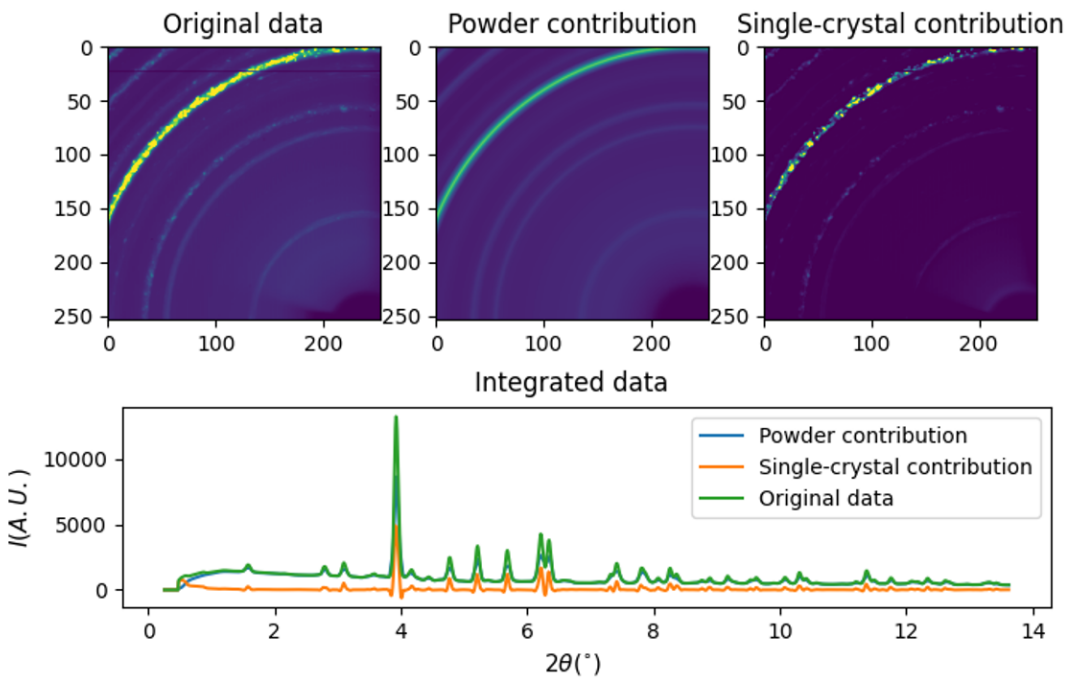

Figure 2.7: Single-crystal contribution removal on sample P18109 from Pompeii. The sample contains mainly calcite in both powder and single-crystal forms.

in-between samples in Figure 2.4). The main advantage is for sample with a phase with smaller powder-like grains and larger single-crystals of the very same phase. By removing them, we can correct the 1D pattern and the intensities should be better fitted. This is exactly the case of the sample P18109 and H75430 (Figure 2.7).

In this case, it appears that the single-crystal contribution for calcite can be separated from the powder part. The Rietveld refinement of the original pattern shows intensities issues due to the single-crystals (Figure 2.8). The reflections $(10\bar{1})$ and $(2\bar{1}3)$ in particular are better refined after correction (Figure 2.8).

We can also note that the quantification results are slightly different. Since we separated a part of the signal contributing to the calcite single-crystals, the relative quantity of calcite is slightly lower by around 4%.

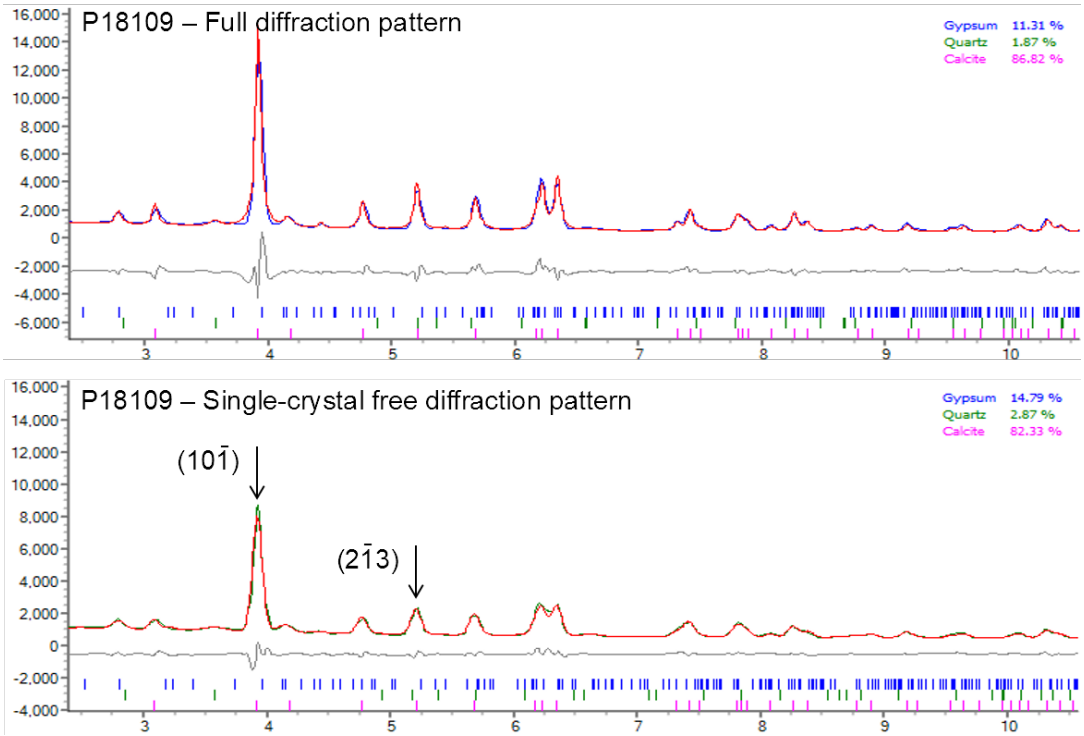

Figure 2.8: Rietveld refinements of P18109 sample with and without the single-crystal contribution (ID22–60keV, Red = Fit, Blue/Green = Observed, Rwp = 6.1 and 5.62 respectively)

Extreme case: In this case a large number of single-crystal peaks are present. This is happening for samples P9505, P12458, HE08 and HE03 (Figure 2.4). Figure 2.9 shows an example of separation carried out on P9505 sample, and even with a large number of spots, the separation works well.

Figure 2.10 shows the evolution of the refinement before and after the single-crystal removal. The refinement is not perfect but, as seen in the previous example, the main sharp peaks are lower in the diffraction pattern free from single-crystals. Due to the width of the peaks, it is not very straightforward to put the corresponding phase reflection from which the signal is lowered.

If we compare the two diffraction patterns in Figure 2.10, the quantification before and after the single-crystal separation is similar with a maximum difference of 4%.

To conclude, in both cases, removing the single-crystal contribution from the diffraction data helps improving the refinement. On the other hand, the quantification results do not show significant changes (less than 5% in the two cases presented here). The 2D data, also collected for PDF analyses, are lacking angular resolution. Knowing that phase quantification may not be profoundly affected by the presence of single-crystals, the HR-XRPD data (that cannot be

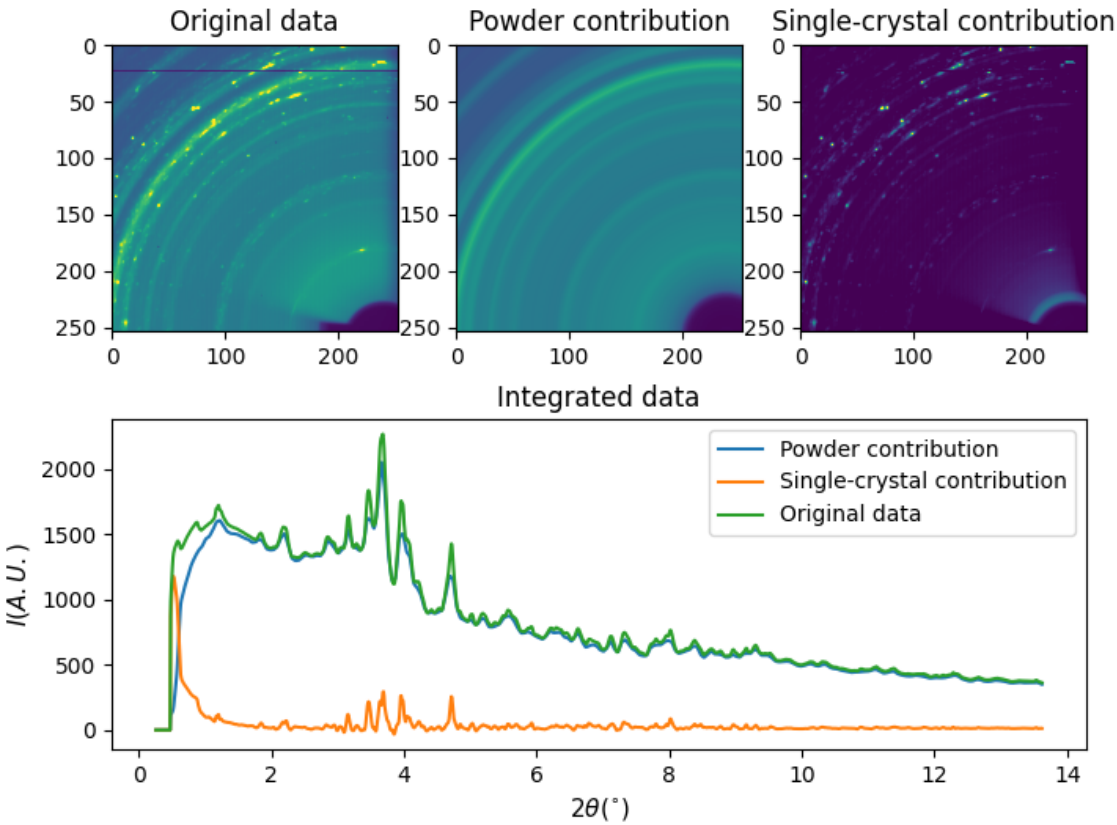

Figure 2.9: Single-crystal contribution removal on sample P9505 from Pompeii. The single-crystal contribution comes mostly from leucite, quartz and orthoclase.

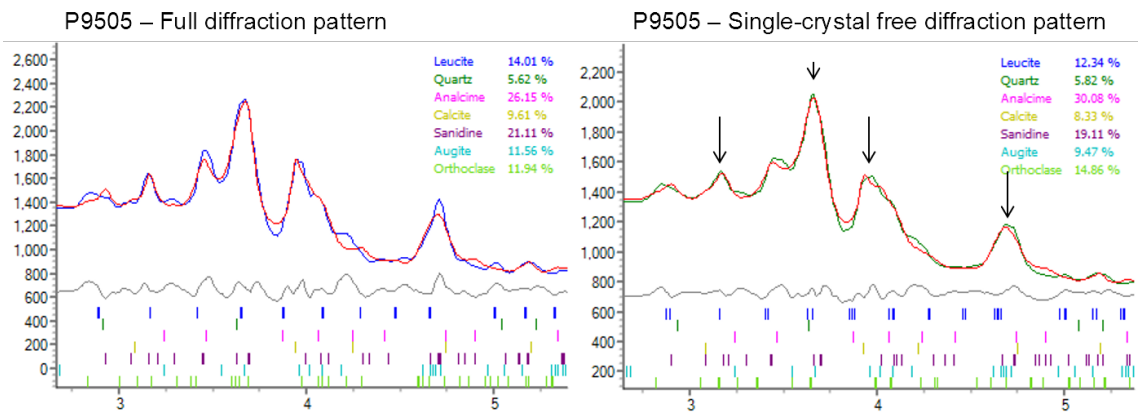

Figure 2.10: Rietveld refinement of the 2D integrated diffraction patterns from sample P9505 (ID22–60keV, Red = Fit, Blue/Green = Observed, Rwp = 2.65 and 1.81 respectively)

corrected from single-crystal contribution) will be used in the following for both phase identification and quantification. The corrected 2D data will be used for PDF analyses.

4.2.2 Phase identification

We have just seen that even with the presence of single-crystals, the quantification of the phases is little affected and we therefore used the HR-XRPD data to both identify and quantify the crystalline phases. The identification of the crystalline phases of each sample is presented in Table 2.4. From the thirteen samples, four are mostly amorphous and eight are presenting various crystalline phases. From these phases, quartz, analcime, and leucite are almost always present.

Table 2.4: Table of the identified phases for each sample. The database used is PDF2-2003 on Diffrac.EVA V5.0. The phases are ordered by EVA semi-quantitative ratio S-Q. Phases in italics represent values of S-Q lower than 3%.

Sample\Reference	**Identified crystalline phases**
P2445	Whitlockite, *Hydroxylapatite*
P3897	*Quartz*, *Augite*, *Leucite*, *Sanidine*, *Gypsum*, *minor unidentified phase*
P9253	Minor unidentified phases
P9505	Leucite, Augite, Sanidine, Anorthite, Calcite, Quartz, Orthoclase, *Analcime*
P11432	*Phosphohedyphane*
P12458	Gypsum, Quartz, Malachite, Calcite, *Analcime, Leucite, Cerussite*
P18109	Calcite, Gypsum, *Quartz*, *Analcime, Leucite*
HE02	Leucite, Augite, Sanidine, Anorthite, *Analcime, Malachite, Quartz*
HE03	Gypsum, Brochantite, Malachite, Calcite, Monohydrocalcite, *Quartz, Analcime*
HE08	Cassiterite, Iron, Malachite, Cerussite, Quartz
HE11	Goethite, Magnetite, Maghemite, Hematite, Sanidine, Leucite, Cristobalite, *Analcime, Calcite*
H75430	Leucite, Augite, Quartz, *Analcime*
H76238	Leucite, Calcite, Augite, Sanidine, Quartz, Orthoclase, *Anorthite, Analcime*

Each identified phase is presented in Table 2.5 with the PDF2-2003 database reference number that matches.

Table 2.5: Principal identified phases with chemical formula and PDF2-2003 [52] reference numbers.

Phase	**Chemical formula**	**PDF reference number**
Analcime	$NaAlSi_2O_6$, H_2O	PDF 41-1478
Anorthite	$CaAl_2Si_2O_8$	PDF 18-1202
Augite	$((Si,Al)_2O_6)(Ca,Mg,Fe,Ti,Al)_2$	PDF 41-1483

Brochantite	$Cu_4SO_4(OH)_6$	PDF 43-1458
Calcite	$CaCO_3$	PDF 05-0586
Cassiterite	SnO_2	PDF 41-1445
Cerussite	$PbCO_3$	PDF 47-1734
Cristobalite	SiO_2	PDF 39-1425
Goethite	$FeO(OH)$	PDF 29-0713
Phosphohedyphane	$Ca_2Pb_3(PO_4)_3Cl$	PDF 60-0659
Gypsum	$CaSO_4$, $2H_2O$	PDF 33-0311
Hematite	Fe_2O_3	PDF 33-0664
Hydroxylapatite	$Ca_5(PO_5)_3(OH)$	PDF 09-0432
Iron	Fe	PDF 06-0696
Leucite	$KAlSi_2O_6$	PDF 38-1423
Magnetite	Fe_3O_4	PDF 19-0629
Malachite	$Cu_2CO_3(OH)_2$	PDF 41-1390
Monohydrocalcite	$CaCO_2$, H_2O	PDF 29-0306
Orthoclase	$KAlSi_3O_8$	PDF 19-0931
Quartz	SiO_2	PDF 46-1045
Sanidine	$K(AlSi_3O_8)$	PDF 19-1227
Whitlockite	$Ca_9(MgFe)(PO_4)_6PO_3OH$	PDF 09-0169

To ensure the validity of the phase identification, we checked the fluorescence signal of each sample. Each fluorescence spectrum was acquired at the same time as the XRPD patterns in the same condition but with a shorter acquisition time. The emission lines of each element present in the spectra were compared to the reference tables as a first guess. Then a fit of each spectrum was made to ensure the validity of the identification.

We used fluorescence signal not with the notion of quantifying the elements present, but for two reasons: i) ensuring that we did not miss (or mismatched) any crystalline phases from the XRPD data after phase identification; ii) if additional elements are present and crystalline phase identification complete, this may give an indication on the composition of the amorphous phase.

In the example of sample HE11 (Figure 2.11), since it contains mostly iron oxides, it is not a surprise to see that the principal emission line is coming from iron. The emission lines of strontium is also clearly identifiable and probably comes from the substitution of calcium from calcite. Other elements are very minor and come most probably from the measurement environment. This is confirmed by their presence in multiple samples. We can cite analcime, augite, sanidine, quartz, or leucite.

After identifying all the crystalline phases in our sample, the next step is to quantify these phases by performing Rietveld refinements.

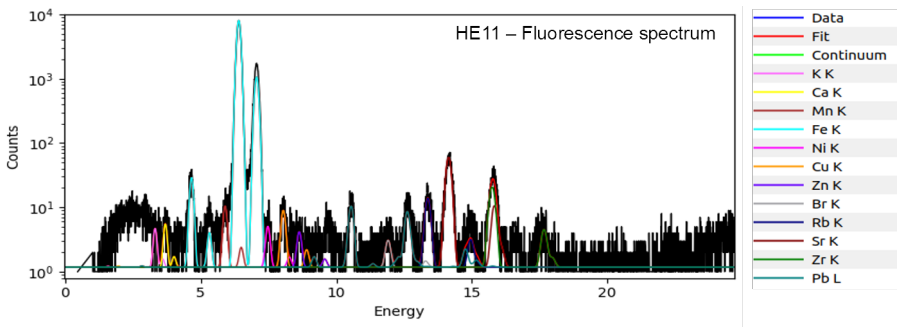

Figure 2.11: Fluorescence spectrum of sample HE11. Intensities are in log scale, energy in keV. Elements with Z<18 are not present due to the absorption in the air.

4.2.3 Rietveld refinements of HR-XRPD data

With the identification of the crystalline contribution of each sample completed, we can focus on quantifying each crystalline phase to obtain the full picture of the crystalline composition of our samples.

To do so, we will perform Rietveld refinements on each of the HR-XRPD patterns collected that contains at least two crystalline phases. For each phase, we will refine the scale factor, the lattice parameters, and the Pseudo-Voigt peak shape parameters. Atom positions and thermal expansion factor were not refined and their values were kept from the .cif structure file. The background will be carefully picked (the amorphous part, if any being included in it) to reduce quantification mistakes. We will discuss here two cases of refinements, one that easily works, and a more complex one.

4.2.3.1 The case of P18109

The sample P18109 is very rich in calcite and gypsum. The Rietveld refinement gives the resulting fit shown in Figure 2.12.

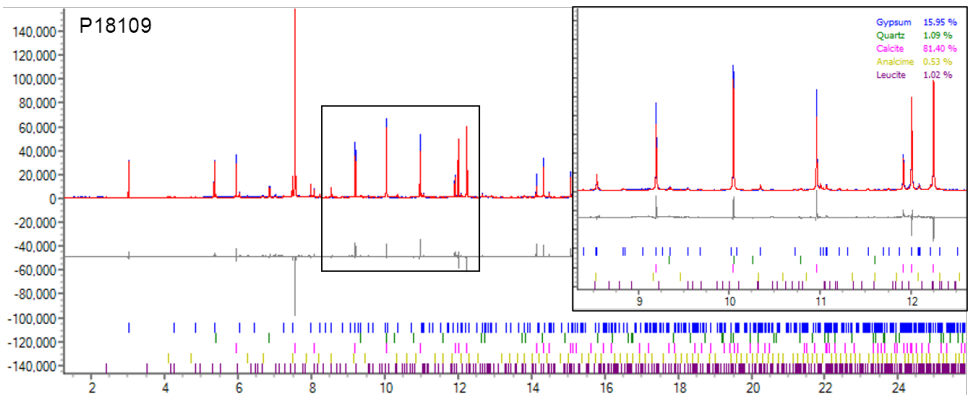

Figure 2.12: Rietveld refinement of P18109 HR-XRPD pattern.(Red = Fit, Blue = Observed, Rwp = 15.2, Rexp = 3.10, Rp = 11.0)

Even if the identified phases correctly match the refinement, we observed some residue on some of the diffraction peaks. We have shown earlier that the intensities of the peaks are maybe affected by the presence of a few single-crystals. In the present case, mainly the peaks of calcite are affected, and indeed, on corresponding 2D images, a few single-crystal spots coming from larger calcite crystals are over-imposed with calcite rings (Figure 2.4). Compared to the refinement done from 2D data, due to the quality of the data, two additional minor phases could be introduced in the fit (analcime and leucite). The quantification is anyway similar, the pattern being dominated by calcite (> 80%) and gypsum (10 to 20%). The three other phases are really minor (<2%).

4.2.3.2 The case of P9505

In this case, we accumulate the difficulties to perform a correct Rietveld refinement (Figure 2.13). We have in total eight identified phases, most of them showing a single-crystal contribution (Figure 2.4). In addition, some phases were not identified, so they are missing in the fit. As a result, the refinement is quite poor. Compared to the refinement from 2D data, anorthite was included in the fit. We observed that the ratio of calcite and analcime is now reversed. If part of this could be coming from an intense single-crystal contribution, this could also be due to the fact that a different region of the capillary was probed.

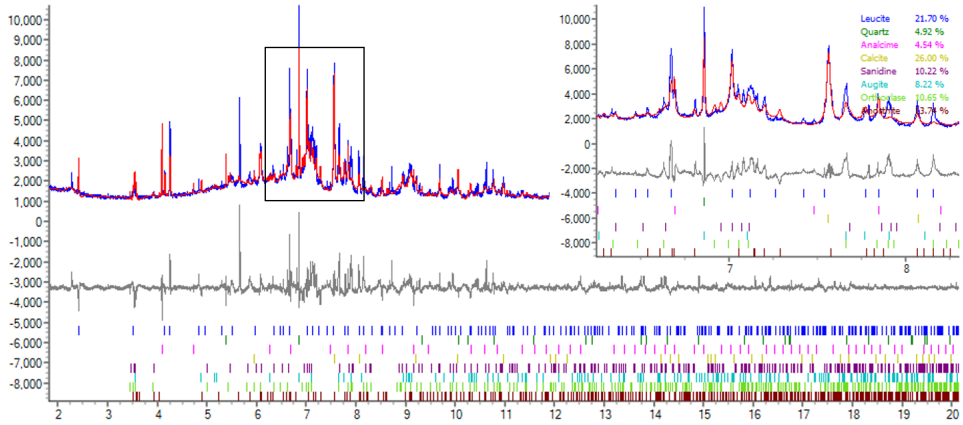

Figure 2.13: Rietveld refinement of sample P9505 (Red = Fit, Blue = Observed, Rwp = 9.15, Rexp = 9.15, Rp = 6.26).

4.2.3.3 Complete results

A Rietveld refinement was performed on all relevant samples. As stated before, some of the samples contain a large number of single-crystal which makes the peak intensities wrong as in the case of P9505, P12458 and P18109 (see Figure 2.4) and the refinement difficult. Other samples do not contain any crystalline signal (or just one phase) which makes the refinement irrelevant (P9253 and P11432). In other cases (e.g. P2445 or H76238), one or two phases only show a strong single-crystal contribution, and these phases were added in the refinement in Pawley mode. Results are shown in Table 2.6.

*Table 2.6: Quantification of crystalline phases of each sample containing mostly powder contributions (ID22–HR-XRPD–31keV). *Refined with Pawley fit because of SC contribution, not taken into account for the quantification*

Sample	**Rietveld quantification of crystalline phases**	**Agreement factors**
P2445	Whitlockite* Hydroxylapatite*	Rwp 4.62 Rexp 3.27 Rp 3.19
P3897	Quartz* Augite* Leucite* Sanidine*	Rwp 3.67 Rexp 5.77 Rp 2.54
P9253	Phases are not identifiable	/

P9505	Leucite **20.4** (0.11) Augite **7.95** (0.18) Sanidine **12.9**(0.24) Anorthite **15.38** (0.21) Calcite **23.54** (0.22) Quartz **4.64** (0.03) Orthoclase **10.91** (0.25) *Analcime **4.28*** (0.02) Malachite*	Rwp 9.80 Rexp 3.20 Rp 6.61
P11432	Phosphoedyphane*	/
P12458	Gypsum **53.3** (0.09) Quartz **4.60** (0.02) Malachite **33.8** (0.09) Calcite **6.05** (0.07) *Analcime **0.28*** (0.03) *Leucite **0.81*** (0.04) *Cerussite **1.23*** (0.01)	Rwp 13.3 Rexp 5.00 Rp 9.26
P18109	Calcite **82.0** (0.1) Gypsum **15.9** (0.09) Quartz **1.00** (0.02) *Analcime **0.51*** (0.03) *Leucite **0.62*** (0.04)	Rwp 15.8 Rexp 3.10 Rp 11.0
HE02	Leucite* Augite* Sanidine* Anorthite* Analcime* *Malachite** *Quartz**	Rwp 10.4 Rexp 3.83 Rp 7.10
HE03	Gypsum **66.6** (0.1) Brochantite **23.3** (0.07) Malachite **4.53** (0.08) Calcite **2.72** (0.05) Monohydrocalcite **2.23** (0.05) *Quartz **0.13*** (0.01) *Analcime **0.53*** (0.03)	Rwp 10.3 Rexp 3.95 Rp 7.62
HE08	Cassiterite* Iron **72.78** (0.29) Malachite* Cerussite **15.71** (0.19) Quartz **11.52** (0.30)	Rwp 7.13 Rexp 2.91 Rp 4.88
HE11	Goethite **60.1** (0.13) Magnetite **11.3** (0.03) Maghemite **8.35** (0.02) Hematite **4.71** (0.01) Sanidine **1.85** (0.01) Leucite **4.56** (0.01) Cristobalite **3.00** (0.01) *Analcime **1.27*** (0.003) *Calcite **1.10*** (0.003)	Rwp 11.86 Rexp 3.57 Rp 8.90
H75430	Leucite **78.0** (0.70) Augite **14.4** (0.6) Quartz* *Analcime **7.60** (0.48)*	Rwp 7.01 Rexp 4.75 Rp 4.93
H76238	Leucite **46.9** (0.1) Calcite **37.4** (0.08) Augite **4.0** (0.15) Quartz **4.7** (0.01) *Sanidine* Analcime **7.0** (0.13)*	Rwp 10.3 Rexp 3.30 Rp 6.80

4.2.4 Conclusions, limits, and improvements

In this part, we were able to identify and quantify the crystalline phases present in most of the samples. High-resolution powder diffraction made the identification of the present mineral particularly easy.

However, the presence of single-crystals in a few of our samples made the quantification not ideal. Therefore, with the help of image processing on 2D diffraction data recorded at 60keV, we were able to improve the quality of our fit of the powder contribution by excluding the signal of the single-crystals contribution. Nevertheless, less than a 5% difference was found in terms of phase quantification after excluding the single-crystal contribution.

4.3 Exploiting the amorphous contribution to the signal with PDF fitting

After sorting out the identification and the quantification of the crystalline part of our samples, we are now focusing on getting information about the amorphous part. To do so, we use the Pair Distribution Function (PDF) analysis. In this part, we will implement a dedicated methodology to separate the crystalline and amorphous contributions from the PDF. This will enable the possibility to compare the amorphous contribution of our samples to the measured standards presented in chapter 1.

4.3.1 Methodology

With the same diffraction data shown previously (ID22–60keV) we did a Fourier transformation through the *pdfgetx3* software. The data used were corrected from single-crystal contributions with our method which is a mandatory key step to perform such analysis. For each sample, we obtain a PDF, representing the distribution of distances between pairs. The histogram is defined by G(r), the probability of finding a particle at a distance r, versus r, the distance.

The first step is to distinguish two ranges, the low-order range, and a longer order range. The long-order range corresponds to high r values, from which the peaks are attributed to the distance between atoms from a crystal (Figure 2.14). On the other hand, low values of r represent short-range order, from which the peaks are from atoms pairs of both crystalline compounds and amorphous compounds.

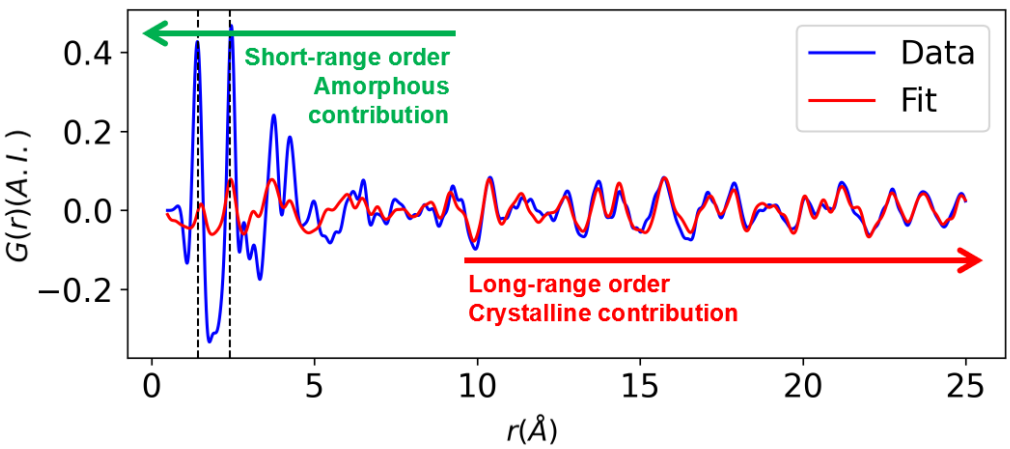

Figure 2.14: PDF of sample P2445 with the fit of the crystalline contribution mainly made of whitlockite.

If we managed to refine the structure of our powders in HR-XRPD, we can also refine it in PDF to fit the long-range order peaks. The idea is to refine the crystalline structure of our sample (i.e. the long range order), then, assuming the refinement is appropriate, subtract the fit to the data. This will reveal the signal of everything that was not fit, i.e. the amorphous contribution at small r values.

After the subtraction, the result will be compared to all the PDF obtained on our amorphous references. The comparison will be assessed by a correlation factor called the Pearson correlation coefficient or PCC. The PCC is calculated with the following formula:

$$r = \frac{\sum(x_i - \bar{x})(y_i - \bar{y})}{\sqrt{\sum(x_i - \bar{x})^2 \sum(y_i - \bar{y})^2}} \tag{2.1}$$

where,

- r = correlation coefficient,

- x_i = values of the x-variable in a sample,
- $\bar{x}$ = mean of the values of the x-variable,
- y_i = values of the y-variable in a sample,
- $\bar{y}$ = mean of the values of the y-variable.

The implementation of the PCC calculation was made through the python function *pearsonr* from *scipy.stats* module, and was implemented in a python code called *pcc.py* also part of PyXRDCT. This code takes into entry the PDF of the sample and outputs the PCC values for each reference sample.

4.3.2 Example

To illustrate this strategy, we will take an example based on the sample from Pompeii P2445. This sample was chosen because it represents the ideal case. It has only one major crystalline phase (whitlockite) with no presence of single-crystals.

After performing the Fourier transform of the XRPD signal we obtain the PDF. This process was detailed in the first chapter. The starting point is a known structure, the very first parameters to set are the space group and the lattice parameters. In practice, after loading a PDF pattern, we enter each crystal structure that we identified previously. The main parameters that we will refine are: the lattice parameters, the DWFs (attenuation because of thermal motion) also noted u, and the atom positions. We can note that in theory, the parameters obtained from the Rietveld refinement on HR-XRPD data should be quite close to the one we expect to obtain. As we decided to enter them directly as a first guess, the refinement should not show major changes for those values.

We keep in mind that the refinement is there to try to fit as best as possible the crystalline part of the sample. Therefore, it is logical to fit a range that represents the best this crystalline part. It was decided to first, refine the parameters based on the signal at a longer-range order (i.e. >15 Å) and then, apply the same parameters to calculate the fit on the entire range.

The first example of such a fit is represented in Figure 2.15.

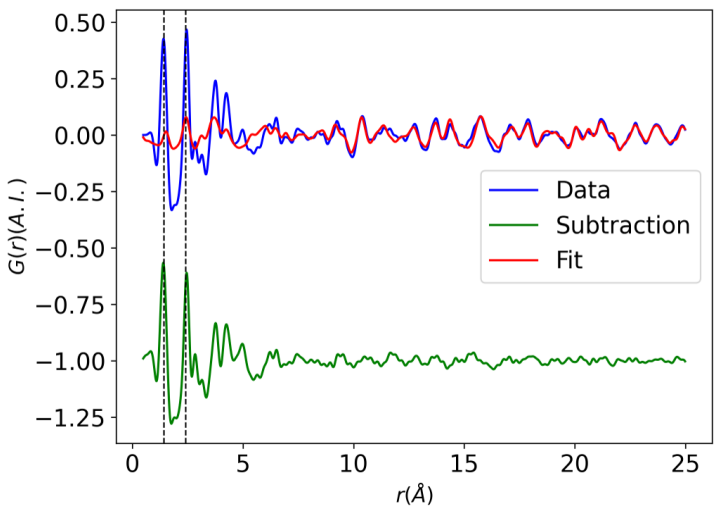

Figure 2.15: PDF fit of sample P2445 (only one crystalline phase (whitlockite) is considered), the data was fit with an r value superior to 15 Å, then it was applied to the whole range (Rw = 0.82). The green curve represents the subtraction of the blue from the red. The two black dotted lines correspond to the two first carbon-carbon bond distances of a graphite layer (1.42 Å and 2.42 Å)

The obtained residue represents the contribution of the amorphous compound from our sample. The first result is that the two peaks characteristics of C-C distances are present, confirming the carbon-based origin of the amorphous part. There are no particular features that remain at high r, which means that the fit of the crystalline part was adequate, with no obvious missing phase.

The next job is to compare this to references and if possible, to associate it with a specific one. Figure 2.16 shows a comparison between the amorphous PDF signal from sample P2445 with the PDF of the references.

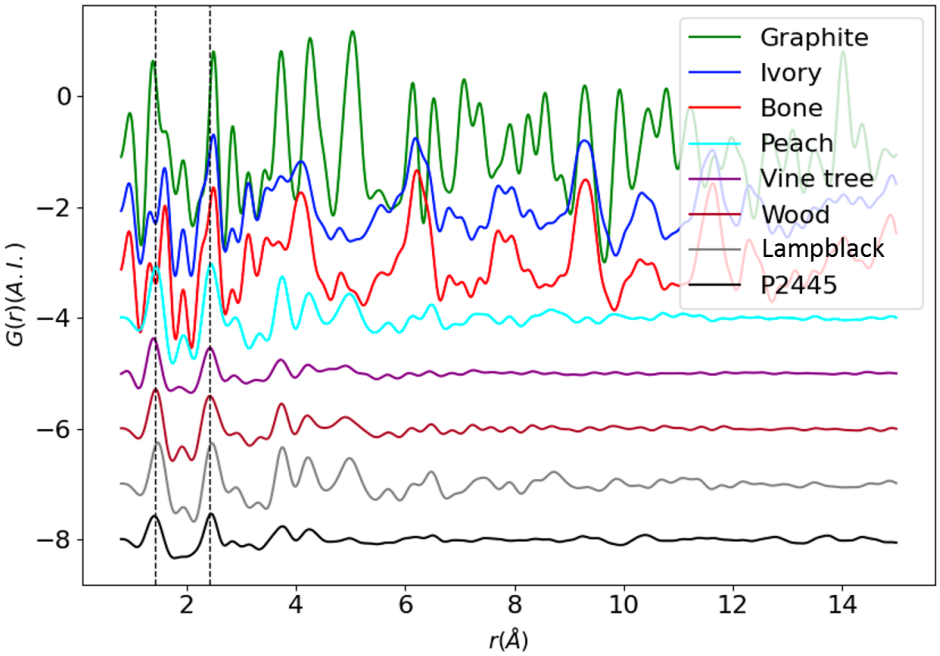

Figure 2.16: Comparison of the PDF signal of all the references with samples P2445 after subtraction of the crystalline signal.

The first conclusion is that the P2445 amorphous part does not correspond to graphite, which is crystalline and would have been identified from HR-RXPD. Concerning ivory black, or bone black, the references were not subtracted from the crystalline part, so direct comparison is less straightforward. The presence of whitlockite in the crystalline part may be related to bone or ivory black, and this is going to be discussed later in a dedicated paragraph. So we will focus on the four other references: peach black, vine tree black, wood charcoal, and lampblack (Figure 2.17).

Visually, P2445 seems closer to wood and vine tree because the signal drops significantly after 7 Å, but considering the low r range, it is more complicated to conclude. That is why we want to formalize the comparison between the spectrum with the PCC values.

4.3.3 Results

The presence of carbon is determined by the presence of the PDF peaks at 1.42 and 2.42 Å (Figure 2.18). These two peaks are present in eight of thirteen samples.

We calculate the PCC (Pearson correlation factor) for each of the four references, and we will compare the values to try to match each amorphous phase to its closest reference. We chose to calculate the PCC over an r range of 1 to 15 Å, but calculating them on a lower range gives globally higher PCC values and similar conclusions. The top range limit being lower makes the importance of the higher values of r lower and so the difference between wood and lampblack, for example, attenuated, thus lowering the differences in the PCC values.

The PCC values of each sample compared to the four references are displayed in Table 2.7.

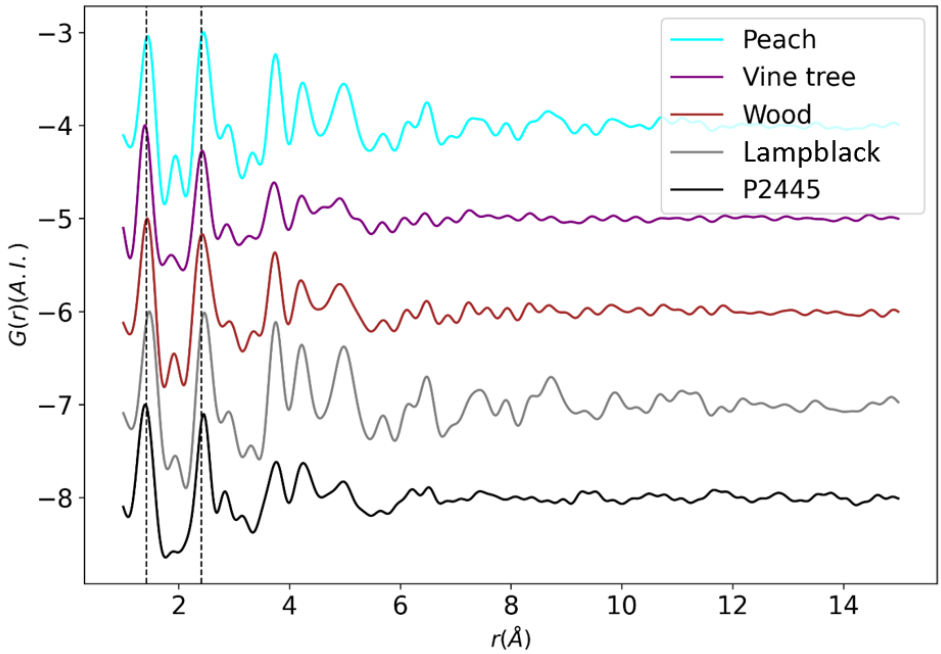

Figure 2.17: PDFs of references and sample P2445 amorphous phase, normalized to the maximum value. By eye, P2445 resembles more to be originated from Vine tree or wood. The two black dotted lines corresponds to the two first carbon-carbon bond distances of a graphite layer (1.42 Å and 2.42 Å)

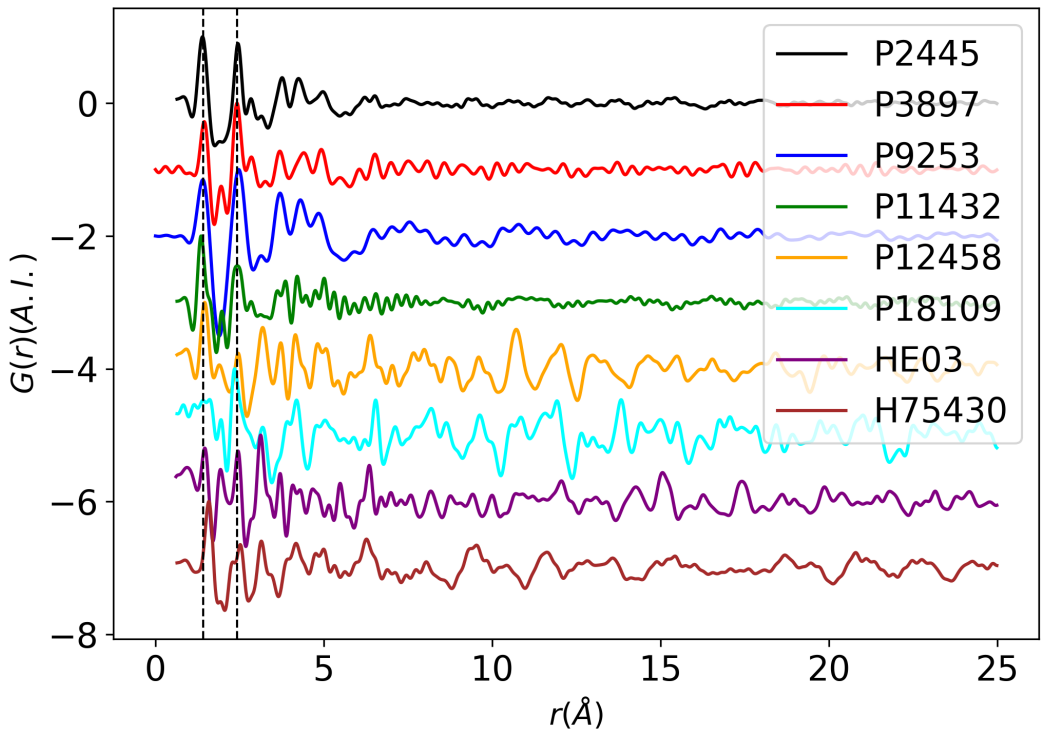

Figure 2.18: PDFs of all samples that comport peaks at 1.42 Å and 2.42 Å suggesting they contain amorphous carbon. The two black dotted lines corresponds to the two first carbon-carbon bond distances of a graphite layer (1.42 Å and 2.42 Å)

Table 2.7: PCC values for each sample compared to four references. (*) Subtraction of the crystalline phases not conclusive.

Sample\Reference	**Carbon Yes/No**	**Peach**	**Vine tree**	**Wood**	**Lampblack**
P2445	Yes	0.899	0.938	0.933	0.825
P3897	Yes	0.866	0.836	0.874	0.771
P9253	Yes	0.783	0.808	0.850	0.748
P9505	No	/			
P11432	Yes	0.808	0.858	0.837	0.739
P12458	Yes	*			
P18109	Yes	*			
HE02	No	/			
HE03	Yes	*			
HE08	No	/			
HE11	No	/			
H75430	Yes	0.244	0.232	0.289	0.349
H76238	No	/			

For three samples (P12458, P18109, HE03), even if they present signs of the presence of an amorphous carbon, the fit of the crystalline part was not good enough. When subtracting the fit of the crystalline phase to the PDF, the residue is not comparable to any of the carbon references. This is due to a high number of crystalline phases, making the PDF fit quite challenging, and most of the time a quantity of amorphous phase that is too low to be distinguishable from the noise after subtraction. In addition, the single-crystal separation process can also be limited by the proportion of the phases being single-crystals thus not leading to a proper PDF fit.

The presence of carbon is determined by the presence of the PDF peaks at 1.42 and 2.42 Å Figure 2.18. These two peaks are present in eight of thirteen samples. The PCC values obtained for four of thirteen samples are between 0.7 and 1, which was also the case of Cersoy *et al.* [4]. However, for the sample H75430, we obtain values around 0.2. It presents the carbon peaks but also other peaks corresponding to an amorphous compound which is also found in samples H76238 and HE02.

These three samples present peaks at regular intervals as shown in Figure 2.19.

These peaks have nothing to do with the presence of amorphous carbon. The presence of peaks at 1.59, 2.53, 3.14, and 4.19 Å could indicate the presence of another amorphous compound such as a type of lipid (oil, fat).

5 Discussion

We measured a total of thirteen black powders. Regarding their black color, eight of the thirteen presents the peaks at 1.4 and 2.4 Å in the PDF signal. This indicates that they contain amorphous carbon which is responsible for their color. In the five other samples, one (HE11) is containing a wide number of iron oxides including a large amount of magnetite which explains its color. One of the samples (HE08) contains a large amount of cassiterite, a black tin oxide. The last three are also black but we do not have any formal explanation of their color. Two hypotheses can be

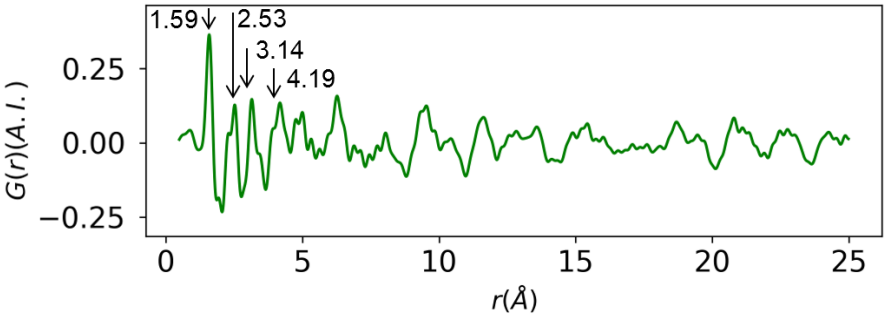

Figure 2.19: PDF fit of sample H75430, the data was fit with an r value superior to 15 Å, then it was applied to the whole range. The green curve represents the subtraction of the blue and the red.

formulated. Either the pigment is amorphous and we were not capable to identify it with our set of methods, either the pigment is carbon black but in a quantity that is too small compared to the crystalline contribution, and we were not able to extract it.

For the eight amorphous carbon-containing samples, we were able to identify two morphologies from the four measured thanks to SEM. The sample P3897 has a morphology of both wood and peach blacks. This was compared to the references shown in the first chapter. This composition is also confirmed thanks to the PCC values calculated between the PDF signal of the samples and the references. The PCC coefficient calculated on three other samples tells also that P2445, P9253, and P11432 have PDF signals closer to a vegetal-based carbon pigment rather than lampblack. The sample P11432 contains phosphohedyphane. The structure of this phase was discovered by Kampf *et al.* [53] in 2006. This lead phosphate was identified in the sample sample analysed by Cersoy *et al.* [4] and also found by Christiansen *et al.* [54] in red inks on papyrus from the Roman period. The origin of this compound remains unclear. Author mention three precursors: pyromorphite that was found on Roman wall paintings and used in a mixture to form a pigment, metallic alloys from vessels containing fertilizer that could degrade over time, or the reaction of hydroxylapatite with litharge (PbO). At this stage, we can only refute the second proposition since our vessel is made out of glass.

The sample P12458 was the only one presenting spheroidal particles of around 100nm that corresponds to lampblack. Sadly, the large amount of mixed crystalline compounds made the PCC analysis non-conclusive because of the difficulty to subtract the crystalline contribution to the PDF signal. The sample H75430 was also presenting some carbon peaks in the PDF but another signal from another amorphous compound is present, lowering drastically the values of the PCC making the conclusion not possible.

About the crystalline phases that are not related to the black color, we observed that several phases are recurrently present. Phases such as analcime, sanidine, leucite, and augite are most probably related to the volcano eruption and were found also in other studies of pigments from Pompeii [55]. The presence of these can also assess if the container was caped or not before the excavation. In our case, we can suppose that only samples P2445, P9253, P11432, and possibly P3897 may have been sealed. Interestingly, these samples are the ones contained in the smallest containers (glass *unguentary*, miniaturistic *olpe*) which are probably easily sealed or clogged.

Several phases are not black and probably not coming from a pollution from the volcano. The presence of gypsum and calcite in a relatively high quantity in some samples (P12458, P18109, HE03) can be explained by its use in the mix to prepare inks. These were explained to be used as drying agents [5]. Malachite was also identified in sample P12458 from which the container is made out of bronze. It was demonstrated that malachite can form upon the degradation of bronze vessels [24] which is most probably our case here. The presence of cassiterite and cerussite in HE08, can also be correlated to the degradation of lead and tin from which some vessels were

made [4].

In three of the samples (H75430, H76238, and HE02), we identified the presence of an amorphous compound that is not a carbon-based pigment. This could be an excipient that was used in the preparation of an ink or a cosmetic. The signal appears only on samples HE02, H75430, and H76238 which are all three from Herculaneum. As mentioned by Gamberini *et al.* [24], excipients regularly found are most of the time oils from cosmetics rather than proteic or glucosidic binder used in ink manufacturing which is more likely to be degraded from the effects of time. To go further, it would be valuable to analyze these compounds with techniques oriented on organic compound characterization such as NMR, IR or CG-MS.

Only one sample is completely different from the others. Indeed, sample P2445 contained whitlockite, a calcium phosphate from which the composition is closed to hydroxylapatite. Hydroxylapatite was also identified in the same sample, but with uncertainty due to extremely low intensities (see Appendix A.). A study around this sample was already published in Cersoy *et al.*, but X-ray diffraction measurements have been carried out with a different setup. This time, our conclusion moves towards the hypothesis upon which whitlockite could have been formed by the degradation of hydroxylapatite. This degradation reaction was demonstrated to be possible at 70°C at a low pH in presence of magnesium [42]. It remains to see if such conditions were present in the sample, but upon the last 2000 years, we could imagine that those could have been reunited. This hypothesis would confirm the use of bone or ivory to produce black pigment. The presence of carbon in this sample was shown by Cersoy *et al.*, as a result of the use of a charred vegetable by both SEM and PCC analysis. Merging all the results obtained on this sample, we could conclude on a potential mix between bone black and chars, but further investigation has to be made.

Concerning the vessels, Cersoy *et al.* categorized the samples into three types:

- *unguentarium*, containing charred vegetals with Ca-P mineral phases, corresponding to either cosmetic or ink recipient,
- *balsamarium*, containing metallic elements from bronze container and lipids, corresponding to a cosmetic recipient,
- *theca atramentaria*, containing charred vegetals with gypsum or common minerals, corresponding to ink recipients.

Since our samples are contained in various containers, we propose a classification based on composition rather than recipient shapes. We have then four categories:

- the pure vegetal chars, (P2445, P3987, P9523, P11432) which are mostly amorphous with almost no contamination and are preserved in small containers (*unguentarium* or *olpe*). They can contain traces of hydroxylapatite. They are most probably used as inks,
- the gypsum-rich powders, (P12458, P18109, HE03) contained in different recipients from which *theca atramentaria* and clay cup. They are most probably used as inks since they contain gypsum, described to be used as a drying agent,
- the lipid-rich powders, (HE02, H75430, H76238), also contained in different recipients such as glass ampoule or clay olla, are most probably cosmetics since they present similar PDF signal as lipids,
- the metallic-element-rich powders, (HE08, HE11) from which we do not have information about the container, appear to be composed of metallic oxides that can be degradation products or were voluntary part of a recipe.

6 Conclusion of the chapter

In this chapter, we dealt with archeological powders that present value in both historical and scientific fields. Using HR-XRPD and PDF analysis coupled with SEM, it was possible to identify and quantify the crystalline phases, and match the amorphous phases to known standards.

Their heterogeneous nature is a real challenge we faced in the journey to understand their origin. To overcome this challenge, we set up a multi-method approach based on what Cersoy and her collaborators started. From there, we extended the number of samples studied. From our study we can conclude that the carbon-based pigments from these Greco-Roman samples are made of chars. However, we faced difficulties due to the amorphous, powder-like, and single-crystal-like combined natures of the samples. The problem around the presence of single-crystal signal in diffraction was resolved thanks to the image processing pipeline that was set up. This demonstrated the usefulness of image processing to improve the quantification of powder-like phases from 2D diffraction patterns.

To move on this method, we can propose two directions. The first one is to use the single-crystal signal separated from the powder as exploitable information. The first step would be to index the reflections and deconvolute the contributions coming for several crystals (if any), look at the orientation of each crystals in the sample, or possibly recover a single-crystal data set for structure refinement (if appropriate). The second direction is in relation to the separation method. Instead of guessing the single-crystal contribution by subtracting a median signal, we would rather mask their contribution from the integration and then retrieve them after the 1D integration. This would eliminate the problem of a too high P-value. On the other hand, we would lose some statistics at small scattering angles if the number of single-crystal peaks is too high.

The ultimate challenge can also be based on the newly developed HR-XRPD stage with a 2D detector recently developed at ID22 [56]. We could imagine recording an HR diffraction pattern with a single-crystal separator algorithm built in the scan that would split the images into powder and single-crystal contributions. This would provide the powder contribution solely in a 1D diffraction pattern and a series of 2D images to be processed. And even further, this would be done at high energies to do PDF analysis with the same data. This would improve majorly the study of heterogeneous materials by providing at the same time exploitable information about single-crystals, powder, and through PDF analysis, some information about the amorphous phases.

Continuing this study, it would be valuable to measure a larger batch of samples, from known containers. This would allow correlating the shape of a specific container, for the storage of a specific powder for a specific use. Also, techniques oriented towards the analysis of the organic compounds present in the powders would be valuable to our study, with the hope to get information on ink binders and cosmetics excipients.

3

Investigation of pigments found on Ancient Egyptian papyrus

Contents

1 Introduction . . . 65
1.1 About colored pigments . . . 65
1.2 Carbon-based black pigments . . . 65
1.3 Corpus and objectives . . . 66
2 Writing and painting on papyrus in Ancient Egypt . . . 67
2.1 Papyrus, support of communication . . . 67
2.2 The Egyptian pigment palette . . . 70
2.3 Methodological approach . . . 74
3 Handling and measuring fragile archeological samples . . . 74
3.1 Finding a suitable support . . . 74
3.2 Potential effects from the measurements . . . 77
4 Analysis results of the papyrus support . . . 78
4.1 Visual observations . . . 78
4.2 SEM and EDX analyses . . . 78
4.3 XRF of papyrus support . . . 80
4.4 XRD of the papyrus support . . . 81
5 Analysis of colored pigments on papyrus from Champollion collection . . . 84
5.1 Fragments and analytical techniques . . . 84
5.2 Identification of colored pigments by XRD and XRF . . . 85
5.3 Intentional and non-intentional phases . . . 101
5.4 Conclusion . . . 107
6 Analysis of black pigment on papyrus from Champollion collection . . . 109
6.1 The fragments . . . 109
6.2 Identification of the black pigment . . . 110
6.3 Elemental and structural analysis of the ink . . . 112
6.4 Looking for structural contrast using XRD . . . 115
6.5 Retrieving contrast using X-ray diffraction and fluorescence tomography 116

6.6 Discussion 123
7 Conclusion of the chapter 124

1 Introduction

In the previous chapter, we studied black pigment powders coming from Pompei's vessels. These free powders presented the advantage of being set in a powder diffraction analysis pipeline, enabling both high-resolution XRD and pair distribution function analysis. In this chapter, we will look at pigments (black, but also colored) found on Ancient Egyptian papyrus. With papyrus fragment study, we add a level of complexity by having the pigment laid on papyrus support. This will restrain the possibility of measurement conditions and the support will be an extra material to take into account in our analysis. In addition, black pigments have a carbon-based nature, as well as the papyrus support, which is an additional constraint. The methodology will have to be different and dedicated, to separate the contributions of the pigment from the papyrus support.

This chapter is dedicated to the study of a set of papyrus from the collection of the Musée Champollion, in Vif, France. The collection contains 280 fragments, the largest showing scenes from the book of the Dead. The fragments have an estimated dating by Egyptologists of the New Kingdom period. They have been preserved in the Champollion family house for the last two centuries with no restoration attempt. These fragments are either painted with bright colors or written with black and red inks. Through this Ph.D., a collaboration with the Champollion museum was initiated, and twelve fragments of the collection were selected. In this chapter, we will discuss the different pigments present in the features of the twelve fragments.

1.1 About colored pigments

Regarding the colored pigments, for the majority, their crystalline structure is identifiable by X-ray diffraction and their elemental composition by X-ray fluorescence. The identification of any of these pigments is an opportunity for us to put the written or painted papyrus into a historical context with the use of specific pigments at specific periods. Even though the palette in Ancient Egypt seems well-identified, only a few studies are using XRD to truly identify pigments [57], [58]. There is a chance for us to identify any pigments that are not described in the literature or to find a mixture of compounds that would lead to a better understanding of a recipe. In addition, identifying a compound resulting from a degradation process would allow understanding possible exposure to degrading agents and potentially preserve other papyrus fragments from such misfortune. Even if the main topic of this work is about carbon-based black pigments, it is important to note how rare it is to have access to papyrus fragments and the opportunity we have to be able to measure them in a synchrotron facility. This is why the first part of the chapter is dedicated to the study of colored pigments.

1.2 Carbon-based black pigments

The main carbon-based black pigment in Ancient Egypt is said to be flame carbon [7]. However, no precise or complete study was able to prove the recurrent use of flame carbon in writing or painting. The certitude is that this pigment is mainly carbon and especially amorphous carbon. As previously mentioned in Chapter 1, three types of amorphous carbon pigments could have been used [1] flame carbon, chars, or cokes. In any of these forms, the carbon does not adopt any crystalline structure. Knowing the amorphous nature of our pigment, we cannot analyze carbon-based pigments in the same manner as mineral-based pigments. For example, X-ray diffraction will not give the same information on our sample if we target the carbon-based pigments. The papyrus support, which is also made of carbon-based compounds, delivers a diffraction signal corresponding to a poorly crystalline compound. Furthermore, the overwhelming quantity of support that has a thickness around nine times higher [25] compared to the pigment in a transverse cut, reduces its contribution. These effects will interfere in the process of isolating the amorphous carbon signal delivered by the black ink or paint.

1.3 Corpus and objectives

The previous subpart settled the basis of what type of pigments we can expect to find on our papyrus. This chapter will deal with the following questions. How can we identify pigments on papyrus fragments? Can we characterize the degradation effects on the papyrus fragments (both support and pigments)? What contribution to the diffraction or spectroscopic signals can be attributed to the papyrus support? In the case of the black pigment, is it possible to separate its spectroscopic or diffraction signals from the support and then compare them to the measured references described in Chapter 1? Can we confirm the use of flame carbon as a black pigment used in the formulation of inks in Ancient Egypt? All these questions will be addressed by investigating papyrus fragments from J.-F. Champollion private collection, from which twelve of them have been selected for the current study. The fragments are stored in a portfolio divided into 263 inventory numbers and several fragments displayed in frames. Each number corresponds to one or several fragments. An additional envelope stored fallen fragments from part of the collection too small to be in the portfolio, thus not having any inventory number. The selected samples along with their labels are shown in Table 3.1.

Papyrus fragment PAP-6 represents god Re, the deity of the sun facing the arms of the deceased. Papyrus fragment PAP-7, presents discernible black and red hieroglyphic writings, and the symbols "mouth", "reed" or "sedge" can be easily identified. The papyrus fragment PAP-10 comports three stripes of white, black, and yellow color. The papyrus fragment PAP-12 represents a cobra with a red solar disk with a column at its back. PAP-11 shows yellow and black colors, with a vertical blue line, all covered by black stripes. The smaller fragments were referenced as PAP-1 to PAP-5, PAP-8, and PAP-9, and were stored separately from the largest.

Table 3.1: Set of twelve papyrus fragments from Champollion museum collection

Fragment		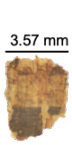				
Inventory Number	Ø	Ø	Ø	Ø	Ø	13
Analysis Num.	3	7	14	15	19	Ø
Manuscript Num.	PAP-1	PAP-2	PAP-3	PAP-4	PAP-5	PAP-6

Fragment						
Inventory Number	149	Ø	Ø	213	96	163
Analysis Num.	Ø	Egypt2	Egypt3	Ø	Ø	Ø
Manuscript Num.	PAP-7	PAP-8	PAP-9	PAP-10	PAP-11	PAP-12

2 Writing and painting on papyrus in Ancient Egypt

2.1 Papyrus, support of communication

2.1.1 The first uses of papyrus

The papyrus plant (*Cyperus Papyrus*) was used in Ancient Egypt for a wide range of applications. Any parts of the plant were transformed: the flowers were used in floral decorations, the rhizomes were eaten but also, used to make bowls, tools, or even burned as fuel. The main use remains from products related to the stem transformation. This stem was woven to make baskets, boxes, sieves, or stools and braided to make shoes or ropes (Figure 3.1 A-B). The oldest traces of papyrus uses is a "reed" mat from predynastic burial [59]. The most valuable use was to prepare sheets as writing or painting support (Figure 3.1 C) [15]. The earliest occurrence of papyrus as communication support was found to be from the first dynasty as a blank roll in the Tomb of Hemaka and dated from 5200 years [58].

Figure 3.1: (A) Pair of sandals from the tomb of Yuya and Tjuyu, New Kingdom, Thebes (ca. 1390-1352 B.C.), Metropolitan Museum of Art, Accession number 10.184.1a, b. (B) Papyrus fiber rope from Amarna, San Diego Museum of Man. (C) Papyrus of Séramon, XXIth dynasty, Thebes (ca. 1081-984 B.C.), Bibliothèque nationale de France, Inv.53.1.

2.1.2 Biology of the papyrus plant

Cyperus Papyrus, also called Nile grass is an aquatic plant belonging to the *Cyperaceae* family. It grows in full sun in swamps and lakeshores (Figure 3.2 A). The plant is leafless and grows up to a height of 3 to 6 meters [60]. The stem has a triangular cross-section thickness of 2 to 35mm topped with threaded shapes stems of around 20 to 30 cm. The inside of the stem reveals a white pith with a ground matrix where fibers are embedded in. This ground corresponds to the parenchymal cells, oriented in the direction of the stem with a honeycomb pattern (Figure 3.2 B). They represent most of the composition of the stem and are the main constituent of the processed papyrus. Regarding the chemical nature of the stem, the parenchymal cells are mostly constituted of cellulose, hemicellulose, and lignin. As in most of the plants, the inside of the cells contains oxalic acid and calcium oxalate [58]. In between these cells, channels carrying nutrients and water are presently called fibro-vascular bundles. The green outer shell called the epidermis protects all these cells.

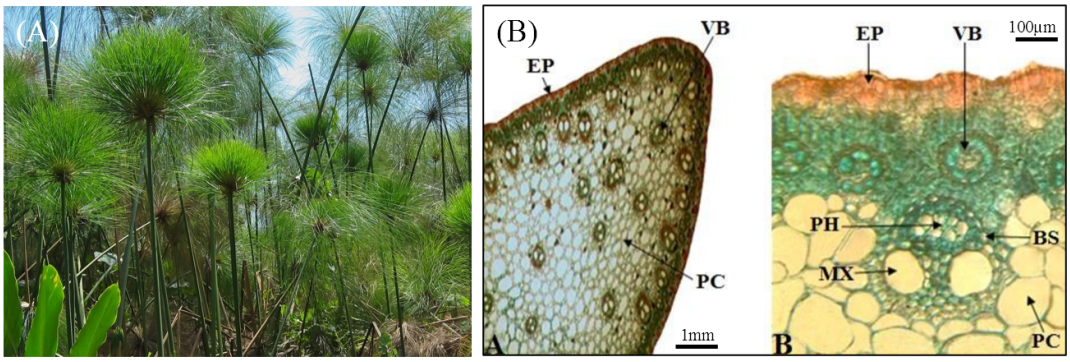

Figure 3.2: Cyperus Papyrus plant in a swamp in Uganda ©Andreas Schieber. (B) Two cross-section cuts from Cyperus Papyrus stem. EP: epidermis, VB: vascular bundle, PC: parenchyma cells, PH: phloem, MX: metaxylem, BS: bundle sheath [61]

2.1.3 Manufacturing papyrus writing support and writing techniques

Pliny the Elder in Natural History is the first to describe the manufacturing process to transform the raw papyrus into writing material [23]. Since no older written testimony is known, only reproduction trials and Ancient Egyptian papyrus observation or analysis can guess which method was used. The detailed process was put down by successful reproduction attempts from several persons: M. Mosiniak [62], B. Gunn [63], J. Cerny [64], S. Baker [65].

The first step is harvesting the stalk. The plant is cut above the water level and the top part is removed. The stem is then split into pieces of around 30cm each. The epidermis is removed and the pith is cut to even strips. Strips are placed side by side and topped with another set of strips at a 90 degrees angle (Figure 3.3). According to Pliny, the strips were moisturized with Nile muddy water that was playing the role of "glue". This was said to be a wrong statement by Lucas & Harris [15] who argues that the sugar or sweetness of the freshly cut papyrus was sufficient to provide adhesion between the strips.

Reproductions attempted by E. Menei [66] validated this statement. The author specifies the requirement of a sustained pressure on the papyrus while it dries to guarantee the adhesion. After being laid down, the strips were covered with an absorbent cloth and then beat with a wooden mallet or a rounded stone.

The next step was to press for several hours to permanently weld the strips. After drying, the resulting product was polished with hardwood or a pebble [15]. From the sheet to the roll, Pliny explains that the junctions between two sheets were made by overlapping and using a starch paste as glue, hammered to be flattened out [58].

The writing technique was based on the use of three tools, represented in the hieroglyph that designates "writing" or "scribe" (Figure 3.4). The first tool is the "pen" made of a type of rush called *Juncus Maritimus*. The portion of the stem was cut and shaped to serve both as a pen or as a little brush. These pens were stored in a piped-shaped box. The second tool is the palette which stores red and black colors in a cake shape (a mixture of pigment and binder), in cavities carved in wood. Palettes are also serving as storage for pens in a reassessed part. The last tool represented on the hieroglyph has two interpretations. One is a little glass recipient to store water to rehydrate the ink cakes, the other interpretation corresponds to a little bag where the scribe was storing the dried ink. The three tools were tied together using a rope to facilitate transport [7].

To write, the scribe was rehydrating either the cake itself or just the tip of the pen and dipping it in the cake. In case of a mistake, it was common to use a wet rag or sometimes even the tongue to erase [15]. If the mistake was too big, cutting the papyrus paper and gluing a new piece was the solution.

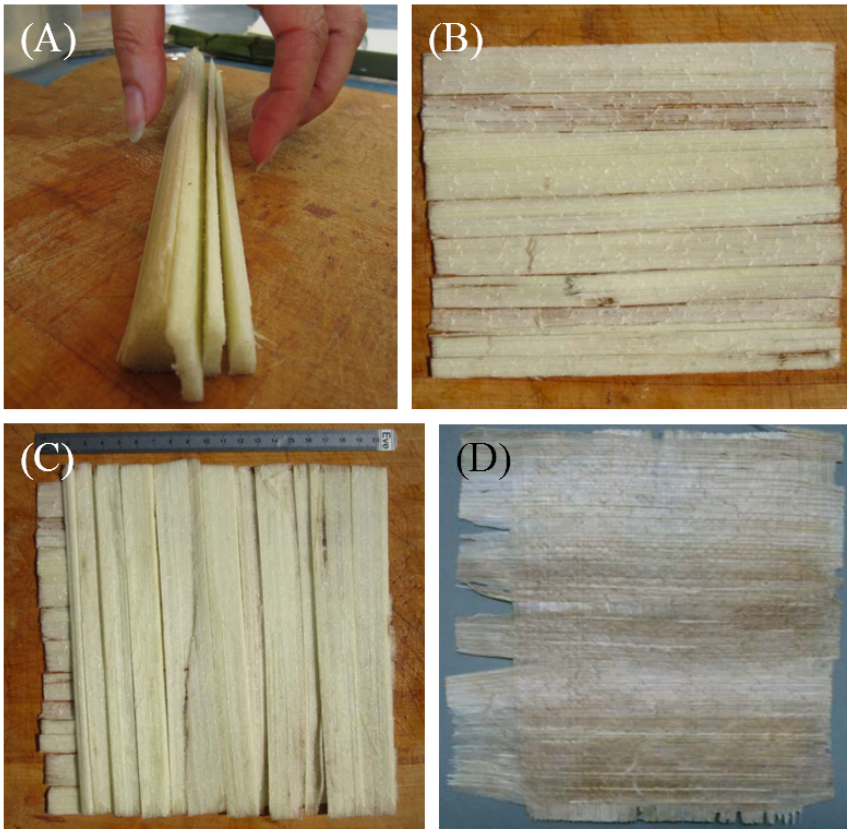

Figure 3.3: Papyrus paper manufacturing steps (Le papyrus comme support d'écriture, E. Menei [66]). (A) Stem cut into strips, (B) First layer of strips, (C) Strips laid down on top with 90 degrees angle, (D) Final product after pressing and drying.

Figure 3.4: Hiergoglyph of the scribe representing the three tools used for writing (left). Palette inscribed for Smendes, High Priest of Amun, Third Intermediate Period, Thebes (ca. 1045-992 B.C.), Metropolitan Museum of Art, Accession number 47.123a-g.

2.1.4 Papyrus illustration in Ancient Egypt

The illustration of funerary documents started as early as the Old Kingdom up to the Roman period. Nevertheless, most of the illustrations were made during the New Kingdom period and they are present on documents for administrative or religious purposes. In most of these documents, illustrations were present with text, written in black or red while the illustrations comport bright colors such as green, yellow, white, or blue in addition to black and red [67].

The New Kingdom illustrations are particularly well colored compared to previous epochs. This trend has to be put with the popularity of painting as a sign of wealth. This probably leads to the apparition of the distinction between text writers and painters [67].

The first appearance of the distinction between illustrated and written parts of papyrus was attested by the study of the papyrus support interlacing procedure of Papyrus Harris I,

manufactured under Ramses IV reign. Clear divisions are seen between written and painted parts attesting the work of at least a writer and several illustrators [67].

Concerning funerary papyrus, the most common document is the Book of the Dead, placed in the coffin or the burial chamber of the deceased. This "book" was a valuable piece of the funerary equipment and a testimony of the wealth of the orderer. A study of a few Books of the Dead from the Louvre museum, focusing on a field of reeds, has shown the presence of preparatory drawings. Most of the time they are made of finely grounded red pigment with some exceptions showing the use of black pigment. The use of specific colors is recurrent: white for clothes, yellow for the reed or for the ships, red for male faces, orange for cows, and blue for running water. Black was used for the contours and the texts, with sometimes red as well [67].

2.2 The Egyptian pigment palette

2.2.1 Minerals used for inks and paints

Before stating the chemical nature of each pigment, it is important to point out the difference between painting and ink products. In terms of pigment composition, it is unlikely to imagine any difference between the pigments used in paintings and writing [7]. The only difference would be regarding the binder used to manufacture the ink or paint. According to Lucas [15], inks were made by mixing the pigment with gum and water. The nature of the gum is supposedly Arabic gum, without any further proof. Concerning the paint, the binder is more likely to be a protein-based animal glue, such as white eggs, or skin glue that has better adhesion properties adapted for painting on rougher surfaces such as walls. This statement remains unclear because of the complexity (time degradation, necessity of sample destruction for organic-based analyses,...) of finding traces of these organic compounds in ancient artifacts.

The pigment palette used in ancient Egypt for writing or paintings is quite well described [68] [57] [69] [70] [71] [72] [73]. It relies mainly on finely ground minerals, most of them being resilient to the effects of time and then remaining in an excellent preservation state (Figure 3.5). The base colors are black, blue, green, orange, red, white, and yellow [15]. In the next subparts, we will describe the palette by type of minerals rather than by color because several minerals can adopt different shades.

Figure 3.5: Painter's Palette Inscribed with the Name of Amenhotep III (Ivory), New Kingdom, Thebes (ca. 1390-1352 B.C.), Metropolitan Museum of Art, Accession number 26.7.1294.

2.2.1.a Copper-based minerals

Copper-based minerals were used to produce two different shades of color, blue and green.

The most known copper-based mineral is cuprorivaite ($CaCuSi_4O_{10}$), also known as Egyptian Blue. Described by Vitruvius with the name coeruleum [21], this compound was demonstrated to have been manufactured [74] by heating together silica and calcium carbonate (both present in sand) with a copper source (often malachite), and natron. The mixture was heated at a temperature

between 850°C and 1050°C [75] [76]. The first use of Egyptian Blue is dated around the fourth dynasty but remains uncertain [15].

Malachite ($Cu_2CO_3(OH)_2$) is a green mineral, naturally found in the Sinai desert and grounded into a fine green powder to obtain a green pigment. The earliest traces of malachite use is from the early predynastic periods [77].

Another green pigment based on the manufacture of cuprorivaite, called Egyptian green was found on paintings on stones, wood, and potteries from the First Intermediate Period [78]. A study revealed that the manufacturing of this turquoise shade pigment is based on the same process as Egyptian blue. The process presents a higher heat treatment (950°C to 1150°C) combined with a lower quantity of copper, which leads to the formation of an amorphous silica-rich glass with parawollastonite ($CaSiO_3$) crystal trapped in [78].

2.2.1.b Iron oxide-based minerals

The two most commonly used iron oxide-based minerals in Ancient Egypt are hematite (Fe_2O_3) and goethite (FeO(OH)). These oxides are found in ochres. There are three categories of iron-rich ochres, yellow, red, and brown ochres. Widely naturally available, they all contain a certain ratio of iron oxides with the addition of clay and sands. The hue of the ochres is determined by the ratio between its constituents [79]. Red ochre is rich in hematite, and in some cases, hematite can be found almost in a pure state [80]. Yellow and brown ochres contain goethite with different degrees of hydration.

2.2.1.c Calcium-based minerals

The main calcium-based minerals used were calcite ($CaCO_3$), easily found in chalk, or calcium sulfate called gypsum ($CaSO_4$,$2H_2O$), both widely available in Egypt [15]. These minerals were used as white pigments and were present as early as the predynastic period. Authors [72] have reported the presence of huntite ($Mg_3(Ca(CO_3)_4)$) used as a pigment dated from the Old Kingdom for painting on walls [73] which presents a brighter shade of white.

2.2.1.d Arsenic-based minerals

Two arsenic-based minerals were used as pigments: realgar (As_4S_4) and orpiment (As_2S_3) [57] [72] [70] [81] [82]. Realgar has a more red-orange shade and has three different polymorphs: α-As_4S_4, β-As_4S_4, and χ -As_4S_4. According to Macchia *et al.* [83], only α and β are from natural origin while χ is synthesized. Studies show that in many cases realgar degrades over time into pararealgar [82]. Pliny wrote in Natural History XXXV [23] in chapter 22 that mines of sandarach (realgar not to be confused with the cypress resin) were exploited on Zabargad Island on the Red Sea but this statement remains uncertain. Orpiment was used more as a coarse powder to produce a yellow hue [68].

2.2.1.e Lead-based minerals

Lead white appeared in Egypt lately, around the Ptolemaic period. Less common in Ancient Egypt, it was found on a Book of the Dead of Amenemhet [9], both in pure form or mixed with other pigments. It was also found on a cartonnage broad collar, dated from between 512 and 351 BC [84]. Lead white is a mix of both cerussite ($PbCO_3$) and hydrocerussite ($PbCO_3$)2,$Pb(OH)_2$. Minum, a red pigment (Pb_3O_4) was used extensively during the Ptolemaic period (in addition to red cinnabar (HgS)) [84] but also during the Second Intermediate period [85]. Its use probably started with the importation of litharge. Also, Walter *et al.* found galena, (PbS) and cerussite, ($PbCO_3$) as well as laurionite, (PbOHCl), and phosgenite, ($Pb_2Cl_2CO_3$) in New Kingdom cosmetic samples [86].

2.2.1.f Carbon-based pigments

As mentioned in the general introduction, black pigments used in black inks in Ancient Egypt, were mainly amorphous carbon-based pigments. More details about carbon-based pigments can be found in Chapter 1.

2.2.1.g Summary

Table 3.2 summarizes all the commonly used minerals for painting and writing in Ancient Egypt. Only classic colors were put on the table knowing that the palette can present colors that are the result of a mix between several minerals.

Table 3.2: Summary of major minerals used as pigments in Ancient Egypt with their formula. The table contains the PDF2-2003 XRPD [52] database references that were used for the phase identifications.

Mineral	Pigment color	Chemical formula	PDF Reference
Cuprorivaite	Blue	$CaCuSi_4O_{10}$	PDF 12-0512
Malachite	Green	$Cu_2CO_3(OH)_2$	PDF 41-1390
Hematite	Red	Fe_2O_3	PDF 33-0664
Minium	Red	Pb_3O_4	PDF 41-1293
Cinnabar	Red	HgS	PDF 06-0256
Goethite	Yellow	$FeO(OH)$	PDF 29-0713
Calcite	White	$CaCO_3$	PDF 43-0697
Gypsum	White	$CaSO_4$, $2H_2O$	PDF 33-0311
Huntite	White	$Mg_3(Ca(CO_3)_4)$	PDF 14-0409
Hydrocerussite	White	$(PbCO_3)_2$, $Pb(OH)_2$	PDF 13-0131
Cerussite	White	$PbCO_3$	PDF 47-1734
Orpiment	Yellow	As_2S_3	PDF 44-1419
Realgar	Orange	As_4S_4	PDF 09-0441

2.2.2 Recent studies carried out on pigments from Egyptian papyrus

Table 3.3 presents the minerals identified on funerary painted papyrus in recent studies. We mostly rely on studies performed with characterization techniques presenting an analytical approach. This is specified because earliest archeological studies, although extremely accurate, could sometimes not give enough precise information, for example, regarding phase identification. For each color, we show the identified mineral, with the mentioned techniques. Most of the papyrus fragments are from the New Kingdom period. The classic palette is well represented during this period, with minerals such as cuprorivaite, Egyptian green, hematite, orpiment, and huntite. On the other hand, the later period, around the Ptolemaic age shows different minerals such as malachite or cinnabar. Di Stefano *et al.* identified potassium lead chloride (KPb_2Cl_5), probably resulting from the degradation of lead white. The principal techniques used are XRD to identify the mineral structure, then XRF, SEM-EDX, and μ-PIXE for elemental composition. FTIR was used as a complement in some of these studies.

Table 3.3: Summary of the minerals found in recent studies on funerary papyrus. DM = Digital Microscopy, ATR-FT-IR = Attenuated Total Reflectance Fourier Transformed Infrared, XRD = X-Ray Diffraction, VIS = Visible Spectroscopy, SEM-EDX = Scanning Electron Microscopy Energy-dispersive X-ray Spectroscopy, PLM = Polarized Light Microscopy, XRF = X-Ray Fluorescence, PIXE = ParticleProton Induced X-ray Emission.

Observed color	**Mineral or mix**	**Authors**	**Papyrus dating**	**Techniques used**
Blue	Cuprorivaite	Di Stefano *et al.* (2011)	Ptolemaic period	DM, ATR-FT-IR, XRD, VIS, SEM-EDX
		Lee *et al.* (2009)	18th Dynasty	PLM, XRD, XRF, SEM-EDX
		Olsson *et al.* (2001)	19th Dynasty	PIXE
		Fuchs *et al.* (2010)	18th Dynasty	DM, VIS, XRD
Green	Egyptian green (green frit)	Lee *et al.* (2009)	18th Dynasty	PLM, XRD, XRF, SEM-EDX
		Wagner *et al.* (2002)	18th Dynasty	SEM-EDX
	Egyptian blue + orpiment	Evans *et al.* (1980)	19th Dynasty	XRF
	Malachite	Lee *et al.* (2009)	30th Dynasty	PLM, XRD, XRF, SEM-EDX
	Egyptian blue + Goethite/yellow ochre	Di Stefano *et al.* (2011)	Ptolemaic period	DM, ATR-FT-IR, XRD, VIS, SEM-EDX
Red	Hematite	Lee *et al.* (2009)	18th Dynasty	PLM, XRD, XRF, SEM-EDX
		Wagner *et al.* (2002)	18th Dynasty	SEM-EDX
		Olsson *et al.* (2001)	19th Dynasty	PIXE
		Christiansen *et al.* (2020)	Roman period	XRF, XRD
	Realgar	Evans *et al.* (1980)	19th Dynasty	XRF
	Cinnabar	Di Stefano *et al.* (2011)	Ptolemaic period	DM, ATR-FT-IR, XRD, VIS SEM-EDX
Yellow	Orpiment	Wagner *et al.* (2002)	18th Dynasty	SEM-EDX
		Olsson *et al.* (2001)	19th Dynasty	PIXE
		Evans *et al.* (1980)	19th Dynasty	XRF
		Lee *et al.* (2009)	18th Dynasty	PLM, XRD, XRF, SEM-EDX
			20th Dynasty	
			30th Dynasty	
	Realgar + orpiment	Daniels *et al.* (2004)	Ptolemaic period	PLM, XRD, XRF, SEM-EDX
			New Kingdom	
		Fuchs *et al.* (2010)	18th Dynasty	DM, VIS, XRD

White	Huntite	Wagner *et al.* (2002)	18th Dynasty	SEM-EDX
		Lee *et al.* (2009)	18th Dynasty	PLM, XRD, XRF, SEM-EDX
			21st-22nd Dynasties	
		Olsson *et al.* (2001)	19th Dynasty	PIXE
	Potassium lead chloride	Di Stefano *et al.* (2011)	Ptolemaic period	DM, ATR-FT-IR, XRD, VIS, SEM-EDX

2.3 Methodological approach

The first information is always coming from direct observation of the sample via an optical microscope. In addition to this, electron microscopy may provide additional details about the surface of the papyrus support and the pigments apposed on it. In particular, this can provide information about the carbon-based material used in the black ink, as we have shown in Chapter 1 and 2 that the morphology of the carbon-based pigments can be, in some cases, easily identifiable.

Then, from the previous studies carried out on papyrus and described in the previous part, it appears that combining structural and elemental probes when looking at pigments on papyrus is an important step. Because of the different colored features painted or written on the papyrus fragments, an adequate spatial resolution is necessary. Also, because of the limited amount of material that can be placed in the beam (the full papyrus thickness is usually less than 500 microns, so the layer of pigment no more than 100 microns in most cases) in the beam, a good incident flux is desirable. In our case, we will combine synchrotron XRF and XRD techniques, and probe in such a way different parts of the fragments. The fragments will be mapped with a 100-to-1000 micron-sized beam at the ID22 beamline. Besides, in order to improve the spatial resolution, enhance the sensitivity of diffraction techniques, and obtain information about depth profile, two selected small fragments will be probed using the XRD-CT and XRF-CT techniques at the ID11 beamline.

Additional insights can be obtained from vibrational spectroscopies. In particular, Raman spectroscopy is well suited to study carbon-based pigments and will be implemented when looking at the black ink found on some of the fragments.

3 Handling and measuring fragile archeological samples

The fragility of the fragments relies on their relative high degradation state compared to recently made papyrus sheets. Aged papyrus fibers are more brittle and have a tendency to break in dust. The manipulation of the fragments is delicate and the challenge is to be able to move them between the experimental setups without breaking them. To do so, it is important to avoid any bending or torsion of the fragment while being grabbed. From our knowledge of handling the fragments, it is always better to slide them across flat surfaces than trying to pinch them. We would want to avoid any torsion or bending that would result in irreversible damage.

3.1 Finding a suitable support

3.1.1 Support adapted for manipulation, transport, and X-ray measurements

To be able to manipulate, transport, and measure the fragments without breaking them a system of support that respects several rules was engineered. It has to be resistant enough to tolerate manipulation, transparent to X-rays for further measurement, which means, open in a certain

area to avoid unwanted signals, and inert to the sample so that no contamination is introduced. Of course, the support has to adapt to the sample perfectly to avoid any risk of losing small fragments.

The choice of the support material, manufacturing, and design made the additive manufacturing process competitive. 3D models of papyrus support were created and adapted to each of the large fragments (>1cm). Then 3D printing technology was used to precisely reproduce this model to the correct scale.

The design of the model was build based on the papyrus scale with the Tinkercad software. The process of creating papyrus support is divided into four steps. The first step is to take sufficiently good pictures and calibrate the distances in the picture to be able to evaluate the dimensions of the support. Using the inner contour of the fragment (adding a 5% additional layer to the width), we obtain the base of the support (Figure 3.6A-B). Then we extrude this base to a rectangular parallelepiped shape that matches the shape of the base (Figure 3.66C). The height of this parallelepiped shape has to be measured to account for the base, the papyrus, and the top lid. The same process is done with the external contour of the sample (with a 3% addition) and extruded to an upper layer of the previous shape.

At this point, we have a perfectly matching bottom part of the support. The next step is to build the top cover that will seal the fragment in a "sandwich" to hold it without crushing it. We start by taking the 1% inner part of the fragment contour to be able to fit the top part into the bottom one (Figure 3.6D). Then we extrude to this shape 4% of the papyrus inner contour to match perfectly the top inner opening to the bottom inner opening (Figure 3.6E). Finally, we add support bars on the top and bottom to hold the center of the papyrus better. Their placement has to be carefully chosen to avoid masking future measurement points (Figure 3.6F).

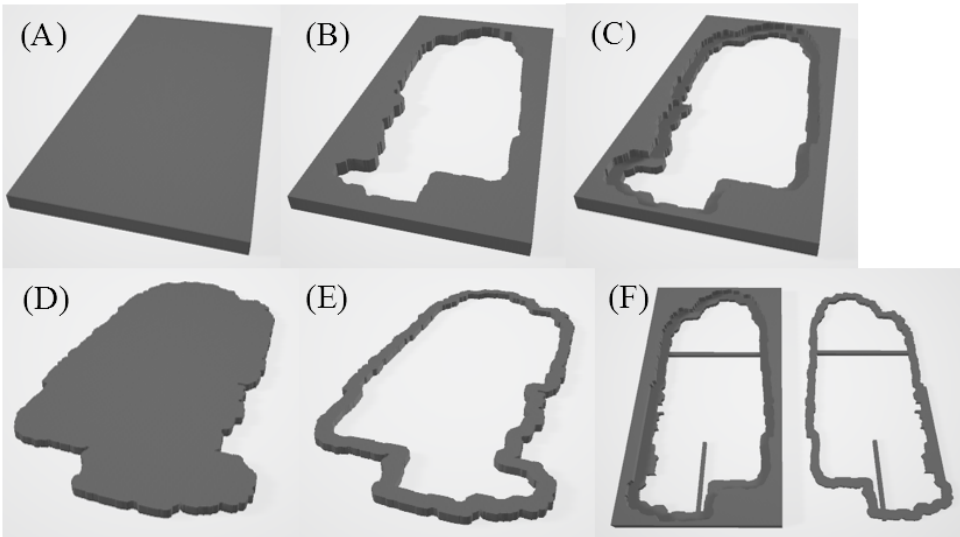

Figure 3.6: 3D modeling steps of the holder of papyrus fragment PAP-12

The 3D model was then 3D printed on a Digital Light projection (DLP) printer. The DLP process is based on the projection of a UV LED signal on micromirrors that can map each layer of the object. We used an Asiga Pico 2 printer (available at the ID22 beamline) with a liquid resin that hardens with UV irradiation. An extra 30 minutes curing step was performed on the methacrylate resin with a UV lamp to ensure complete polymerization and avoid any sample contamination. The printing is fast as each layer of the object is processed in a few seconds. The whole support was printed in seven minutes with a resolution of around 30µm. The result of the process is shown in the following Figure 3.7, with the fragment PAP-12 in its support mounted on the ID22 beamline stage.

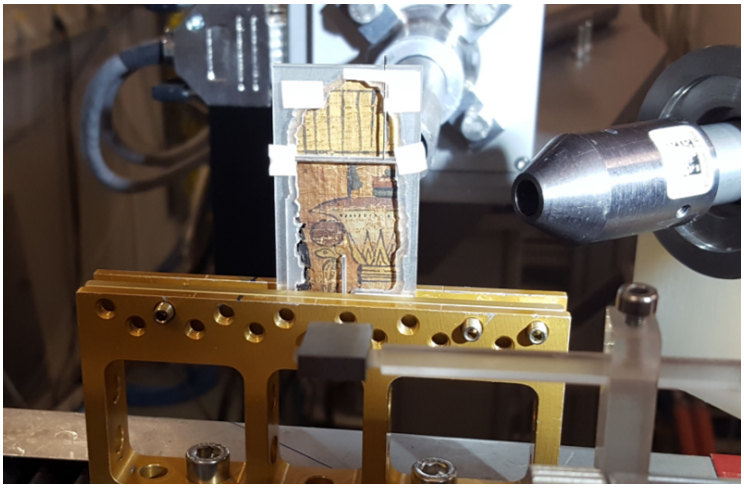

Figure 3.7: Experimental setup on ID22 beamline with papyrus fragment PAP-12 mounted on the 3D printed support.

3.1.2 Specific sample mounting for SEM and EDX

The first issue faced to perform papyrus fragment observation in the SEM is to build a reliable mounting solution, which is both safe for the fragment and suitable for the observation. The mount has to be both inert for the fragment (i.e. to avoid any contamination of the elements composing the mount) and compatible with the vacuum of the machine. The first guess was to use aluminum foils for the small fragments. It is easy to shape and cut to the size of the sample while being inexpensive and vacuum safe (Figure 3.8A).

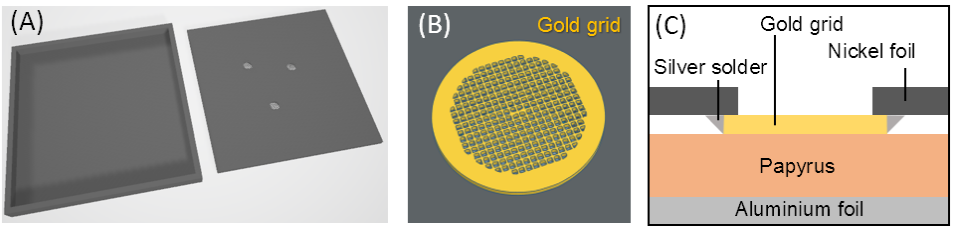

Figure 3.8: Design steps of papyrus sample holder for SEM observation and EDX. (A) Aluminium holder (left), drilled nickel sheet with three holes covered with the gold grids (right), (B) Gold grid laid on the nickel sheet. (C) Cut view of the superposition of all the elements of the support.

However, to perform EDX analysis, the problem is different. All the previous constraints remain with a few more. The elemental composition of the holder must be quite different from any element we could expect to have (i.e. any element that Egyptian could have used). Another issue is to address any potential charge effect that could occur due to a high concentration of charges because of poor surface conductivity. This would appear especially on some pigments containing non-conductive crystals. We came up with another sample holder design that suits also bigger fragments, avoiding all these pitfalls.

The design is based on the aluminum foil one, with some upgrades. The top part of the holder is now made of a sheet of nickel. This sheet is cut to the dimensions of the sample and flattened to have a flat surface. The sheet would be led flat on the fragments while 2mm holes through it would allow the beam to go through. It was calculated to put the holes in a specific area to obtain the best global view of the sample. Then after holes were drilled using a drill press, we had to address the possible charging effect from the sample.

To solve this, we imagined a grid that could be placed in the hole with a small mesh that would

catch the charges during observation. The grid was a TEM 200 gold mesh (Figure 3.8B), with gold being both inert to the sample and never used as a pigment agent in inks or paints. To assemble the grid and the sheet, we used silver glue on the edges of the sample while taking care of gluing the grid on the side which is going later to touch the sample to be sure that it will evacuate the charges with a contact (Figure 3.8C).

At last, the nickel sheet was carefully put on top of the sample and aligned with the targeted observation areas. Then the aluminum foil was folded on top to secure the sample and the sheet together ensuring the rigidity of the sample holder.

3.2 Potential effects from the measurements

3.2.1 Scanning electron microscopy

Papyrus fragments, both the support and the pigments, may be sensitive to any environmental perturbations such as humidity, UV radiations, or heat. In the case of the SEM technique, they are two risks of potential damage. The first risk is in relation to the high concentration of electrons accumulating at the surface due to the electron beam. This can cause thermal effects on the sample leading to irreversible damage. The second risk is the vacuum present in the observation chamber. The vacuum is problematic with organic-based samples because of the dehydration effect of the sample due to easy water evaporation occurring at low pressures. Nevertheless, exploring the bibliography, we saw that from some earlier SEM studies [87] performed on papyrus fragments, no visible damage to the sample was reported.

To lower the risk of major damage, we first measured really small fallen (<1mm) parts made of raw papyrus that were present around the main fragments. We started with low voltages (3kV, 3mm of working distance) and we increased progressively up to the nominal voltage (20kV, 8mm of working distance). No short-term visible degradation effect was visible from neither vacuum nor electron beam. Assuming the composition of the fragment containing black ink was close to the test samples, we carried on the observations at a safe voltage of 3kV with a working distance of around 3mm.

3.2.2 X-ray measurements

With the same objective as previously detailed for SEM studies, we wanted to anticipate any risk of damaging the papyrus fragments while performing our synchrotron X-ray measurements.

First, it is important to note that the literature tells us that papyrus fragments were already measured with X-ray-based techniques at synchrotron sources [54] [27] [88], without reporting any subsequent damage to the samples. In our case, the principal source of damage would be by overexposing the sample to X-rays. Any material absorbs a part of the incident X-rays and the absorption leads to heating. The absorption value depends on the type of the element exposed, the heavier the element, the more it absorbs. The intensity and the energy of the incoming beam are also to be taken into account.

With blank papyrus, the risk of damage is quite limited. However, the variety of elements that inks and paints can have, shows us the importance of making preliminary tests starting at low beam intensities.

First, a modern papyrus was put in the beam, at 31keV, and kept in the beam for a long exposure time. As no visible damage was observed, a series of tests on ancient papyrus micro fragments were carried out. The tests consisted to illuminate the sample with the X-ray beam at increasing exposure time while recording a 2D diffraction pattern. Optically, no damage was observed at any point in our test. With the diffraction pattern measurement, we tried to see any evolution of the diffraction signal that would show a sign of degradation, but no evolution was observed. These tests made on several colors guaranteed the absence of visible damage of our X-ray measurements on the papyrus fragments.

3.2.3 Raman spectroscopy

Raman spectroscopy involves the illumination of the sample by a laser beam (633nm in our case, see Chapter 1). To avoid beam damage that would result from heating, we decided to limit laser power and exposure times. Previous studies [70] [89] involving Raman spectroscopy suggested limiting the power to 0.5mW and 75 seconds at a wavelength of 633nm. After performing several tests at 0.5mW of power and 75 seconds of exposure time in the same conditions, we decide to increase the power to 1mW after testing on loose fragments parts. Since no visible damage was observed, we kept this power level that gives a better signal-to-noise ratio.

4 Analysis results of the papyrus support

By observing and probing the papyrus support first, we will be able to isolate what signal is associated with it, thus taking it into account when we will analyze the dual signal of the ink/pigments and the support. Recording a baseline measurement of the support is key in this approach.

4.1 Visual observations

As mentioned earlier, the support is made of stacks of papyrus strips, hammered and pressed together before polishing [58], and the resulting orthogonal pattern with fibers running horizontally and vertically is still clearly visible on most of the fragments (Figure 3.9). During the manufacturing process, papyrus strips could be either cut off or peeled down from the plant pith, and Wallert has shown that these two preparation methods could be identified by SEM on freshly prepared papyrus [90]. Nevertheless, the unevenness of the surface resulting from the peeling method tends to disappear after the polishing and drying of the papyrus, making our observations on our ancient papyrus fragments non-conclusive.

Figure 3.9: Papyrus fragment PAP-4 from Champollion collection, papyrus stripes are stacked in two layers, 90° apart

4.2 SEM and EDX analyses

As shown in the figure (Figure 3.10) recorded at the surface of PAP-1, we can observe by SEM papyrus cells with grains lying on top. The papyrus fibers at a larger scale are complex to observe by SEM because of the intense charging effect that occurs. The cell size is around 50 to 100µm. This result is in agreement with what P. Scora *et al.* [91] observed on a papyrus cross-section.

The grains lying on top of the papyrus were analyzed with EDX on the same area (Figure 3.11).

Spectrum 6 represents the summed spectrum from the data retrieved from the map shown in Figure 3.11A, and corresponds to the blank papyrus support. Similar compositions have been found in other fragments. Indeed, we saw that chemical elements such as calcium (Ca), potassium (K), manganese (Mn), silicon (Si), and sodium (Na) were found in most of them. These elements

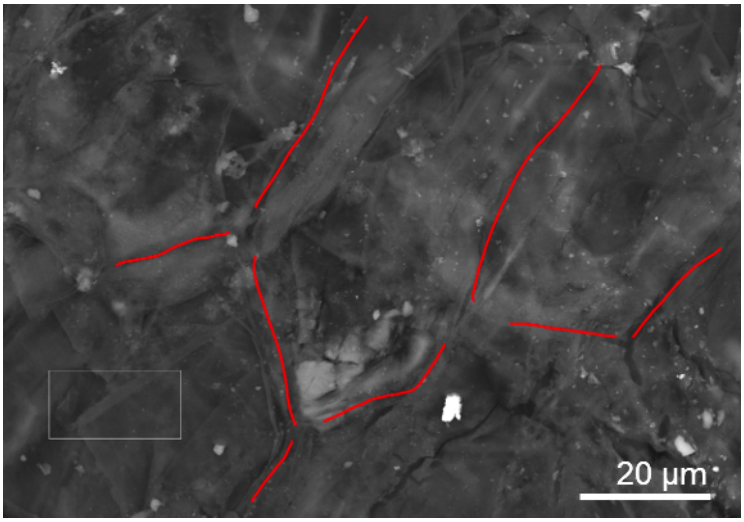

Figure 3.10: SEM image in SE2 mode of blank papyrus surface, red stripes show the limitation between papyrus cells.

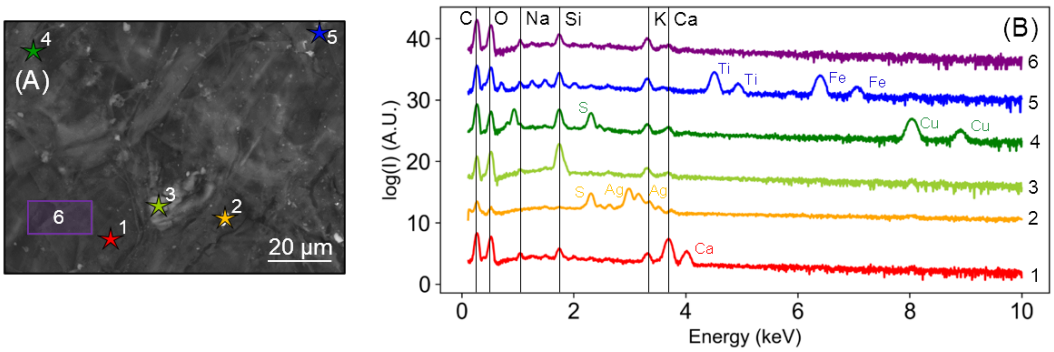

Figure 3.11: (A) SEM image from PAP-1 blank papyrus area (1kx, 20kV, WD=8.3mm), (B) EDX spectra from five points, and one map (spectrum 6) from PAP-1 papyrus support.

were proven to be part of the plant growth [60], and their respective concentrations vary depending on the growing locations of the papyrus [92].

The grains 2,4 and 5 found on the papyrus support (Figure 3.11A-B) contain metallic elements. Copper is found in some pigments such as cuprorivaite (see later) and a crystal could have jumped from another place or fragment. The titanium and iron-based grain are not common but both of the elements are regularly present at the surface of the papyrus as shown by Christiansen *et al.* [9]. The only grain with an uncommon element is grain 2 with silver. Its presence remains to be explained. Grains 1 and 3 mostly containing calcium and silicon, correspond most likely to calcium oxalate and quartz. These phases will be discussed later in the part of X-ray powder diffraction.

In addition to these, lead (Pb), and tin (Sn) were also detected in some other papyrus supports. These latter elements exclusively appear as micron-sized clusters at the surface of the fragments. Although these surface clusters may result from contamination introduced by the hammering and polishing process of the papyrus support in ancient times, late pollution from the environment or storing process may also be the cause.

Since few grains were identified, it cannot be argued that they are representative of the entire sample set. However, this points out the variety of elements that can be found on the papyrus surface. EDX gives valuable information on the elemental composition of these grains especially on light elements which is complementary to the analyses based on XRF or XRD.

4.3 XRF of papyrus support

Several points have been measured over a vertical line on PAP-1 Figure 3.12. This point- to-point variation is in accordance with what was also observed and measured with SEM-EDX, the presence of localized grains of metallic elements.

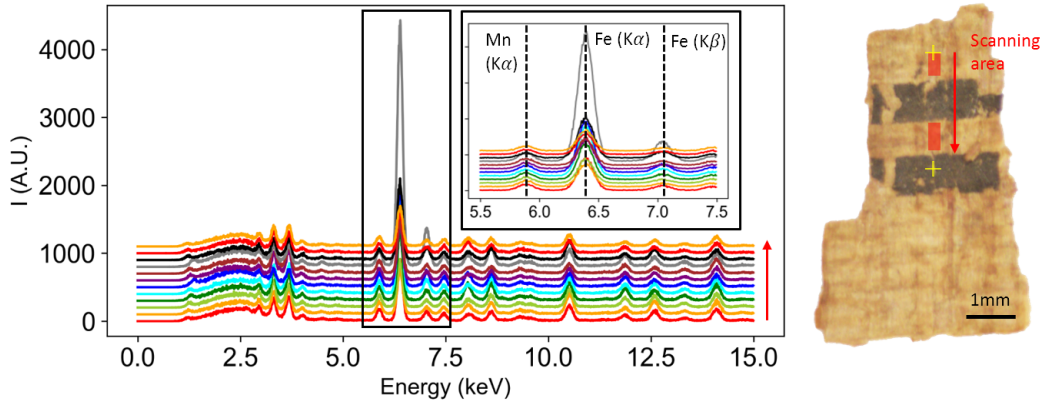

Figure 3.12: XRF signal of eleven measurement points of blank papyrus from PAP-1 (incident energy : 31.0 keV)

The average XRF spectrum recorded on PAP-1 is given in Figure 3.13. The peaks corresponding to the emission lines were fitted to identify the elements. The elements found by EDX are also identified, and several of them such as manganese, nickel, or lead were also found. All of them were mentioned by Christiansen *et al.* [9]. The elemental composition of a selection of fragments (PAP-1 to PAP-5) retrieved by XRF, is given in Table 3.4. For all these fragments, the measurements were made over vertical or horizontal scan lines and the number of points is indicated in the table. Only the points done on the papyrus support are discussed here. The resulting values correspond to the average over the number of measured points. A normalization was made by dividing the number of counts of each element by the counts measured for the potassium Kα line. This element has been chosen as a reference because it presents the smallest variability in intensity. We show here only the elements with Z>18 because of both detector setup and measurement in air. Eight elements of interest for this study are presented in Table 3.4.

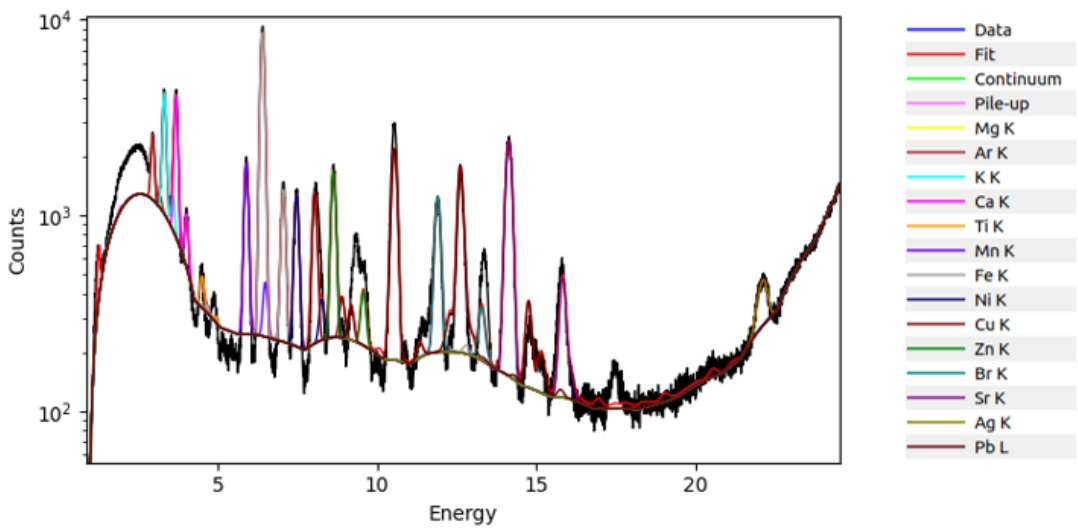

Figure 3.13: Fluorescence signal averaged over eleven points of blank papyrus from PAP-1

Table 3.4: Elemental composition obtained from XRF analyses. For each fragment, several data points (the number of points is indicated in the second column) were collected on papyrus support. The resulting values correspond to the average signal over the number of measured points corresponding to the main emission line, divided by the value of potassium (K).

Sample	No. points	K	Ca	Mn	Fe	Cu	Zn	Pb	Sr
PAP-1	4	1	0.87	0.43	1.65	0.19	0.25	0.41	0.40
PAP-2	10	1	0.69	0.52	**10.89**	0.74	0.53	1.02	0.67
PAP-3	3	1	0.98	0.45	**4.92**	0.50	0.26	1.52	0.73
PAP-4	7	1	1.04	1.01	2.71	0.38	0.30	0.56	0.66
PAP-5	7	1	0.98	0.57	3.14	0.23	0.79	0.32	0.63

The table shows that most elements are present in similar quantities in the papyrus supports. The variability shown for PAP-1 in Figure 3.12 is probably similar for all the fragments as the resulting average values show little difference. Only PAP-2 and PAP-3 show a higher iron content that we assume to be due to the presence of a really large iron-based grain at its surface.

4.4 XRD of the papyrus support

4.4.1 Phase identification

A diffraction pattern measured on a blank zone of PAP-1 is shown in Figure 3.14. This corresponds to the pattern shown in light green (top one) in Figure 3.15. Three main phases were identified, and a Rietveld refinement was performed. The pattern is dominated by cellulose, the major component of papyrus. Some features on the main peaks of cellulose (a sharp contribution associated with a larger one) may indicate the presence of two cellulosic phases of varying crystallinity (both based on cellulose I_β structure), and this is going to be discussed in the next part.

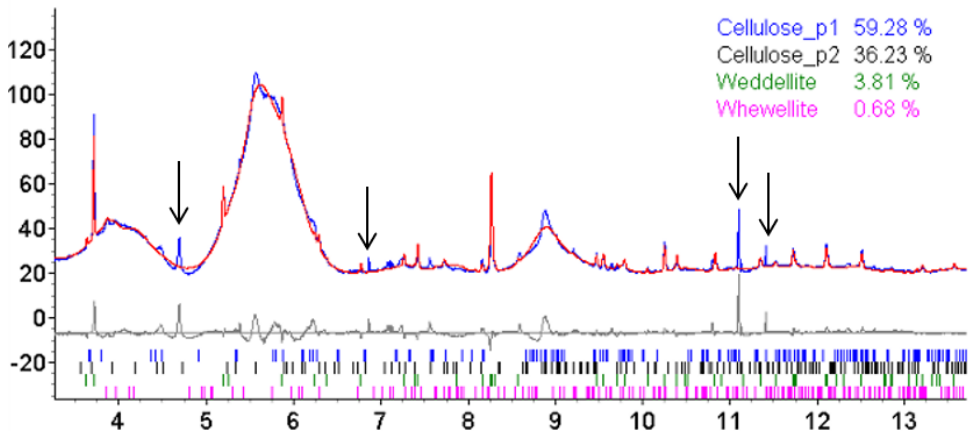

Figure 3.14: Rietveld refinement of a powder diffraction pattern recorded on the papyrus support of PAP-1 (λ= 0.4009Å). The I_β structural model was used for both Cellulose_p1 and Cellulose_p2 (Blue: experimental data, Red: calculated pattern, Grey: difference curve, Rwp = 5.13). Black arrows indicate non-indexed diffraction peaks.

As a result, two phases of cellulose were considered. In addition to cellulose, two hydrated calcium oxalate phases, weddellite ($Ca(C_2O_4), 2H_2O$), and whewellite ($Ca(C_2O_4), H_2O$) were included in the fit. The presence of these two phases results from the reaction between the oxalic

acid present in fast-growing plants (e.g. papyrus) with calcium extracted by the plant from the soil [60]. The peak shape of the four phases was described with a pseudo-Voigt function. The refinement was carried out, and the scale factors, lattice parameters, peak profile parameters, and instrumental zero point were allowed to vary.

A number of diffraction peaks present in the diffraction pattern could not be indexed. The presence of quartz identified in a few other patterns can be explained by the abundance of sand in the environment [9]. No crystalline phases in relation to the Sn, Pb, or Fe elements, found in XRF analysis, were identified. This may be explained by the random presence of these grains at the surface of the papyrus, their small amount, possibly their non-crystalline nature, or, as shown by the presence of non-indexed peaks in the diffraction pattern displayed in Figure 3.14, the absence of the relevant structures in the powder diffraction databases we consulted (PDF2-2003 and PDF4+ 2019) [52].

4.4.2 Structure of cellulose

As mentioned in the previous part, two phases of cellulose were introduced in the Rietveld refinement of the papyrus support, and the reason for this is going to be discussed here. A series of powder diffraction patterns were recorded on the papyrus support of PAP-1, and are shown in Figure 3.15. The 200 reflection of cellulose present some particular features (see insert Figure 3.15). Two different contributions, shifted in 2θ, seem to be present, as shown by the presence of a sharper peak and a larger one, with a variation in intensity from one measurement point to the other. Then in order to check for the possibility to have two cellulose phases with different crystallinity and/or preferred orientation effect, two phases of cellulose were introduced in the fit.

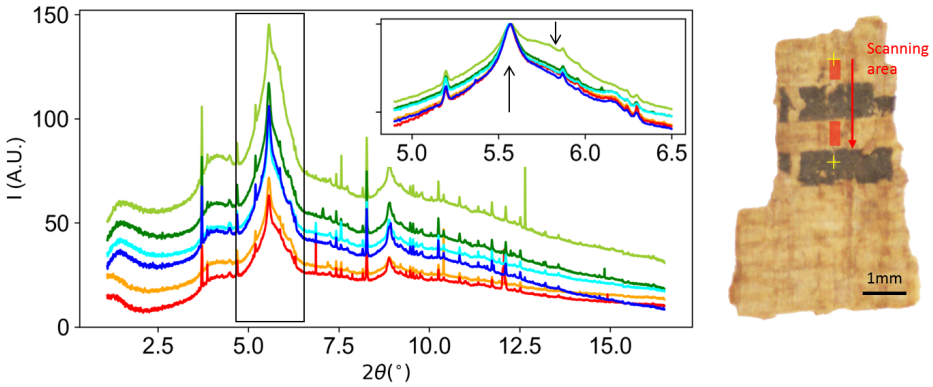

Figure 3.15: XRD signal of six measurement points recorded on black papyrus from fragment PAP-1. Insert: 200 reflection of cellulose. The two arrows indicate the presence of the two contributions. Data have been normalized on the diffraction peak at 5.51°.

Cellulose presents both crystalline and amorphous domains. Crystalline cellulose has four polymorphs, denoted cellulose I (which decomposes further in I_α and I_β), II, III, and IV [93]. The cellulose found in papyrus corresponds to cellulose I_β, as previously reported by Łojewska *et al.* [94]. Cellulose I_β has a monoclinic unit cell (P21, a=7.784(8) Å, b=8.201(8) Å, c=10.380(10) Å, γ=96.5°) [11], and this structure was used as a starting model to refine the diffraction pattern recorded on the papyrus support of PAP-1.

Possible effects for preferred orientation were taken into account using the preferred orientation spherical harmonics implemented in TOPAS-6. The symmetry-adapted spherical harmonics expansion [95] for fixed sample orientation was used. In the refinement, we have modeled the orientation of the cellulose fibers using a fourth-order spherical harmonics model,

and resulting 3-D plots are shown in Figure 3.16A. The first phase of cellulose does not show any particularly preferred orientation. On the other hand, a strong preferred orientation along c can be seen for the second cellulose phase, the direction along which the cellulose chains grow (Figure 3.16B). In addition to this, the FWHM of the second cellulose phase was found to be smaller than for the first one, confirming a difference in crystallinity.

The cell parameters of the two cellulose phases retrieved after refinement are given in Table 3.5. Cell parameters obtained on modern cellulose (I_β phase) by Gong *et al.* [93] and Nishiyama *et al.* [11] are also indicated. Compared to modern cellulose, the lattice parameter *a* of the cellulose of ancient papyrus supports has larger values. On the other hand, both *b* and *c* parameters are shorter. These effects on the cellulose structure are illustrated in Figure 3.16B. In particular, the increase of the *a* parameter indicates that the cellulose chains of ancient papyrus are going further away from each other. The shrinking in **b** and **c** directions may be correlated to a small distortion/rearrangement of the molecular unit, but further investigations are necessary to check this.

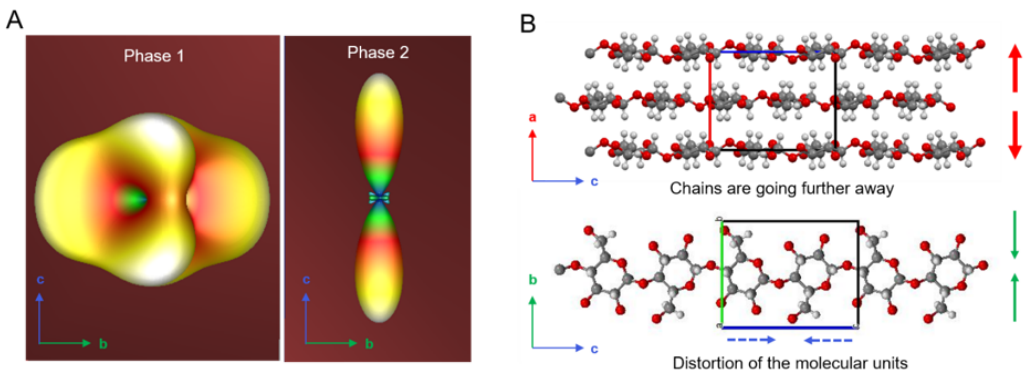

Figure 3.16: (A) 3D model of fourth-order spherical harmonics of cellulose structure. (B) Evolution of the lattice showing the potential distortion and the delamination of the polymeric chains.

Table 3.5: Lattice parameters found from Rietveld refinement of cellulose structure from XRPD pattern measured on PAP-1, ESRF ID22.

	Gong *et al.* [93]	**Nishiyama *et al.* [11]**	**This work: Phase 1**	**This work: Phase 2**
a (Å)	7.78	7.784(8)	7.9582(1)	8.2631(3)
b (Å)	8.20	8.201(8)	8.0188(2)	7.7890(1)
c (Å)	10.38	10.380(10)	10.2876(4)	10.3337(2)
γ (°)	96.5	96.5	98.311(3)	93.694(8)

We interpret the presence of two phases of cellulose, one being more crystalline and strongly oriented in the **c** direction, and the increase of distance between the different chains composing the cellulose structure as a possible indication of an aging process. Additional investigations are necessary to precise this process (oxidation of the chains, transformation of the molecular unit,...). The intensity variation of the two phases from one measurement point to the other, as shown in Figure 3.16, is potentially related to the orientation of the fibers in the papyrus, and this could be investigated further by mapping by XRD a larger region of the papyrus support. The Rietveld refinement could also be improved by introducing the atomic structure of cellulose as a rigid body, to authorize a refinement of the distortion angles in the molecular unit.

5 Analysis of colored pigments on papyrus from Champollion collection

5.1 Fragments and analytical techniques

In this part, we are going to look at fragments PAP-6, PAP-7, PAP-10, PAP-11, and PAP-12 (Figure 3.17). All the fragments were presented in Table 3.1, but the ones that are going to be analyzed in this part are shown in Figure 3.17.

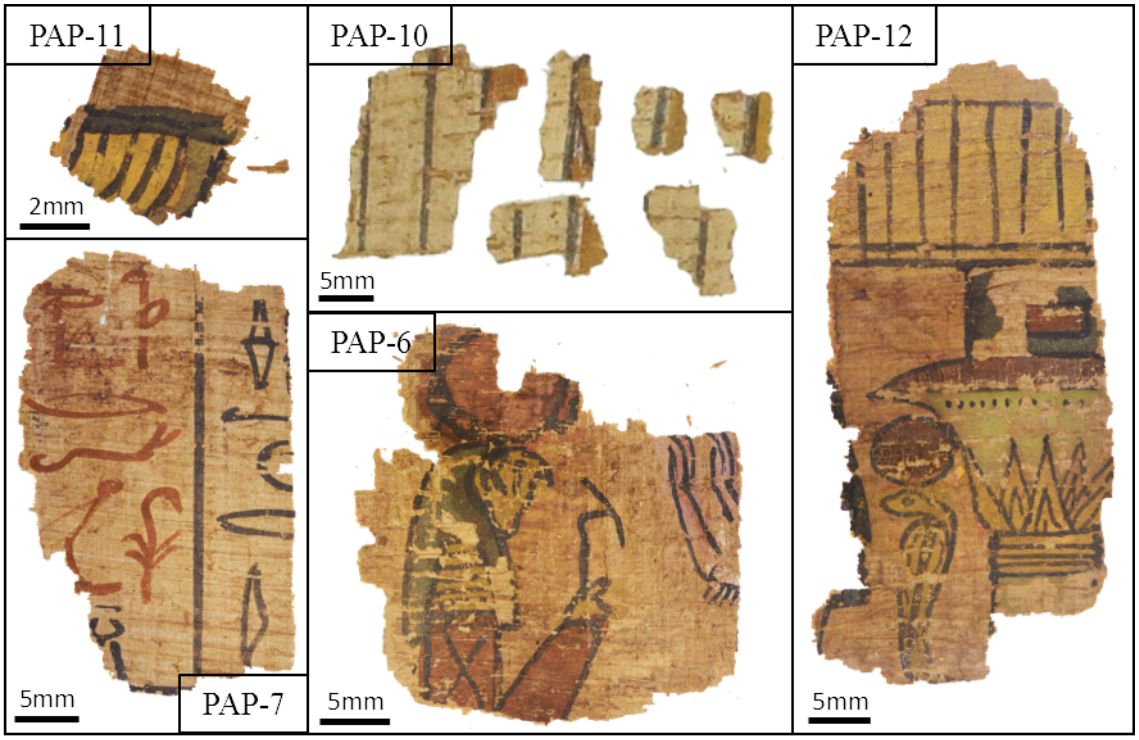

Figure 3.17: Champollion museum colored fragment set. (Nikon D3200, 50-200mm lens)

Fragment PAP-11 is composed of six black stripes with solid yellow paint color and a green stripe on its right. The top part is a blue stripe that comports a darkened shade. Fragment PAP-10 are papyrus fragments covered with white paint and black stripes, two of the small parts having yellow paint. Both fragments PAP-10 and PAP-11 do not comport discernible features that are sufficient to attribute them to a particular drawing. However, fragments PAP-6, PAP-7, and PAP-12 are presenting scenes with more discernible features that were described earlier.

All these fragments are part of our study around the identification of the pigments used to paint and write in ancient Egypt. The summary of the analytical techniques performed on these fragments is presented in Table 3.6.

Table 3.6: Measurements made on the papyrus fragments from the Champollion museum. XRF and XRD have in common the beam size (250x250µm) and a counting time of 1 second in XRF and 4 seconds in XRD (E=31keV).

Sample	**XRF**	**XRD**
PAP-6	Map 1: 40x36 points (VxH)	7 points
	Map 2: 19x15 points (VxH)	
PAP-7	Map 1: 15x22 points (VxH)	1 point
PAP-10	/	1 point
PAP-11	Map 1: 10x12 points (VxH)	4 points
PAP-12	Map 1: 20x20 points (VxH)	5 points
	Map 2: 28x8 points (VxH)	

5.2 Identification of colored pigments by XRD and XRF

5.2.1 PAP-6 – Re

5.2.1.1 Phase identification with XRD

We focused our attention on seven points on the sample from which we recorded seven diffraction patterns. Each point was selected to be able to identify each pigment in the sample. The location of the seven measurement points is shown in Figure 3.18.

Figure 3.18: XRD measurement point locations on papyrus fragment PAP-6

With XRD, we were able to identify the phases shown in Table 3.7. The origin of the phases will be discussed in the following part. Each phase was identified with the search-match algorithm link to the PDF2-2003 database.

Table 3.7: Summary of all identified phases on papyrus fragment PAP-6 (cellulose, weddellite and whewellite phases are always present, thus not indicated). Phases that are probably present but not surely identified are written in italic.

Point number	**Apparent color**	**Phases**
1	Blue	Cuprorivaite ($CaCuSi_4O_{10}$), quartz (SiO2), orpiment (As_2S_3), realgar (As_4S_4), wollastonite ($CaSiO_3$), *aphthitalite ($K_3Na(SO_4)_2$), hematite (Fe_2O_3)*
2	Blue	Cuprorivaite ($CaCuSi_4O_{10}$), quartz (SiO_2), wollastonite ($CaSiO_3$)
3	Dark red	Syngenite ($K_2Ca(SO_4)_2$,(H_2O)), hematite (Fe_2O_3), *magnetite (Fe_3O_4)*
4	Pink	Challacolloite (KPb_2Cl_5), hematite (Fe_2O_3)
5	White	Challacolloite (KPb_2Cl_5), calcite ($CaCO_3$)
6	Yellow	Orpiment (As_2S_3), realgar (As_4S_4), *aphthitalite ($K_3Na(SO_4)_2$), quartz (SiO_2)*
7	Dark red	Syngenite ($K_2Ca(SO_4)_2$,(H_2O)), hematite (Fe_2O_3), *magnetite (Fe_3O_4)*

By taking a closer look at the diffraction pattern of measurement point 1 (Figure 3.19B), we observe that three peaks in the pattern have a very high intensity compared to the rest. These peaks correspond to the effect of the diffraction of single crystals of cuprorivaite as shown as bright spots in Figure 3.19A. When possible, the rotation of the sample would reduce or even avoid this effect, but this is not possible in our case.

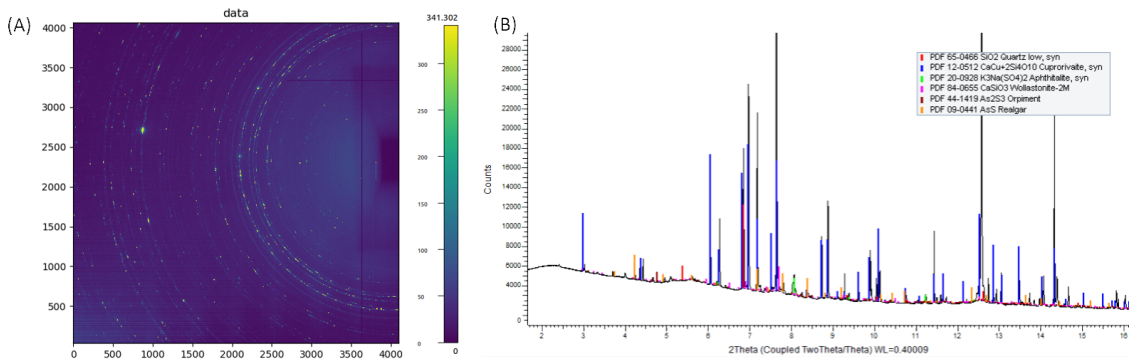

Figure 3.19: (A) 2D diffraction pattern of sample PAP-6 on measurement point 1. (B) 1D diffraction pattern of papyrus PAP-6 on measurement point 1. Weddellite, whewellite and cellulose are present but not shown in the phase identification.

5.2.1.2 Refinements

The presence of a single-crystal signal measured on point 1 implies the impossibility to perform a suitable Rietveld refinement to obtain quantitative information point when large crystals of cuprorivaite are present.

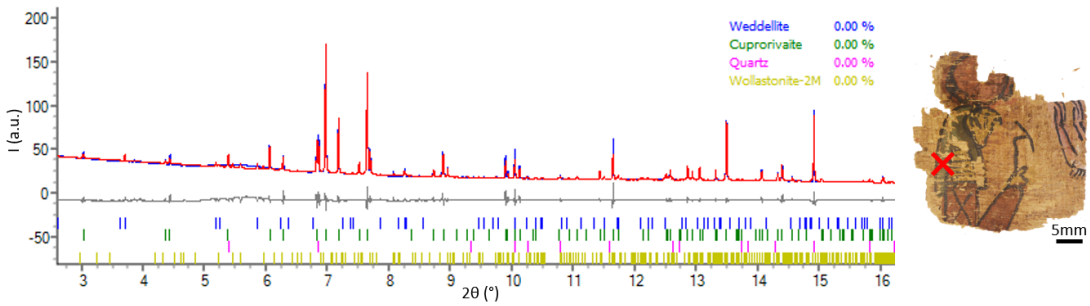

Figure 3.20: Pawley fit of measurement point 2 of fragment PAP-6. (Red = Fit, Blue = Observed)

With the single-crystal separate method developed in the Chapter 2, we would have removed most of the signal of the cuprorivaite which renders the quantification irrelevant. One option would be to control the size at which the separate function distinguish powder from single-crystal, thus providing a quantification of the powder up to a certain crystal size.

To confirm this identification it is still possible to perform a Pawley fit on point 2 which does not contain realgar and orpiment compared to point 1(Figure 3.20). A Rietveld refinement was performed on point 6 that does not contain cuprorivaite compared to point 1 (Figure 3.21). Realgar appears as the major phase (almost 50%), followed by aphthitalite (22%), weddellite (20%), and orpiment (10%).

The Rietveld refinement carried out on measurement point 5 (white) is shown in Figure 3.23. The refinement tells us two things: potassium lead chloride is present as the major phase (> 99%), with only weddellite and calcite as secondary minority phases. No other lead-based phase was identified. Secondly, the phase is very well crystallized with good powder behavior.

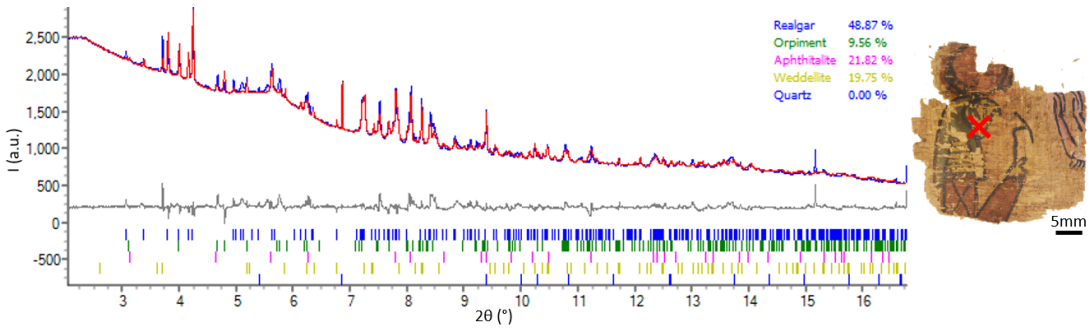

Figure 3.21: Rietveld refinement of measurement point 6 of fragment PAP-6. (Red = Fit, Blue = Observed, Rwp = 2.58, Rexp = 2.85, Rp = 1.56)

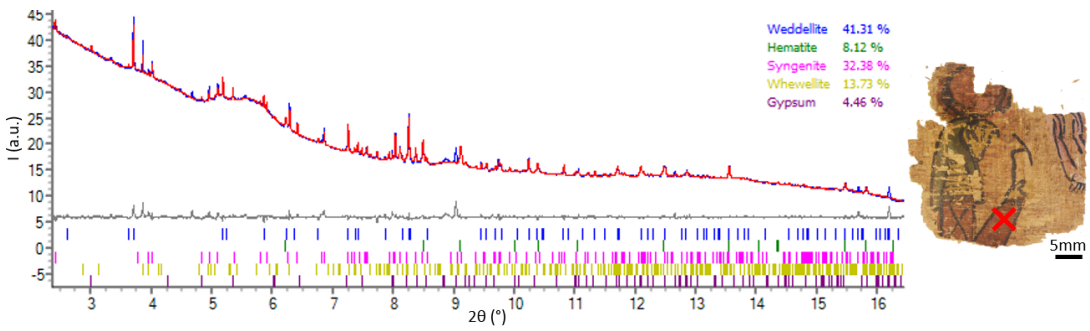

Figure 3.22: Rietveld refinement of measurement point 3 of fragment PAP-6. (Red = Fit, Blue = Observed, Rwp = 1.2, Rexp = 22.85, Rp = 0.65)

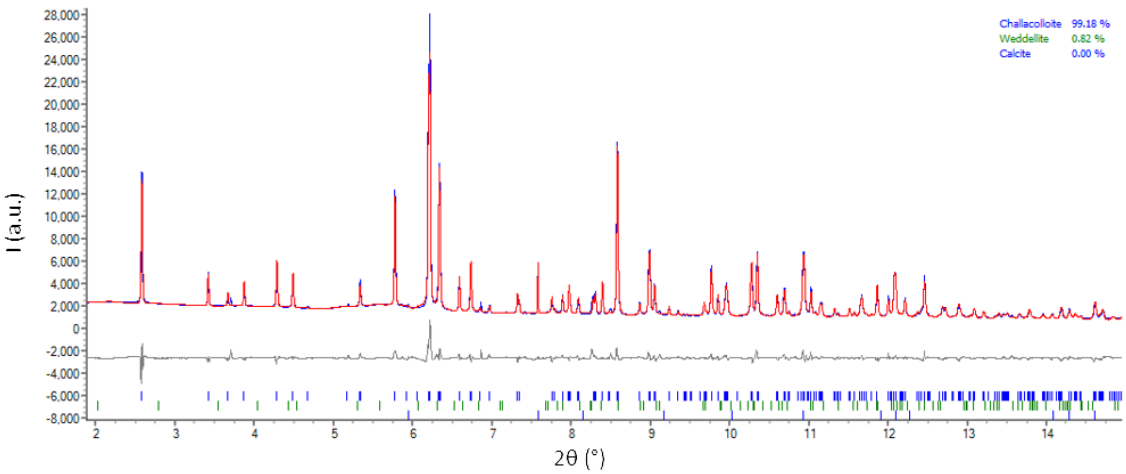

Figure 3.23: Rietveld refinement of point 5 of PAP-6. Calcite was added using pattern matching refinement to fit the peak at 7.6°, coming from single-crystal diffraction behavior. Cellulose contribution was part of the background (Red = Fit, Blue = Observed, Rwp = 5.99, Rexp = 2.34, Rp = 3.95).

The origin of the presence of potassium lead chloride, also known as challacolloite, will be commented on later in the manuscript.

5.2.1.3 XRF and pigment layer superposition

As shown in the previous part, we managed to identify the crystalline phases present on several measurement points on the sample. The XRF spectra recorded on each colored area tell us the nature of the elements present in each pigment. Then we verify if each element is explained by the phase identification in XRD. In addition, XRF maps made on the fragments will tell us more about the repartition of the different paint layers in the sample.

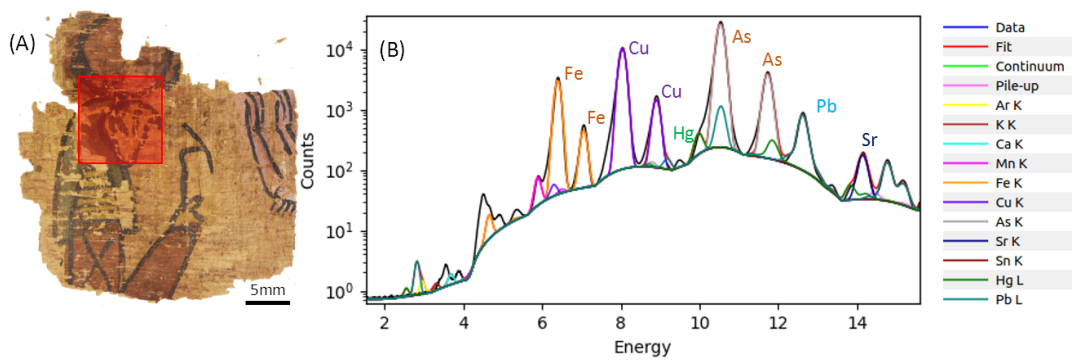

Figure 3.24: XRF map location with summed XRF spectrum and fit of the major elements.

The first XRF map (Map 1, Table 3.6) was focused on Re's head. Figure 3.24A shows the measured area. The summed XRF spectrum of the map (Figure 3.24B) shows the presence of elements such as iron (Fe), copper (Cu), arsenic (As), which is in agreement with the main phases identified by XRD (Point 1, 6 and 7, see Table 3.7). In addition, strontium (Sr), lead (Pb), and mercury (Hg) were also identified, and the presence of these elements is going to be discussed below.

The maps of the principal elements are shown in Figure 3.25. On the iron map, the contour of the god head is clearly visible. Nevertheless, we can see on this iron map the face of Re with a very different design from the face we see on the optical image. This drawing is certainly an

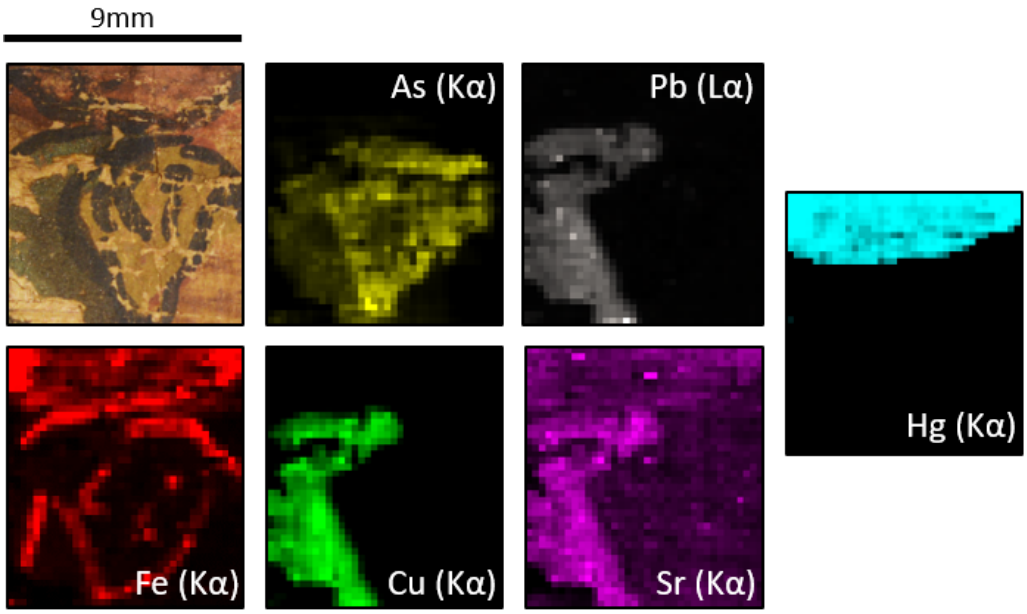

Figure 3.25: XRF maps of major elements, each map represents the ROI around the main emission line (i.e. Kα or Lα) (mercury (Hg) map is displayed on a log scale).

underdrawing that was the first sketch done by a scribe before coloring the papyrus and apposing the final black line. The first layer is optically not visible. The underdrawing, also called preparatory drawing and often done in red with an hematite-based pigment, is mentioned in the literature [57] but not well described.

Looking at arsenic and copper maps, they correspond to the face of Re painted in yellow (orpiment) and to the blue area (cuprorivaite) marking the headdress of the god, respectively. We can assume that the copper-based paint present on Re's headdress was put on top of arsenic paint because the emitted As-K fluorescence photons are partially absorbed by the copper layer, thus leading to a lower signal on the map. Since we have acquired the signal on both arsenic-rich and arsenic plus copper-rich areas, we can try to deduce the thickness of the upper layer of copper from this absorption observation.

By applying the exponential attenuation law (Equation 3.1) on the two fluorescence spectra, normalized to the incoming beam intensity we can extract x_{Cu}, the thickness of the copper layer. To do so, we assume that the layers are strictly on top of each other and that the copper-rich layer is purely cuprorivaite ($CaCuSi_4O_{10}$).

$$I = I_0 \cdot e^{-\mu x} \tag{3.1}$$

where,

- I is the measured intensity of the emission line,
- I_0 is the incoming beam intensity,
- μ is the linear absorption coefficient in cm^{-1},
- x is the thickness of the layer in cm.

Taking into account a two-layers superposed model, we obtain two equations :

$$\begin{cases} I_{As(K\alpha)} = I_0 \cdot e^{-\mu_{As} x_{As}} \\ I_{As(K\alpha)+Cupr} = I_0 \cdot e^{-(\mu_{As} x_{As} + \mu_{Cupr} x_{Cupr})} \end{cases} \tag{3.2}$$

This implies the following equation:

$$x_{Cupr} = \frac{1}{\mu_{Cupr}} \left(\ln(I_{As(K\alpha)}) - \ln(I_{As(K\alpha)+Cupr}) \right) \tag{3.3}$$

where,

- x_{Cupr} is the thickness of the cuprorivaite layer,
- μ_{Cupr} is the linear absorption coefficient of cuprorivaite,
- $I_{As(K\alpha)}$ is the measured intensity of the Kα emission line of an arsenic-rich area,
- $I_{As(K\alpha)+Cupr}$ is the measured intensity of the Kα emission line of an arsenic-rich area covered by cuprorivaite.

The value of μ_{Cupr} is calculated by multiplying the mass attenuation coefficients of each element contained in cuprorivaite by their mass fractions. The mass attenuation coefficient is taken from NIST tables and interpolated at 31keV.

$$\mu_{Cupr} = \rho_{Cupr} \left(x_{Ca} \frac{\mu_{Ca}}{\rho_{Ca}} + x_{Cu} \frac{\mu_{Cu}}{\rho_{Cu}} + x_{Si} \frac{\mu_{Si}}{\rho_{Si}} + x_{O} \frac{\mu_{O}}{\rho_{O}} \right) \tag{3.4}$$

$$\mu_{Cupr} = 8.36 cm^{-1} \text{ at 31 keV} \tag{3.5}$$

We measured $I_{As(K\alpha)}$ and $I_{As(K\alpha)+Cupr}$ values directly on the XRF spectrum (Figure 3.26).

We obtain that the thickness of the layer is 1.03mm. This result is around ten times larger than what we could expect from the literature [96]. This can be explained by the presence of other elements/phases in the top layer that were not taken into account in our simple calculations. By taking a look at the fluorescence maps (Figure 3.26), we see that the copper-rich region contains also lead and strontium. The presence of these two elements was not explained by any diffraction pattern phase identification. The presence of these two elements would explain the result we obtained and adding it to the calculation would obviously increase the absorption factor and thus lower the calculated thickness.

Finally, the fluorescence map shows also the presence of a low amount of mercury (Figure 3.25). The mercury-containing area is specifically on the dark red solar disk on top of Re's head. This attests that the red paint used in the underdrawing has a different chemical composition compared to the darker red color found on the solar disk. The crystalline structure of the mercury compound was not identified, mostly due to the low amount of mercury present which is most probably not enough for the HR- XRD to be sensitive to. Whether or not there was a voluntary addition of a mercury-based compound to the dark red pigment used to paint the solar disk remains to be explained. Since the mercury is present in a low amount, we can formulate the hypothesis that the ore from which the iron-based pigment (hematite) was pulled out is different for the red underdrawing and the dark red pigment. The dark red pigment ore may have contained some mercury in a small fraction with a mineral such as cinnabar (HgS).

At this stage, we can conclude on the paint layer superposition over this first map (Map 1, Table 3.6). Scribes started with the underdrawings with an iron-based ink, most probably hematite. Then, the yellow color containing orpiment and realgar was put in, with the dark red solar disk containing hematite and a small fraction of mercury. After that, Egyptian blue was added, covering a part of the yellow paint from Re's face. Finally, the contours of the painting were done with a black paint, most probably carbon-based as it did not give any contrast either by XRD or XRF. This black layer appears optically as the last layer. Since the underdrawing and the contour layer are so different, we can assume that at least two scribes painted this papyrus. Then it is probable that

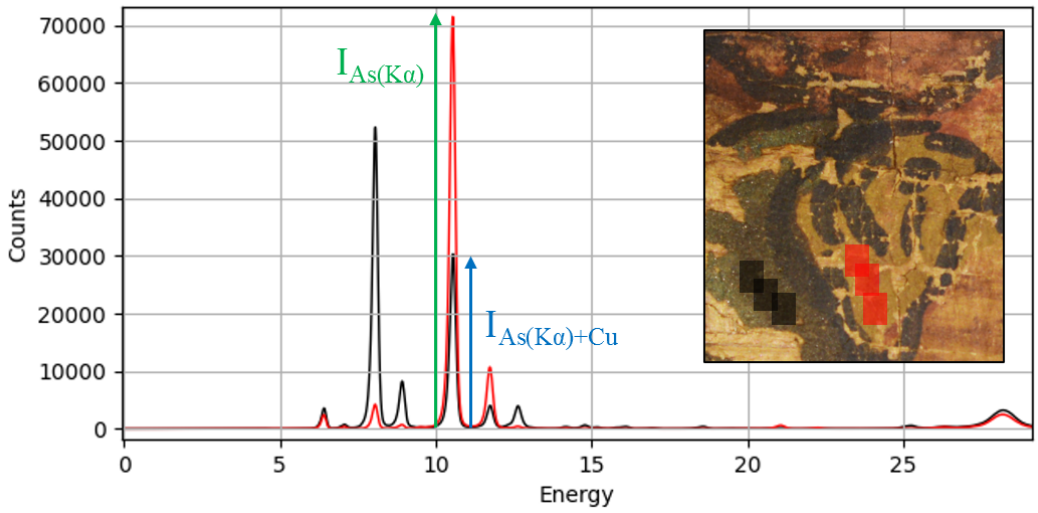

Figure 3.26: Intensity measured for the arsenic Kα emission lines on two fluorescence spectra averaged from two ROI on papyrus fragment PAP-6.

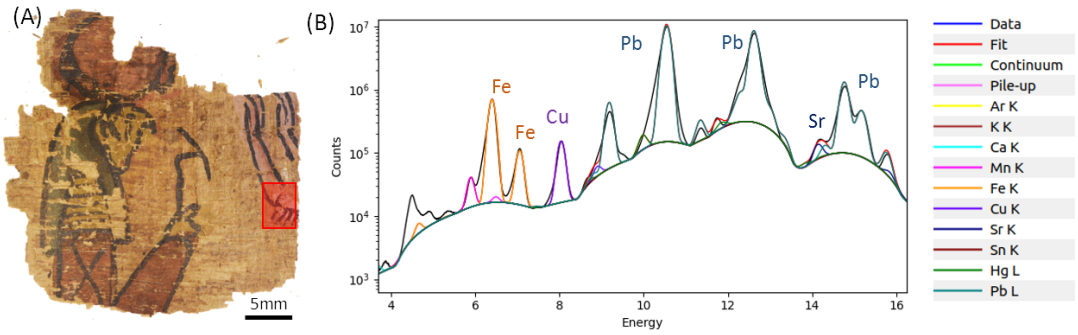

Figure 3.27: (A) Papyrus fragment PAP-6 fluorescence mapping acquisition on the deceased's arms area. (B) Summed fluorescence spectra.

the colors were put on top of the underdrawing by a specialized scribe, but this is more complex to attest.

The second fluorescence mapping area (Map 2, Table 3.6) is located on the elbow of the deceased (Figure 3.27). The summed fluorescence pattern shows the presence of iron, copper, and lead as major elements. A small amount of strontium was also detected. The presence of iron and lead corresponds to the phases of hematite and challacolloite identified by XRD (measurement points 4 and 5, Table 3.7), respectively. If the presence of strontium stays unexplained, copper is associated with crystals of cuprorivaite. The signal showed on the copper map (Figure 3.28) illustrates possible pollution of the sample by free grains of cuprorivaite. These crystals most likely come from the copper-rich pigment found on Re head.

The maps shown in Figure 3.28B reveals the presence of lead located on the white paint which was identified as potassium lead chloride (challacolloite). We can comment on the slight contrast on the lead map below the elbow of the deceased. The four fringes of black paint appear to contain lead as well as the diagonal black stripe starting on the top left part of the map (Figure 3.28B) does not present any traces of it. At this stage, it is highly possible that the lead white-based paint was spread by the painter's tool while painting the black stripes.

Regarding the iron, which corresponds to hematite (Table 3.7, point 4), it looks like the pink part of the arm corresponds to its signal. We saw in the previous map (Map 1, Table 3.6) that hematite may have also been used to do the underdrawing of the head of Re. Because of this, we cannot exclude the presence of an underdrawing under the deceased arm. The layer superposition

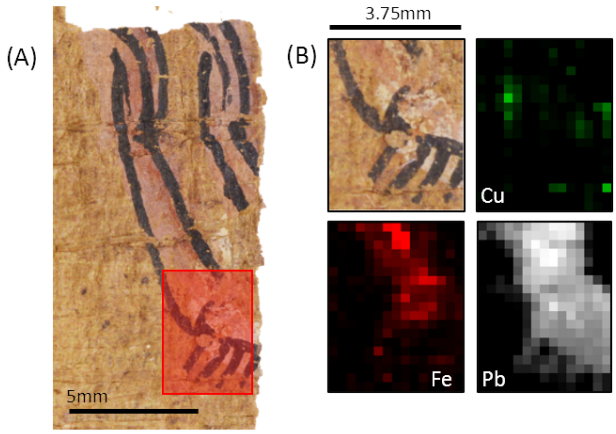

Figure 3.28: XRF maps of major elements, each map represents the ROI around the main emission line (i.e. Kα or Lα)

is optically visible (Figure 3.28A) with a potential underdrawing first, then the white paint from the deceased cloth, the pink paint from the deceased arm, and at the end the contour made with black ink.

To conclude on the layer superposition over the whole fragment, we extracted each color contribution on the papyrus to schematize the order in which the visible layers were put (Figure 3.29). The underdrawing shown in Figure 3.25 is not visible on the photograph because it is complex to superpose it to this view, however, it would have been present as the first layer laid on top of the raw papyrus.

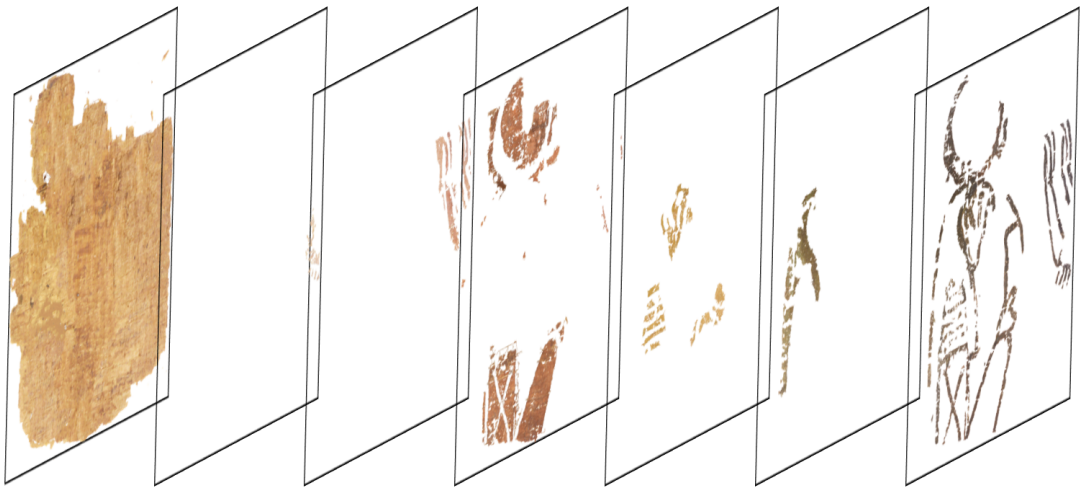

Figure 3.29: Visible ink layers superposition on papyrus fragment PAP-6. The deposition order is from left to right: raw papyrus, white, pink, red, yellow, blue and black. The layers are obtained by filtering colors from optical images. Any underdrawing not visible optically cannot appear in this view.

5.2.2 PAP-11 – Black and yellow stripes

This fragment is the smallest of the batch. It comports four different colors, yellow, green, blue, and black. Optically, the blue color is not obvious to see (Figure 3.45), and only bright blue crystals, as opposed to the matte shade of the black ink, can differentiate both colors.

5.2.2.1 Phase identification with XRD

Several measurement points were made on the fragment to disentangle the contribution of each phase to the different pigments. The four points are presented in the following figure (Figure 3.30).

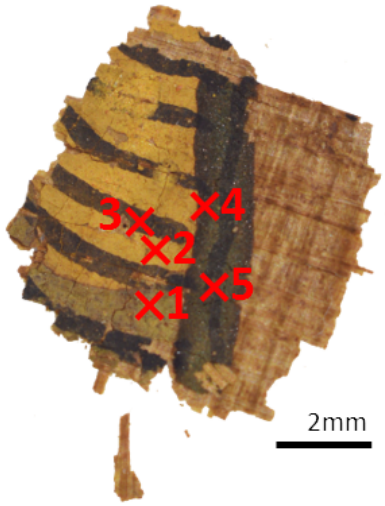

Figure 3.30: Location of the XRD measurement points made on papyrus fragment PAP-11.

The following table (Table 3.8) summarizes the identification of the phases with XRD.

Table 3.8: Summary of all identified phases on papyrus fragment PAP-11 (weddellite and whewellite phases are always identified, thus not shown). Phases that are probably present but not surely identified are put in italic.

Point number	**Apparent color**	**Phases**
1	Green	Aphthitalite ($K_3Na(SO_4)_2$), orpiment (As_2S_3), realgar (As_4S_4), quartz (SiO_2), hematite (Fe_2O_3), lavendulan ($NaCaCu_5(AsO_4)_4Cl$, $5H_2O$), moolooite ($Cu(C_2O_4)$,$0.4H_2O$), atacamite ($Cu_2Cl(OH)_3$)
2	Yellow	Orpiment (As_2S_3), realgar (As_4S_4), quartz (SiO_2), aphthitalite ($K_3Na(SO_4)_2$)
3	Blue/black	Cuprorivaite ($CaCuSi_4O_{10}$), quartz (SiO_2), orpiment (As_2S_3), realgar (As_4S_4), wollastonite ($CaSiO_3$), aphthitalite ($K_3Na(SO_4)_2$), *hematite (Fe_2O_3), syngenite ($K_2Ca(SO_4)_2$,(H_2O))*
4	Blue/black	Cuprorivaite ($CaCuSi_4O_{10}$), quartz (SiO_2), wollastonite ($CaSiO_3$), orpiment (As_2S_3), realgar (As_4S_4)
5	Blue/black	Cuprorivaite ($CaCuSi_4O_{10}$), quartz (SiO_2), wollastonite ($CaSiO_3$)

The phase identification performed on the diffraction patterns of the green area (point 1) indicates the presence of realgar and orpiment, usually associated with a yellow color. This indicates the presence of a yellow paint layer under the green one or a mix between a blue and yellow pigment to form the green. However, three uncommon phases were also identified: moolooite ($Cu(C_2O_4)$,$0.4H_2O$), atacamite ($Cu_2Cl(OH)_3$), and lavendulan ($NaCaCu_5(AsO_4)_4Cl$, $5H_2O$). Hematite is also found in that point, which could indicate the presence of an

underdrawing but the lack of larger fluorescence measurement data makes the hypothesis impossible to validate.

5.2.2.2 Refinements

Orpiment and realgar are the two main phases found in point 2. Corresponding Rietveld refinement, is shown in Figure 3.31.

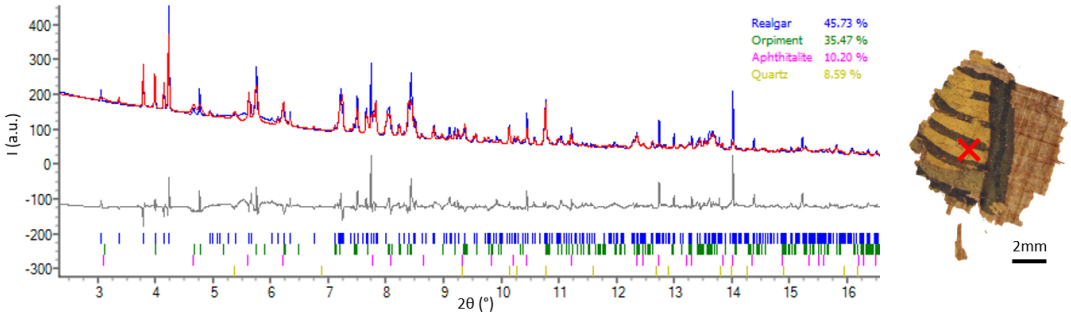

Figure 3.31: Rietveld refinement of point 2 on fragment PAP-11. (Red = Fit, Blue = Observed, Rwp = 8.30, Rexp = 10.12, Rp = 4.98)

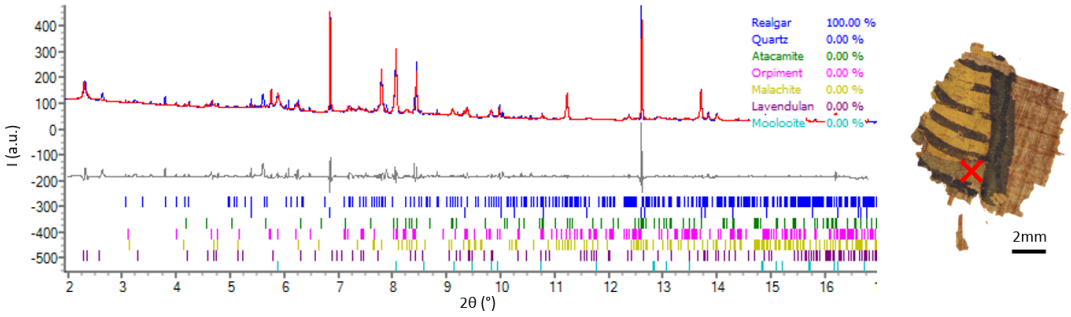

Figure 3.32: Rietveld refinement of point 1 on fragment PAP-11. (Red = Fit, Blue = Observed, Rwp = 7.37, Rexp = 10.78, Rp = 4.08)

Even if this refinement is not perfect because of several single-crystals, it confirms both the identification of the phase and also provides an approximate quantification, with the pattern dominated by realgar (46%) and orpiment (36%). In the next part, we will compare this quantification with the different measurement points made on other fragments. We can quickly note that even if the present color is yellow, realgar, which is a red to orange mineral appears to be present in a higher quantity. A Pawley fit was performed on the pattern collect in the green zone (point 1), and phase identification was confirmed (Figure 3.32), validating the simultaneous presence of yellow (orpiment and realgar), red (hematite), and green pigments (e.g. atacamite).

5.2.2.3 XRF and pigment layer superposition

The fluorescence mapping (Figure 3.33) confirms that the arsenic (coming from orpiment and realgar) is indeed present in the green area. The signal of iron seems to indicate the presence of a preparatory drawing as a vertical stripe.

Regarding the layer superposition, we can now conclude by combining results from optical observation (Figure 3.33B), XRD measurements, and XRF mapping. A preparatory drawing made of hematite is probably present. The first layer is the yellow pigment. Then the green layer has been deposited on top, as shown by the presence of realgar and orpiment found on measurement

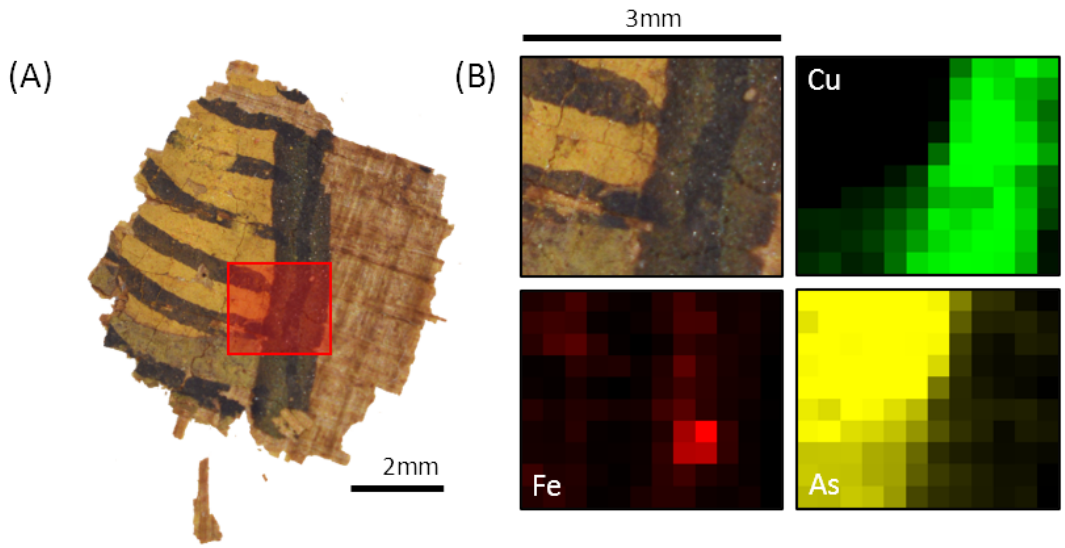

Figure 3.33: (A) PAP-11 fluorescence mapping acquisition. (B) Fluorescence maps of copper Kα (Cu), iron Kα (Fe) and arsenic Kα (As).

point 1 located in the green area. The blue layer, in which cuprorivaite was identified, covers both green and yellow and at the end, the black contour is laid on top. The thickness of the layer was not calculated because of the large number of phases identified in point 1.

5.2.3 PAP-12 – Cobra and column

5.2.3.1 Phase identification with XRD

This fragment is the largest of the batch and in total, seven XRD measurement points were made to identify the pigments (Figure 3.34). The points are shown in Figure 3.34 and the identified phases in Table 3.9.

Figure 3.34: Location of the XRPD measurement points made on fragment PAP-12.

In the two measurement points (points 1 and 4) done on the yellow color, the diffraction signal shows the presence of realgar (As_4S_4) and orpiment (As_2S_3). Although both measurement

Table 3.9: Summary of all identified phases on papyrus fragment PAP-12 (weddellite and whewellite phases are always identified, thus not shown). Phases that are probably present but not surely identified are put in italic

Point number	**Apparent color**	**Phases**
1	Yellow	Orpiment (As_2S_3), realgar (As_4S_4), aphthitalite ($K_3Na(SO_4)_2$), *hematite (Fe_2O_3)*
2	Green	Quartz (SiO_2), moolooite ($Cu(C_2O_4)$,$0.4H_2O$), orpiment (As_2S_3), realgar (As_4S_4), lavendulan ($NaCaCu_5(AsO_4)_4Cl$, $5H_2O$)
3	Green/black	Quartz (SiO_2), moolooite ($Cu(C_2O_4)$,$0.4H_2O$), atacamite ($Cu_2Cl(OH)_3$), cuprorivaite ($CaCuSi_4O_{10}$)
4	Yellow	Orpiment (As_2S_3), realgar (As_4S_4), aphthitalite ($K_3Na(SO_4)_2$), *quartz (SiO_2)*
5	Green	Quartz (SiO_2), moolooite ($Cu(C_2O_4)$,$0.4H_2O$), atacamite ($Cu_2Cl(OH)_3$)
6	Red	Hematite (Fe_2O_3), syngenite ($K_2Ca(SO_4)_2$,(H_2O)), gypsum ($CaSO_4$,$2H_2O$), aphthitalite ($K_3Na(SO_4)_2$)
7	Blue	Cuprorivaite ($CaCuSi_4O_{10}$), quartz (SiO_2), wollastonite ($CaSiO_3$)

points present the same crystalline phases, there is a signal coming from aphthitalite ($K_3Na(SO_4)_2$) combined with the signal of hematite also present but extremely weak, and this could be attributed to an underdrawing. The weakness of the XRD signal of hematite is reinforced by the overlapping effect of the layers of orpiment/realgar absorbing the diffracted signals. The three measurement points (points 2, 3, and 5) in the green parts show the presence of moolooite, lavendulan, and atacamite. In addition, measurement point 2 shows the presence of orpiment, due to the proximity of the yellow pigment (Figure 3.34).

5.2.3.2 Refinements

Rietveld refinements were performed on points 4, 5, and 6 respectively yellow, green and red. Point 7 (blue) could not be fitted through Rietveld refinement for the same reason as previously explained (presence of large crystals of cuprorivaite on Figure 3.20), but a Pawley fit was carried out (Figure 3.38), confirming the exclusive presence of cuprorivaite, wollastonite and quartz.

The refinement performed on point 4 (yellow) shows that realgar (68%) and orpiment (20%) are the two main phases, followed by aphthitalite (10%). On point 5, weddellite (29%) and quartz (62%) are dominating, and atacamite and moolooite, two phases in relation with the green color, represent less than 10%. Finally, the Rietveld refinement performed on point 6 (red) shows the dominating presence of hematite (29%) and syngenite (16%) (in addition to the classic weddellite and whewelite phases).

5.2.3.3 XRF and pigment layer superposition

Two XRF maps were carried out (Table 3.6), and the first one, on the cobra head, is shown in Figure 3.39. The elemental distribution shows easily that the yellow pigment is rich in arsenic, as expected from XRD results (orpiment and realgar). A small amount of lead was detected on one

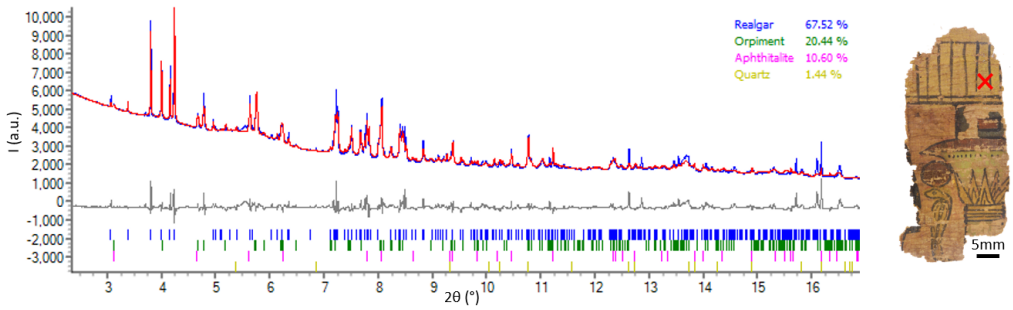

Figure 3.35: Rietveld refinement of point 4 on fragment PAP-12. (Red = Fit, Blue = Observed, Rwp = 3.52, Rexp = 1.92, Rp = 2.00)

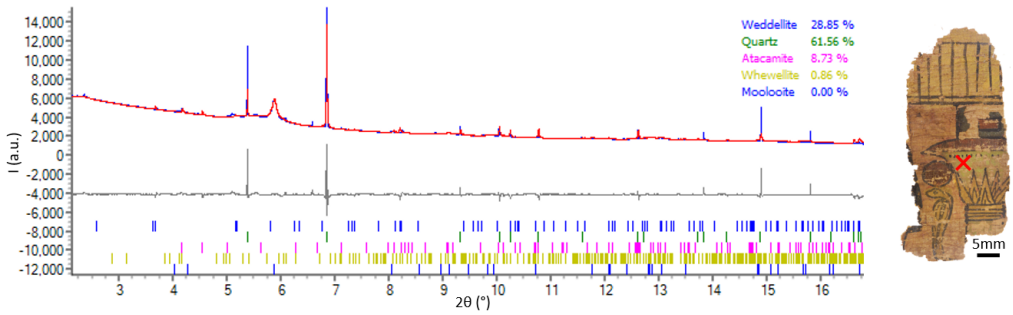

Figure 3.36: Rietveld refinement of point 5 on fragment PAP-12 (moolooite was refined with a Pawley fit). (Red = Fit, Blue = Observed, Rwp = 4.74, Rexp = 1.85, Rp = 1.85)

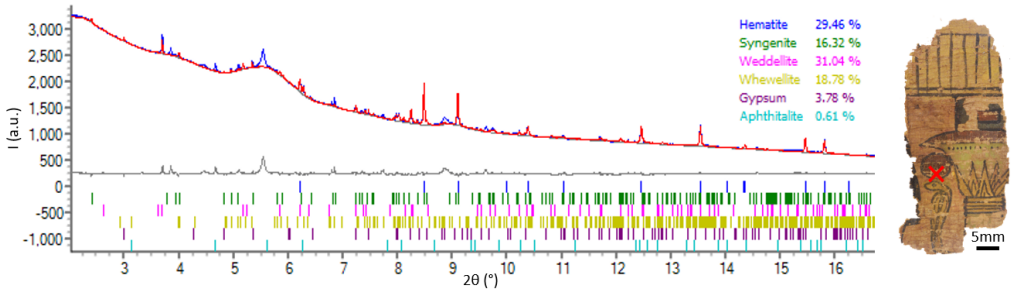

Figure 3.37: Rietveld refinement of point 6 on fragment PAP-12. (Red = Fit, Blue = Observed, Rwp = 16.60, Rexp = 1.98, Rp = 7.21)

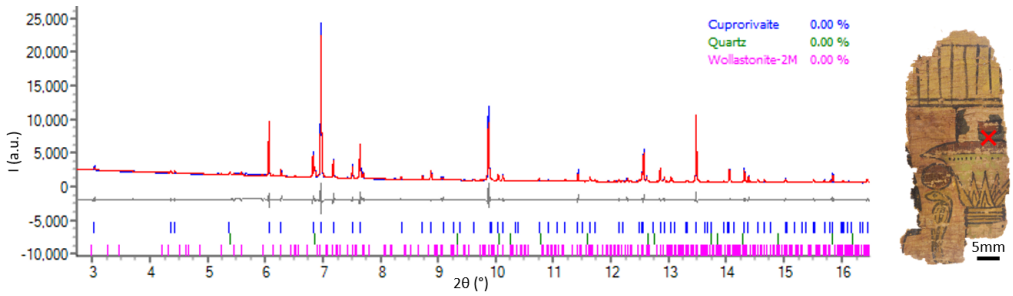

Figure 3.38: Pawley refinement of point 7 on fragment PAP-12. (Red = Fit, Blue = Observed, Rwp = 5.71, Rexp = 2.43, Rp = 3.69)

side, but this does not seem to be related to any color used for the cobra head.

Taking a closer look at the iron and arsenic maps, iron (attributed to hematite) is not quite

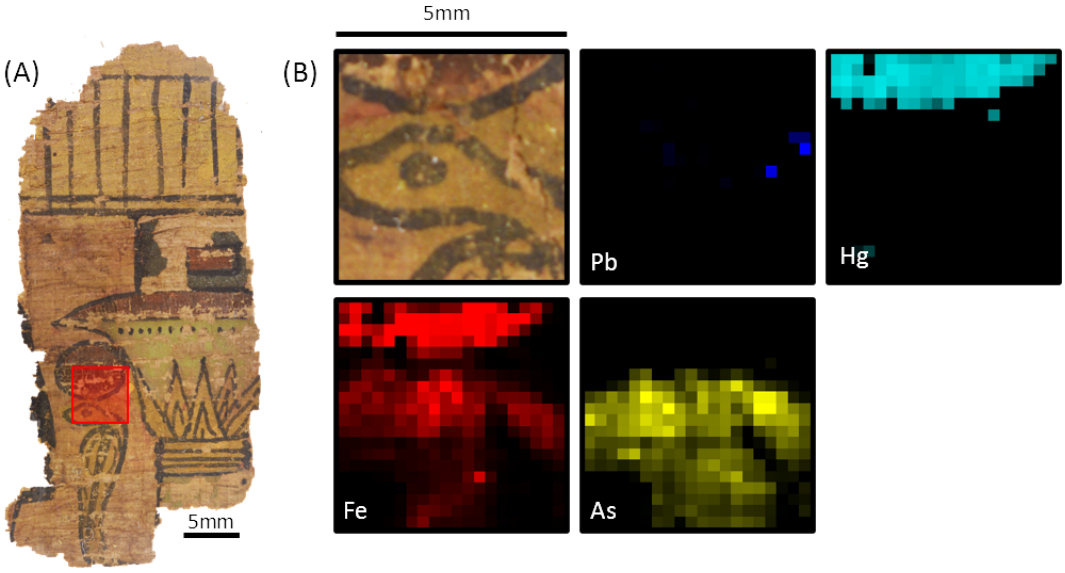

Figure 3.39: (A) PAP-12 fluorescence mapping acquisition (Map 1 (Table 3.6), 20x20 points of 250µm) on the cobra area.(B) Measured area with fluorescence maps of lead Lβ (Pb), iron Kα (Fe), arsenic Kα (As), and mercury Lα (Hg)

located at the same places as arsenic, with the addition of the solar disk. There is a very high probability that the signal of iron in the cobra head corresponds to a preparatory drawing. The signal of mercury is also illustrating the same chemical difference between dark red used for the solar disk and preparatory drawing pigments as observed on papyrus fragment PAP-6.

The difference between the dark red pigment used for the solar disk of the cobra and the one used for the preparatory drawing is visible on the top of the cobra's nose (Figure 3.39B), where the preparatory drawing was poorly covered and remained visible.

From these results, we deduced that the painting of the cobra was started by the preparatory drawing, then the yellow paint, the dark red, and finally the black contour.

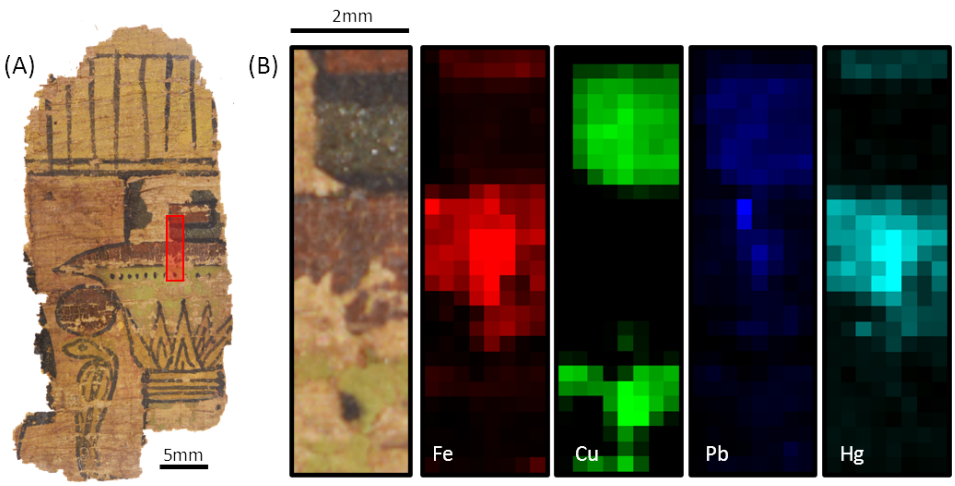

Figure 3.40: (A) PAP-12 fluorescence mapping acquisition (Map 2 (Table 3.6), 28x8 points of 250µm) in the column area. (B) Measured area with fluorescence maps of iron Kα (Fe), copper Kα (Cu), lead Lα (Pb) and mercury Lα (Hg).

A second XRF map around the vertical column was made, and from this, the order in which the color was stacked in this place can be also guessed. Figure 3.40 shows the fluorescence map

of the chemical elements composing the column (Fe, Cu, Pb and Hg).

The pigments do not appear to overlap in the column area. Iron and mercury are both presents in the dark red pigment while a slight contrast is found on lead (no lead-based phase was identified by XRD) in the blue area. Copper is present in both blue and green areas, which is not surprising as we identified the phases such as moolooite and atacamite in the green. Even if we did not perform any XRD measurement in the blue part, most probably, cuprorivaite was used.

The presence of an underdrawing is difficult to assess, even if a small contrast with iron can be seen over the green part, matching copper signal.

5.2.4 PAP-7 – Writings

The analysis of the color on this fragment was targeting the red ink. Compared to the three previous fragments, this one is a fragment of written papyrus.

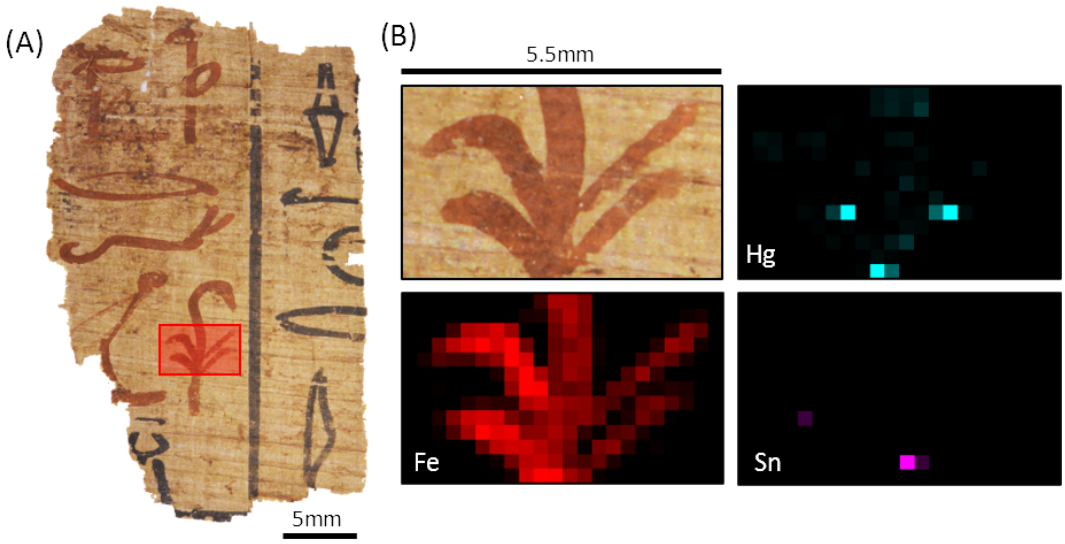

Figure 3.41: (A) PAP-7 fluorescence mapping acquisition on "wheat" hieroglyph area. (B) Fluorescence maps of mercury Lα (Hg), iron Kα (Fe), and tin Kα (Sn).

The fluorescence map presented in the figure (Figure 3.41) is centered on the lower part of the hieroglyph that designates "wheat". The hieroglyph resembles a wheat plant with a stem, lower leaves, and an ear of wheat bent on the top. Lucas [97] writes that the red ink was used at the beginning of a subject or for the division of certain sentences.

The map reveals the presence of iron in the red ink, from which the origin is hematite, identified by XRD. Several grains rich in tin and mercury were also found. Their presence does seem to correlate with the presence of the red ink. At this stage, it is hard to explain their presence since we do not have any information regarding their structure. It would be valuable to evaluate their size and their disposition (embedded in the fiber, ink, or just laid on the surface) to conclude on their origin.

In addition to hematite, the phase identification revealed the presence of syngenite, gypsum, weddellite, and whewellite in the red ink. We performed a Rietveld refinement to quantify the relative concentration of each compound. The refinement is presented in Figure 3.42.

The obtained ratio of each phase will be compared with other red inks or paints in the next part.

5.2.5 The art of papyrus painting

Our measurement of these four papyrus fragments leads us to conclude on a specific pictural technique used by scribes in ancient Egypt. From the preparatory drawings to the color

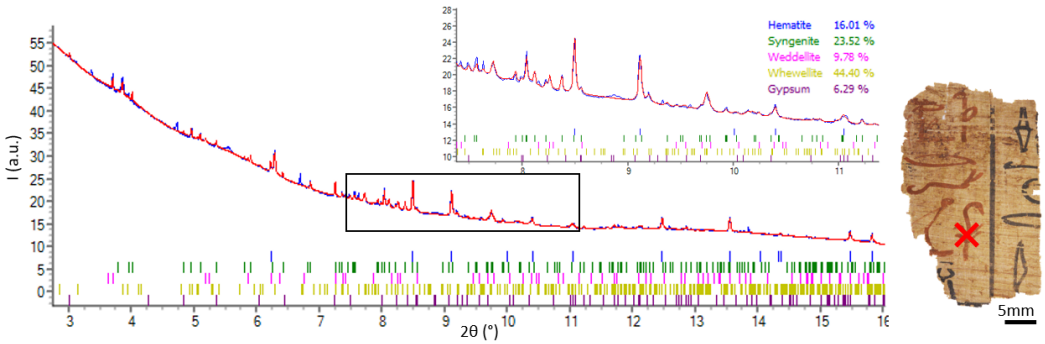

Figure 3.42: Rietveld refinement of XRD data taken on the red ink from papyrus fragment PAP-7 (Red = Fit, Blue = Observed, Rwp = 1.47, Rexp = 20.87, Rp = 1.17).

superposition choice and the different imperfections in the drawing, we can draw three conclusions.

The first conclusion is the use of a preparatory drawing as a first draft for scribes. In certainly two of the three painted papyrus, we identified that a light red paint was used as a draft. The identification was first made with XRF. Then by taking a closer look at the optical images, we managed to observe details that attest of their presence. Figure 3.43 shows a series of light red features that are part of these preparatory drawings.

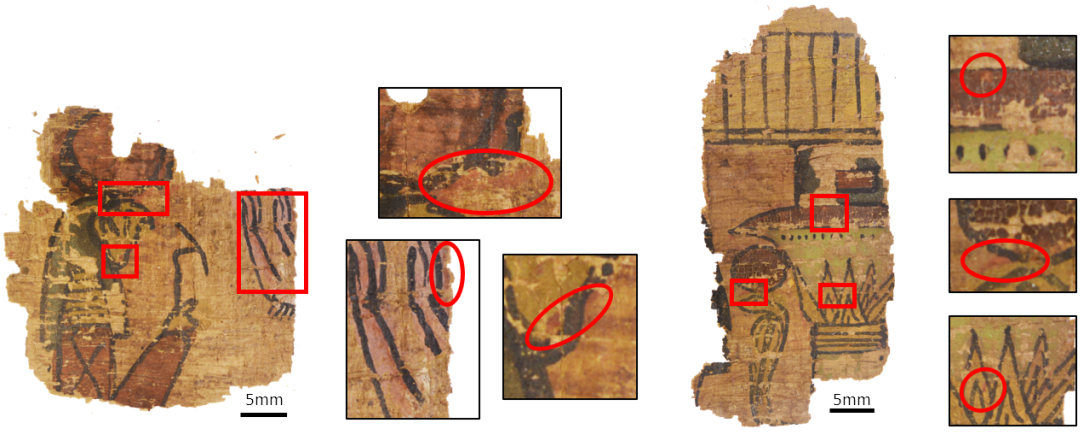

Figure 3.43: Optical observation of the visible parts of the preparatory drawings on papyrus fragments PAP-6 and PAP-12.

The second conclusion we can make regards the layer superposition. From all the measurements, we can conclude that the layer superposition is always starting from the lightest colors to the darkest ones. Yellow is the first, then green, blue, or dark red, and at the end the black contour. This painting technique is understandable since dark colors tend to be noticeable through lighter.

The last conclusion is about the scribes that painted the papyrus. The fragment PAP-6 tells us that there were most probably two diverging opinions on whether how to paint Re's face. The final contour shows quite different shapes than what has been drafted in the first place. In between the first draft and the deposition of the black contour, pigments were applied, probably partially hiding the red underdrawing. The scribe who finalizes the drawing may have simply given his own interpretation. The area where it is the most visible is Re's beak, where the first draft displayed a straight shape, when the final beak is curved. This is also seen in the position of Re's eye and the shape of its neck (Figure 3.44).

The scribe that put colors in place may also be different from the two others because he was

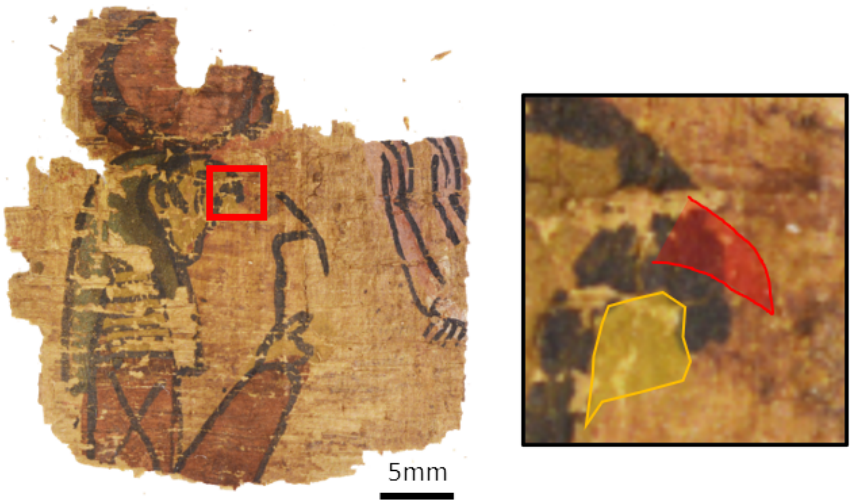

Figure 3.44: Illustration of Re's beak shape and the placement of yellow paint on papyrus fragment PAP-6, compared to the black contour

not respecting the indications given by the red pre-drawing.

This manufacturing technique was already mentioned by Lucas *et al.* [15] and by Etienne *et al.* [67], and briefly described in part 2.1.1. Papyrus manufacturing was a real industry at a certain epoch of ancient Egypt. Being able to observe it with a careful look and deduct these facts is always rewarding.

5.3 Intentional and non-intentional phases

In this part, we will discuss the results color by color. We will try to put in perspective which phases found in the different drawings are present intentionally or non-intentionally. Intentionally means that the measured phase is the one that Egyptian use at that time, while non-intentionally groups the phases that are either degradation phases of intentional phases either pollution phases.

5.3.1 The case of blue

As identified in the previous part, the blue color is exclusively due to the presence of cuprorivaite, also known as Egyptian blue.

Cuprorivaite is present on papyrus fragments PAP-6, PAP-11, and PAP-12, with wollastonite and quartz, known to be a by-product and non-consumed reactive of the synthesis, respectively. The measurements made in the previous part show that most of the time, the diffraction pattern includes cuprorivaite single-crystal contributions. This is due to the cuprorivaite's large grain size large enough compared to the X-ray beam size to scatter the beam as single crystals. This effect makes the Rietveld refinements really difficult and so, no quantitative information can be discussed.

An optical observation shows that the blue pigment has a dark shade. The apparent color is not at all what we expect from the cuprorivaite color. Under the microscope (Figure 3.45) we see that the crystals are appearing with the expected blue color, but the matrix around is dark. This matrix is most probably the rest of the mixture of the paint, including the binder or any additive that would have been present.

This blackening of Egyptian blue paint was already shown by Daniels *et al.* [98] on mummy cases. It was attributed to the browning of the binder, gum arabic. Authors precise that the blackening is even more present due to the transparency of cuprorivaite crystals that accentuate the phenomenon. With that, we can only agree with the authors, but we do not have more proof to confirm binder degradation.

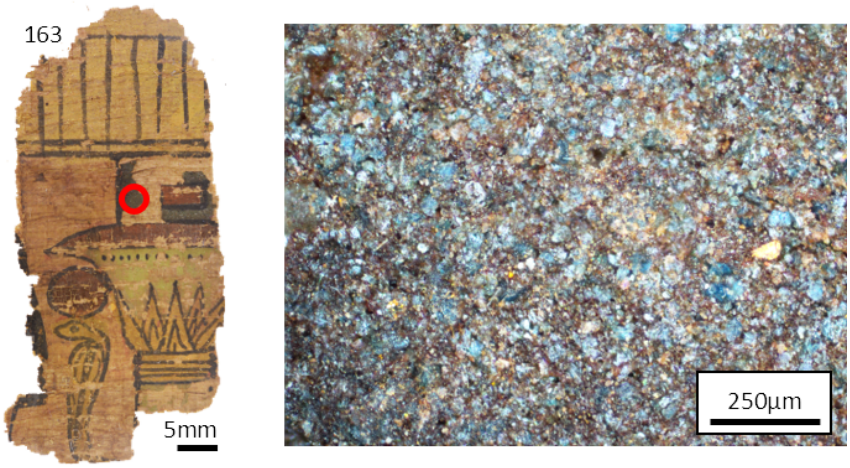

Figure 3.45: Optical microscope image (x20) of papyrus fragment PAP-12 on a cuprorivaite-rich area

In addition, the maps made on samples PAP-6 and PAP-12 revealed the presence of lead. This contrast is seen only with the presence of the blue pigment, and not with any other pigment. The lead source was not identified by XRD as coming from a mineral. The addition of a lead-based compound (litharge, lead white) in the binder to help the drying of the painting was reported for later periods by Sabin *et al.* [99] and extensively discussed by Cotte *et al.* [100]. In a recent study, Christiansen *et al.* [54] have shown the presence of lead compounds in the ink accounted as drying agents on papyrus from the 100 to 200 CE period. This could also account for the blackening of the area observed around cuprorivaite. Additional experiments using for example IR spectroscopy would be necessary to check for the validity of such possibility in the papyrus of the Champollion collection. Since the lead is not even present in the green pigment manufactured by the use malachite ore, it leads us to conclude that the lead may be coming from the manufacturing process.

Finally, the fact that this blackening happens only around cuprorivaite may be related to the properties of this compound, in particular the size of the crystals, with the necessity to use a larger amount of binder, or one with a different recipe to help the drying process.

5.3.2 The case of red

Red pigments are present on papyrus fragments PAP-6, PAP-7, and PAP-12. We will discuss two types of red pigments, light red and dark red. It will be noted that the red pigment from papyrus fragment PAP-7 will correspond to a pigment used for writing while the two others will be discussed as used in paint. Even if we make this difference, there is no evidence of whether or not it exists in reality.

The phase identification shows the presence of hematite (α-Fe_2O_3), syngenite ($K_2Ca(SO_4)_2,(H_2O)$), and gypsum ($CaSO_4$). In our case, we can assume that the absence of both clay and silica refutes the assumption that the present pigment is raw red ochre but rather coming from a pure hematite ore or a purified red ochre.

From the three refinements made on the three samples (Figure 3.42 for PAP-7, Figure 3.37 for PAP-12, and Figure 3.22 for PAP-6), we can deduce that in all cases there is the presence of hematite with gypsum and syngenite.

The presence of syngenite ($K_2Ca(SO_4)_2,(H_2O)$) seems to be in relation to a salt-rich environment. It was found as a degradation phase on paintings from Jan Davidszoon de Heem by Vanmeert *et al.* [101]. The authors describe the formation of this hydrated potassium calcium sulfate salt by the action of sulfates and potassium salts from the internal of the painting or

restoration agent, on gypsum. The presence of both gypsum and syngenite indicates that, in our case, this reaction could be conceivable.

The following chart (Figure 3.46) compares the concentration of each mineral found in the red parts excluding the weddellite and the whewellite, which we assumed to be related to the support. The first result is that the sum of the concentration of hematite, syngenite, and gypsum is constant. This explains the fact that the three painted or written areas present roughly the same concentration of mineral elements compared to the support. On the other hand, the three fragments have three different concentrations of hematite which are, as the sum shows, exactly compensated by the sum of gypsum and syngenite. Two hypotheses arise from these results; either the hematite catalyzes the degradation reaction of gypsum in syngenite and explains the syngenite concentrations or the syngenite concentration differences compared to the consistency of gypsum concentrations is due to the difference in papyrus ages or to salt exposure.

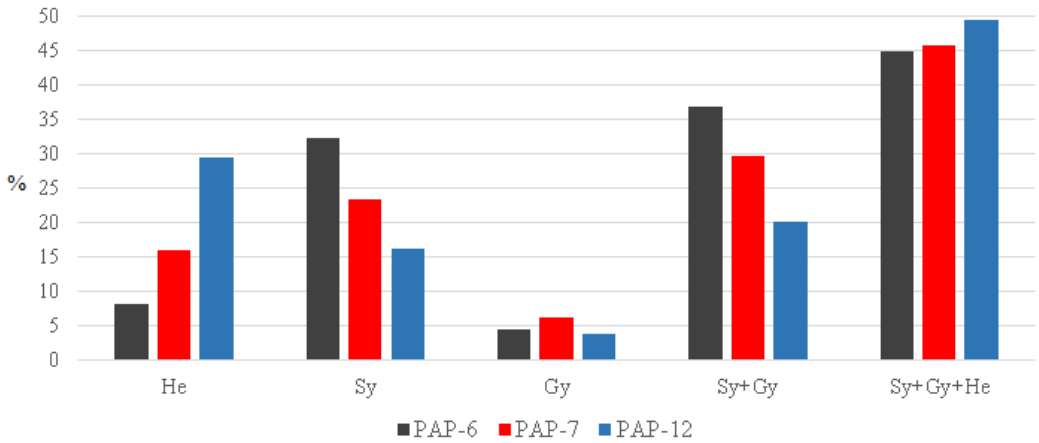

Figure 3.46: Chart that represents the percentage of mineral elements present in the ink or paints from the three papyrus fragments PAP-6, PAP-7, and PAP-12. He=Hematite, Sy=Syngenite, Gy=Gypsum

The main conclusion of these results is as follows. Considering the presence of gypsum and syngenite, combined with hematite, it is highly probable that the Egyptians who manufactured these pigment mixtures were using gypsum and hematite in different concentrations to match different shades. Because we analyzed only three points, there is no evidence of specific use of one mix or the other to a specific use (ink or paint). It still remains to correlate the concentrations of hematite, syngenite, and gypsum to the color shade by measuring a broader range of fragments, taking into account that the shade could change with the addition of other elements either in a weak concentration or in an amorphous state.

Going further on this point, it could be interesting to obtain better data measured from the red ink from the underdrawings of more papyrus to compare it to our results. An extensive study targeted on the red inks and paint could be done on those papyrus but was not part of this project.

On another note, we saw the presence of mercury in the red area by XRF. The signal was very localized for PAP-7 while being more evenly spread for PAP-6 and PAP-12. We were not able to isolate any crystalline phase from XRD phase identification. This could be explained on PAP-6 and PAP-12 because of either the Hg-based phase quantity that was not sufficient to be above the noise level, either the phase is amorphous and so not identifiable by our XRD process. On PAP-7 the XRD data were not recorded from a specific mercury-rich part of the sample, and we can suppose that a careful measurement on a precisely located area may allow us to get a diffraction signal from this mercury-rich area. The presence of mercury remains to be explained, but we can suggest that its presence may be coming from traces of minerals found in hematite ore [102].

5.3.3 The case of yellow

The yellow color is present on the three painted papyrus fragments: papyrus fragments PAP-6, PAP-11, and PAP-12. It was identified as a combination of orpiment and realgar.

Orpiment is quite often found as a yellow pigment on funerary papyrus. On the other hand, realgar is naturally red and is frequently found in a small amount with orpiment [57] [103], which is our case. Realgar often degrades upon light exposure into its isomer pararealgar, which changes the red-orange color to a more yellow color [104] but it was not identified in our case.

The Rietveld refinements of the yellow pigment (Figure 3.21 for PAP-6, Figure 3.31 for PAP-11, Figure 3.35 for PAP-12) indicate that the relative concentration of realgar and orpiment is not constant. Indeed, the orpiment to realgar ratio was found to be 49%, 46% and 69% for PAP-6, PAP-11 and PAP-12, respectively. When looking at each yellow area more closely with an optical microscope, we could see that the distribution of realgar, appearing as red dots, is not even.

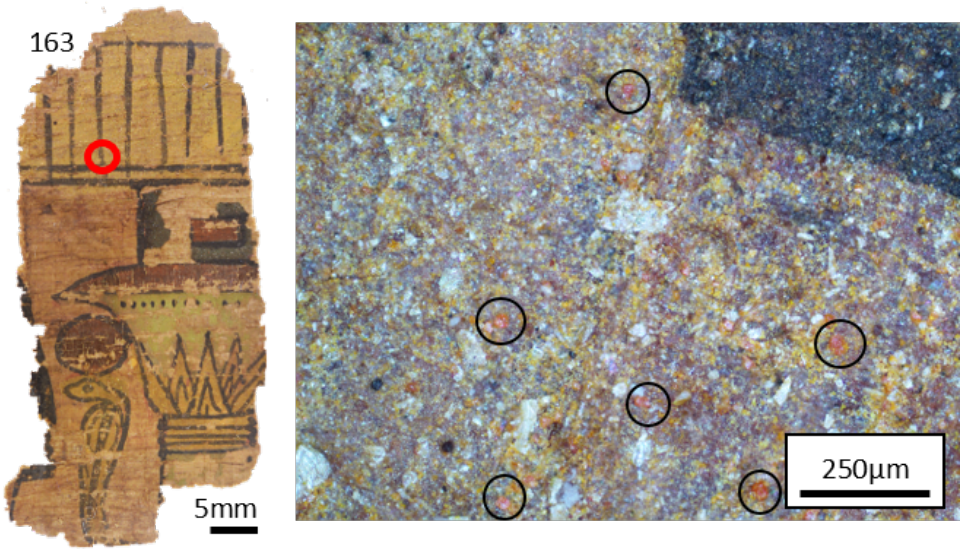

Figure 3.47: Optical microscope image (x20) of papyrus fragment PAP-12 on a yellow area. Black circles indicate the area of realgar grains.

This means that on the same sample we can obtain extremely different concentrations from one measurement point to the other. Comparison of the orpiment to realgar ratio between samples is then meaningless in our case, as only one measurement point was recorded in each case.

The last crystalline phase found in the yellow parts (also identified on green and blue parts in PAP-11 and PAP-12 but probably because of the presence of the yellow pigment under the blue pigment layer) is aphthitalite ($K_3Na(SO_4)_2$). This phase is not documented with papyrus studies but is usually mentioned as a result of salt weathering on walls and stone sculptures [105]. The authors explain that salts halite (NaCl), niter (KNO3), and sylvite (KCl) can crystallize at the surface of walls of rocks in caves because of percolating water and runoffs.

In our case, we can make two hypotheses. The presence of aphthitalite can be considered as the result of the degradation of some compounds present in the paint because of the exposition to a salt-rich environment. The presence of this sulfate salt could also be explained either by a voluntary addition while manufacturing the ink or the presence of such crystal salts during the collection of the coloring agent by the Egyptians.

5.3.4 The case of white

Lead white (mix of cerusite and hydrocerussite) was used extensively in the Antiquity for cosmetics and pigments. It was described by Pliny as made from metallic lead shaving that

dissolves upon the action of strong vinegar. After being pounded and sifted it was dried in sun to obtain the final product [23].

The XRF mapping of the deceased arm (PAP-6, Figure 3.28) revealed a lead-rich area. With this sample, the phase identification of this lead-based white pigment showed the presence of a non-expected lead-based pigment, different from lead white: potassium lead chloride (KPb_2Cl_5). The presence of this phase in the papyrus from the Champollion collection was confirmed with an analysis of papyrus fragment PAP-10. This mineral was recently discovered and identified as a naturally occurring mineral called challacolloite in a silver mine in the Atacama desert, northern Chile [106]. This compound was found in very few occurrences in paintings and on papyrus fragments:

- Papyrus fragments from Amenemhet, middle Ptolemaic period (around 305 B.C.), Di Stefano *et al.* [57],
- Egyptian papyrus from the Roman period from Tebtunis (100 to 200 C.E.), Christiansen *et al.* [54],
- Roman–Egyptian mummy portraits from Tebtunis on wood (100 to 200 C.E.), Salvant *et al.* [107].

An explanation of the presence of potassium lead chloride in ancient artifacts was given by Bezur *et al.* [108]. Authors studied a terracotta relief of *Virgin and the Child* by Michele da Firrenze and discovered challacolloite at its surface. They wrote that potassium lead chloride was formed by the reaction of lead white with potassium carbonate forming potassium lead carbonate, which is then transformed into potassium lead chloride in presence of hydrochloric acid.

Since no lead white traces were found in our case, we could not rule out the possibility for the ancient Egyptian to have manufactured the pigment. Egyptians were mastering lead chemistry and it would have been reasonably possible for them to produce such a compound. To verify this hypothesis, it was necessary to try to reproduce the compound.

The project of reproducing the pigment was carried out by Thomas Lesueur, a third-year bachelor student. Several authors mention reactions to produce KPb_2Cl_5, either by mixing cotunnite ($PbCl_2$) and sylvite (KCl) in solution or by mixing and heating both powders. The first attempt was to follow the guidelines described by Jansen *et al.* [109] to produce potassium lead chloride. It starts with the products cotunnite ($PbCl_2$) and sylvite (KCl) with a molecular ratio of 1 to 30 dissolved in water. The expected reaction is described by Bezur *et al.* [108] :

$$2PbCl_2 + KCl \leftrightarrow KPb_2Cl_5 \tag{3.6}$$

We manipulated different n($PbCl_2$)/n(KCl) ratios to obtain KPb_2Cl_5. Each compound formed has been identified by XRD on a D8 Endeavor Bruker diffractometer (Institut Néel) and then observed using scanning electron microscopy. By moving the equilibrium to a higher concentration of KCl, KPb_2Cl_5 was obtained with some leftover $PbCl_2$.

Figure 3.48 shows the microstructure of potassium lead chloride crystals from both papyrus fragments and the reproduction. The microstructures are not much different, and it is complicated to go further. The synthesis process would require more investigations.

Nevertheless, since the presence of other potassium-based minerals (aphthitalite ($K_3Na(SO_4)_2$) and syngenite ($K_2Ca(SO_4)_2$,(H_2O))) have been attested on the yellow and red parts, respectively, of the same fragment, we tend to conclude that the challacolloite phase identified as white pigment results from the degradation of lead white with a complete transformation, and certainly happened through contact with a potassium-based reagent which remains to identified.

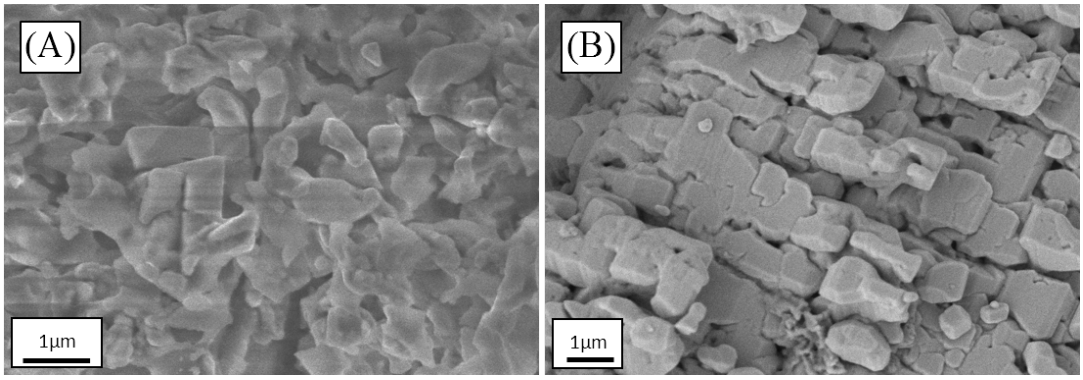

Figure 3.48: Scanning electron microscopy images in SE2 mode. (A) Papyrus fragment PAP-10 surface on white pigment area. (B) Image of a KPb_2Cl5 crystals

5.3.5 The case of green

For the green color (PAP-11 and PAP-12), three main phases were identified, moolooite ($Cu(C_2O_4)$,$0.4H_2O$), atacamite ($Cu_2Cl(OH)_3$) and in two cases lavendulan ($NaCaCu_5(AsO_4)_4Cl$, $5H_2O$).

Moolooite is a naturally hydrated copper oxalate that was first found in Western Australia in a sulfide-bearing quartz outcrop [110]. It was associated with the reaction of copper sulfides with bird guano-derived solutions containing phosphates and oxalates. Authors write that moolooite was found in presence of other minerals such as atacamite, gypsum, and whewellite, minerals that we found also on our papyrus. No explanations concerning potential copper reactive or degradation reactions are given.

However, the mineral was found to be a degradation product of malachite ($Cu_2CO_3(OH)_2$) on a 19th-century wallpaper [111]. The authors also report the presence of weddellite, evidence of fungal activity, which is also present naturally in the papyrus. Fungi release oxalic acid, which transforms to weddellite by reaction with calcium naturally present in the plant. Once the calcium carbonate is consumed, the oxalic acid degrades the pigments. They propose a series of reactions that transforms malachite into moolooite with two different paths Figure 3.49.

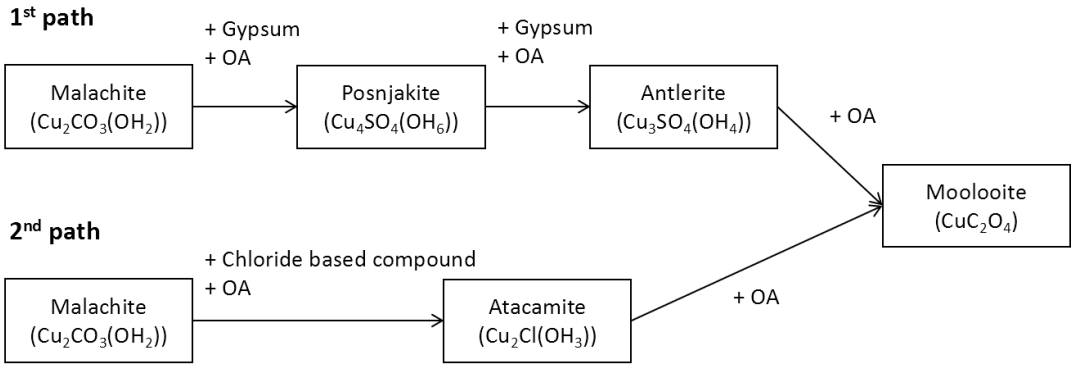

Figure 3.49: Degradation reaction paths from malachite to moolooite according to Castro et al. *[82] (OA=Oxalic Acid).*

The first path corresponds to the degradation in a sulfate-rich environment due to the presence of gypsum. This series of degradation reactions involve the formation of posnjakite ($Cu_4SO_4(OH_6)$) and antlerite ($Cu_3SO_4(OH_4)$). None of those minerals were identified, making this reaction chain less probable in our case.

However, if the chloride concentration is higher, a second transformation path would be preferred. This involves atacamite as a degradation product from the first reaction between oxalic

acid, malachite, and a chloride-rich reactive. Since evidence of degradation from potassium and chloride have been revealed in the previous subpart on papyrus fragment PAP-6, and that atacamite was identified in the green part of that fragment, there is a high probability of this chain of reaction happening. The last unknown remains the nature and structure of the chloride source. This source was not identified with XRD because of either total absence or a non-crystalline structure.

The last uncommon identified phase to be discussed in green parts is lavendulan ($NaCaCu_5(AsO_4)_4Cl$, $5H_2O$). To the best of our knowledge, this mineral has never been found on a papyrus fragment so far. The identification of this mineral with XRD relies mainly on a single wide peak at d=9.9Å (I=100) and a series of low intensities peaks (I<16) at higher angles. It was identified on a multi-polychrome statue by Li *et al.* [112]. Authors concluded that lavendulan was formed by degradation of Emerald green ($Cu(C_2H_3O_2)_2$,$3Cu(AsO_2)_2$) from environmental elements. They point out the possibility of Emerald green forming acetic acid with arsenite ($HAsO_2$) that transforms to arsenate ions ($(AsO_4)^{3-}$) which then react with Cu^{2+}, Na^+, Ca^{2+}, and Cl^- to form lavendulan.

In our case, the chemical nature of lavendulan ($NaCaCu_5(AsO_4)_4Cl$, $5H_2O$) is close to both malachite ($Cu_2CO_3(OH)_2$), atacamite ($Cu_2Cl(OH)_3$), and orpiment (As_2S_3) or realgar (As_4S_4). A hypothesis would be that malachite or atacamite reacted with the yellow underlay of fragment PAP-11 to form lavendulan at the interface. The Rietveld refinements performed on two diffraction patterns, one on the green area of PAP-12 and one on the green part on top of the yellow pigment of PAP-11 are shown in Figure 3.32 and Figure 3.36, respectively. Lavandulan is only present in the second case, in the green area lying on top of the yellow pigment, which tends to confirm our hypothesis. Nevertheless, additional investigations are necessary to detail the exact reaction pathway.

5.4 Conclusion

To summarize we can establish the following table (Table 3.10) correlating colors observed to pigment composition.

Table 3.10: Summary of crystalline phases identified for each point measured by XRD. Weddellite, whewellite have been excluded from this table because it appears that they are always present in a small quantity in any measurement points made. In italic the phases resulting from a degradation effect.

Color	**Phases participating in the color**	**Additional phases**
Red	Hematite (Fe_2O_3)	Gypsum ($CaSO_4$, $2H_2O$) *Syngenite ($K_2Ca(SO_4)_2$, H_2O)*
Yellow	Orpiment (As_2S_3) Realgar (As_4S_4)	*Aphthitalite ($K_3Na(SO_4)_2$)*
Blue	Cuprorivaite ($CaCuSi_4O_{10}$)	Cristobalite (SiO_2) Quartz(SiO_2) Wollastonite($CaSiO_3$)
Green	*Atacamite ($Cu_2Cl(OH)_3$)* *Moolooite ($Cu(C_2O_4)$, $0.5H_2O$)* *Lavendulan ($NaCaCu_5$, $2(AsO_4)$ $4Cl$, $5H_2O$)*	Quartz (SiO_2)
White	*Challacolloite (KPb_2Cl_5)*	/

Although numerous studies were made on Egyptian papyrus, only a few probed the pigments with extensive XRD analysis, pointing out any crystalline phases identifiable in the fragments. XRF is also extremely helpful to map the sample and enabled us to reveal the presence of preparatory drawings in some of them. On the other hand, in some cases, quantitative analysis through Rietveld refinement remains difficult because of the single crystal properties of some pigments.

By using XRD we were able to identify degradation phases such as challacolloite, moolooite, and lavendulan. Most probably, these pigments were originally lead white and malachite, respectively. They suffered from a major degradation effect from potassium and the chloride-based compound which remains to be identified. This degradation phenomenon is also shown by the presence of syngenite, degradation phase of gypsum, and aphthilatite.

Now a new field is opening to try to understand what are the reaction processes behind the formation of these non-intentional phases. Chemical reactions with potential by-products, the effect of humidity, UV-light, or time remain to be explored. To understand further the degradation process, it also envisaged using XRD-CT to probe the depth of the sample to precise the distribution of the different phases along with the layers. If any interactions between the ground, paint layers, and surface exposed to the air appear, we would be able to identify and locate each phase within the layers. This study on Ancient Egyptian colored pigments gives new insights into the nature and the degradation effects on the Ancient Egyptian colors used for painting and writing.

In addition, the presence of malachite as a green pigment and most probably lead white as white pigment seems to indicate a dating of some of the papyrus fragments later than the New Kingdom period. When comparing our results to some recent studies, specifically Di Stefano *et al.* [57], we can put our fragments PAP-6 and PAP-10 in the context of the Ptolemaic period.

Finally, the painting method used for the manufacturing of these papyrus was shown to be divided into three steps, the preparatory drawing with red paint, the colors laid down from light to dark, and at the end, the black contour. This confirms the organization around funerary papyrus painting in ancient Egypt. We can envisage continuing this study with other fragments from the Champollion collection to continue exploring degradation phases, and pictural techniques.

6 Analysis of black pigment on papyrus from Champollion collection

6.1 The fragments

Ten papyrus fragments were selected from the Champollion collection to study the black pigments. These fragments, from a couple of hundreds of micrometers to few centimeters in size, show one or more black ink lines at their surface (Figure 3.50). The selection of the fragment was based on the ability to obtain easily a contrast with analysis based on scanning. Thus PAP-1, PAP-3, and PAP-4 were technically more suitable because of the clear stripes that are "in theory" easier to isolate in a scan line.

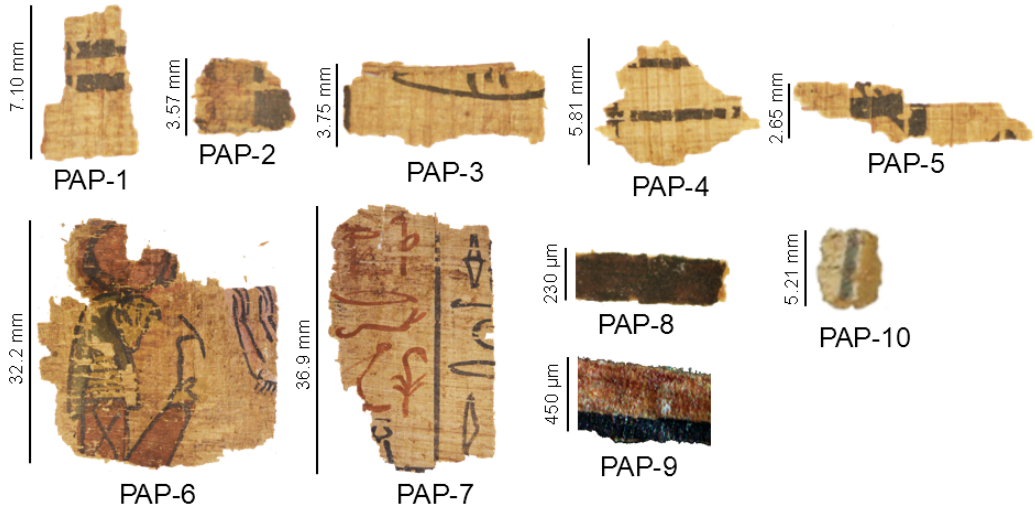

Figure 3.50: Papyrus fragments from the Champollion collection used to investigate the black pigments. The pictures were taken with a Nikon D3200 camera equipped with a 50-200 mm lens (ISO-200, f/8, exposure time 1/160 sec, focal length 102 mm, dimensions 6016x4000 pixels, and resolution 300 dpi).

In the case of black pigments, assumed to be non-crystalline, it is necessary to use several analytical techniques to better characterize them as we saw in chapter 1. All the analyses performed on each sample are summarized in Table 3.11.

Table 3.11: Summary of the analyses of black pigments performed on each of the ten fragments (denoted PAP-1 to PAP-10) of the Champollion collection.

Sample	SEM	EDX	Raman	XRF	XRD	XRD-CT	XRF-CT
PAP-1	x	x	x	x	x		
PAP-2	x		x	x	x		
PAP-3	x	x	x	x	x		
PAP-4	x			x	x		
PAP-5	x			x	x		
PAP-6			x	x	x		
PAP-7	x			x	x		

PAP-8	x	x				x	x
PAP-9	x	x				x	x
PAP-10			x				

6.2 Identification of the black pigment

6.2.1 Raman spectroscopy

To start with we performed Raman spectroscopy targeting first the signal of the black pigment and potentially any joint compounds that could be present.

The Raman spectrum collected on PAP-6 is shown in Figure 3.51. Two bands pointing at 1338 cm^{-1} and 1593 cm^{-1} are present in the Raman spectrum. These bands can be immediately correlated to the ink, as blank papyrus does not show any particular Raman signal in the relevant wavenumber domain (not shown). Carbonaceous materials show preeminent features in the 1000-1800 cm^{-1} region depending on their degree of disorder and crystallinity [113]. In crystalline graphite, a narrow band around 1580 cm^{-1}, the G band, corresponds to the in-plane stretching vibrational mode of sp^2 carbons in aromatic rings, with E_{2g} symmetry [114]. When the disorder of sp^2 carbons increases, the G band broadens, and new bands, called D bands, appear, resulting in a larger band centered at ~1340 cm^{-1}. Both G and D bands were identified on the Raman spectra collected on the black ink of our papyrus fragments, in agreement with the use of a carbon-based pigment in an amorphous state. This is confirming the carbon-based nature of black pigments of the inks found on Champollion papyrus collection.

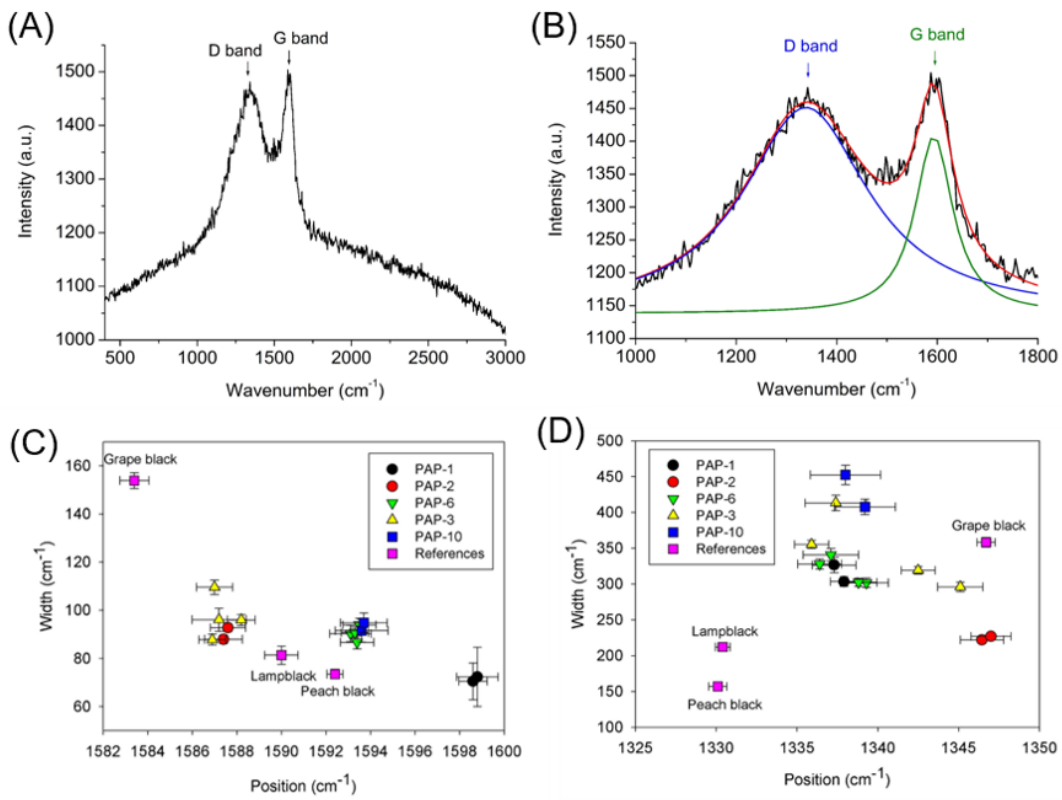

Figure 3.51: (A) Raman spectrum recorded on the black scepter, of god Re from papyrus fragment PAP-6 (B) Fit of the D and G Raman bands of carbon using a 2-band model, (C) Width as a function of position for the G band, (D) Width as a function of position for the D band.

It has been shown that spectral parameters such as the position of the G and D bands, their width, and intensities can be used to discriminate between several kinds of carbon-based pigments [17], [115] and to retrieve the age of the writings [89] on ancient papyrus. All the spectra collected on the carbon-based pigments of our papyrus fragments were fitted using a 2-band model. The fit obtained from a spectrum collected on the black scepter of god Re (PAP-6) is shown in Figure 3.51B.

Assessment of the background proved to be difficult, with a strong and variable fluorescence arising from the papyrus support.

Because of this, intensities of the G and D bands, poorly trustable, were not extracted. The widths of G and D bands as a function of their respective positions are plotted in Figure 3.51C and Figure 3.51D, respectively. Data points corresponding to three of our carbon-based reference pigments (peach black, grape black, and lampblack) are also shown. Data points retrieved from the same papyrus fragment tend to form homogeneous groups when using the spectral parameters of the G band (Figure 3.51C). This clustering could be a way to identify which fragment from the Champollion collection may belong to the same papyrus. On the other hand, comparison to the reference data points does not bring any further information to clarify the origin of the carbon-based pigment. Matching the reference data to the papyrus surface data requires more investigations. Concerning the spectral parameters of the D band, higher dispersion of the data is observed (Figure 3.51D), the fit of this broader band is possibly more influenced by any background fluctuation.

6.2.2 Morphology of black pigment

The morphology of the carbon-based pigment was investigated using SEM, and a picture obtained for PAP-2 is shown in Figure 3.52A.

By imaging the surface of all mentioned papyrus fragments with SEM, the same overall morphology for the carbon-based pigment has been found for all the fragments: spheroidal particles of about 85 nm (+/- 10nm) in diameter (Figure 3.52A). This value was obtained by measuring the diameter of a set of 50 randomly chosen particles.

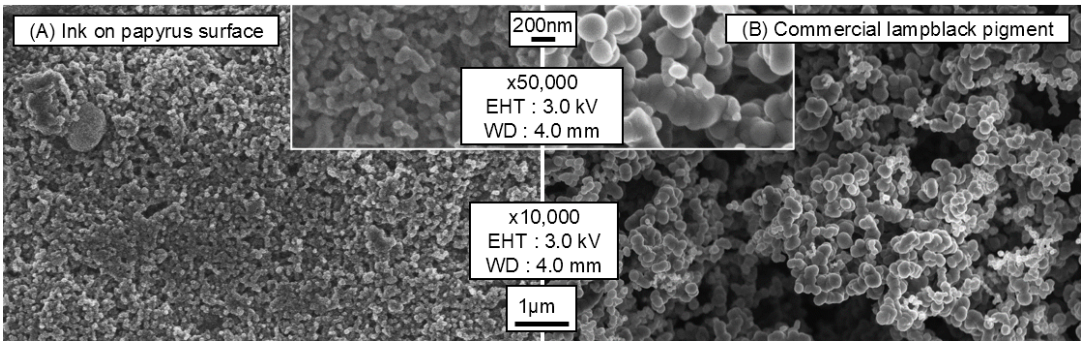

Figure 3.52: SEM observations of (A) Ink at the surface of PAP-1, (B) Kremer pigmente lampblack pigment.

The SEM pictures obtained from six of our reference pigments shown in the first chapter are reproduced in Figure 3.53A to F. All of them are showing a specific morphology that presents angular edges, holes, and irregular grains. Lampblack is the seventh standard shown in figure Figure 3.52B. Compared to the six others, lampblack is characterized by regular spherical particles of about 170 nm, as expected for such a kind of carbon-based pigment [1], [116]. We can not that this morphology is common to the flame carbons (lampblack or soot).

Knowing that the size of flame carbon particles may vary from 80 to 200 nm [1], [116], the carbon-based pigment found in the ink of ancient papyrus from the Champollion collection is unambiguously attributed to a flame carbon. However, since the particle size and the distribution

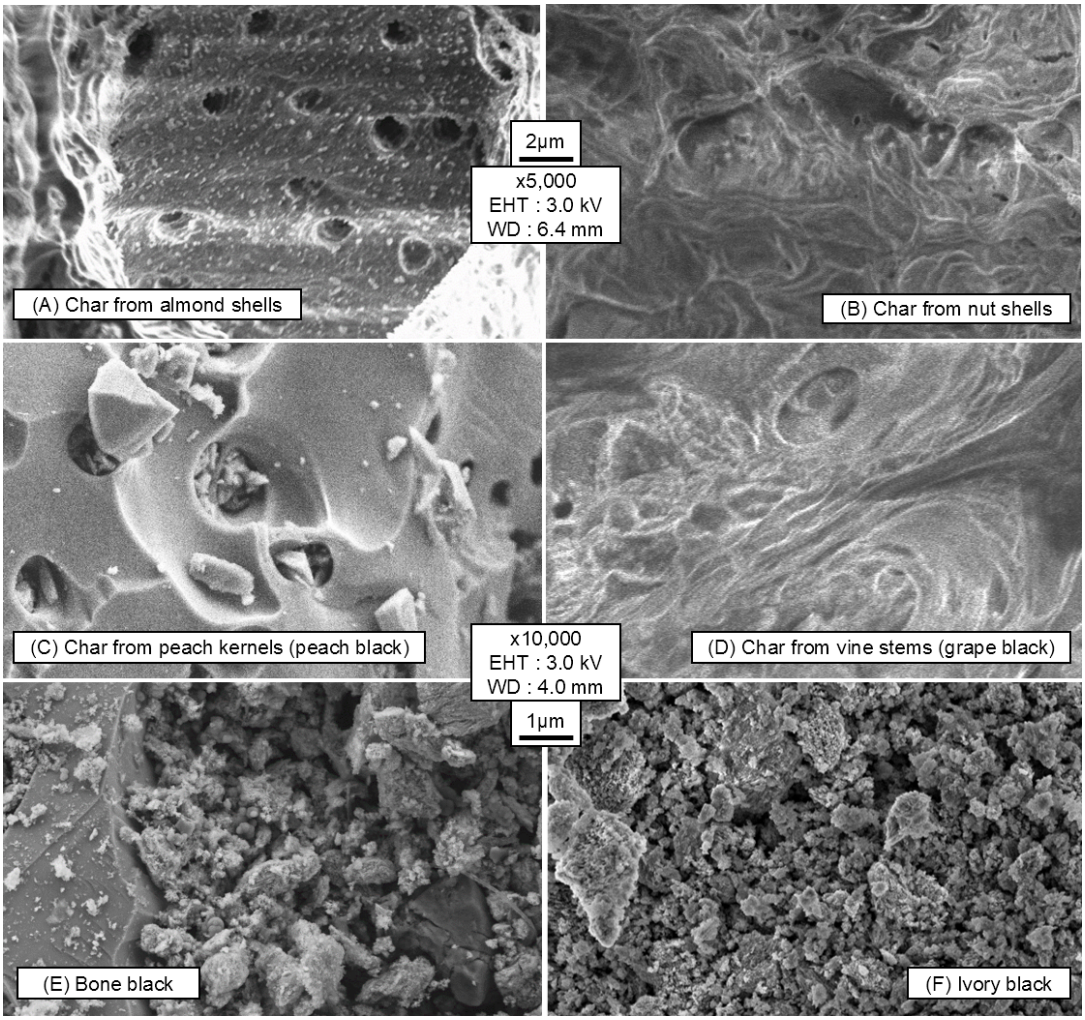

Figure 3.53: SEM observation of six carbon pigment references.

are not the same between the papyrus and the standard, the reason for the size difference remains to be explained. The standard lampblack was produced through a confidential industrial process. On the other hand, Egyptian flame carbon is more likely coming from burning animal fat or oil. Further study would imply other references from lampblacks and soot produced in different ways to look for closer similarities.

6.3 Elemental and structural analysis of the ink

The ink area was first probed using EDX analysis. Two examples of measurements made on PAP-1 are shown in Figure 3.54. The elements found at the surface of the papyrus covered by ink are sodium (Na), magnesium (Mg), aluminum (Al), silicon (Si), sulfur (S), and potassium (K). These elements are also found in the raw papyrus. On the overall fragments measured, no major variation of these values was observed. However, some regions present heterogeneities as previously found when analyzing the surface of the papyrus support by SEM-EDX (see subsection 4.2). For example, a tin cluster can be seen at the surface of PAP-1 in the ink area (Figure 3.54B), most probably resulting from contamination from the environment or storing process.

The ink deposited on Champollion papyrus was further investigated using XRF, and for each fragment, the elemental composition of the ink was compared to the one obtained from the papyrus support (Table 3.12). We mainly focused on three elements, copper, iron, and lead, as

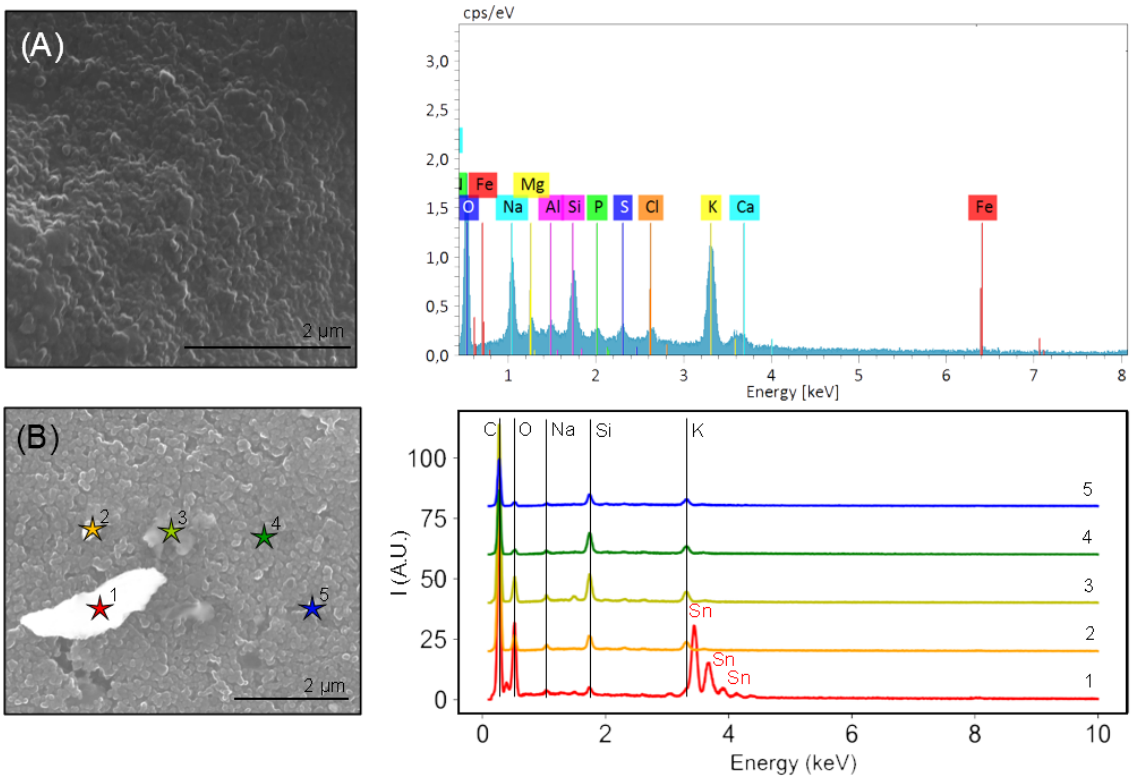

Figure 3.54: (A) EDX spectra recorded on a map at the surface of PAP-1, with corresponding SEM secondary electrons image (20kV, WD=8.2mm) (B) EDX spectra recorded at five different positions at the surface of PAP-1, with corresponding SEM backscattering image (20kV, WD=8.2mm) in the insert. A Sn cluster was identified.

these have been reported by several authors in earlier studies [81], [28], [88], [8], [27], [3]. No contrast between the ink and the blank papyrus was revealed when using copper as a discriminating element. On the other hand, a larger amount of lead was found in the ink of PAP-6, and PAP-7 (Table 3.12), and indeed for these two fragments, a contrast is visible on corresponding chemical maps (Figure 3.55AB).

Table 3.12: Elemental composition obtained from XRF analyses. For each fragment, several data points (the number of points is indicated in the third column) were collected on both ink and non-ink areas. The resulting values correspond to the average over the number of measured points, with the sum of the eight elements normalized to 100. Because of both detector setup and absorption from the air, only the elements with Z>18 were accessible. The energy calibration was achieved by collecting XRF data from iron, copper, silver, molybdenum, and lead foils and the processed using PyMCA software.

Sample	**Position**	**No. points**	**K**	**Ca**	**Mn**	**Fe**	**Cu**	**Zn**	**Pb**	**Sr**
PAP-1	Ink	4	14.7 (2.1)	14.6 (1.5)	7.6 (0.9)	32.1 (5.9)	6.1 (3.3)	7.1 (2.3)	10.5 (0.9)	7.4 (0.6)
	No-ink	4	19.2 (1.5)	16.7 (2.0)	8.2 (0.6)	31.7 (4.3)	3.6 (0.2)	4.8 (0.6)	7.9 (1.1)	7.7 (1.3)
	Ratio		0.92	1.05	1.11	1.21	2.01	1.76	1.59	1.15

PAP-2	Ink	7	8.2 (0.9)	6.2 (1.3)	3.8 (0.6)	58.7 (5.3)	5.9 (1.4)	3.8 (0.5)	7.9 (1.8)	5.5 (1.5)
	No-ink	10	6.2 (0.4)	4.3 (0.5)	3.2 (0.3)	67.8 (21.7)	4.6 (1.6)	3.3 (0.4)	6.4 (0.7)	4.2 (0.4)
	Ratio		1.14	1.24	1.01	0.75	1.10	0.98	1.07	1.14
PAP-3	Ink	4	12.4 (0.9)	17.3 (1.6)	6.7 (0.2)	31.1 (5.0)	4.7 (1.4)	3.3 (0.6)	11.0 (1.7)	13.6 (3.8)
	No-ink	3	9.6 (2.9)	9.5 (4.1)	4.4 (1.6)	47.4 (13.8)	4.8 (1.8)	2.5 (0.5)	14.7 (3.0)	7.1 (3.3)
	Ratio		1.24	1.76	1.47	0.63	0.93	1.27	0.72	1.86
PAP-4	Ink	4	13.5 (1.1)	12.9 (2.2)	12.5 (1.2)	38.0 (3.7)	3.8 (0.3)	3.5 (0.6)	7.2 (2.9)	8.7 (1.1)
	No-ink	7	13.1 (1.0)	13.6 (2.1)	13.2 (1.6)	35.4 (6.4)	4.9 (0.6)	3.9 (0.7)	7.3 (1.0)	8.6 (2.0)
	Ratio		1.12	1.03	1.02	1.15	0.82	0.96	1.06	1.08
PAP-5	Ink	5	14.6 (2.5)	13.0 (3.5)	8.0 (1.5)	43.9 (11.5)	4.8 (0.9)	5.0 (3.2)	3.0 (0.7)	7.7 (2.2)
	No-ink	7	13 (2.8)	12.8 (3.2)	7.4 (0.82)	41.0 (7.0)	3.0 (0.5)	10.4 (7.5)	4.2 (1.2)	8.3 (3.4)
	Ratio		0.76	0.70	0.74	0.73	1.10	0.33	0.48	0.63
PAP-6	Ink	22			1.0 (0.1)	12.0 (4.2)	5.2 (2.0)	0.5 (0.1)	78.8 (33.5)	2.5 (0.3)
	No-ink	55			1.3 (0.2)	16.1 (6.3)	5.8 (2.4)	0.6 (0.1)	72.9 (22.5)	3.2 (0.5)
	Ratio				1.08	1.08	1.30	1.26	1.57	1.11
PAP-7	Ink	18			8.1 (0.9)	44.8 (18.3)	7.6 (4.1)	3 (0.8)	24.5 (7.6)	11.9 (3.0)
	No-ink	24			14.5 (2.7)	40.9 (12.7)	6.0 (2.1)	5.0 (1.2)	13.1 (3.9)	20.4 (5.6)
	Ratio				1.14	2.25	2.59	1.25	3.84	1.20
PAP-8	Ink	439	12.5 (6.6)	9.8 (6.8)	5.1 (5.6)	25.3 (13.0)	4.2 (4.9)	3.2 (4.3)	17.3 (17.1)	22.5 (20.8)
	No-ink	787	26.1 (12.7)	9.5 (11.8)	7.4 (11.2)	7.0 (10.5)	5.9 (8.6)	6.5 (9.8)	19.9 (20.4)	17.8 (39.5)
	Ratio		1.07	2.31	1.54	8.06	1.61	1.09	1.94	2.83
PAP-9	Ink	475	14.4 (12.5)	20.7 (23.8)	4.8 (6.5)	20.0 (24.8)	7.0 (12.2)	5.4 (10.2)	23.6 (18.5)	4.1 (6.8)

	No-ink	5083	19.4 (22.0)	15.4 (23.2)	6.5 (13.2)	28.0 (139.4)	7.1 (16.5)	9.3 (18.3)	10.2 (16.4)	4.1 (9.8)
	Ratio		1.20	2.18	1.19	1.16	1.60	0.94	3.76	1.61

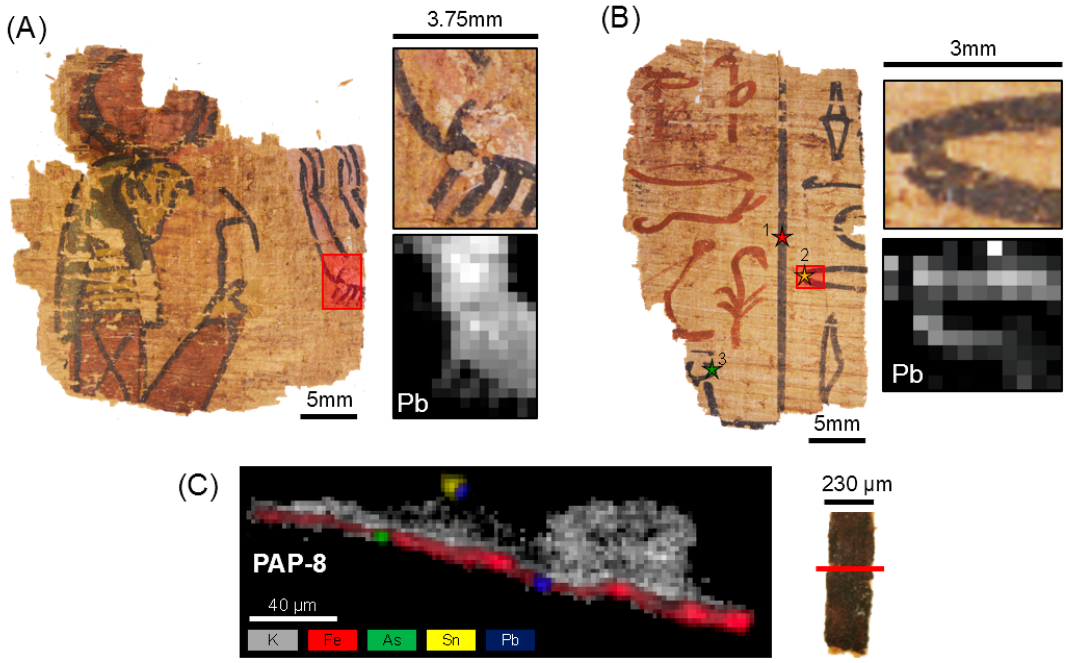

Figure 3.55: XRF investigation of PAP-6 and PAP-7. (A) An XRF map was retrieved from the deceased's arm of PAP-6. The lead-based contrast on the four stripes of the garment is most probably related to the presence of lead white used to color the white cloth and the skin. (B) The XRF mapping carried out on the 'mouth' hieroglyph of PAP-7 shows a lead-based contrast. (C) XRF-CT of PAP-8 fragment, the image is a transverse cut of the fragment and is build by overlapping contributions of elements K, Fe, As, Sn and Pb.

Both the arm garment decoration on PAP-6 and the shape of the mouth hieroglyph of PAP-7 are distinguishable from the surrounding. However, in the case of PAP-6, the contrast is present only in the four black stripes of the garment and does not appear on the black line delimitating the arm. As explained before (see part paragraph 5.2.1.1), we suggest that the lead-based contrast in this specific case is most probably due to the white lead-based paint lying underneath being spread by the black brush stroke that made the decorative stripes. PAP-8 is the only fragment for which a contrast with iron was obtained. The corresponding map, retrieved from XRF-CT, is shown Figure 3.55C and will be discussed later in the manuscript (see part 6.5.5).

Analysis of the XRD data collected on the ink of the fragments showing lead- and iron-based chemical contrast did not provide additional insights into the possible presence of lead- and iron-based crystalline phases. Only similar phases as the ones found in blank papyrus were identified. A really low content and/or their amorphous nature may explain the lack of sensitivity of the XRD techniques towards the presence of additional lead- and iron-based phases.

6.4 Looking for structural contrast using XRD

To look for a structural contrast between the pigment and the papyrus support, we measured the diffraction patterns of a series of papyrus fragments both on ink and ink-free areas. This was done to compare the signal of the support with the signal measured on the inked area.

The black scepter region of PAP-6 was mapped using XRD, and two diffraction patterns collected on the black scepter of god Re and the sole papyrus support are displayed in Figure 3.56. These patterns are quite similar to the one collected on blank papyrus, dominated by the diffraction signal of cellulose, and comparing inked and non-ink areas do not show any obvious difference. As we have demonstrated in the previous part (see subsubsection 6.2.2) that the main pigment used in the ink was flame carbon, we mainly focused at 1.75Å^{-1}, where the main diffraction peak of reference lampblack is expected, with no success.

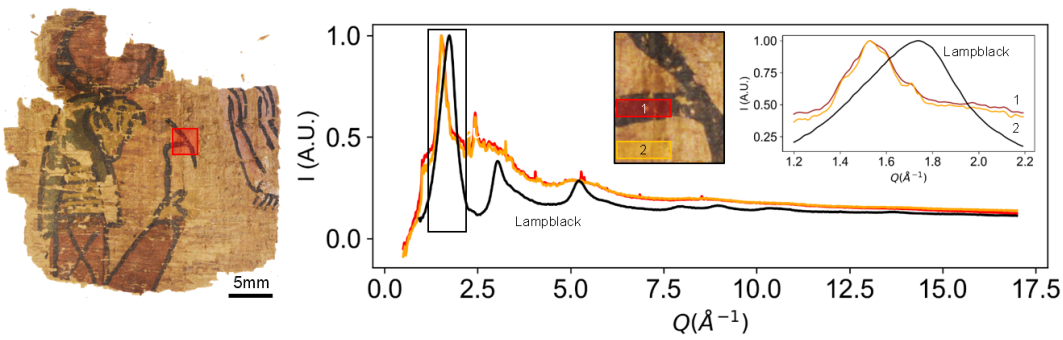

Figure 3.56: XRPD patterns taken on ink and ink-free areas superposed with lampblack diffraction pattern.

This absence of structural contrast was expected, first because of the small diffracting volume of pigment compared to the volume of papyrus, and because of the main characteristics of both carbon-based pigment and papyrus: they are both made of carbon and have both a quasi-amorphous structure.

To try to reveal a finer contrast, we have performed a series of subtractions between the support signal measured alone and the measurement of ink and support together. Figure 3.57 shows diffraction patterns of a line scan made on PAP-1 before and after subtraction. The subtracted diffraction pattern was obtained by subtracting one of the ink-free diffraction patterns from the rest of them with a scale factor taken between 0 and 1. The scale factor is carefully chosen to avoid subtracting too much signal which would lead to a resulting negative signal. The peak obtained at 2θ=1.9° is coming from the Kapton sheet used to hold the sample in place. Its position helped us to match the sample position with the recorded signal.

Plotting the diffraction pattern of the line scan does not show any obvious differences between measurement points. However, after subtracting the signal of the papyrus, several diffraction patterns present a bump at around 2θ=5.6°. Nevertheless, diffraction patterns showing this bump do not seem to be correlated to the ink regions. To check this further, we have followed the intensity of the bump over the scan region, and the corresponding map is displayed in figure Figure 3.57.

We have selected two pairs of subtracted patterns from each of the two ink regions of PAP-1 (Figure 3.58). The resulting patterns are clearly different between the two ink regions, so we conclude that the obtained signal showing the bump is not a characteristic of the ink. On the other hand, this signal presents similar features as the one from the papyrus support alone (see subsection 4.4), and we attribute this to one type of cellulose which is more present in some localized areas than others.

6.5 Retrieving contrast using X-ray diffraction and fluorescence tomography

Understanding the limits of the previous attempts, the objective is now to try to better isolate the diffraction and fluorescence signal from the papyrus and the ink. As we discussed in the last part, fluorescence signal contrast from the ink is sometimes due to the presence of lead or iron, so we

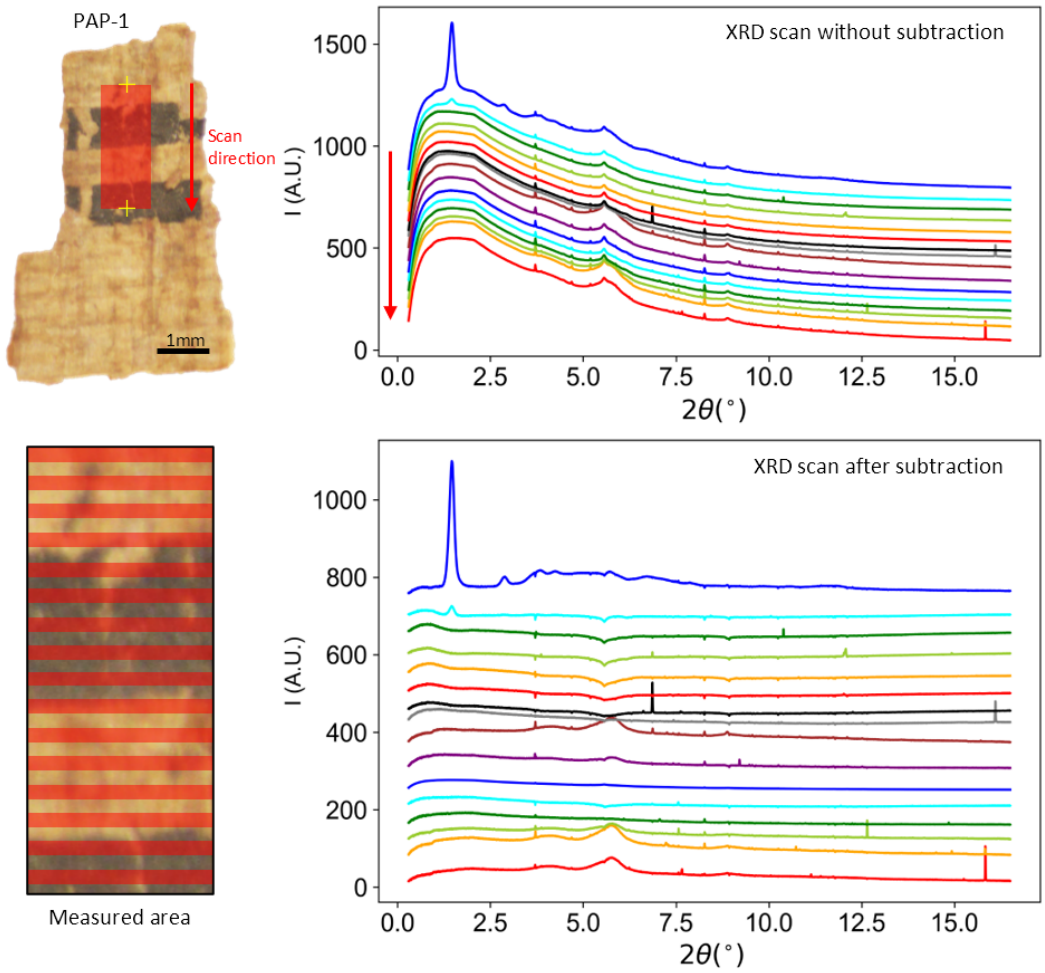

Figure 3.57: Diffraction patterns acquired in a vertical scan line on PAP-1, with and without subtraction. The diffraction peak at 1.9° seen on the first two patterns corresponds to kapton.

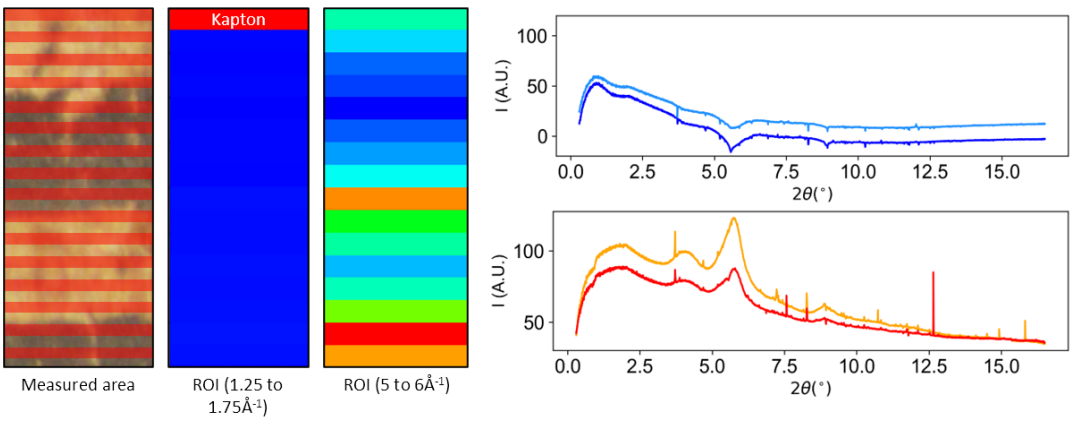

Figure 3.58: Average of two pairs of diffraction patterns acquired in a vertical scan line on PAP-1 (after papyrus subtraction). Patterns pairs were taken on both ink-rich areas.

expect to collect sufficient data to isolate the chemical composition of the ink from the papyrus support. Regarding the X-ray diffraction analysis, the challenge is to catch the structural difference between two mostly amorphous compounds: the black pigment and the cellulosic papyrus matrix.

A way to enhance the sensitivity of diffraction techniques is to use X-ray diffraction

computed tomography [12]. Such an approach has proven to be efficient to detect phases down to 0.1% in volume [12] and can be applied to the investigation of both crystalline and non-crystalline materials [13]. In addition, XRD-CT would allow us to probe the sample with a sufficient spatial resolution to distinguish the ink layer from the medium. Then the XRD will indicate if the diffraction pattern of the ink, isolated from the papyrus, corresponds to the one of lampblack.

The implementation of the XRD-CT technique applied to this type of sample was developed in this project. The experiments were made on ID11 beamline at the ESRF. The data reduction process was developed from scratch in this project to account for several corrections. The development was set around a python 3 library that was build based on preexisting python packages (pyMCA, numpy, matplotlib,...) and is distributed on the Github platform under the name pyXRDCT. In the next parts, we will describe the data acquisition, reduction, and analysis that were performed during this project on the papyrus fragments.

6.5.1 Sample mounting

Starting with a sample mounting strategy, it was necessary to select a sample that is suitable for the technique in terms of acquisition time, and with a sample mount corresponding to its size. Regarding the duration of the scan, with a resolution of 2µm, and a target of a 1 second acquisition time per image, we were looking at a total of about 57600 images per scan. By dividing by the number of rotations which is generally 180, we obtain 320 points horizontally which leads to a maximum horizontal dimension of 640µm.

It was decided to select detached parts of fragments that were spread across each of the plastic films protecting them. Two small fragments (Figure 3.59) comporting an inked area were selected. The first attempt was to put the fragments in a glass capillary to handle them. After attempting it with the first sample, we realized the risk of damaging the micro fragment in the process. Thus it was decided to put each of the samples onto a Mitegen microgrid mounted itself on a pin that would be placed onto the XRD-CT stage at the ID11 beamline. The two fragments were laid on the loop under the optical microscope making sure that the ink part was outside of the microgrid to avoid any contribution of the Kapton grid on the measured signal.

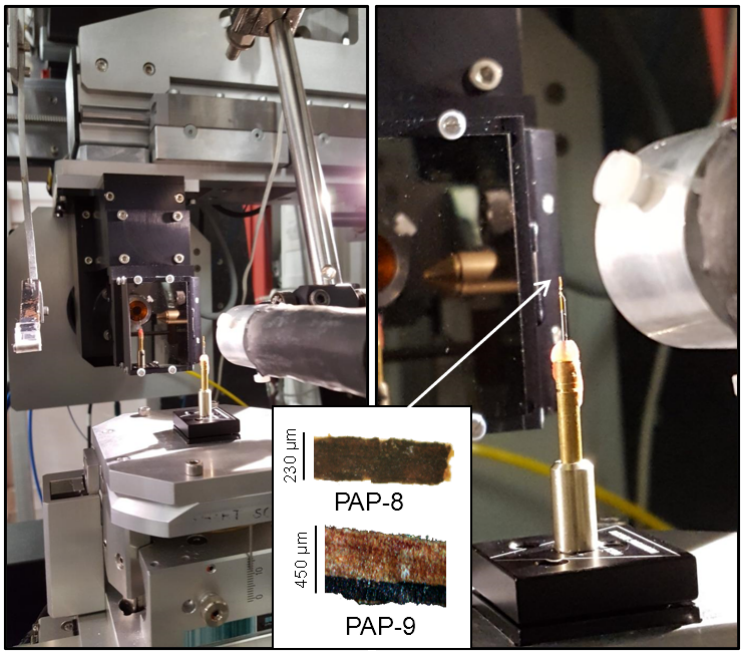

Figure 3.59: XRD-CT experimental setup on ID11 with PAP-8 and PAP-9.

After that, the pin with the loop on top was fixed on a double XYZ stage where the sample had to be aligned. The aligning procedure relies on putting the sample center (i.e. the center of the slice) as close as possible from the center of rotation of the stage. To do so we had to move the stage under the rotation axis which allows aligning both of these axes. This is done by doing back and forth rotation followed by a translation while observing the movement on a camera. Once the rotation axis is well centered we are ready for the data acquisition.

6.5.2 Data optimization

As described in chapter 1, data were recorded by scanning the sample keeping fixed rotation angles. 180 rotations were achieved in such a way, collecting both XRD and XRF data simultaneously. Considering the non-uniform shape of the sample (ultra-thin in one direction and large in the other) and to reduce the number of empty images recorded, the number of scanning steps was redefined for each rotation angle, speeding up the acquisition by a factor two. This was achieved by applying a function describing an ellipsoidal shape with fewer measurement points in the direction where the sample is thin (Figure 3.60). This technique reduces drastically the measurement of points in air thus leading to a much shorter acquisition time. A total of 45000 diffraction images and XRF spectra were collected in approximately 20 hours for each sample (1 slice per sample), which is slightly less than the maximum of 57600 images first calculated.

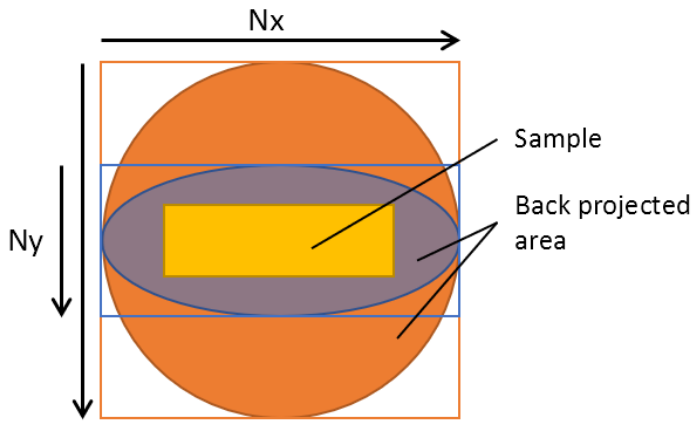

Figure 3.60: Optimisation of acquisition time in XRD-CT. The classic acquisition has Nx=Ny, in this case, Ny < Nx to match the sample shape. The reconstructed area is now an ellipse instead of a circle.

Since we perform 20 hours long scans, we are not prevented from an issue occurring while the scan is running. The scan has chances to stop for several reasons: technical issues, synchrotron beam loss, or sample problem. To ensure that the scan will be still exploitable in the case for example of beam failure, we adopted a strategy to scan the sample with large angles steps to map the sample evenly. In practice, we perform a first line-scan then we rotate the sample not by a step of 1 degree but by 11 degrees. Eleven was chosen so that after i*11[180] rotations (i being the number of rotation increase), we had mapped out each angle over the required 180 degrees. If the scan happens to fail, we would still have some exploitable data that represent an even image of the sample, while a scan where only the first 90 degrees of the sample was collected would not have been exploitable.

Last quick optimization is while performing the horizontal scan between two rotations. It is good practice to scan in one way (e.g. X positive) and after the rotation, the other way (X negative) to avoid moving the motor back to the same starting point all the time.

Just these three optimization makes the data collection much faster. This has still a drawback, as the person in charge to retrieve the scan and stack them together in proper order will have a

hard time figuring out how to put back everything in the proper order. In addition to this, classic corrections, already described in Chapter 1 had to be implemented before retrieving the correct sinogram (Figure 3.61).

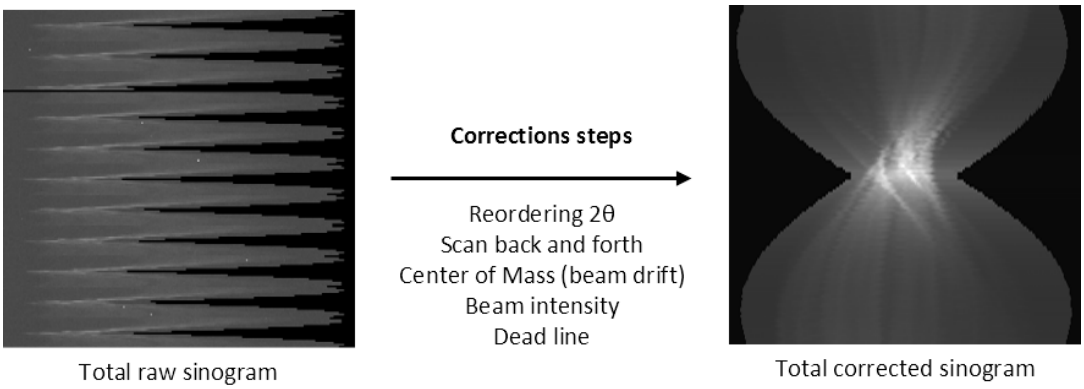

Figure 3.61: Starting point sinogram and corrected sinogram with correction steps. (see subsubsection 3.4.5)

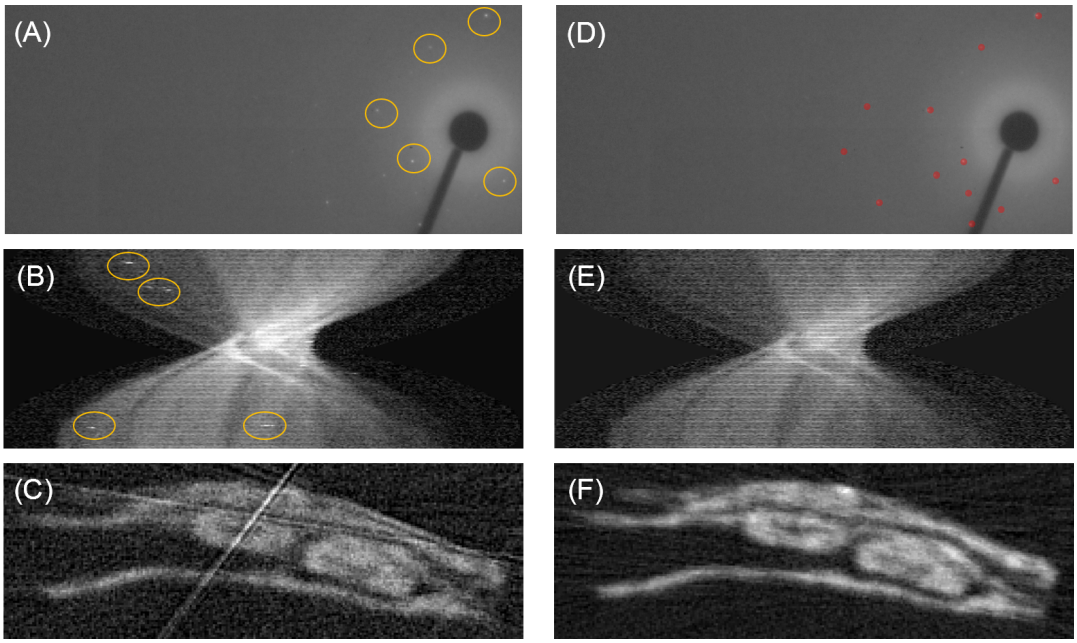

Figure 3.62: Removal of single-crystal contribution process illustration from PAP-9 sample. (A) 2D diffraction pattern image with the single-crystal contribution. (B) Sinogram showing the single crystals as small dots. (C) Reconstruction presenting straight lines from single-crystal contribution. (D) Illustration of the effect of the separate algorithm, with the masking of the single crystals. (E) Single-crystal contribution-free sinogram, (F) Reconstruction with no single-crystals.

6.5.3 Specific data reduction and corrections for XRD

With the classic correction of the scan already mentioned previously in the first chapter, namely beam drift, beam intensity, bad lines, and 2θ sorting, we now face sample-specific issues. The presence of a single-crystal signal in XRD-CT is a deal-breaker. Single crystals are appearing not consistently in the sinogram at certain angles and positions as localized points. After the reconstruction, these points are becoming lines. These lines are not only masking the signal of a more powder-like area but also bring poorly valuable information.

To tackle that, the strategy is to separate this single-crystal contribution from the rest of the sinogram. With that, we will be able to obtain a single crystal-free sinogram, which will be exploitable, and, on the other hand, the stand-alone signal of the single crystals that could be analyzed separately for a phase identification for example.

This separating step has to be performed back to the raw 2D diffraction images recorded before the integration. The single crystal contribution was filtered out using the function 'separate' from the PyFAI library [6]. Same strategy was already explained and implemented in Chapter 2. The algorithm sorts out for each diffraction angle the value which is higher than a certain percentage of the average, these points are then masked out and do not appear in the integrated pattern (Figure 3.62). Then the output is two 1D diffraction patterns, one only with powder contribution and the other one with the single crystal contribution (Figure 3.62).

6.5.4 Separating pigment from papyrus contributions

After obtaining a sinogram free from single-crystal contribution, we focused on obtaining a contrast between the ink and the papyrus support. Three different strategies were explored:

- Reconstruction of the corrected sinogram and reverse analysis on both ink and ink-free area (Figure 3.63A, B)
- Removing the contribution of the air by subtracting an air averaged signal from the surroundings of the sample, and then reconstructing the sinogram and performing the reverse analysis (Figure 3.63C, D)
- Removing the contribution of the papyrus signal by subtracting an averaged signal from the papyrus itself after normalization at high Q-range values, and then reconstructing the sinogram and performing the reverse analysis. (Figure 3.63E, F)

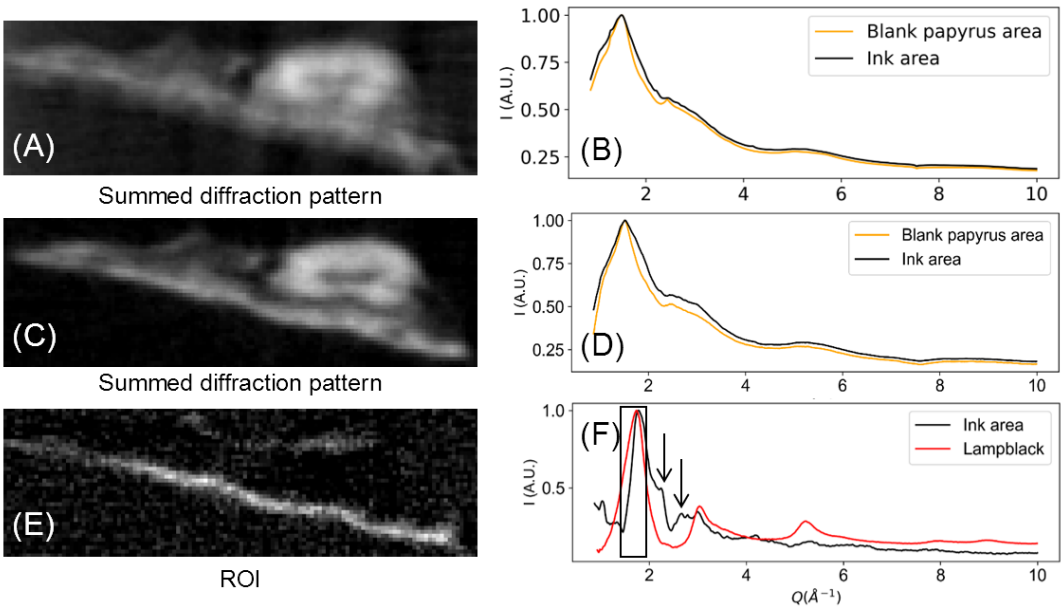

Figure 3.63: The three steps of XRD-CT leading to the obtaining of the ink signal. (A) and (B) Reconstruction and reverse analysis of the first corrected sinogram, (C) and (D) Reconstruction and reverse analysis of the first corrected sinogram after subtraction of the air in the diffraction patterns. (E) and (F) Reconstruction and reverse analysis of the first corrected sinogram after subtraction of the air and the papyrus signals in the diffraction patterns, with an ROI (see black rectangle) between Q = 1.35 Å^{-1} and 1.84 Å^{-1}. Black arrows indicate non-identified phases.

In the end, we obtain a clear image of our sample after the air subtraction (Figure 3.63C). Nevertheless, no contrast was obtained. Only after subtracting the average signal of the papyrus, the contribution of the ink solely was obtained. It is important to stress out how small the difference is between the scattering signal of the ink and ink-free area. It is visible in figure Figure 3.63D at around 1.8 $Å^{-1}$, and the diffraction pattern of the ink area was selected on the ink-rich area and separated from the rest of the papyrus bulk. Even with this selection, the signal difference remains extremely weak.

6.5.5 Results

XRD-CT data were collected on samples PAP-8 and PAP-9, and the reconstructed slices are shown in Figure 3.64A and Figure 3.64D, respectively. Thanks to the dedicated data processing explain in 6.5, in both reconstructed slices, a contrast appeared, and the papyrus side on which the ink is apposed was revealed, especially for a Q value of around 1.60 $Å^{-1}$ (dotted lines in Figure 3.64C and Figure 3.64F). The diffraction signal corresponding to the highlighted area in Figure 3.64B and Figure 3.64E was extracted by reverse analysis and is shown in Figure 3.64C and Figure 3.64F, respectively. The extracted diffraction signal was compared to the diffraction signal of standard lampblack, and, in both cases, a good match was obtained. This confirms that contrast between the ink and the papyrus support can also be extracted by relying only on the diffraction signal of the carbon-based pigment. To the best of our knowledge, this is the first time that such a pigment-based contrast is revealed, and this result has been published in Autran *et al.*, 2020 [117].

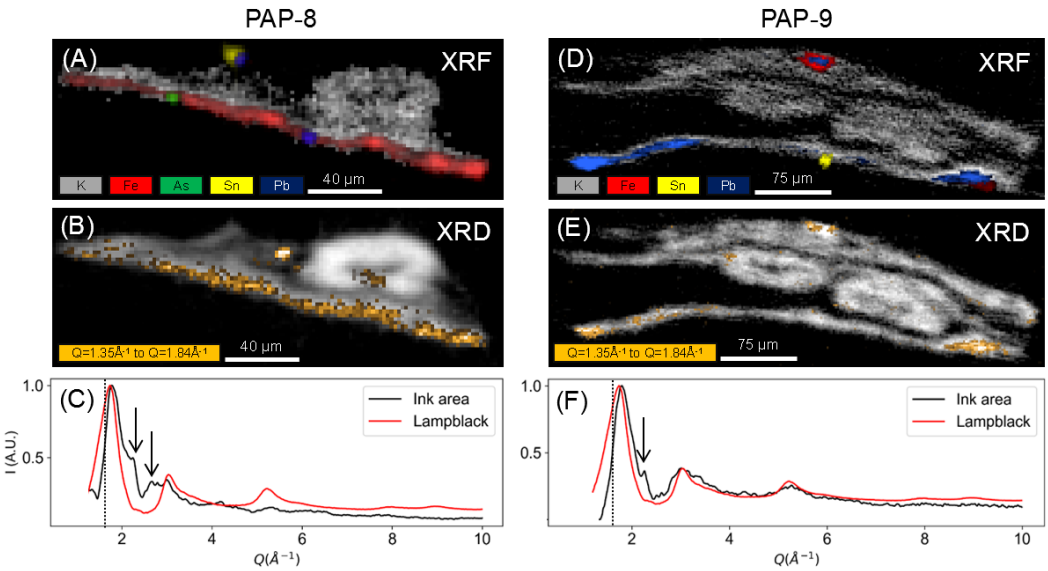

Figure 3.64: XRF-CT and XRD-CT reconstructed slices of PAP-8 and PAP-9. (A) and (D) XRF-CT of PAP-8 and PAP-9 papyrus fragment, respectively. Iron signal and lead signal match the inked surface of the papyrus of PAP-8 and PAP-9, respectively. (B) and (E) XRD-CT of PAP-8 and PAP-9, respectively. The white color represents the summed diffraction signal and the orange color the contribution of the signal between Q = 1.35 $Å^{-1}$ and 1.84 $Å^{-1}$ (lampblack diffraction peak position). The contrast, concerning the presence of the carbon-based pigment in the ink, is obtained only after the subtraction of the average signal. Orange dots found away from the pigment signal correspond to undetermined crystalline phases. (C) and (F) XRD-CT reverse analysis after subtraction of an averaged signal of the blank papyrus, from the ink areas highlighted in orange in (B) and (E), respectively. The XRD pattern of a lampblack standard is given for comparison. The black arrows indicate diffraction peaks from additional unidentified crystalline phases.

A few additional highlighted spots in the papyrus support can be seen in figure Figure 3.64B and Figure 3.64E. They do not correspond to the same carbon-based phase identified in the ink, but to additional phases with a diffraction contribution at a similar Q-value. The phase identification of these phases is complex for two reasons: the high Q-range limits the angular resolution of the pattern, and the size of the beam leads to a single-crystal diffraction signal resulting in a highly textured pattern.

A similar contrast between ink and papyrus support has also been obtained by XRF-CT, using lead (Figure 3.64A) and iron (Figure 3.64D) elements as discriminating agents, and this is strengthening the results obtained by XRD-CT.

6.6 Discussion

6.6.1 Ink recipe

If we compile the results obtained by XRD, XRF, and Raman spectroscopy, for more than half of the fragments, the ink seems to be mainly based on flame carbon pigment (in addition to the binder, which is not discussed here), without any additional compound that could have resulted in a chemical contrast with blank papyrus. Concerning the samples for which a chemical contrast was obtained (PAP-6, PAP-7, PAP-8, and PAP-9), only PAP-8 could be compatible with the use of a mixed ink, where a carbon-based pigment is associated with iron salts.

Nevertheless, in the present case, the iron-based compound could not be identified, and its presence may also result from non-intentional contamination of the ink during its manufacturing or preparation process. Furthermore, this quasi-absence of iron/copper elements in the carbon-based inks from the Champollion collection is in agreement with the fact that the two largest fragments are probably not from the late periods of Ancient Egypt where the use of mixed inks containing copper and iron salts emerged [118].

In agreement with former publications on Egyptian papyrus [81], [28], [88], [8], [27], [3], we also report a higher content of lead in the black ink of a few fragments. Our attempt to identify the original lead-based compound being unsuccessful, the question about the intentional addition of such compound or accidental contamination stays open. Egyptians from ancient times had great expertise in manipulating lead-based compounds, with the development of complex chemical processes, for example resulting in the large-scale production of cosmetics with specific therapeutic properties [86]. Lead compounds are also known to facilitate the drying of oil paintings or varnishes [119], and the use of litharge (PbO) as a drying agent is reported by Galen as early as the 2nd C. A.D. and by Marcellus (4th C. A.D.) [25]. Recently, Christiansen *et al.* [54] identified lead phosphates in papyrus from the early third century CE, and they interpreted the presence of these compounds as ink drying agents. Owing to the advanced knowledge of Ancient Egyptian about lead chemistry, the use of lead compounds to favor the drying of the ink is indeed an acceptable possibility. Nevertheless, artifacts made of lead or lead alloys dating from Ancient Egypt have been excavated in several places [58], and this includes vessels [120] that could have been used to prepare the ink, thus providing a potential source of contamination, as previously discussed by Tack *et al.* [25].

6.6.2 Writing on papyrus

Thanks to XRD-CT and XRF-CT, we can observe the internal structure of the papyrus fragment without damaging it. The section of two parenchymal cells can be seen for PAP-9, sandwiched into two walls, probably made of similar tube-like parenchymal cells running parallel to the slice (Figure 3.64B). The flattened oval shape of the cells is compatible with a phase of hammering during the manufacturing process, as described in 2.1.4 and mentioned in earlier works [58]. Similar features are seen for PAP-8, with the section of one parenchymal cell visible

(Figure 3.64C). The cross-section does not show the full thickness of the original papyrus and is more likely to be a fragment of the surface part.

Both XRF-CT and XRD-CT results indicate that the ink does not form a distinctive layer at the surface of the papyrus, but has diffused in the papyrus fiber running parallel to the reconstructed slice. This is in agreement with Christiansen *et al.* [27] observations. In addition to this, we show that we can recover the thickness of the diffusion, which is about 15 to 20 microns in-depth, with both papyrus and ink signals present at the same time. This penetration of the ink could affect the cellulose chains, thus leading potentially to a different evolution with time of this cellulose compared to the bulk cellulose.

6.6.3 Contrast in XRD-CT

We have demonstrated that using an XRD-CT approach, the diffraction signal of the carbon-based pigment used in the ink of ancient papyrus can be extracted and separated from the one of the papyrus support. This may open a new way to investigate ancient and damaged papyrus, and use the structural contrast coming from the carbon-based pigment itself in the absence of chemical contrast. In this study, only two slices from two different papyrus fragments of a few hundred of microns in size were reconstructed. "Reading" of unrolled or damaged papyrus would require scanning a much larger area, and so adjust our XRD-CT approach to larger volumes.

One of the drawbacks of the XRD-CT technique is the time spent for the measurement, as the sample is scanned for a series of rotation angles, the spatial resolution being imposed by the size of the beam. From our reconstruction, we have shown that the diffraction signal of the carbon-based pigment is concentrated over the first 15 to 20 microns inside the papyrus and that the contrast is obtained after carefully subtracting an averaged diffraction pattern of the papyrus support to the data. A spatial resolution of about 20 microns should be sufficient to reveal a contrast, thus decreasing the number of scanning steps by a factor of ten compared to our measurements. Besides, several synchrotron sources around the world are undertaking major upgrades [121], [122], and measurements that were taking several hours will be reduced to a few minutes, which could also benefit the Cultural Heritage community [123]. This upgrade would also push towards the PDF analysis from XRD-CT data, which currently relies on either longer data acquisition or lower statistics. In our case, the possibility to distinguish diverse carbon origins, as demonstrated by Cersoy *et al.* [4] and in the Chapter 2 was not possible. Other diffraction approaches conferring a depth resolution to the measurements could also be a good alternative [56], as shown by a study from Vanmeert *et al.* in which the stratigraphy of an illuminated manuscript was reconstructed [124].

7 Conclusion of the chapter

In this chapter, the colored and black pigments of twelve papyrus fragments coming from the Champollion collection were investigated, combining a series of microscopy, spectroscopy, and diffraction techniques.

We have shown that the morphology of the papyrus support keeps a trace of the manufacturing process. We were able to identify the main phases, with the presence of two calcium oxalates, weddellite and whewellite, and cellulose. Cellulose is most probably divided into two phases, resulting possibly from an aging process, which requires further investigations. Also, the presence of metallic elements aggregated in grain-shape features across the papyrus surface was shown to be recurrent, but could not be correlated to any crystalline phase.

The colored pigments studied on the papyrus collection were identified and associated with the traditional Egyptian pigment palette with, for example, the presence of cuprorivaite, orpiment, hematite, and carbon black. However, several colors such as green or white presented degraded phases resulting from the action of potassium and chloride-rich weathering agent. This is seen in

particular with the identification of potassium lead chloride, syngenite, aphtitalite, and moolooite. The exact chemical degradation paths remain to be clarified. Finally, the drawing technique was clarified, with the presence of layers of paint, starting with a preparatory drawing, application of light and then dark colors, and the black contour as a final step. Each of these steps was performed separately, possibly by several skilled scribes.

The identification of the pigments shows that the first estimation of the New Kingdom period may have to be rediscussed, at least for some fragments. The presence of a lead-based compound in the white pigment, most probably resulting from the degradation of lead white, attests to a painting epoch closer to the Ptolemaic period. This statement will have to be further discussed with Egyptologists.

The carbon-black pigment of the ink was identified as a flame carbon, and in several cases, a chemical contrast between the ink and the papyrus support was retrieved using lead and iron as discriminating agents, the origin of both still being under debate. Also, we demonstrated that a structural contrast could be obtained, using the sole diffraction signal of the carbon-black pigment, then offering a new possibility to read unrolled or damaged papyrus. This result was possible because of a dedicated development in data processing of XRD-CT data, developed through this thesis project.

Additional insights into the ink manufacturing process would be gained by analyzing a larger corpus of samples, and dedicated methodology should be developed to study the organic binder medium also part of both ink and paint. Indeed, as suggested by Zerdoun [7], the type of binder may be the only difference in the formulation, depending on the use as writing or painting material.

General conclusion

The objective of this thesis was to unravel the mysteries around the carbon-based black pigments used in Antiquity. To do so, we investigated black powders from Pompei and Herculaneum as well as papyrus fragments from ancient Egypt from Champollion Museum. In our methodological approach, we used a combination of microscopy, spectroscopy, and diffraction techniques. These techniques were chosen to tackle the main challenge of our samples: heterogeneity. With a wide range of crystallite sizes and phases of different crystallinity, archeological samples are often complex materials. Gaining new insights into such materials often requires a dedicated methodology, as shown in this thesis.

By studying black powders from Pompei and Herculaneum sites using XRD and Rietveld refinements, we identified and quantified the main crystalline phases present in the powders. Some of these were related to the volcanic eruption and others result from the degradation of either a compound present in the powder or from the container. Then, after a Fourier transform of the powder diffraction pattern, a PDF analysis was carried out to gain information on the amorphous part of the sample, in particular the carbon-based phases. One of the challenges we had to face was the presence of large crystals in our samples. If phase quantification is not so much affected by their presence, this is a major issue for relevant PDF analysis. By collecting 2D-diffraction data, we were able to separate the powder from the single-crystal contributions, and the single-crystal-free powder part was used to calculate the PDF. Knowing the crystalline content of the sample, the long-range behavior of the PDF could be quantitatively modeled, and the difference curve between the observed PDF and the calculated PDF provides the PDF of the amorphous part. The PDF of the amorphous part was compared to those of carbon-based references. Combining these results with SEM observations, we concluded that most of the samples contain carbon-based pigments coming from burned vegetables (chars). Combining results obtained on crystalline and amorphous phases, we suggested probable uses of these black powders in Antiquity. The presence of gypsum indicates that most of our powders are ink-related while several powders containing traces of oil material indicate that they are more cosmetics-related.

Papyrus fragments from the Champollion museum either written and/or painted were then investigated. Compared to the study of the black powders from Pompeii and Herculaneum, the additional challenge was to separate the diffraction signal of the black pigment from that of its support. Papyrus support is made of cellulose, and two calcium oxalate crystalline phases were also identified. We identified some particular features on the diffraction pattern of cellulose possibly related to an aging effect but further studies are needed to confirm it.

Most of the colored pigments found on the fragments are consistent with the classical Egyptian palette. However, the white and green colors contained phases that we attributed to chemical degradation due to interaction between constituents that have evolved over time. Additional analyses will be necessary to clarify the reaction chain, but such chemical alterations could help to understand the evolution of mixtures with time, and better preserve the papyrus fragments. Finally, the presence of a lead-based white pigment in several fragments may indicate an approximative dating from at the earliest around the Ptolemaic period (when the lead white started to be used), a later period as what was first hypothesized.

In all the papyrus fragments with traces of black ink, the black pigment used in the ink is exclusively flame carbon. Even if additional elements have been detected, no crystalline phases could be associated with those, which is in accordance with the use of carbon-only inks. By comparing the XRD signal of the support alone and the one of the black ink (plus support) we understood that the papyrus support represents a massive contribution. In order to gain spatial selectivity, we used the XRD/XRF-CT technique. We were able to extract the XRD contribution of the carbon-based pigment from the papyrus support which is, to the best of our knowledge,

the first time that such a contrast is revealed. The use of XRD-CT opens new possibilities to investigate ancient papyrus and use the structural contrast coming from the carbon-based pigment itself in the absence of chemical contrast to be able to "read" the writings or illustrations of unrolled or damaged papyrus.

To conclude on the two different time periods and types of sample we have studied, we observe that black inks from the Egyptian period were exclusively made of flame black pigment, while the samples identified as inks from Pompei were obtained from carbonized vegetables. If this trend may simply be an artefact due to the limited number of samples we analyzed, it could also be an indication of a change of practice.

To continue on this project several routes could be explored. The first one concerns the possibility to analyze a larger corpus of carbon-based samples, both free powder from Roman time and ink on papyrus from Egyptian time. In particular, accessing papyrus from known period would help understanding better possible ink recipe evolution in Ancient Egypt. Concerning the black powders from Pompei, the samples analyzed in this thesis are completing the first batch analyzed by Cersoy et al. Nevertheless, concluding on the type of containers versus the use of the powder in Antiquity stays challenging, and looking at a larger corpus would help clarify it.

A second route to explore concerns the black color itself. We have looked at carbon-based black pigments from different periods and for different use, and it would be interesting to quantify better the black shade of each of them. We can propose the use of colorimetry, or calibrated photography on painted surfaces with a prepared ink containing various concentrations of each reference pigment, and compare them with the ancient ones. This would be a way to try to answer the question about why certain types of carbon sources would have been used rather than others. We guess that some pigments would bring a specific tint or a better adhesion to the support.

Finally, it would also be interesting to look at the organic components of the ink, paint, or cosmetic mixture. This requires a more dedicated methodology, with the use of infrared spectroscopy, or other techniques such as gas chromatography mass spectroscopy techniques (even if destructive in the last case). This could give information about possible evolution of the recipe with time from the point of view of the binder, as well as recipe difference depending on the type of use of the black powder.

An additional route to explore concerns the methodological part. Indeed, a data analysis protocol has been implemented in this thesis to analyze the XRD-CT data, collected in 2018 at the ID11 beamline. Since then, the ESRF machine was upgraded (EBS, Extremely Brilliant Source), offering a beam of unprecedented brilliance. As a result, scans are now faster, which implies the possibility of measuring more samples or larger samples in the same amount of time. In addition, several beamlines were equipped with faster photon-counting pixel detectors. Using the set of programs developed in this thesis, the 2D-to-1D integration alone was taking around 4h for each scan. Using now data collected at 500Hz over five hours with the recently commissioned Eiger2 4M CdTe detector from Dectris available at ID11, 40 hours would be necessary to do the reconstruction. Data analysis tools have to be optimized, and/or new strategies developed to handle such a larger amount of data. The PyXRDCT library should evolve in the near future, in particular to take advantage of possible parallelization through CPU or GPU to run over multiple cores. Combining several techniques, using both labs- and synchrotron-based sources, we have improved our knowledge of black inks used in ancient Egypt and Roman periods, a further step toward deciphering messages from the past still hidden in Cultural Heritage materials.

Bibliography

[1] J. Winter, "The characterization of pigments based on carbon," *Studies in Conservation*, vol. 28, pp. 49–66, May 1983.

[2] A. Montague, "Writing materials and books among the ancient romans," *American Anthropologist*, vol. 3, no. 4, p. 337, 1890.

[3] E. Brun, M. Cotte, J. Wright, M. Ruat, P. Tack, L. Vincze, C. Ferrero, D. Delattre, and V. Mocella, "Revealing metallic ink in Herculaneum papyri," *Proceedings of the National Academy of Sciences*, vol. 113, pp. 3751–3754, Apr. 2016.

[4] S. Cersoy, P. Martinetto, P. Bordet, J. L. Hodeau, E. Van Elslande, and P. Walter, "Identifying and quantifying amorphous and crystalline content in complex powdered samples: application to archaeological carbon blacks," *Journal of Applied Crystallography*, vol. 49, pp. 585–593, Apr. 2016.

[5] C. Canevali, P. Gentile, M. Orlandi, F. Modugno, J. J. Lucejko, M. P. Colombini, L. Brambilla, S. Goidanich, C. Riedo, O. Chiantore, P. Baraldi, C. Baraldi, and M. C. Gamberini, "A multi-analytical approach for the characterization of powders from the Pompeii archaeological site," *Analytical and Bioanalytical Chemistry*, vol. 401, pp. 1801–1814, Oct. 2011.

[6] G. Ashiotis, A. Deschildre, Z. Nawaz, J. P. Wright, D. Karkoulis, F. E. Picca, and J. Kieffer, "The fast azimuthal integration Python library: *pyFAI*," *Journal of Applied Crystallography*, vol. 48, pp. 510–519, Apr. 2015.

[7] Y. Ragib and M. Z. Bat-Yehouda, "Les encres noires au Moyen Age (jusqu'a 1600)," *Studia Islamica*, no. 64, p. 170, 1986.

[8] V. Mocella, E. Brun, C. Ferrero, and D. Delattre, "Revealing letters in rolled Herculaneum papyri by X-ray phase-contrast imaging," *Nature Communications*, vol. 6, p. 5895, May 2015.

[9] T. Christiansen, D. Buti, K. N. Dalby, P. E. Lindelof, K. Ryholt, and A. Vila, "Chemical characterization of black and red inks inscribed on ancient Egyptian papyri: The Tebtunis temple library," *Journal of Archaeological Science: Reports*, vol. 14, pp. 208–219, Aug. 2017.

[10] T. Jawhari, A. Roid, and J. Casado, "Raman spectroscopic characterization of some commercially available carbon black materials," *Carbon*, vol. 33, no. 11, pp. 1561–1565, 1995.

[11] Y. Nishiyama, P. Langan, and H. Chanzy, "Crystal Structure and Hydrogen-Bonding System in Cellulose I from Synchrotron X-ray and Neutron Fiber Diffraction," *Journal of the American Chemical Society*, vol. 124, pp. 9074–9082, Aug. 2002.

[12] P. Bleuet, E. Welcomme, E. Dooryhée, J. Susini, J.-L. Hodeau, and P. Walter, "Probing the structure of heterogeneous diluted materials by diffraction tomography," *Nature Materials*, vol. 7, pp. 468–472, June 2008.

[13] M. Álvarez Murga, P. Bleuet, and J.-L. Hodeau, "Diffraction/scattering computed tomography for three-dimensional characterization of multi-phase crystalline and amorphous materials," *Journal of Applied Crystallography*, vol. 45, pp. 1109–1124, Dec. 2012.

[14] T. Christiansen, "Manufacture of Black Ink in the Ancient Mediterranean," p. 29.

[15] A. Lucas and J. R. Harris, *Ancient Egyptian materials and industries*. London: Histories & Mysteries of Man, 4. ed., rev. and enl ed., 1989. OCLC: 246583480.

[16] *Mond, R; Myers, OH - Cemeteries of Armant I Text (1937).*

[17] E. P. Tomasini, E. B. Halac, M. Reinoso, E. J. Di Liscia, and M. S. Maier, "MicroRaman spectroscopy of carbonbased black pigments," *Journal of Raman Spectroscopy*, vol. 43, pp. 1671–1675, Nov. 2012.

[18] P.-G. de Gennes and J. Badoz, "The Egyptian Scribe, Arabic Gum, and Chinese Ink," in *Fragile Objects: Soft Matter, Hard Science, and the Thrill of Discovery*, pp. 29–39, New York, NY: Springer New York, 1996.

[19] Y. Garlan, "Recherches de poliorcétique grecque, bibliothèque des écoles françaises dathènes et de rome," *Diffusion de Boccard, Paris*, 1974.

[20] P. Karl, *Papyri Graecae magicae. Die Griechischen Zauberpapyri, herausgegeben und übersetzt von Karl Preisendanz*, vol. 2. Teubner, Berlin, 1931.

[21] Vitruvius Pollio, *Ten books on architecture*, vol. VII, 10. Cambridge: Cambridge University Press, 1999. OCLC: 754088468.

[22] T. A. Osbaldeston, *Dioscorides de materia medica*. Johannesburg: Ibidis, 2000. OCLC: 803864954.

[23] J. Bostock and H. T. Riley, *Pliny the Elder: The Natural History*, vol. XXXV, 25. 1855.

[24] M. C. Gamberini, C. Baraldi, F. Palazzoli, E. Ribechini, and P. Baraldi, "MicroRaman and infrared spectroscopic characterization of ancient cosmetics," *Vibrational Spectroscopy*, vol. 47, pp. 82–90, July 2008.

[25] P. Tack, M. Cotte, S. Bauters, E. Brun, D. Banerjee, W. Bras, C. Ferrero, D. Delattre, V. Mocella, and L. Vincze, "Tracking ink composition on Herculaneum papyrus scrolls: quantification and speciation of lead by X-ray based techniques and Monte Carlo simulations," *Scientific Reports*, vol. 6, p. 20763, Aug. 2016.

[26] E. Delange, M. Grange, B. Kusko, and E. Menei, "Apparition de l'encre métallogallique en Égypte à partir de la collection de papyrus du Louvre," *Revue d'Égyptologie*, no. 0, pp. 213–217, 1990. Place: Belgium Publisher: Peeters online journals.

[27] T. Christiansen, M. Cotte, R. Loredo-Portales, P. E. Lindelof, K. Mortensen, K. Ryholt, and S. Larsen, "The nature of ancient Egyptian copper-containing carbon inks is revealed by synchrotron radiation based X-ray microscopy," *Scientific Reports*, vol. 7, p. 15346, Dec. 2017.

[28] T. Ghigo, I. Rabin, and P. Buzi, "Black Egyptian inks in Late Antiquity: new insights on their manufacture and use," *Archaeological and Anthropological Sciences*, vol. 12, p. 70, Mar. 2020.

[29] V. Solé, E. Papillon, M. Cotte, P. Walter, and J. Susini, "A multiplatform code for the analysis of energy-dispersive X-ray fluorescence spectra," *Spectrochimica Acta Part B: Atomic Spectroscopy*, vol. 62, pp. 63–68, Jan. 2007.

[30] H. M. Rietveld, "A profile refinement method for nuclear and magnetic structures," *Journal of Applied Crystallography*, vol. 2, pp. 65–71, June 1969.

[31] A. A. Coelho, "TOPAS and TOPAS-Academic : an optimization program integrating computer algebra and crystallographic objects written in C++," *Journal of Applied Crystallography*, vol. 51, pp. 210–218, Feb. 2018.

[32] P. Juhás, T. Davis, C. L. Farrow, and S. J. L. Billinge, "*PDFgetX3* : a rapid and highly automatable program for processing powder diffraction data into total scattering pair distribution functions," *Journal of Applied Crystallography*, vol. 46, pp. 560–566, Apr. 2013.

[33] C. L. Farrow, P. Juhas, J. W. Liu, D. Bryndin, E. S. Boin, J. Bloch, T. Proffen, and S. J. L. Billinge, "PDFfit2 and PDFgui: computer programs for studying nanostructure in crystals," *Journal of Physics: Condensed Matter*, vol. 19, p. 335219, Aug. 2007.

[34] J.-L. Hodeau, P. Bordet, M. Anne, A. Prat, A. N. Fitch, E. Dooryhee, G. Vaughan, and A. K. Freund, "Nine-crystal multianalyzer stage for high-resolution powder diffraction between 6 keV and 40 keV," (San Diego, CA, USA), p. 353, Dec. 1998.

[35] J. P. Wright, G. B. Vaughan, and A. N. Fitch, "Merging data from a multi-detector continuous scanning powder diffraction system," *Commission on Crystallographic Computing*, p. 92, 2003.

[36] U. Kleuker, P. Suortti, W. Weyrich, and P. Spanne, "Feasibility study of x-ray diffraction computed tomography for medical imaging," *Physics in Medicine & Biology*, vol. 43, no. 10, p. 2911, 1998.

[37] F. Natterer and F. Wübbeling, *Mathematical Methods in Image Reconstruction*. Society for Industrial and Applied Mathematics, Jan. 2001.

[38] R. Gordon, R. Bender, and G. T. Herman, "Algebraic reconstruction techniques (art) for three-dimensional electron microscopy and x-ray photography," *Journal of theoretical Biology*, vol. 29, no. 3, pp. 471–481, 1970.

[39] J. A. Scales, "Tomographic inversion via the conjugate gradient method," *Geophysics*, vol. 52, no. 2, pp. 179–185, 1987.

[40] J.-B. Donnet, *Carbon black: science and technology*. 2018. OCLC: 1064620207.

[41] I. Lewis, "Chemistry of carbonization," *Carbon*, vol. 20, no. 6, pp. 519–529, 1982.

[42] H. L. Jang, H. K. Lee, K. Jin, H.-Y. Ahn, H.-E. Lee, and K. T. Nam, "Phase transformation from hydroxyapatite to the secondary bone mineral, whitlockite," *J. Mater. Chem. B*, vol. 3, no. 7, pp. 1342–1349, 2015. Publisher: The Royal Society of Chemistry.

[43] J. Wilson, I. Pulford, and S. Thomas, "Sorption of cu and zn by bone charcoal," *Environmental geochemistry and health*, vol. 25, no. 1, pp. 51–56, 2003.

[44] N. A. Medellin-Castillo, R. Leyva-Ramos, R. Ocampo-Perez, R. F. Garcia de la Cruz, A. Aragon-Pina, J. M. Martinez-Rosales, R. M. Guerrero-Coronado, and L. Fuentes-Rubio, "Adsorption of fluoride from water solution on bone char," *Industrial & Engineering Chemistry Research*, vol. 46, no. 26, pp. 9205–9212, 2007.

[45] R. Wilson, J. Elliott, and S. Dowker, "Rietveld refinement of the crystallographic structure of human dental enamel apatites," *American mineralogist*, vol. 84, no. 9, pp. 1406–1414, 1999.

[46] C. Calvo and R. Gopal, "The crystal structure of whitlockite from the palermo quarry," *American Mineralogist: Journal of Earth and Planetary Materials*, vol. 60, no. 1-2, pp. 120–133, 1975.

[47] M. Verezhak, *Caractérisation multi-échelle du minéral osseux: apport de l'imagerie structurale par contraste de diffraction des rayons X et d'électrons*. PhD thesis, Université Grenoble Alpes, 2016.

[48] R. E. Franklin, "The interpretation of diffuse x-ray diagrams of carbon," *Acta crystallographica*, vol. 3, no. 2, pp. 107–121, 1950.

[49] Y. Rew, A. Baranikumar, A. Tamashausky, S. El-Tawil, and P. Park, "Electrical and mechanical properties of asphaltic composites containing carbon based fillers," *Construction and Building Materials*, vol. 135, pp. 394–404, 03 2017.

[50] I. Reiche, C. Vignaud, and M. Menu, "Heat induced transformation of fossil mastodon ivory into turquoise odontolite. structural and elemental characterisation," *Solid State Sciences*, vol. 2, no. 6, pp. 625–636, 2000.

[51] H. L. Jang, H. K. Lee, K. Jin, H.-Y. Ahn, H.-E. Lee, and K. T. Nam, "Phase transformation from hydroxyapatite to the secondary bone mineral, whitlockite," *Journal of Materials Chemistry B*, vol. 3, no. 7, pp. 1342–1349, 2015.

[52] S. Gates-Rector and T. Blanton, "The Powder Diffraction File: a quality materials characterization database," *Powder Diffraction*, vol. 34, pp. 352–360, Dec. 2019.

[53] A. R. Kampf, I. M. Steele, and R. A. Jenkins, "Phosphohedyphane, ca2pb3 (po4) 3cl, the phosphate analog of hedyphane: Description and crystal structure," *American Mineralogist*, vol. 91, no. 11-12, pp. 1909–1917, 2006.

[54] T. Christiansen, M. Cotte, W. de Nolf, E. Mouro, J. Reyes-Herrera, S. de Meyer, F. Vanmeert, N. Salvadó, V. Gonzalez, P. E. Lindelof, K. Mortensen, K. Ryholt, K. Janssens, and S. Larsen, "Insights into the composition of ancient Egyptian red and black inks on papyri achieved by synchrotron-based microanalyses," *Proceedings of the National Academy of Sciences*, vol. 117, pp. 27825–27835, Nov. 2020.

[55] I. Marcaida, M. Maguregui, H. Morillas, M. Veneranda, N. Prieto-Taboada, S. Fdez-Ortiz de Vallejuelo, and J. M. Madariaga, "Raman microscopy as a tool to discriminate mineral phases of volcanic origin and contaminations on red and yellow ochre raw pigments from Pompeii," *Journal of Raman Spectroscopy*, vol. 50, no. 2, pp. 143–149, 2019. _eprint: https://onlinelibrary.wiley.com/doi/pdf/10.1002/jrs.5414.

[56] C. Dejoie, M. Coduri, S. Petitdemange, C. Giacobbe, E. Covacci, O. Grimaldi, P.-O. Autran, M. W. Mogodi, D. iak Jung, and A. N. Fitch, "Combining a nine-crystal multi-analyser stage with a two-dimensional detector for high-resolution powder X-ray diffraction," *Journal of Applied Crystallography*, vol. 51, pp. 1721–1733, Dec. 2018.

[57] L. M. Di Stefano and R. Fuchs, "Characterisation of the pigments in a Ptolemaic Egyptian Book of the Dead papyrus," *Archaeological and Anthropological Sciences*, vol. 3, pp. 229–244, Sept. 2011.

[58] P. T. Nicholson and I. Shaw, eds., *Ancient egyptian materials and technology*. Cambridge: Cambridge Univ. Pr, 1. aufl.; 5. neudr ed., 2009. OCLC: 449825743.

[59] B. B. Baumann, "The botanical aspects of ancient Egyptian embalming and burial," *Economic Botany*, vol. 14, pp. 84–104, Jan. 1960.

[60] H. G. Wiedeman and G. Bayer, "Papyrus The Paper of Ancient Egypt," *Analytical Chemistry*, vol. 55, pp. 1220A–1230A, Oct. 1983.

[61] Y. A. El-Amier and A. M. Abd El-Gawad, "Anatomical investigation of three emergent Cyperus species growing naturally on the canal banks of the Nile delta, Egypt," *Journal of Scientific Agriculture*, vol. 1, p. 294, Nov. 2017.

[62] M. Mosiniak and J. Roland, "Variations spontanées du rythme d'assemblage des parois cellulaires à texture hélicoïdale: l'exemple du papyrus," *Ann. Sci. Nat. Bot.*, vol. 13, pp. 175–212, 01 1985.

[63] B. Gunn, "The rhind mathematical papyrus: Introduction, transcription, translation and commentary," *The Journal of Egyptian Archaeology*, vol. 12, no. 1, pp. 123–137, 1926.

[64] J. Černỳ, *Paper & books in ancient Egypt: an inaugural lecture delivered at University College, London, 29 May, 1947*. College, 1952.

[65] C. A. Baker, "Sodium carboxymethylcellulose (scmc) re-evaluated for paper, book, papyrus, and parchment conservation," *Book Paper Group Ann*, vol. 26, pp. 177–185, 2007.

[66] E. Menei, "Le papyrus comme support d'écriture," *C. Laroque (éd.), Papiers et protopapiers: les supports de lécrit ou de la peinture, Paris*, pp. 138–160, 2017.

[67] M. Etienne and S. Pages-Camagna, *L' art du contour: le dessin dans l'Égypte ancienne : Illustrer un papyrus*. Paris: Somogy, 2013. Meeting Name: Exposition OCLC: 931083608.

[68] D. A. Scott, "A review of ancient Egyptian pigments and cosmetics," *Studies in Conservation*, vol. 61, pp. 185–202, July 2016.

[69] A.-M. Olsson, T. Calligaro, S. Colinart, J. Dran, N. Lövestam, B. Moignard, and J. Salomon, "Micro-PIXE analysis of an ancient Egyptian papyrus: Identification of pigments used for the Book of the Dead," *Nuclear Instruments and Methods in Physics Research Section B: Beam Interactions with Materials and Atoms*, vol. 181, pp. 707–714, July 2001.

[70] L. Burgio and R. J. H. Clark, "Comparative pigment analysis of six modern Egyptian papyri and an authentic one of the 13th century BC by Raman microscopy and other techniques," *Journal of Raman Spectroscopy*, vol. 31, pp. 395–401, June 2000.

[71] D. A. Scott, "Ancient Egyptian Pigments: The Examination of Some Coffins from the San Diego Museum of Man," *MRS Bulletin*, vol. 35, pp. 390–396, May 2010.

[72] S. B. Hedegaard, T. Delbey, C. Brøns, and K. L. Rasmussen, "Painting the Palace of Apries II: ancient pigments of the reliefs from the Palace of Apries, Lower Egypt," *Heritage Science*, vol. 7, p. 54, Dec. 2019.

[73] M. Uda, S. Sassa, K. Taniguchi, S. Nomura, S. Yoshimura, J. Kondo, N. Iskander, and B. Zaghloul, "Touch-free in situ investigation of ancient Egyptian pigments," *Naturwissenschaften*, vol. 87, pp. 260–263, June 2000.

[74] A. P. Laurie, W. F. P. Mclintock, and F. D. Miles, "Egyptian blue," *Proceedings of the Royal Society of London. Series A, Containing Papers of a Mathematical and Physical Character*, vol. 89, pp. 418–429, Jan. 1914.

[75] H. Jaksch, W. Seipel, K. L. Weiner, and A. E. Goresy, "Egyptian blue ? Cuprorivaite a window to ancient Egyptian technology," *Naturwissenschaften*, vol. 70, pp. 525–535, Nov. 1983.

[76] H. G. Wiedemann and G. Bayer, "The bust of Nefertiti," *Analytical Chemistry*, vol. 54, pp. 619–628, Apr. 1982.

[77] J. E. Quibell and F. W. Green, *Hierakonpolis*, vol. II. 1902. Publisher: University Library Heidelberg Version Number: 1.0.

[78] S. Pages-Camagna and S. Colinart, "The Egyptian Green pigment: its manufacturing process and links to Egyptian Blue*," *Archaeometry*, vol. 45, pp. 637–658, Nov. 2003.

[79] A.-M. Bakr, T. Kawiak, M. Pawlikowski, and Z. Sawlowicz, "Characterisation of 15th century red and black pastes used for wall decoration in the Qijmas El-Eshaqi mosque (Cairo, Egypt)," *Journal of Cultural Heritage*, vol. 6, pp. 351–356, Dec. 2005.

[80] C. Calza, M. Anjos, S. Mendonça de Souza, A. Brancaglion Jr., and R. Lopes, "X-ray microfluorescence with synchrotron radiation applied in the analysis of pigments from ancient Egypt," *Applied Physics A*, vol. 90, pp. 75–79, Nov. 2007.

[81] D. B. Gore, M. Choat, D. E. Jacob, and G. Gloy, "Which elements are useful for understanding the composition of ancient papyrus inks?," *Powder Diffraction*, vol. 32, pp. S90–S94, Dec. 2017.

[82] V. Daniels and B. Leach, "The Occurrence and Alteration of Realgar on Ancient Egyptian Papyri," *Studies in Conservation*, vol. 49, pp. 73–84, Jan. 2004.

[83] A. Macchia, S. N. Cesaro, L. Campanella, A. Maras, M. Rocchia, and G. Roscioli, "Which light for cultural heritage: comparison of light sources with respect to realgar photodegradation," *Journal of Applied Spectroscopy*, vol. 80, no. 5, pp. 637–643, 2013.

[84] D. A. Scott, L. S. Dodd, J. Furihata, S. Tanimoto, J. Keeney, M. R. Schilling, and E. Cowan, "An Ancient Egyptian Cartonnage Broad Collar - Technical Examination of Pigments and Binding Media," *Studies in Conservation*, vol. 49, pp. 177–192, Sept. 2004.

[85] C. P. Bryan and G. E. Smith, *Ancient Egyptian medicine: the papyrus ebers*, vol. 6. Ares Chicago, 1974.

[86] P. Walter, P. Martinetto, G. Tsoucaris, R. Brniaux, M. A. Lefebvre, G. Richard, J. Talabot, and E. Dooryhee, "Making make-up in Ancient Egypt," *Nature*, vol. 397, pp. 483–484, Feb. 1999.

[87] E. Franceschi, G. Luciano, F. Carosi, L. Cornara, and C. Montanari, "Thermal and microscope analysis as a tool in the characterisation of ancient papyri," *Thermochimica Acta*, vol. 418, pp. 39–45, Aug. 2004.

[88] T. Arlt, H.-E. Mahnke, T. Siopi, E. Menei, C. Aibéo, R.-R. Pausewein, I. Reiche, I. Manke, and V. Lepper, "Absorption edge sensitive radiography and tomography of Egyptian Papyri," *Journal of Cultural Heritage*, vol. 39, pp. 13–20, Sept. 2019.

[89] S. Goler, J. T. Yardley, A. Cacciola, A. Hagadorn, D. Ratzan, and R. Bagnall, "Characterizing the age of ancient Egyptian manuscripts through micro-Raman spectroscopy: Characterizing the age of ancient Egyptian manuscripts," *Journal of Raman Spectroscopy*, vol. 47, pp. 1185–1193, Oct. 2016.

[90] A. Wallert, "The reconstruction of papyrus manufacture: a preliminary investigation," *Studies in Conservation*, vol. 34, pp. 1–8, Feb. 1989.

[91] P. E. Scora and R. W. Scora, "Some observations on the nature of papyrus bonding," *Journal of Ethnobiology*, vol. 11, pp. 193–202, 1991.

[92] J. J. Gaudet, "Mineral Concentrations in Papyrus in Various African Swamps," *The Journal of Ecology*, vol. 63, p. 483, July 1975.

[93] J. Gong, J. Li, J. Xu, Z. Xiang, and L. Mo, "Research on cellulose nanocrystals produced from cellulose sources with various polymorphs," *RSC Advances*, vol. 7, no. 53, pp. 33486–33493, 2017.

[94] J. ojewska, I. Rabin, D. Pawcenis, J. Bagniuk, M. A. Aksamit-Koperska, M. Sitarz, M. Missori, and M. Krutzsch, "Recognizing ancient papyri by a combination of spectroscopic, diffractional and chromatographic analytical tools," *Scientific Reports*, vol. 7, p. 46236, May 2017.

[95] M. Järvinen, "Application of symmetrized harmonics expansion to correction of the preferred orientation effect," *Journal of Applied Crystallography*, vol. 26, pp. 525–531, Aug. 1993.

[96] J. Labaune, J. B. Jackson, S. Pagès-Camagna, I. N. Duling, M. Menu, and G. A. Mourou, "Papyrus imaging with terahertz time domain spectroscopy," *Applied Physics A*, vol. 100, pp. 607–612, Sept. 2010.

[97] A. Lucas, "The inks of ancient and modern Egypt," *The Analyst*, vol. 47, no. 550, p. 9, 1922.

[98] V. Daniels, R. Stacey, and A. Middleton, "The Blackening of Paint Containing Egyptian Blue," *Studies in Conservation*, vol. 49, p. 217, Jan. 2004.

[99] A. H. Sabin, *The industrial and artistic technology of paint and varnish*. J. Wiley & sons, Incorporated, 1917.

[100] M. Cotte, E. Checroun, W. De Nolf, Y. Taniguchi, L. De Viguerie, M. Burghammer, P. Walter, C. Rivard, M. Salomé, K. Janssens, *et al.*, "Lead soaps in paintings: friends or foes?," *Studies in Conservation*, vol. 62, no. 1, pp. 2–23, 2017.

[101] F. Vanmeert, N. de Keyser, A. van Loon, L. Klaassen, P. Noble, and K. Janssens, "Transmission and Reflection Mode Macroscopic X-ray Powder Diffraction Imaging for the Noninvasive Visualization of Paint Degradation in Still Life Paintings by Jan Davidsz. de Heem," *Analytical Chemistry*, vol. 91, pp. 7153–7161, June 2019.

[102] A. R. Cabral, O. G. Rocha Filho, and R. D. Jones, "Mercury in itabirite-hosted soft hematite ore in the quadrilátero ferrífero of minas gerais," *Journal of Geochemical Exploration*, vol. 96, no. 1, pp. 69–76, 2008.

[103] R. A. Nicholson, "A morphological investigation of burnt animal bone and an evaluation of its utility in archaeology," *Journal of Archaeological Science*, vol. 20, no. 4, pp. 411–428, 1993.

[104] M.-C. Corbeil and K. Helwig, "An Occurrence of Pararealgar as an Original or Altered Artists' Pigment," *Studies in Conservation*, vol. 40, p. 133, May 1995.

[105] P. Kypru, ed., *Salt weathering on buildings and stone sculptures: [proceedings from the international conference], 19-22 october 2011, University of Cyprus*. 2011. Meeting Name: International Conference OCLC: 839777454.

[106] J. Schlüter, D. Pohl, and S. Britvin, "The new mineral challacolloite, KPb2Cl5, the natural occurrence of a technically known laser material," *Neues Jahrbuch für Mineralogie - Abhandlungen*, vol. 182, pp. 95–101, Nov. 2005.

[107] J. Salvant, J. Williams, M. Ganio, F. Casadio, C. Daher, K. Sutherland, L. Monico, F. Vanmeert, S. De Meyer, K. Janssens, *et al.*, "A roman egyptian painting workshop: Technical investigation of the portraits from tebtunis, egypt," *Archaeometry*, vol. 60, no. 4, pp. 815–833, 2018.

[108] A. Bezur, G. Kavich, J. Stenger, E. Torok, and C. Snow, "Discovery of challacolloite, an uncommon chloride, on a fifteenth-century polychrome terracotta relief by Michele da Firenze," *Applied Physics A*, vol. 121, pp. 83–93, Oct. 2015.

[109] P. W. J. Jansen, "The unit cell dimensions of some alkali lead and alkali strontium halides," *Recueil des Travaux Chimiques des Pays-Bas*, vol. 87, pp. 1021–1024, Sept. 2010.

[110] R. M. Clarke and I. R. Williams, "Moolooite, a naturally occurring hydrated copper oxalate from Western Australia," *Mineralogical Magazine*, vol. 50, pp. 295–298, June 1986.

[111] K. Castro, A. Sarmiento, I. Martínez-Arkarazo, J. M. Madariaga, and L. A. Fernández, "Green Copper Pigments Biodegradation in Cultural Heritage: From Malachite to Moolooite, Thermodynamic Modeling, X-ray Fluorescence, and Raman Evidence," *Analytical Chemistry*, vol. 80, pp. 4103–4110, June 2008.

[112] Z. Li, L. Wang, H. Chen, and Q. Ma, "Degradation of emerald green: scientific studies on multi-polychrome Vairocana Statue in Dazu Rock Carvings, Chongqing, China," *Heritage Science*, vol. 8, p. 64, Dec. 2020.

[113] A. Sadezky, H. Muckenhuber, H. Grothe, R. Niessner, and U. Pöschl, "Raman microspectroscopy of soot and related carbonaceous materials: spectral analysis and structural information," *Carbon*, vol. 43, no. 8, pp. 1731–1742, 2005.

[114] T. P. Mernagh, R. P. Cooney, and R. A. Johnson, "Raman spectra of Graphon carbon black," *Carbon*, vol. 22, no. 1, pp. 39–42, 1984.

[115] A. Coccato, J. Jehlicka, L. Moens, and P. Vandenabeele, "Raman spectroscopy for the investigation of carbon-based black pigments: Investigation of carbon-based black pigments," *Journal of Raman Spectroscopy*, vol. 46, pp. 1003–1015, Oct. 2015.

[116] E. Tomasini, G. Siracusano, and M. Maier, "Spectroscopic, morphological and chemical characterization of historic pigments based on carbon. Paths for the identification of an artistic pigment," *Microchemical Journal*, vol. 102, pp. 28–37, May 2012.

[117] P.-O. Autran, C. Dejoie, P. Bordet, J.-L. Hodeau, C. Dugand, M. Gervason, M. Anne, and P. Martinetto, "Revealing the nature of black pigments used on ancient egyptian papyri from champollion collection," *Analytical Chemistry*, vol. 93, no. 2, pp. 1135–1142, 2021. PMID: 33316154.

[118] C. Colini, O. Hahn, O. Bonnerot, S. Steger, Z. Cohen, T. Ghigo, T. Christiansen, M. Bicchieri, P. Biocca, M. Krutzsch, and I. Rabin, "The Quest for the Mixed Inks," vol. Manuscript cultures, 11, 2018.

[119] C. S. Tumosa and M. F. Mecklenburg, "The influence of lead ions on the drying of oils," *Studies in Conservation*, vol. 50, pp. 39–47, June 2005.

[120] W. M. F. Petrie, *Objects of daily use*. No. 6] in [The Petrie Egyptian Collection and Exavations, Warmister, Wiltshire: Aris & Phillips [u.a.], 1974. OCLC: 247599588.

[121] P. Raimondi, "ESRF-EBS: The Extremely Brilliant Source Project," *Synchrotron Radiation News*, vol. 29, pp. 8–15, Nov. 2016.

[122] V. Sajaev, "Commissioning simulations for the Argonne Advanced Photon Source upgrade lattice," *Physical Review Accelerators and Beams*, vol. 22, p. 040102, Apr. 2019.

[123] M. Cotte, P.-O. Autran, C. Berruyer, C. Dejoie, J. Susini, and P. Tafforeau, "Cultural and Natural Heritage at the ESRF: Looking Back and to the Future," *Synchrotron Radiation News*, vol. 32, pp. 34–40, Nov. 2019.

[124] F. Vanmeert, W. De Nolf, J. Dik, and K. Janssens, "Macroscopic X-ray Powder Diffraction Scanning: Possibilities for Quantitative and Depth-Selective Parchment Analysis," *Analytical Chemistry*, vol. 90, pp. 6445–6452, June 2018.

List of Figures

1 Images MEB (électrons secondaires, Institut Néel) obtenues sur deux poudres noires d'un contenant du site archéologique de Pompéi, et sur des références. Les morphologies du noir de pêche, du bois carbonisé (Winter, 1983 [1]) et du noir de fumée sont clairement visibles. iii

2 (A) Exemple d'affinement de Rietveld d'une poudre noire (HE03) prélevée dans un récipient découvert sur le site de Herculanum (bleu: données expérimentales, rouge: modèle calculé, gris : différence). Sept phases cristallines ont été identifiées. (Rwp = 10.29, Rexp = 3.95, Rp = 7.62) (B) Affinement de la PDF à grande distance (échantillon P2445) après identification et quantification des phases cristallines (bleu: données expérimentales, rouge: modèle calculé, vert: résidu, qui correspond à la PDF de la phase amorphe à identifier). (C) Comparaison de la PDF de la phase amorphe obtenue en B avec les PDFs des échantillons de référence. iv

3 Illustration de la procédure de pré-traitement des données de diffraction 2D avec pyFAI. Sur l'image brute, les anneaux de poudre et les taches des monocristaux coexistent. Les contributions poudre et monocristalline peuvent être séparées, ce qui permet d'intégrer l'image de la contribution poudre puis de calculer la PDF. . v

4 (A) Exemple du fragment de papyrus PAP-1 de la collection du Musée Champollion (Vif, département de l'Isère) montrant des hiéroglyphes écrits à l'encre noire et rouge. (B) Spectre Raman (Institut Néel, Grenoble) enregistré sur l'encre noire du fragment PAP-1. La largeur et l'intensité relative des deux bandes D et G sont caractéristiques d'un composé carboné désordonné. (C) Photo MEB de l'encre noire à la surface du fragment de papyrus PAP-1, correspondant au noir de fumée (Institut Néel, Grenoble). vii

5 (A) Vue d'un fragment de papyrus (Musée Champollion) monté dans un porte-échantillon dédié imprimé en 3D sur le setup expérimental de la ligne de lumière ID22. (B) Affinement de Rietveld d'un diffractogramme de poudre enregistré sur le papyrus vierge (bleu: données expérimentales, rouge: diagramme calculé, gris: différence). Les flèches noires indiquent des pics de diffraction non indexés. . . . viii

6 Modifications de la structure cristalline de la cellulose dans le cas du papyrus ancien. viii

7 Diagrammes de diffraction de poudre enregistrés sur une zone couverte d'encre et une zone vierge autour du sceptre Ouas du Dieu Rê (Musée Champollion). Le diagramme de diffraction du noir de fumée est également montré pour comparaison. ix

8 (A) Vue du setup de ID11 pour enregistrer les données XRD-CT sur un petit fragment de papyrus (Champollion Museum). (B) Section reconstruite par XRD-CT. La couleur blanche représente le signal de diffraction sommé et la couleur orange la contribution du signal entre Q = 1.15 Å et 1.64 Å (position du pic de diffraction principal noir de fumée). Le diffractogramme de la zone d'encre obtenue par analyse inverse correspond à celui du noir de fumée. x

1.1 PAP-6 fragment surface observed at a black part to white ink junction. The picture is recorded with x20 objective lens. 8

1.2 XRF setup on ID22 beamline with SDD fluorescence detector. The sample is on XYZ stage to acquire 2D maps. 11
1.3 Examples of PDF signals of two carbon phases: 9B pencil lead composed mostly of crystalline graphite, and an amorphous compound: lampblack. 16
1.4 ID22 Robot setup with a cryostream (left) 18
1.5 (A) X-ray beam path on HR-XRPD setup. (B) Silicon 111 reflection recorded at 31 keV from ID22 beamline setup. 19
1.6 Schematic representation of ID22 beamline multi-analyzer stage. 19
1.7 ID22 setup for 2D detector experiment 20
1.8 Example of the azimuthal integration of a 2D diffraction pattern (Silicon) 20
1.9 Example of the pipeline of an X-ray tomography experiment 21
1.10 XRD-CT experimental setup on the ID11 beamline 22
1.11 Data analysis pipeline for an XRD-CT experiment. The numbers are based on a sample size of 100x400µm size with a beam size of 2x2µm 23
1.12 Reconstruction of XRD-CT signal using the filtered back-projection algorithm (FBP) 24
1.13 Buckets containing commercial black pigments. 26
1.14 Evolution of the oven temperature in function of time to carbonize vegetable sample. 26
1.15 Vegetables before and after carbonization: hazelnut shells (top-left), vine branches (top-right), almond shells (bottom-left), and walnut shells (bottom-right). 26
1.16 HR-XRPD diffraction patterns from ID22 beamline of the reference containing mostly crystalline phases. (KRE = Kremer pigmente) 27
1.17 Diffraction pattern from ID22 2D detector of the mostly amorphous references (the air was subtracted from the signal). (KRE = Kremer Pigmente, DOU = Dousselin, HM = Home Made) 27
1.18 HR-XRPD diffraction patterns from ID22 beamline of bone and ivory blacks. Pawley fits are shown in red, with Rwp_{bone} = 3.11 and Rwp_{ivory} = 1.93 29
1.19 PDF signals of the amorphous references with the graphene structural model and carbon atom distances. 30
1.20 Sample stage with four samples put on carbon tape. These pieces of carbon tape were not carefully cut to be easily identifiable. 31
1.21 SEM images of references black pigments. Group 1 corresponds to vegetal-based morphologies with holes, big angular chunks, or wave-like patterns. Group2 is the bone or ivory-based pigments with small angular chunks. Group 3 is the flame carbon with spheroidal particles of 200nm size. 31
1.22 Scanning electron micrograph of sugar-pine char (left), Scanning electron micrographs of cork char (right) [1]. 32
1.23 HR-XRPD setup with hot air blower for the in-situ experiment on ID22. 32
1.24 (A) XXth ivory century propeller pencil (B) XXth century bone handle knife. . . . 33
1.25 Evolution of the diffraction pattern of ivory with temperature (exposed to oxygen). The top diffraction pattern was recorded at RT after the experiment (temperatures are displayed on each curve in °C). 33
1.26 XRPD patterns of bone black and ivory black references with results of in-situ carbonization of bone and ivory. We observe WH only on the industrial ivory black. The carbonized ivory and bones patterns were taken at 600°C which is the reason for the offset. WH = Whitlockite, Q = Quartz 34

2.1 Examples of vessels found on Pompeii site with their corresponding inventory numbers. From left to right: glass *unguentary*, *fictile fritillo* on foot, and bronze *theca cilindrica atramentaria con coperchio* 40
2.2 Samples on carbon tape, mounted on the SEM nine-holes stage. 41

2.3 SEM secondary electrons image of the seven samples (P3897 has two distinct morphologies) (20kV, WD=7.4mm) 42
2.4 2D diffractions patterns of Pompeii and Herulaneum black powders (60keV, PerkinElmer detector, ID22–ESRF). The pictures are 512x512 pixels out of 4096x4096 to obtain a better view of the single-crystal signal. The direct beam position is corresponding to the bottom corner of each image (Black dot = mostly-amorphous powders, red dot = single-crystal-rich, orange dot = single-crystal-rich). 44
2.5 Separation of single-crystal and powder contribution from a 2D diffraction pattern portion of sample P18109. 45
2.6 Influence of the percentile on the single-crystal/powder contribution separations. (A) P=0.01, the percentile is too low and powder rings are assimilated as single-crystals, the obtained powder pattern lacks some powder data. (B) P=0.95, the percentile is too high, some single crystals are not detected and the algorithm compensates with a negative signal, (C) P=0.30, the percentile is correctly chosen and the single-crystal signal remains positive. The single-crystal contribution is correctly removed. 46
2.7 Single-crystal contribution removal on sample P18109 from Pompeii. The sample contains mainly calcite in both powder and single-crystal forms. 46
2.8 Rietveld refinements of P18109 sample with and without the single-crystal contribution (ID22–60keV, Red = Fit, Blue/Green = Observed, Rwp = 6.1 and 5.62 respectively) 47
2.9 Single-crystal contribution removal on sample P9505 from Pompeii. The single-crystal contribution comes mostly from leucite, quartz and orthoclase. 48
2.10 Rietveld refinement of the 2D integrated diffraction patterns from sample P9505 (ID22–60keV, Red = Fit, Blue/Green = Observed, Rwp = 2.65 and 1.81 respectively) 48
2.11 Fluorescence spectrum of sample HE11. Intensities are in log scale, energy in keV. Elements with Z<18 are not present due to the absorption in the air. 51
2.12 Rietveld refinement of P18109 HR-XRPD pattern.(Red = Fit, Blue = Observed, Rwp = 15.2, Rexp = 3.10, Rp = 11.0) 51
2.13 Rietveld refinement of sample P9505 (Red = Fit, Blue = Observed, Rwp = 9.15, Rexp = 9.15, Rp = 6.26). 52
2.14 PDF of sample P2445 with the fit of the crystalline contribution mainly made of whitlockite. 54
2.15 PDF fit of sample P2445 (only one crystalline phase (whitlockite) is considered), the data was fit with an *r* value superior to 15 Å, then it was applied to the whole range (Rw = 0.82). The green curve represents the subtraction of the blue from the red. The two black dotted lines correspond to the two first carbon-carbon bond distances of a graphite layer (1.42 Å and 2.42 Å) 55
2.16 Comparison of the PDF signal of all the references with samples P2445 after subtraction of the crystalline signal. 56
2.17 PDFs of references and sample P2445 amorphous phase, normalized to the maximum value. By eye, P2445 resembles more to be originated from Vine tree or wood. The two black dotted lines corresponds to the two first carbon-carbon bond distances of a graphite layer (1.42 Å and 2.42 Å) 57
2.18 PDFs of all samples that comport peaks at 1.42 Å and 2.42 Å suggesting they contain amorphous carbon. The two black dotted lines corresponds to the two first carbon-carbon bond distances of a graphite layer (1.42 Å and 2.42 Å) 57
2.19 PDF fit of sample H75430, the data was fit with an r value superior to 15 Å, then it was applied to the whole range. The green curve represents the subtraction of the blue and the red. 59

3.1 (A) Pair of sandals from the tomb of Yuya and Tjuyu, New Kingdom, Thebes (ca. 1390-1352 B.C.), Metropolitan Museum of Art, Accession number 10.184.1a, b. (B) Papyrus fiber rope from Amarna, San Diego Museum of Man. (C) Papyrus of Séramon, XXIth dynasty, Thebes (ca. 1081-984 B.C.), Bibliothèque nationale de France, Inv.53.1. 67
3.2 Cyperus Papyrus plant in a swamp in Uganda ©Andreas Schieber. (B) Two cross-section cuts from Cyperus Papyrus stem. EP: epidermis, VB: vascular bundle, PC: parenchyma cells, PH: phloem, MX: metaxylem, BS: bundle sheath [61] 68
3.3 Papyrus paper manufacturing steps (Le papyrus comme support d'écriture, E. Menei [66]). (A) Stem cut into strips, (B) First layer of strips, (C) Strips laid down on top with 90 degrees angle, (D) Final product after pressing and drying. . 69
3.4 Hiergoglyph of the scribe representing the three tools used for writing (left). Palette inscribed for Smendes, High Priest of Amun, Third Intermediate Period, Thebes (ca. 1045-992 B.C.), Metropolitan Museum of Art, Accession number 47.123a-g. 69
3.5 Painter's Palette Inscribed with the Name of Amenhotep III (Ivory), New Kingdom, Thebes (ca. 1390-1352 B.C.), Metropolitan Museum of Art, Accession number 26.7.1294. 70
3.6 3D modeling steps of the holder of papyrus fragment PAP-12 75
3.7 Experimental setup on ID22 beamline with papyrus fragment PAP-12 mounted on the 3D printed support. 76
3.8 Design steps of papyrus sample holder for SEM observation and EDX. (A) Aluminium holder (left), drilled nickel sheet with three holes covered with the gold grids (right), (B) Gold grid laid on the nickel sheet. (C) Cut view of the superposition of all the elements of the support. 76
3.9 Papyrus fragment PAP-4 from Champollion collection, papyrus stripes are stacked in two layers, 90° apart 78
3.10 SEM image in SE2 mode of blank papyrus surface, red stripes show the limitation between papyrus cells. 79
3.11 (A) SEM image from PAP-1 blank papyrus area (1kx, 20kV, WD=8.3mm), (B) EDX spectra from five points, and one map (spectrum 6) from PAP-1 papyrus support. 79
3.12 XRF signal of eleven measurement points of blank papyrus from PAP-1 (incident energy : 31.0 keV) 80
3.13 Fluorescence signal averaged over eleven points of blank papyrus from PAP-1 . . 80
3.14 Rietveld refinement of a powder diffraction pattern recorded on the papyrus support of PAP-1 (λ= 0.4009Å). The I_β structural model was used for both Cellulose_p1 and Cellulose_p2 (Blue: experimental data, Red: calculated pattern, Grey: difference curve, Rwp = 5.13). Black arrows indicate non-indexed diffraction peaks. 81
3.15 XRD signal of six measurement points recorded on black papyrus from fragment PAP-1. Insert: 200 reflection of cellulose. The two arrows indicate the presence of the two contributions. Data have been normalized on the diffraction peak at 5.51°. 82
3.16 (A) 3D model of fourth-order spherical harmonics of cellulose structure. (B) Evolution of the lattice showing the potential distortion and the delamination of the polymeric chains. 83
3.17 Champollion museum colored fragment set. (Nikon D3200, 50-200mm lens) . . 84
3.18 XRD measurement point locations on papyrus fragment PAP-6 85
3.19 (A) 2D diffraction pattern of sample PAP-6 on measurement point 1. (B) 1D diffraction pattern of papyrus PAP-6 on measurement point 1. Weddellite, whewellite and cellulose are present but not shown in the phase identification. . . 86

3.20 Pawley fit of measurement point 2 of fragment PAP-6. (Red = Fit, Blue = Observed) 87
3.21 Rietveld refinement of measurement point 6 of fragment PAP-6. (Red = Fit, Blue = Observed, Rwp = 2.58, Rexp = 2.85, Rp = 1.56) 87
3.22 Rietveld refinement of measurement point 3 of fragment PAP-6. (Red = Fit, Blue = Observed, Rwp = 1.2, Rexp = 22.85, Rp = 0.65) 87
3.23 Rietveld refinement of point 5 of PAP-6. Calcite was added using pattern matching refinement to fit the peak at 7.6°, coming from single-crystal diffraction behavior. Cellulose contribution was part of the background (Red = Fit, Blue = Observed, Rwp = 5.99, Rexp = 2.34, Rp = 3.95). 88
3.24 XRF map location with summed XRF spectrum and fit of the major elements. . . 88
3.25 XRF maps of major elements, each map represents the ROI around the main emission line (i.e. Kα or Lα) (mercury (Hg) map is displayed on a log scale). . . 89
3.26 Intensity measured for the arsenic Kα emission lines on two fluorescence spectra averaged from two ROI on papyrus fragment PAP-6. 91
3.27 (A) Papyrus fragment PAP-6 fluorescence mapping acquisition on the deceased's arms area. (B) Summed fluorescence spectra. 91
3.28 XRF maps of major elements, each map represents the ROI around the main emission line (i.e. Kα or Lα) 92
3.29 Visible ink layers superposition on papyrus fragment PAP-6. The deposition order is from left to right: raw papyrus, white, pink, red, yellow, blue and black. The layers are obtained by filtering colors from optical images. Any underdrawing not visible optically cannot appear in this view. 92
3.30 Location of the XRD measurement points made on papyrus fragment PAP-11. . . 93
3.31 Rietveld refinement of point 2 on fragment PAP-11. (Red = Fit, Blue = Observed, Rwp = 8.30, Rexp = 10.12, Rp = 4.98) 94
3.32 Rietveld refinement of point 1 on fragment PAP-11. (Red = Fit, Blue = Observed, Rwp = 7.37, Rexp = 10.78, Rp = 4.08) 94
3.33 (A) PAP-11 fluorescence mapping acquisition. (B) Fluorescence maps of copper Kα (Cu), iron Kα (Fe) and arsenic Kα (As). 95
3.34 Location of the XRPD measurement points made on fragment PAP-12. 95
3.35 Rietveld refinement of point 4 on fragment PAP-12. (Red = Fit, Blue = Observed, Rwp = 3.52, Rexp = 1.92, Rp = 2.00) 97
3.36 Rietveld refinement of point 5 on fragment PAP-12 (moolooite was refined with a Pawley fit). (Red = Fit, Blue = Observed, Rwp = 4.74, Rexp = 1.85, Rp = 1.85) . 97
3.37 Rietveld refinement of point 6 on fragment PAP-12. (Red = Fit, Blue = Observed, Rwp = 16.60, Rexp = 1.98, Rp = 7.21) 97
3.38 Pawley refinement of point 7 on fragment PAP-12. (Red = Fit, Blue = Observed, Rwp = 5.71, Rexp = 2.43, Rp = 3.69) 97
3.39 (A) PAP-12 fluorescence mapping acquisition (Map 1 (Table 3.6), 20x20 points of 250µm) on the cobra area.(B) Measured area with fluorescence maps of lead Lβ (Pb), iron Kα (Fe), arsenic Kα (As), and mercury Lα (Hg) 98
3.40 (A) PAP-12 fluorescence mapping acquisition (Map 2 (Table 3.6), 28x8 points of 250µm) in the column area. (B) Measured area with fluorescence maps of iron Kα (Fe), copper Kα (Cu), lead Lα (Pb) and mercury Lα (Hg). 98
3.41 (A) PAP-7 fluorescence mapping acquisition on "wheat" hieroglyph area. (B) Fluorescence maps of mercury Lα (Hg), iron Kα (Fe), and tin Kα (Sn). 99
3.42 Rietveld refinement of XRD data taken on the red ink from papyrus fragment PAP-7 (Red = Fit, Blue = Observed, Rwp = 1.47, Rexp = 20.87, Rp = 1.17). . . . 100
3.43 Optical observation of the visible parts of the preparatory drawings on papyrus fragments PAP-6 and PAP-12. 100

3.44 Illustration of Re's beak shape and the placement of yellow paint on papyrus fragment PAP-6, compared to the black contour 101
3.45 Optical microscope image (x20) of papyrus fragment PAP-12 on a cuprorivaite-rich area 102
3.46 Chart that represents the percentage of mineral elements present in the ink or paints from the three papyrus fragments PAP-6, PAP-7, and PAP-12. He=Hematite, Sy=Syngenite, Gy=Gypsum 103
3.47 Optical microscope image (x20) of papyrus fragment PAP-12 on a yellow area. Black circles indicate the area of realgar grains. 104
3.48 Scanning electron microscopy images in SE2 mode. (A) Papyrus fragment PAP-10 surface on white pigment area. (B) Image of a KPb_2Cl5 crystals 106
3.49 Degradation reaction paths from malachite to moolooite according to Castro *et al.* [82] (OA=Oxalic Acid). 106
3.50 Papyrus fragments from the Champollion collection used to investigate the black pigments. The pictures were taken with a Nikon D3200 camera equipped with a 50-200 mm lens (ISO-200, f/8, exposure time 1/160 sec, focal length 102 mm, dimensions 6016x4000 pixels, and resolution 300 dpi). 109
3.51 (A) Raman spectrum recorded on the black scepter, of god Re from papyrus fragment PAP-6 (B) Fit of the D and G Raman bands of carbon using a 2-band model, (C) Width as a function of position for the G band, (D) Width as a function of position for the D band. 110
3.52 SEM observations of (A) Ink at the surface of PAP-1, (B) Kremer pigmente lampblack pigment. 111
3.53 SEM observation of six carbon pigment references. 112
3.54 (A) EDX spectra recorded on a map at the surface of PAP-1, with corresponding SEM secondary electrons image (20kV, WD=8.2mm) (B) EDX spectra recorded at five different positions at the surface of PAP-1, with corresponding SEM backscattering image (20kV, WD=8.2mm) in the insert. A Sn cluster was identified. 113
3.55 XRF investigation of PAP-6 and PAP-7. (A) An XRF map was retrieved from the deceased's arm of PAP-6. The lead-based contrast on the four stripes of the garment is most probably related to the presence of lead white used to color the white cloth and the skin. (B) The XRF mapping carried out on the 'mouth' hieroglyph of PAP-7 shows a lead-based contrast. (C) XRF-CT of PAP-8 fragment, the image is a transverse cut of the fragment and is build by overlapping contributions of elements K, Fe, As, Sn and Pb. 115
3.56 XRPD patterns taken on ink and ink-free areas superposed with lampblack diffraction pattern. 116
3.57 Diffraction patterns acquired in a vertical scan line on PAP-1, with and without subtraction. The diffraction peak at 1.9° seen on the first two patterns corresponds to kapton. 117
3.58 Average of two pairs of diffraction patterns acquired in a vertical scan line on PAP-1 (after papyrus subtraction). Patterns pairs were taken on both ink-rich areas. 117
3.59 XRD-CT experimental setup on ID11 with PAP-8 and PAP-9. 118
3.60 Optimisation of acquisition time in XRD-CT. The classic acquisition has Nx=Ny, in this case, Ny < Nx to match the sample shape. The reconstructed area is now an ellipse instead of a circle. 119
3.61 Starting point sinogram and corrected sinogram with correction steps. (see subsubsection 3.4.5) 120

3.62 Removal of single-crystal contribution process illustration from PAP-9 sample. (A) 2D diffraction pattern image with the single-crystal contribution. (B) Sinogram showing the single crystals as small dots. (C) Reconstruction presenting straight lines from single-crystal contribution. (D) Illustration of the effect of the separate algorithm, with the masking of the single crystals. (E) Single-crystal contribution-free sinogram, (F) Reconstruction with no single-crystals. 120
3.63 The three steps of XRD-CT leading to the obtaining of the ink signal. (A) and (B) Reconstruction and reverse analysis of the first corrected sinogram, (C) and (D) Reconstruction and reverse analysis of the first corrected sinogram after subtraction of the air in the diffraction patterns. (E) and (F) Reconstruction and reverse analysis of the first corrected sinogram after subtraction of the air and the papyrus signals in the diffraction patterns, with an ROI (see black rectangle) between Q = 1.35 $Å^{-1}$ and 1.84 $Å^{-1}$. Black arrows indicate non-identified phases. 121
3.64 XRF-CT and XRD-CT reconstructed slices of PAP-8 and PAP-9. (A) and (D) XRF-CT of PAP-8 and PAP-9 papyrus fragment, respectively. Iron signal and lead signal match the inked surface of the papyrus of PAP-8 and PAP-9, respectively. (B) and (E) XRD-CT of PAP-8 and PAP-9, respectively. The white color represents the summed diffraction signal and the orange color the contribution of the signal between Q = 1.35 $Å^{-1}$ and 1.84 $Å^{-1}$ (lampblack diffraction peak position). The contrast, concerning the presence of the carbon-based pigment in the ink, is obtained only after the subtraction of the average signal. Orange dots found away from the pigment signal correspond to undetermined crystalline phases. (C) and (F) XRD-CT reverse analysis after subtraction of an averaged signal of the blank papyrus, from the ink areas highlighted in orange in (B) and (E), respectively. The XRD pattern of a lampblack standard is given for comparison. The black arrows indicate diffraction peaks from additional unidentified crystalline phases. 122

List of Tables

1 Tableau 1 : Résumé des principaux résultats obtenus sur les échantillons noirs de Pompéi (P) et d'Herculanum (H). Les phases "volcaniques" sont traduites par la présence d'analcime, de sanidine, de leucite ou d'augite. Phases de dégradation (malachite, cassitérite); Charbon veg. = charbons végétaux; Cosm. = cosmétiques; Ox. de fer = oxyde de fer (magnétite). Les quatre catégories d'échantillons ont été mises en évidence avec des couleurs différentes. vi

2 Tableau 2 : Paramètres de maille des deux phases de cellulose (papyrus ancien) après affinement. Les valeurs de Nishiyama *et al.* [11], correspondant à la cellulose "moderne", sont également données à titre de comparaison. ix

1.1 Phase identification of the crystalline phases contained in the set of reference samples from ID22 HR-XRPD setup (and 2D detector for amorphous samples) . 28

2.1 The three studies based on Pompeii black powders from Casa di Bacco House with the techniques used, the identified phases, and the containers. (FT-IR = Fourier-transform infrared spectroscopy, RS = Raman spectroscopy, EPR = Electron paramagnetic resonance spectroscopy, CG/MS = Gas chromatography-mass spectrometry) 39

2.2 7 samples from Pompeii (P) and six samples from Herculaneum (HE)) 40

2.3 Observations of seven powder samples. The type corresponds to the aspect of the powder at 100x, either in big chunks or spreads particles. 42

2.4 Table of the identified phases for each sample. The database used is PDF2-2003 on Diffrac.EVA V5.0. The phases are ordered by EVA semi-quantitative ratio S-Q. Phases in italics represent values of S-Q lower than 3%. 49

2.5 Principal identified phases with chemical formula and PDF2-2003 [52] reference numbers. 49

2.6 Quantification of crystalline phases of each sample containing mostly powder contributions (ID22–HR-XRPD–31keV). *Refined with Pawley fit because of SC contribution, not taken into account for the quantification 52

2.7 PCC values for each sample compared to four references. (*) Subtraction of the crystalline phases not conclusive. 58

3.1 Set of twelve papyrus fragments from Champollion museum collection 66

3.2 Summary of major minerals used as pigments in Ancient Egypt with their formula. The table contains the PDF2-2003 XRPD [52] database references that were used for the phase identifications. 72

3.3 Summary of the minerals found in recent studies on funerary papyrus. DM = Digital Microscopy, ATR-FT-IR = Attenuated Total Reflectance Fourier Transformed Infrared, XRD = X-Ray Diffraction, VIS = Visible Spectroscopy, SEM-EDX = Scanning Electron Microscopy Energy-dispersive X-ray Spectroscopy, PLM = Polarized Light Microscopy, XRF = X-Ray Fluorescence, PIXE = ParticleProton Induced X-ray Emission. 73

3.4 Elemental composition obtained from XRF analyses. For each fragment, several data points (the number of points is indicated in the second column) were collected on papyrus support. The resulting values correspond to the average signal over the number of measured points corresponding to the main emission line, divided by the value of potassium (K). 81
3.5 Lattice parameters found from Rietveld refinement of cellulose structure from XRPD pattern measured on PAP-1, ESRF ID22. 83
3.6 Measurements made on the papyrus fragments from the Champollion museum. XRF and XRD have in common the beam size (250x250µm) and a counting time of 1 second in XRF and 4 seconds in XRD (E=31keV). 85
3.7 Summary of all identified phases on papyrus fragment PAP-6 (cellulose, weddellite and whewellite phases are always present, thus not indicated). Phases that are probably present but not surely identified are written in italic. 86
3.8 Summary of all identified phases on papyrus fragment PAP-11 (weddellite and whewellite phases are always identified, thus not shown). Phases that are probably present but not surely identified are put in italic. 93
3.9 Summary of all identified phases on papyrus fragment PAP-12 (weddellite and whewellite phases are always identified, thus not shown). Phases that are probably present but not surely identified are put in italic 96
3.10 Summary of crystalline phases identified for each point measured by XRD. Weddellite, whewellite have been excluded from this table because it appears that they are always present in a small quantity in any measurement points made. In italic the phases resulting from a degradation effect. 107
3.11 Summary of the analyses of black pigments performed on each of the ten fragments (denoted PAP-1 to PAP-10) of the Champollion collection. 109
3.12 Elemental composition obtained from XRF analyses. For each fragment, several data points (the number of points is indicated in the third column) were collected on both ink and non-ink areas. The resulting values correspond to the average over the number of measured points, with the sum of the eight elements normalized to 100. Because of both detector setup and absorption from the air, only the elements with Z>18 were accessible. The energy calibration was achieved by collecting XRF data from iron, copper, silver, molybdenum, and lead foils and the processed using PyMCA software. 113

A

Physico-chemical analysis data

1 Pompei and Herculaneum samples

1.1 P2445

1.1.1 Diffraction patterns phase identification

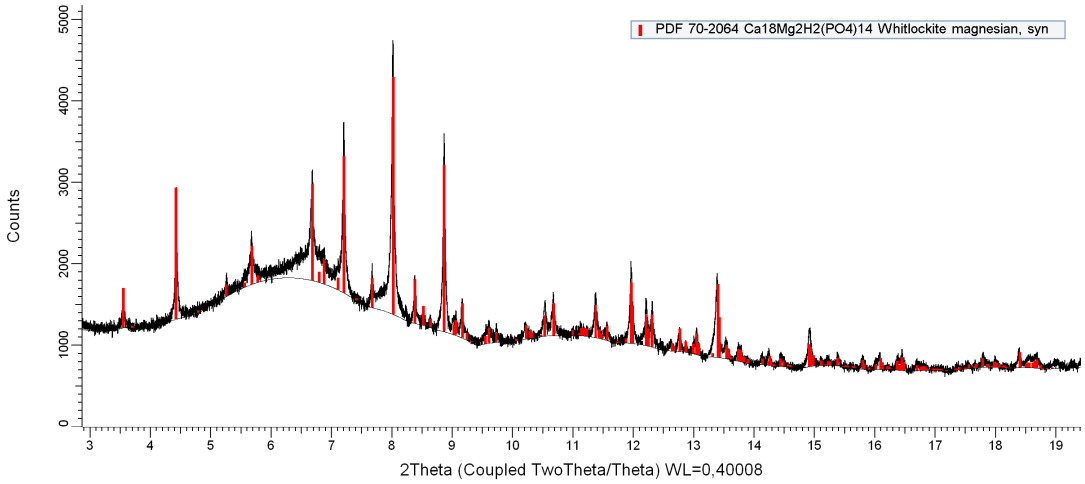

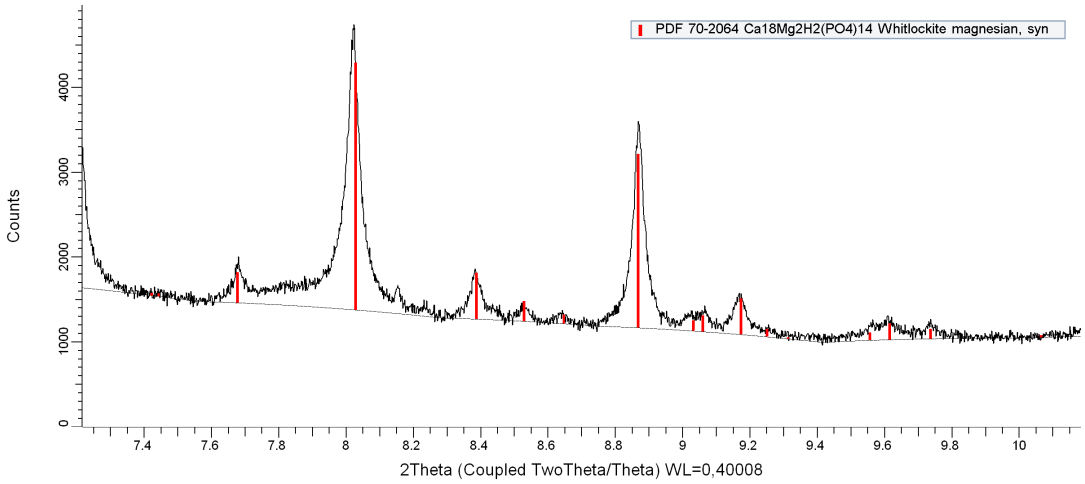

1.1.2 Diffraction patterns Pawley fit

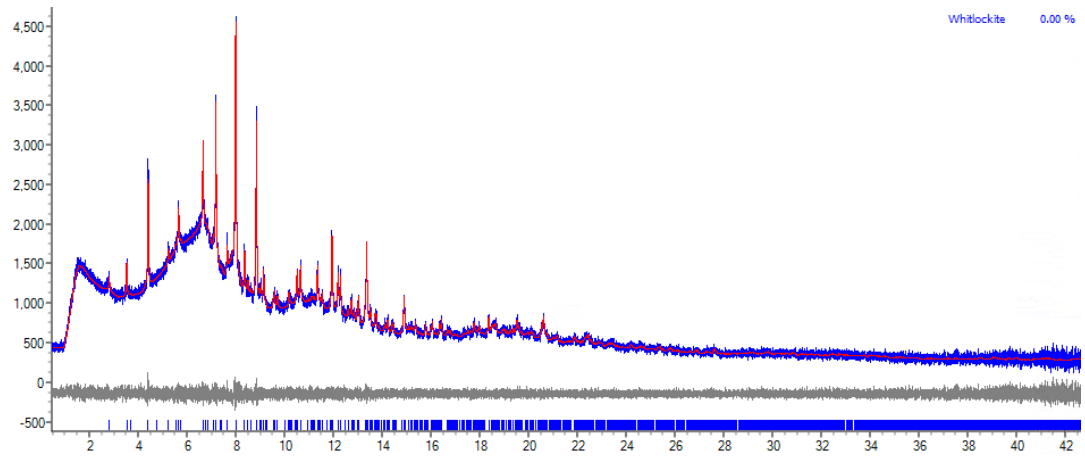

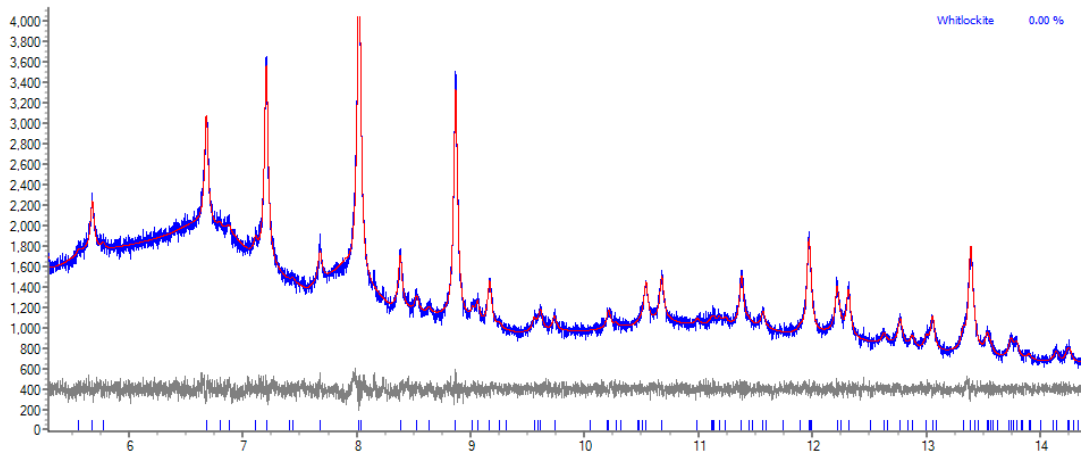

1.1.3 Diffraction patterns 2D and PDF

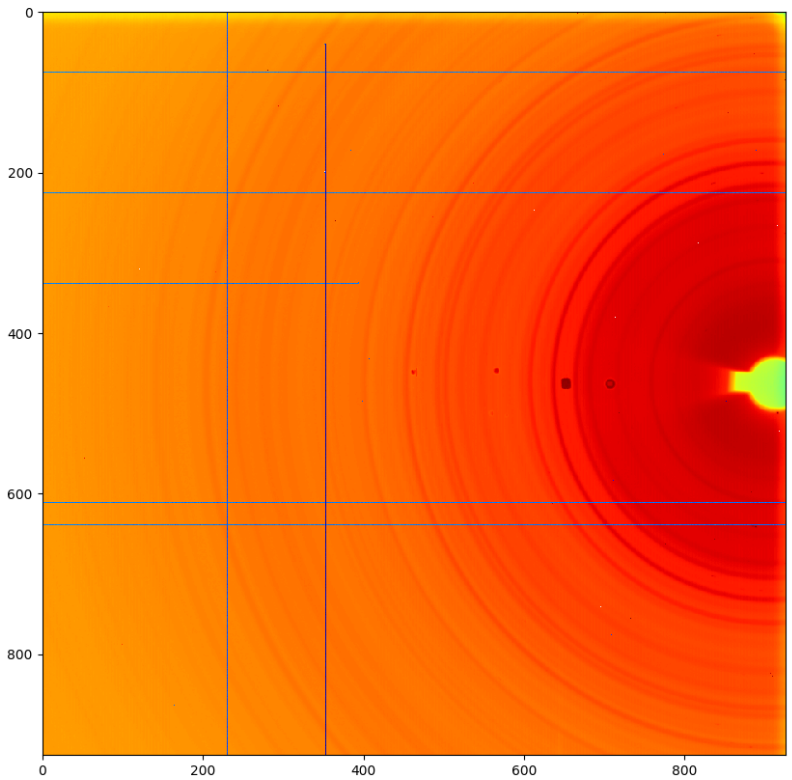

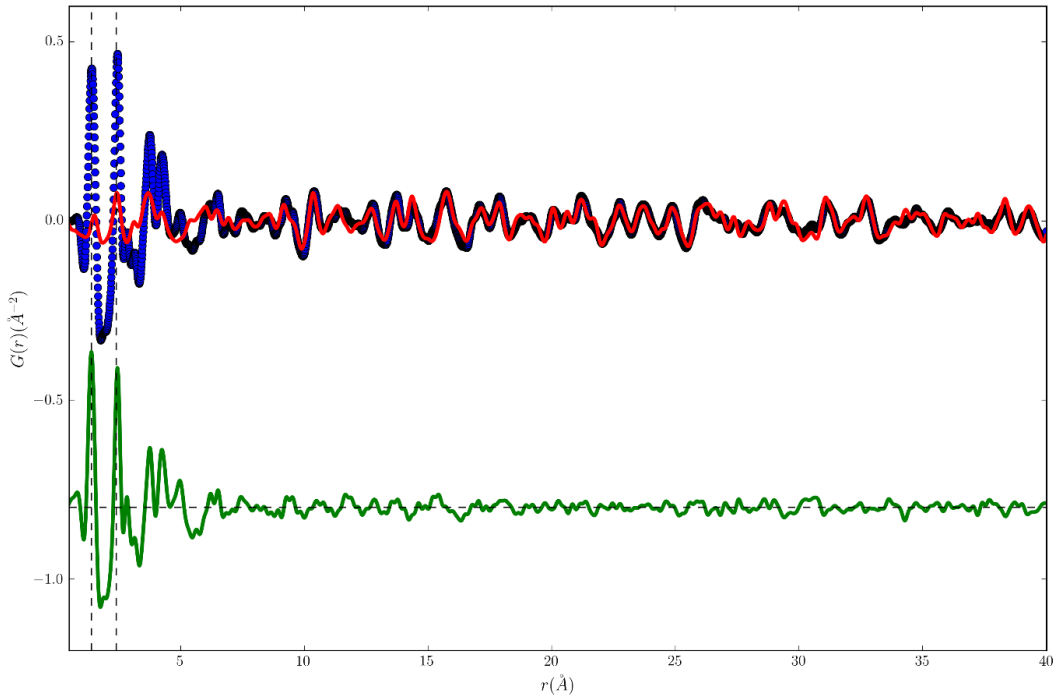
0.5
0.0
−0.5
−1.0
$G(r)(\AA^{-2})$
5
10
15
20
25
30
35
40
$r(\AA)$

1.2 P3897

1.2.1 Diffraction patterns phase identification

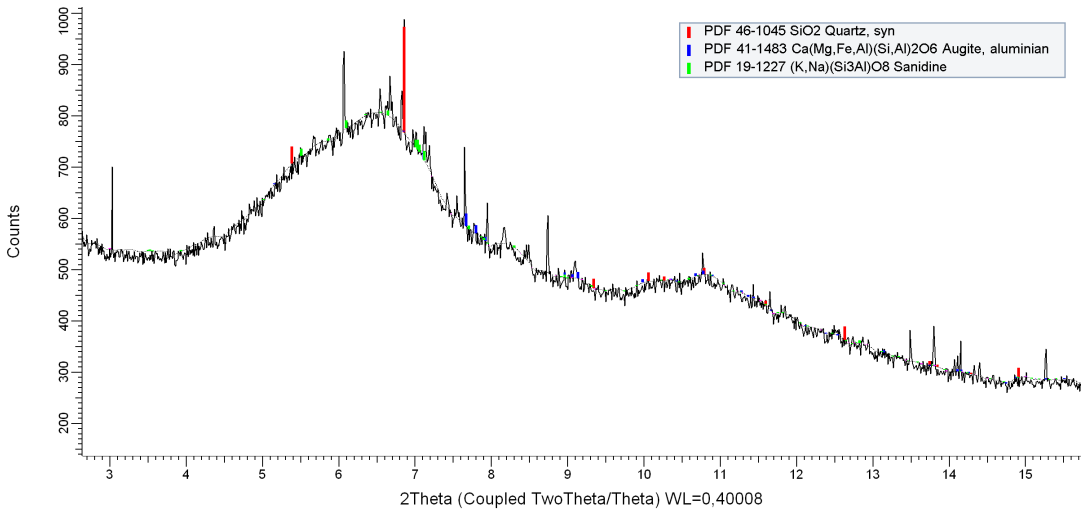

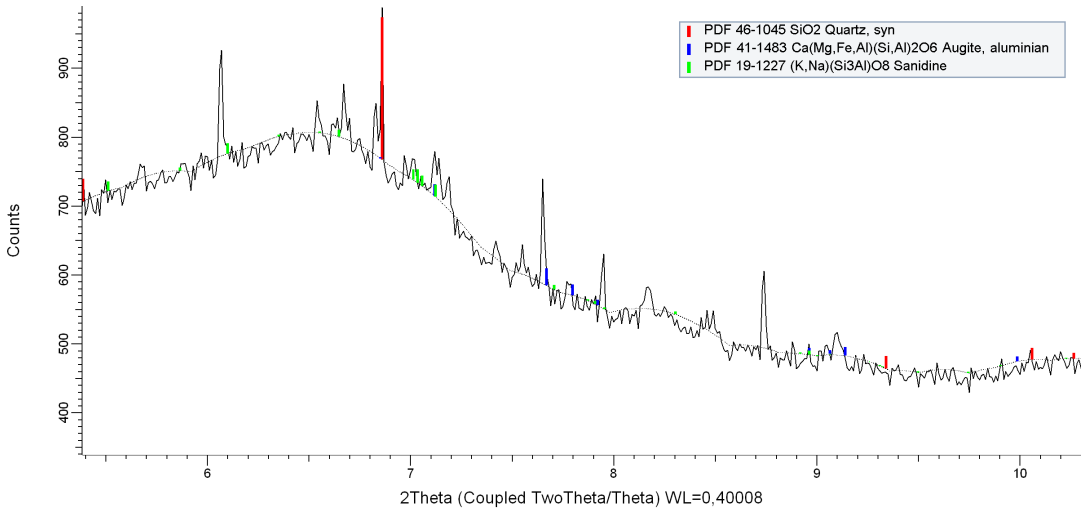

1.2.2 Diffraction patterns 2D and PDF

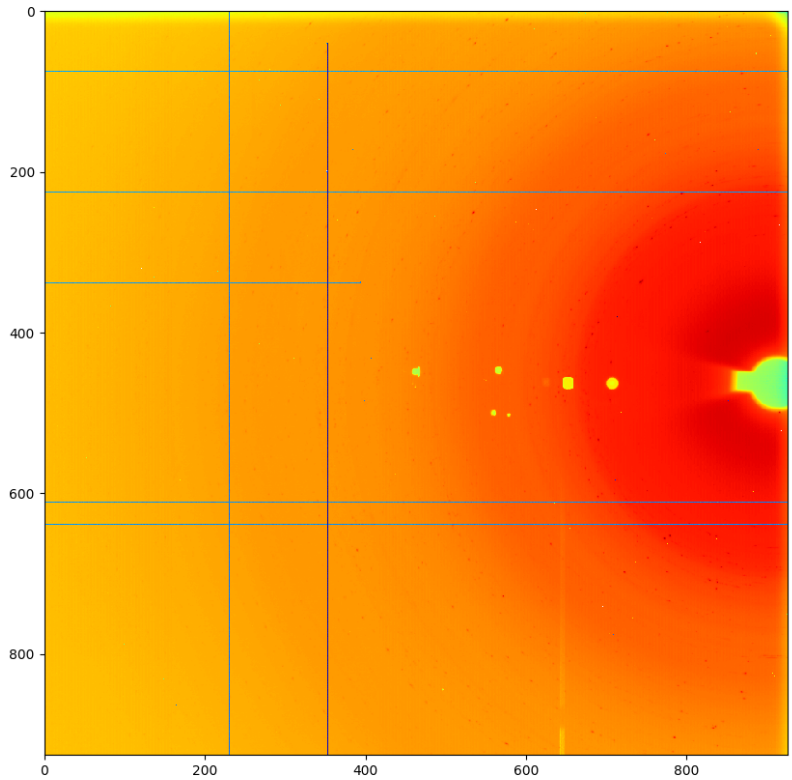

1.3 P9505

1.3.1 Diffraction patterns phase identification

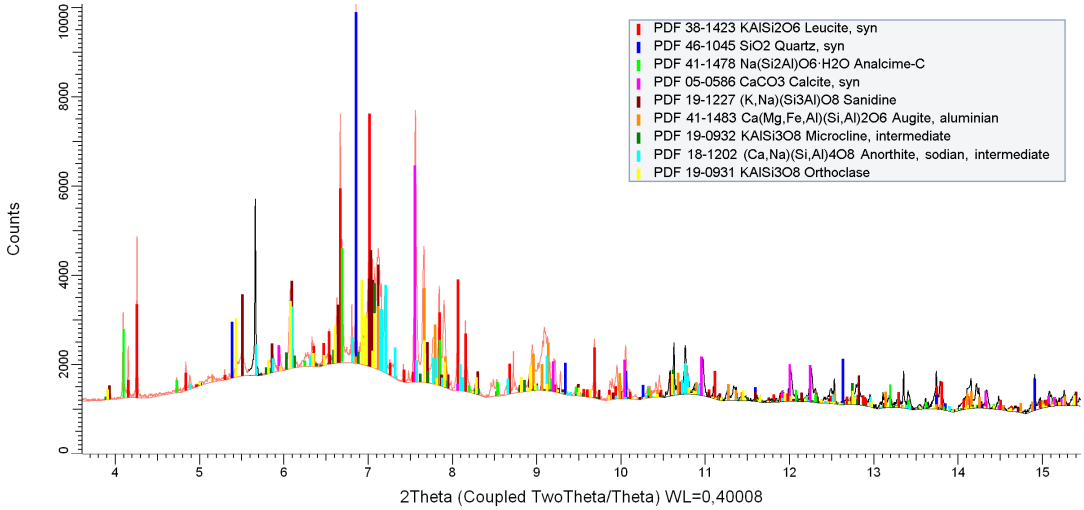

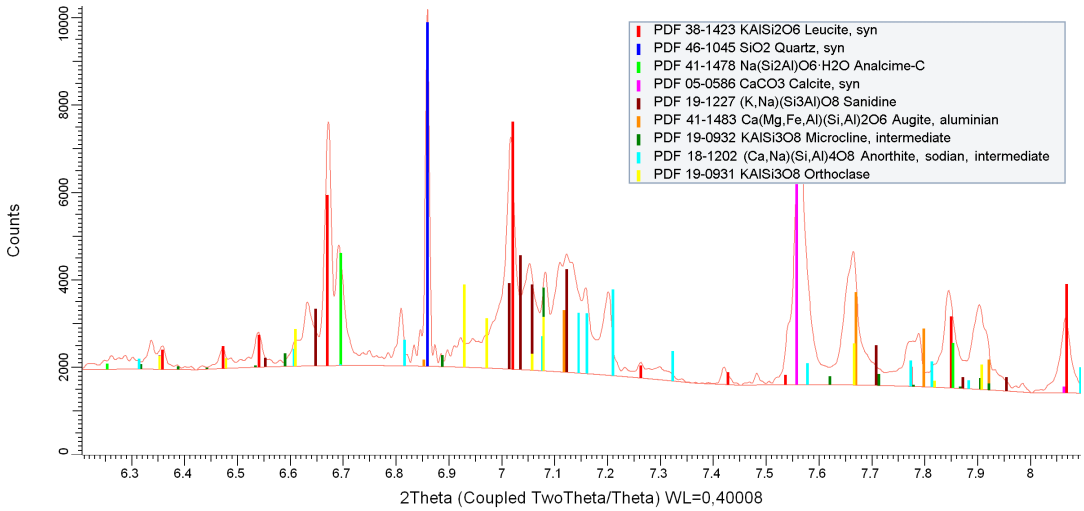

1.3.2 Diffraction patterns Pawley fit

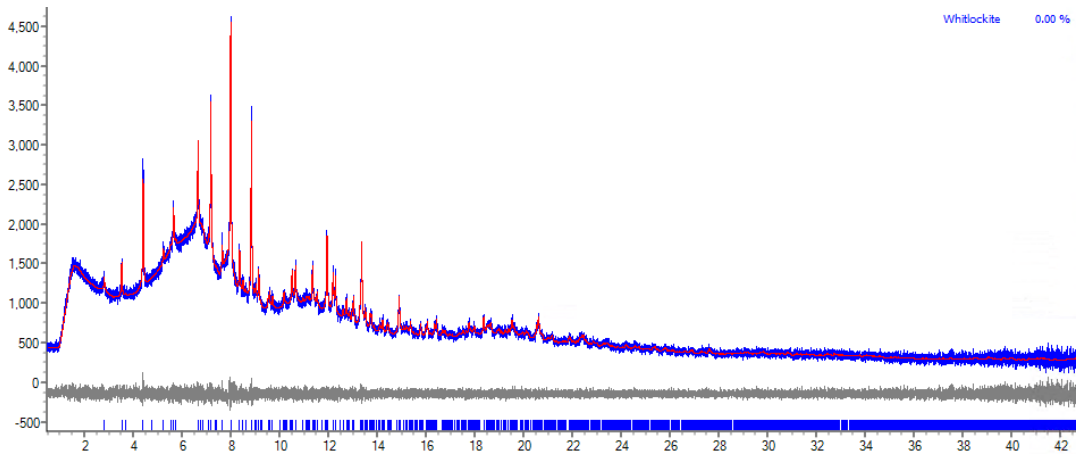

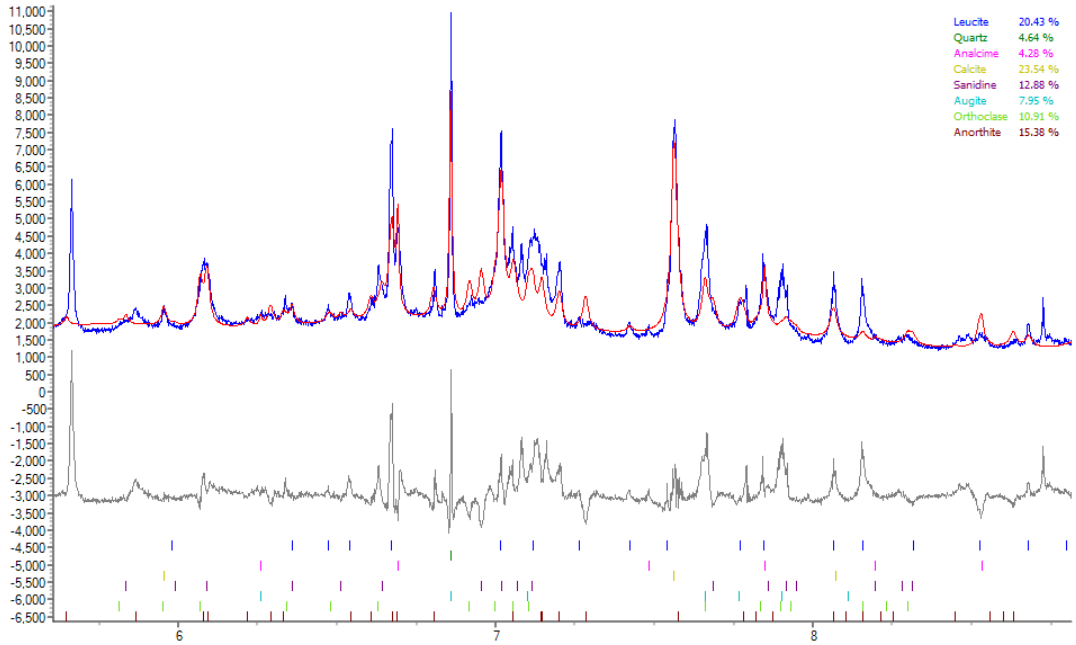

1.3.3 Diffraction patterns 2D and PDF

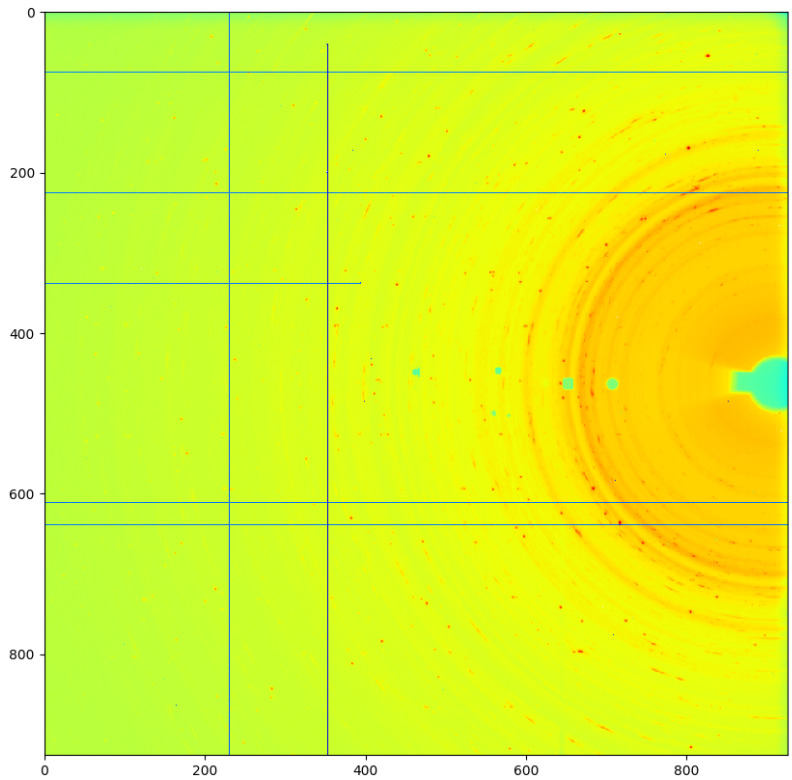

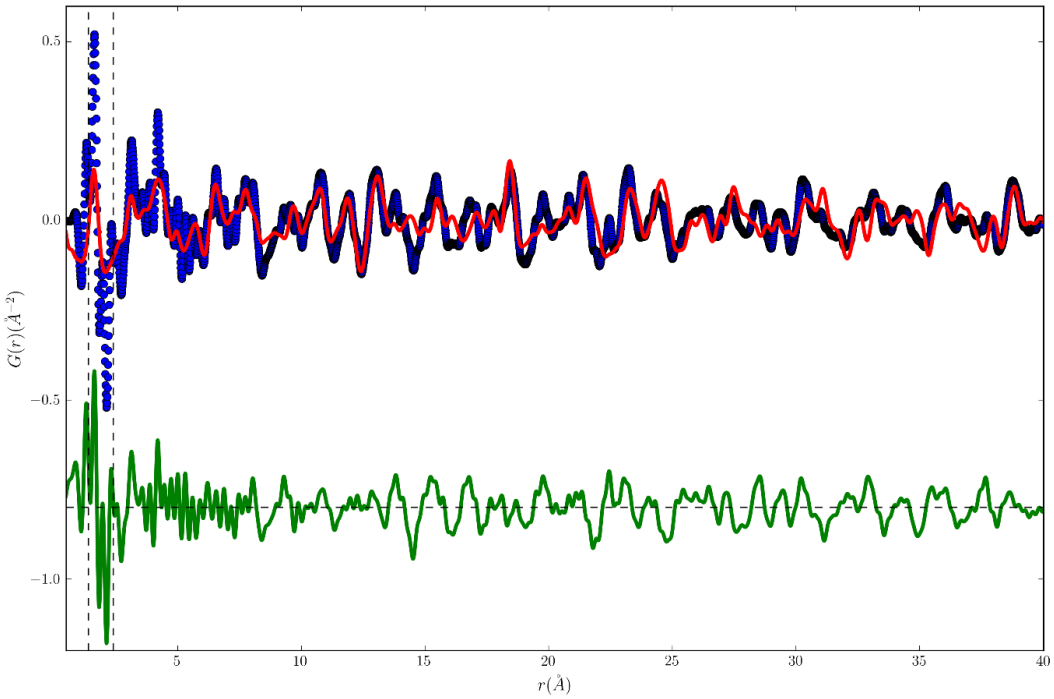
0.5
0.0
−0.5
−1.0
$G(r)(\AA^{-2})$
5
10
15
20
25
30
35
40
$r(\AA)$

1.4 P11432

1.4.1 Diffraction patterns phase identification

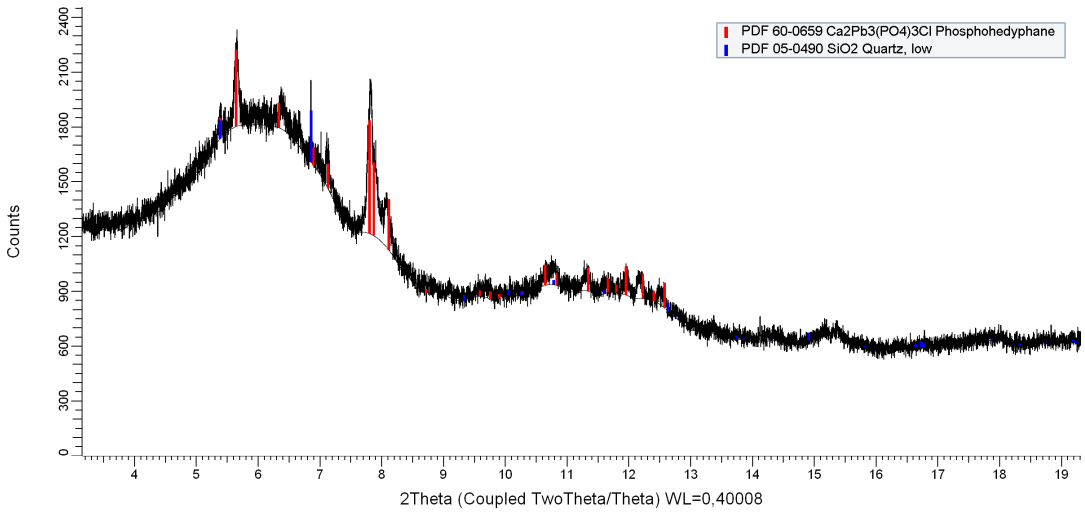

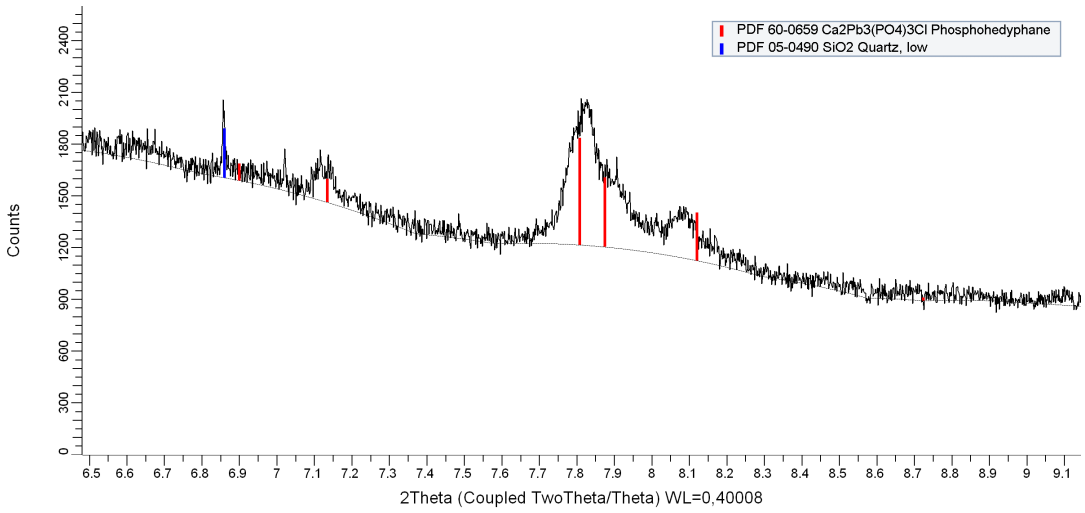

1.4.2 Diffraction patterns Pawley fit

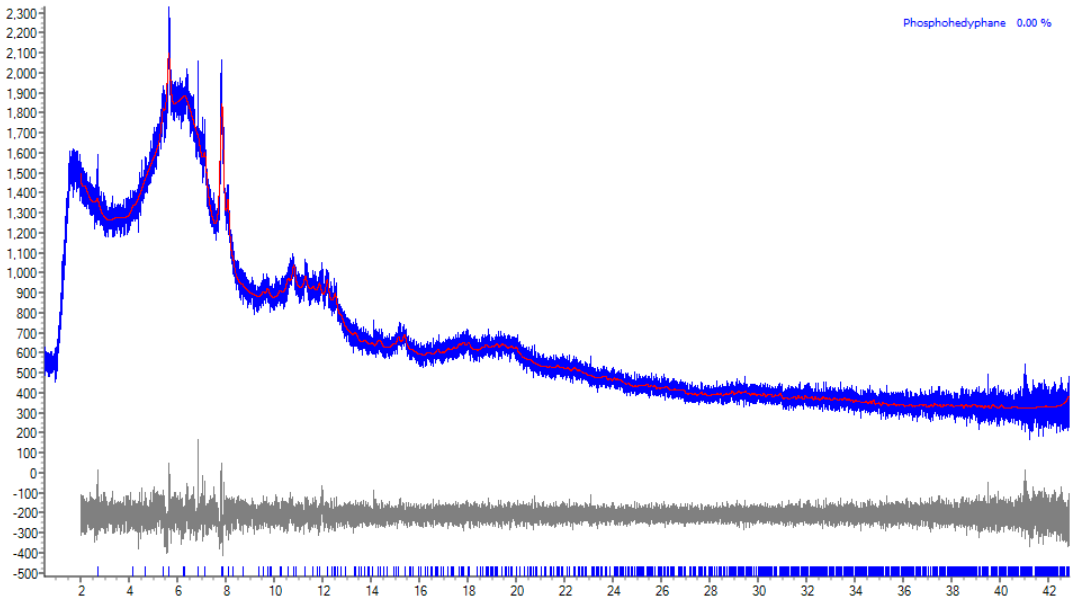

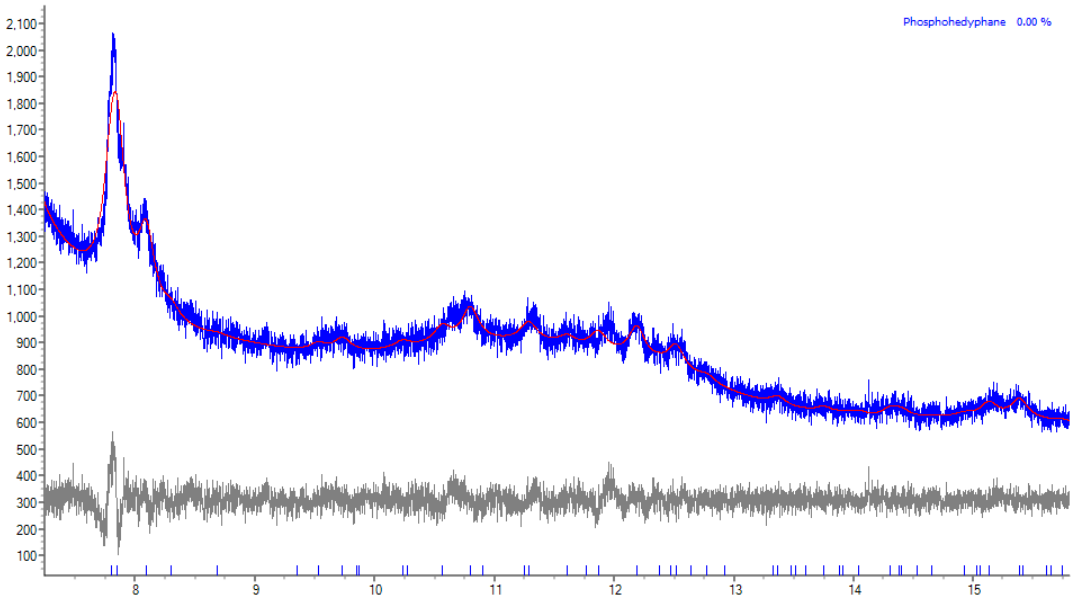

1.4.3 Diffraction patterns 2D and PDF

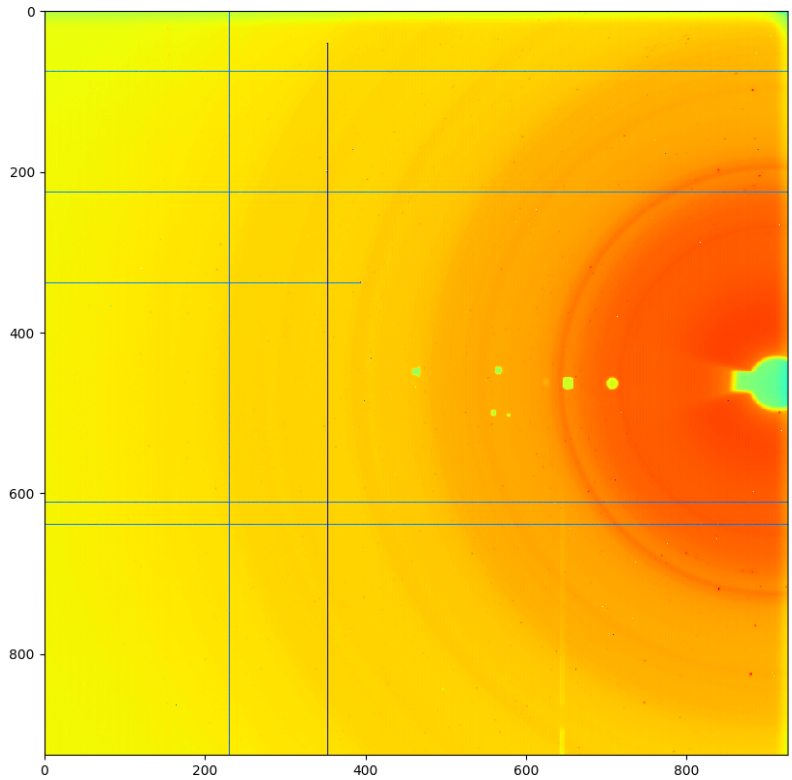

1.5 P12458

1.5.1 Diffraction patterns phase identification

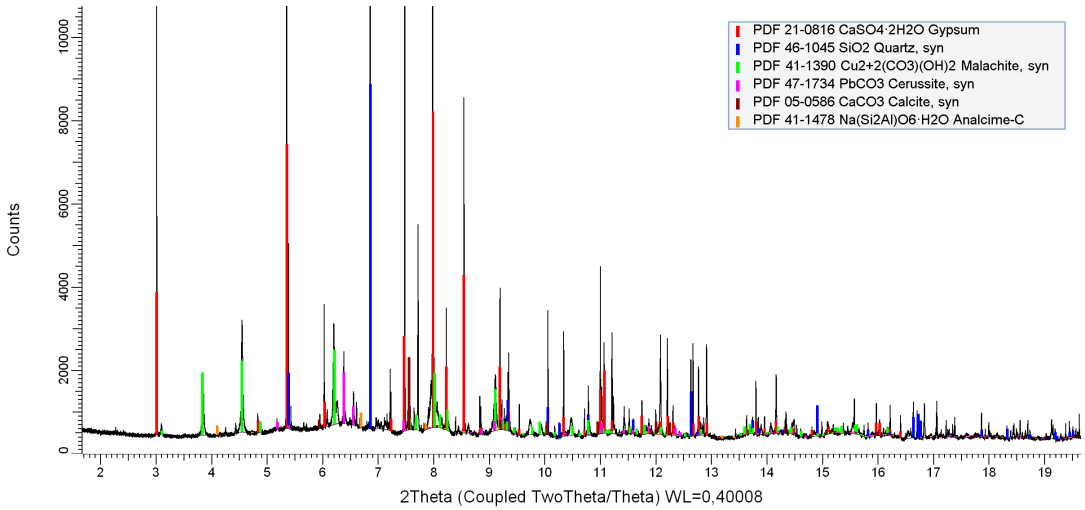

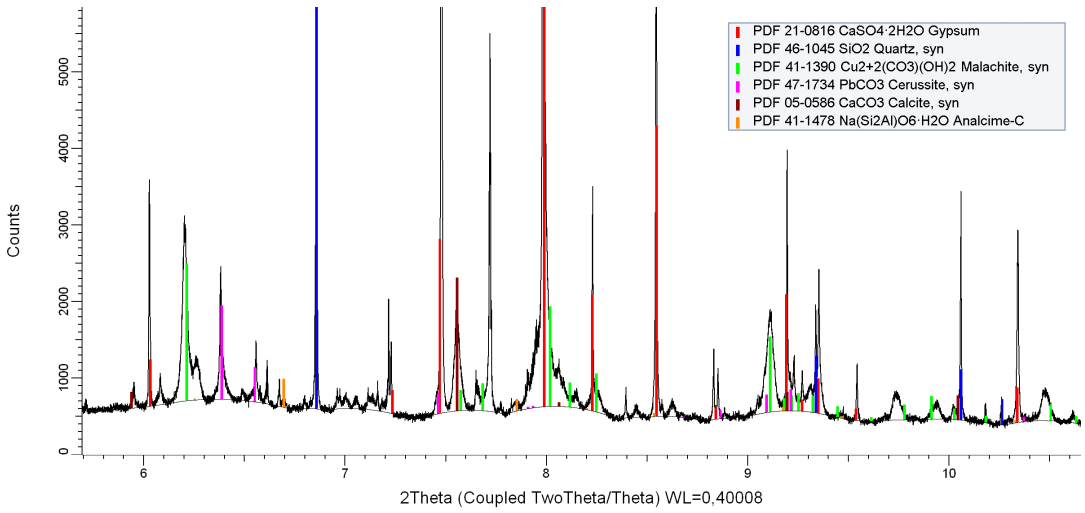

1.5.2 Diffraction patterns Pawley fit

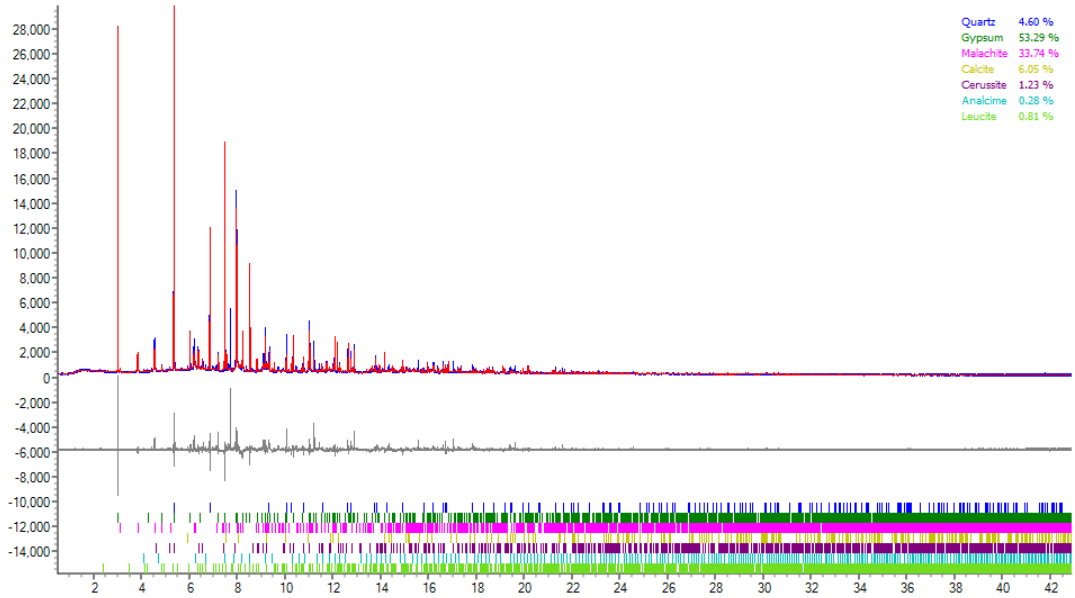

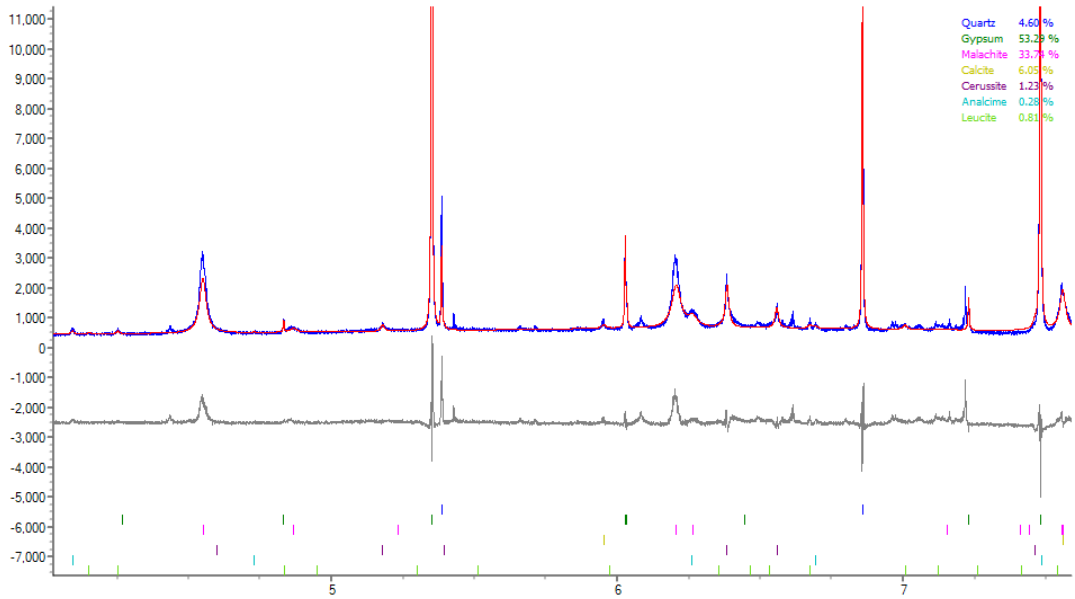

1.5.3 Diffraction patterns 2D and PDF

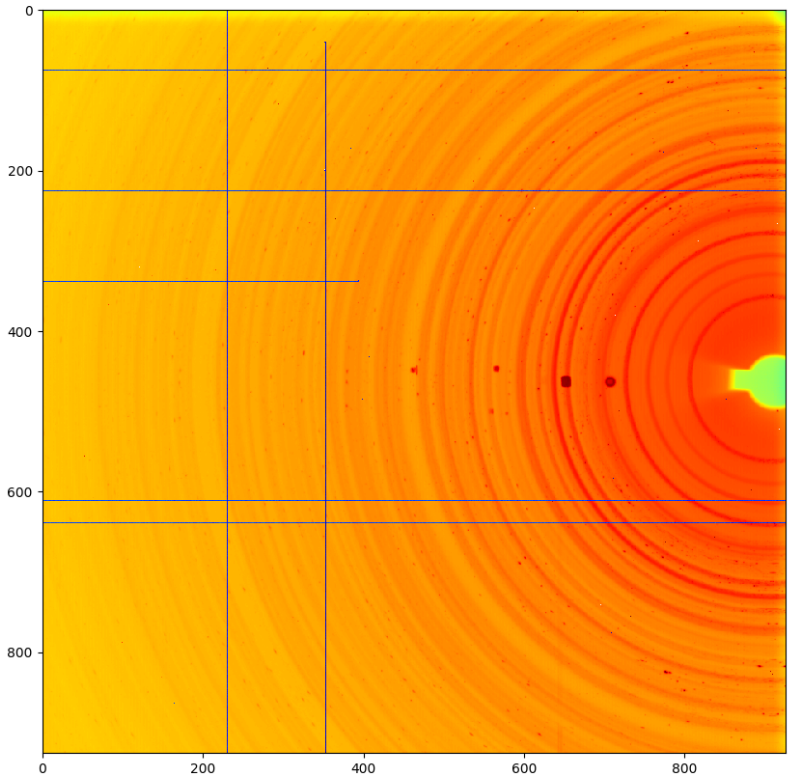

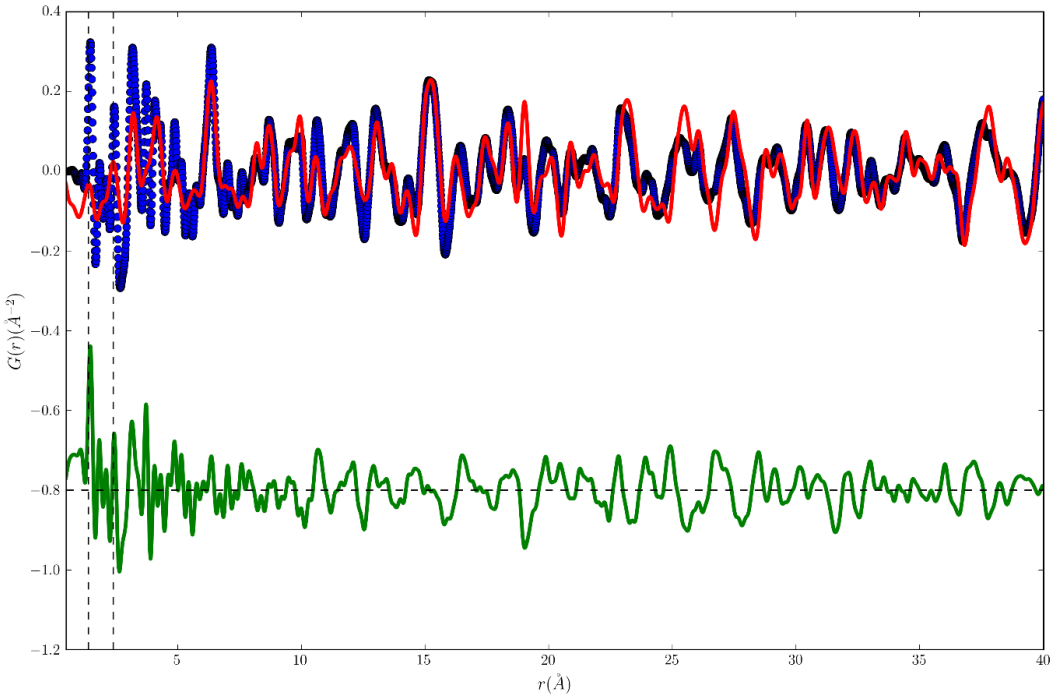

1.6 P18109

1.6.1 Diffraction patterns phase identification

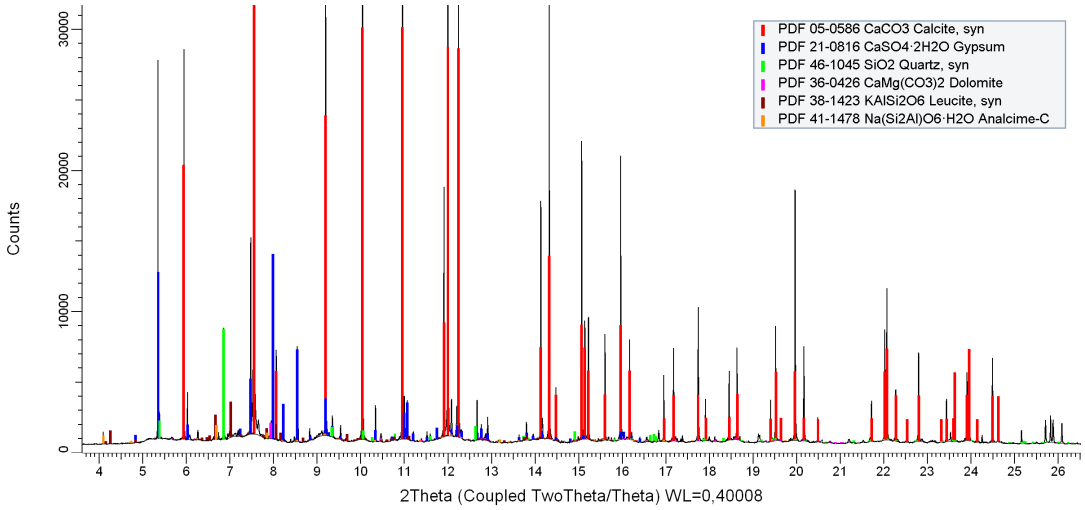

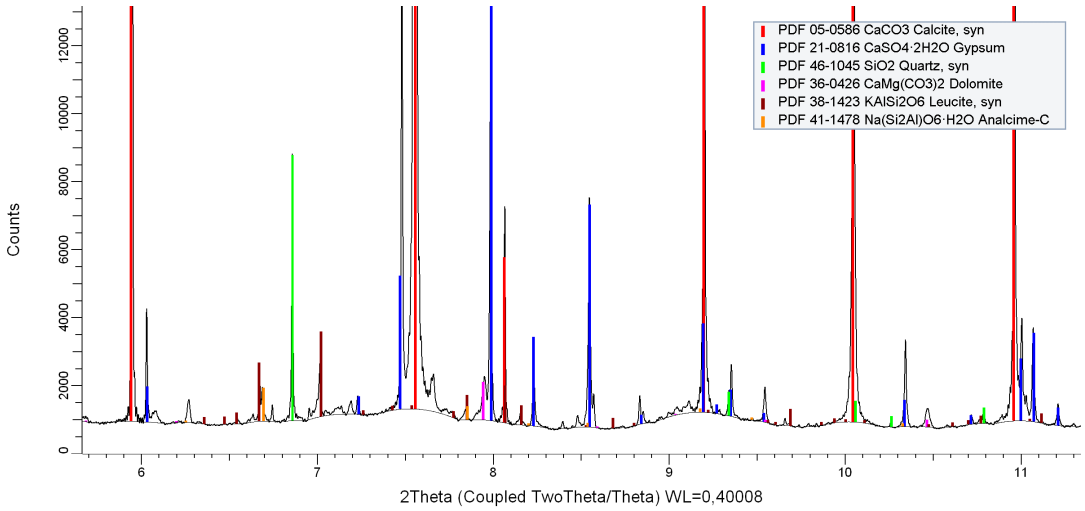

1.6.2 Diffraction patterns Pawley fit

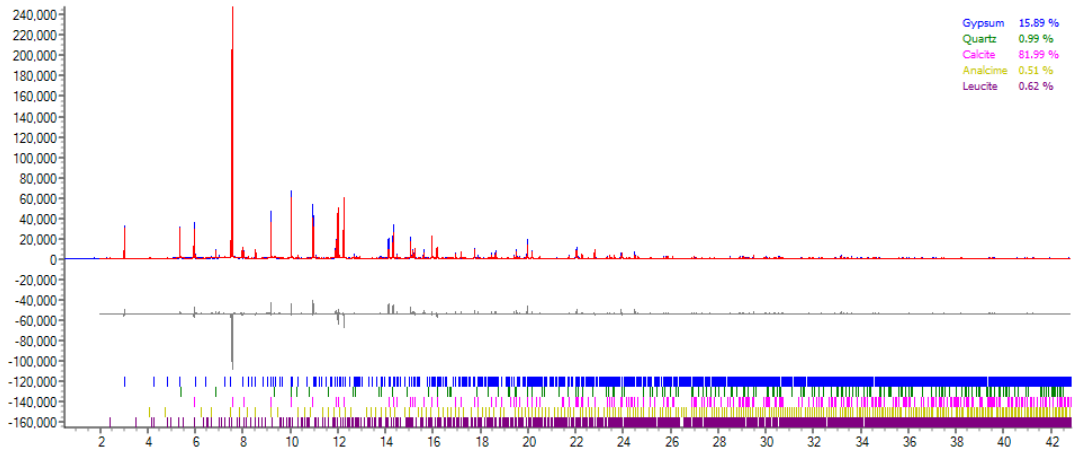

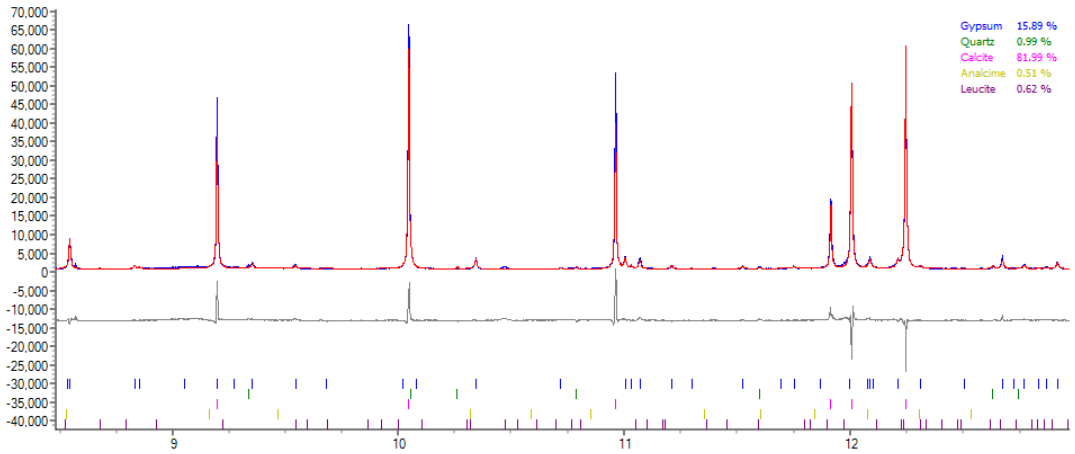

1.6.3 Diffraction patterns 2D and PDF

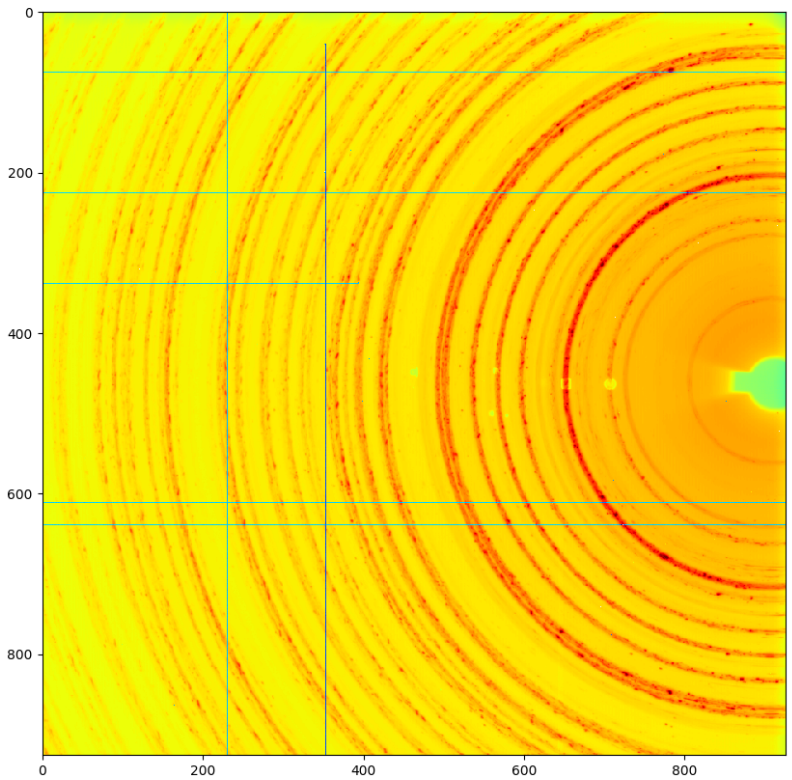

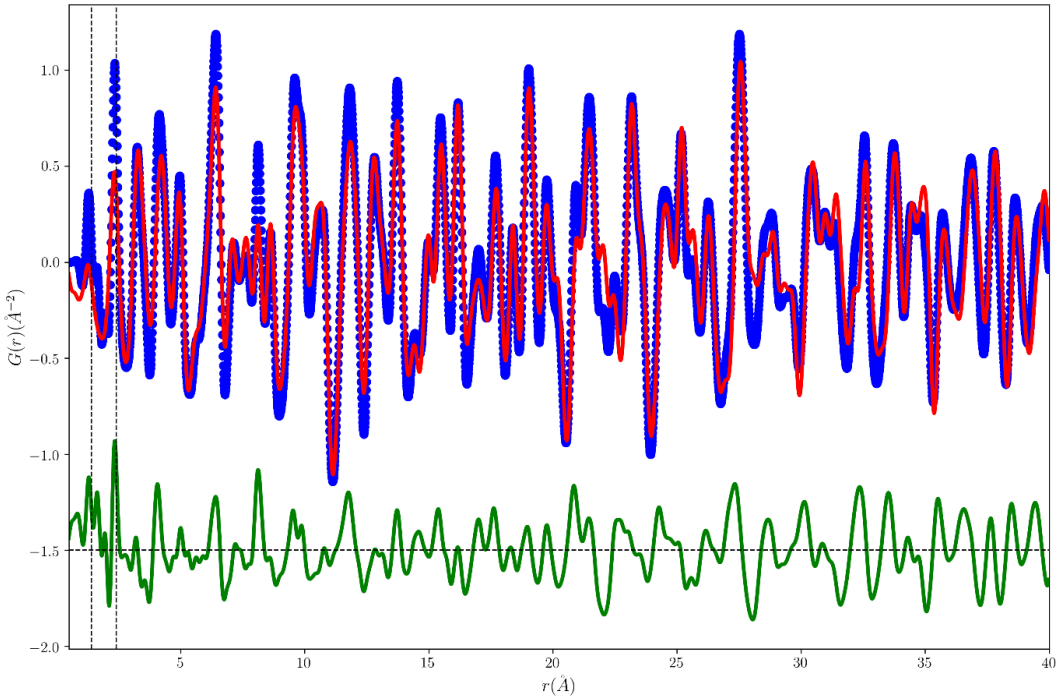
1.0
0.5
0.0
−0.5
−1.0
−1.5
−2.0
$G(r)(\AA^{-2})$
5
10
15
20
25
30
35
40
$r(\AA)$

1.7 HE02

1.7.1 Diffraction patterns phase identification

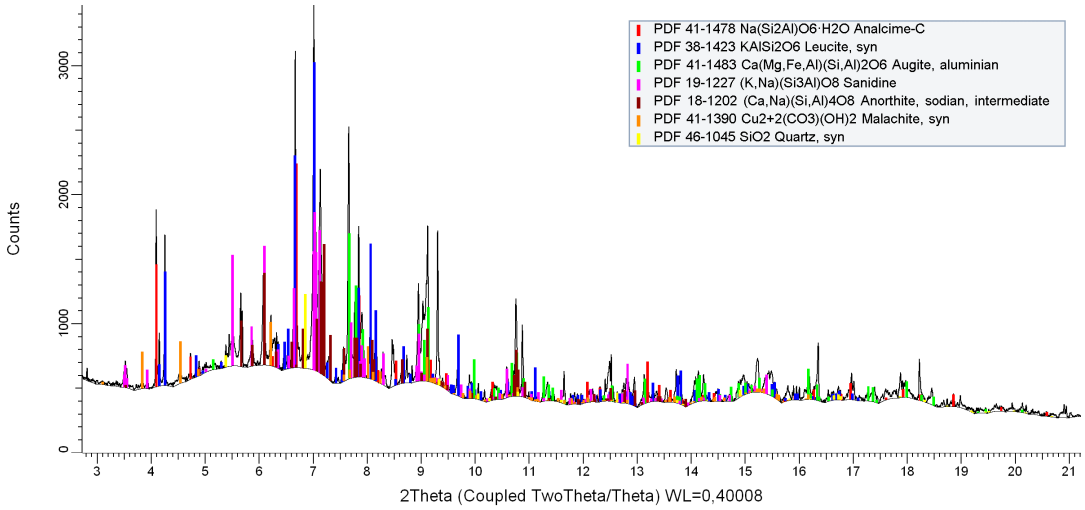

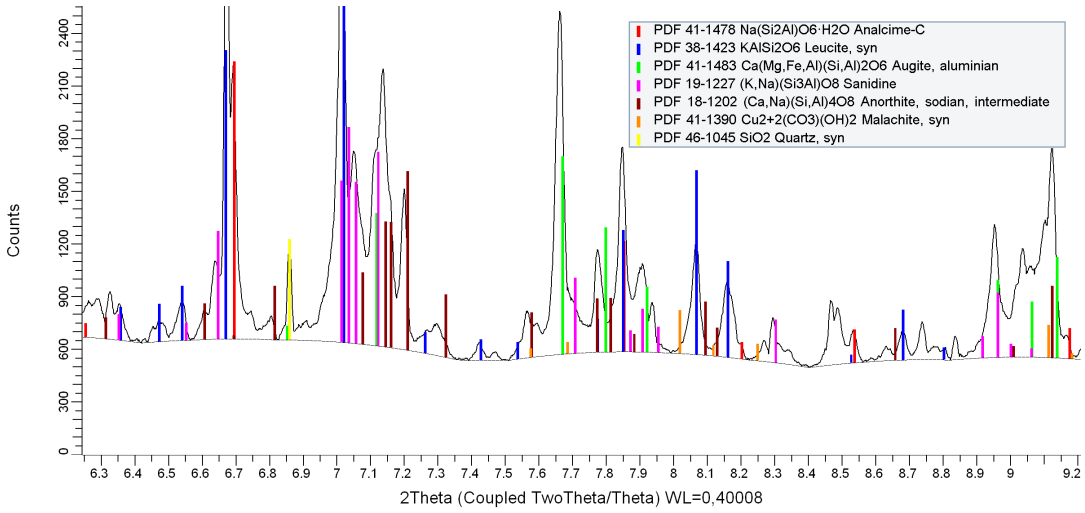

1.7.2 Diffraction patterns Pawley fit

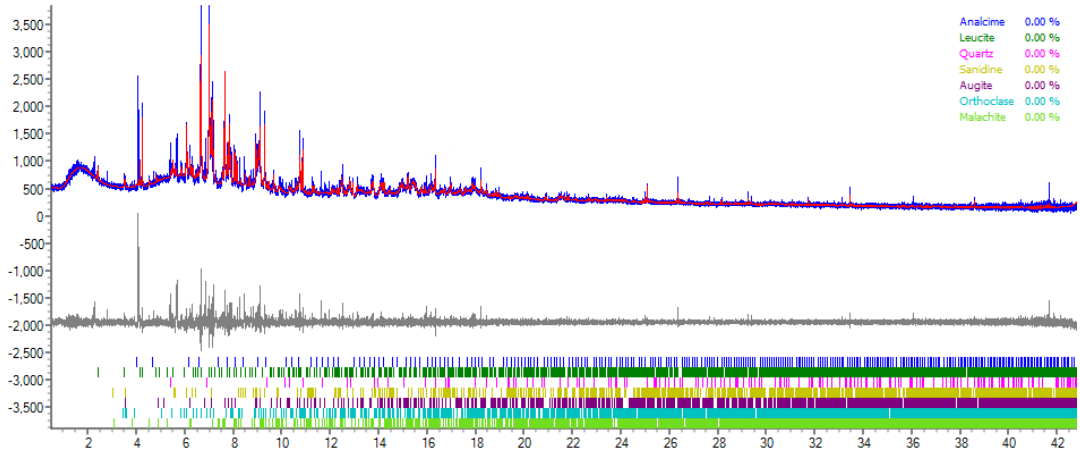

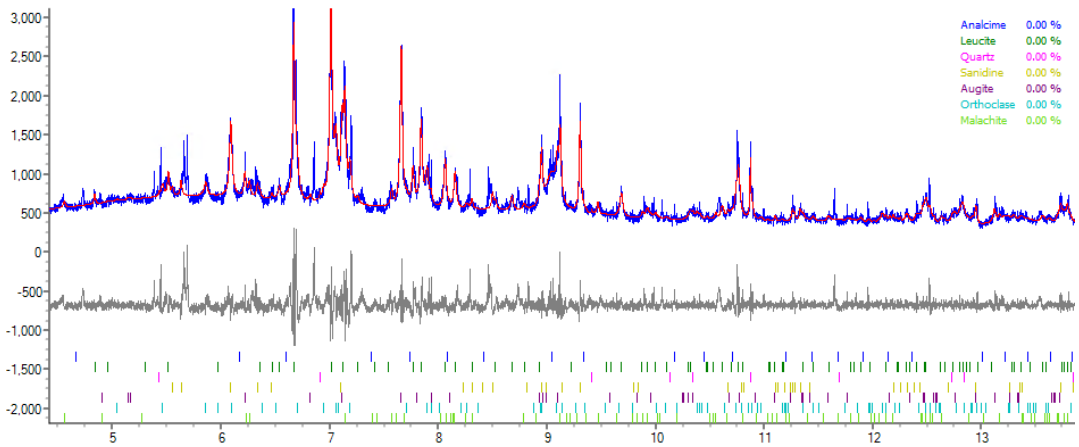

1.7.3 Diffraction patterns 2D and PDF

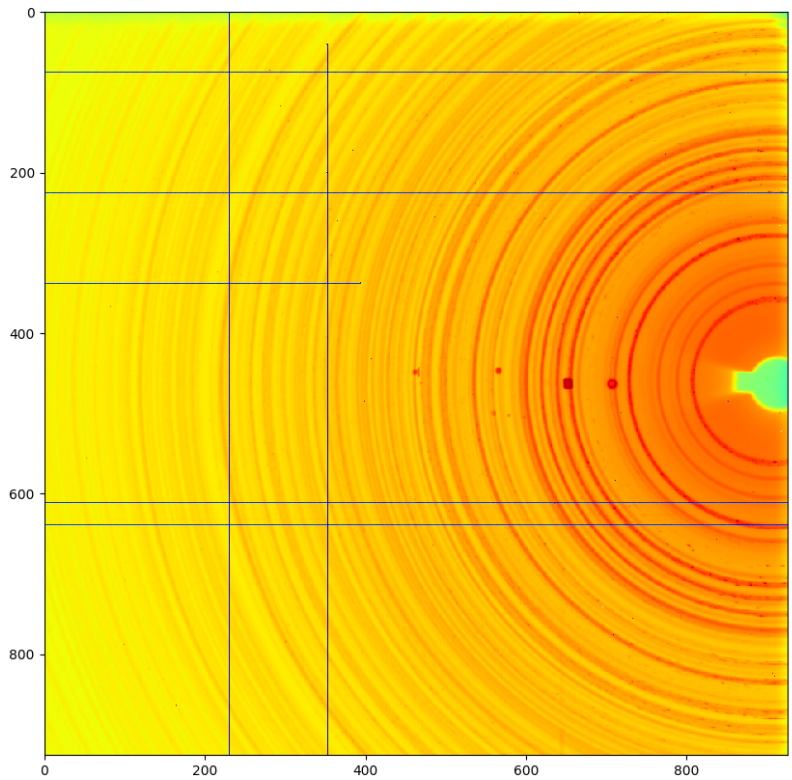

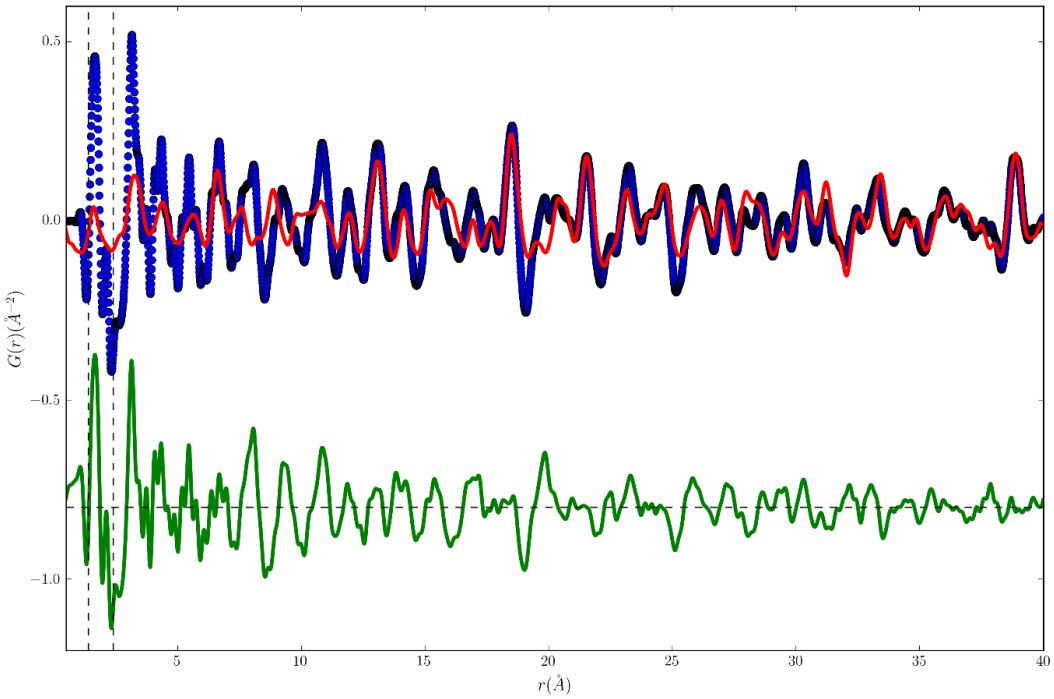
0.5
0.0
−0.5
−1.0
$G(r)(\AA^{-2})$
5
10
15
20
25
30
35
40
$r(\AA)$

1.8 HE03

1.8.1 Diffraction patterns phase identification

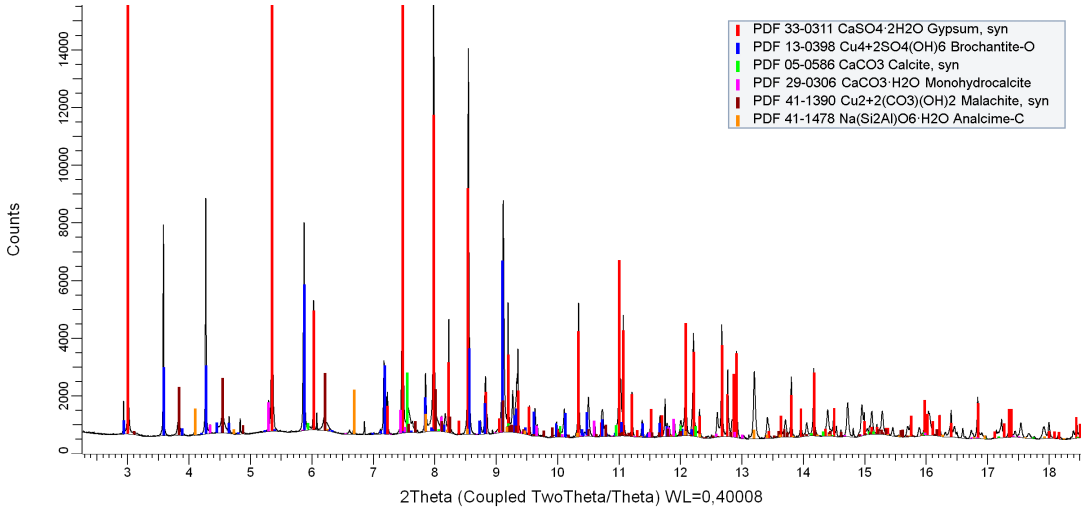

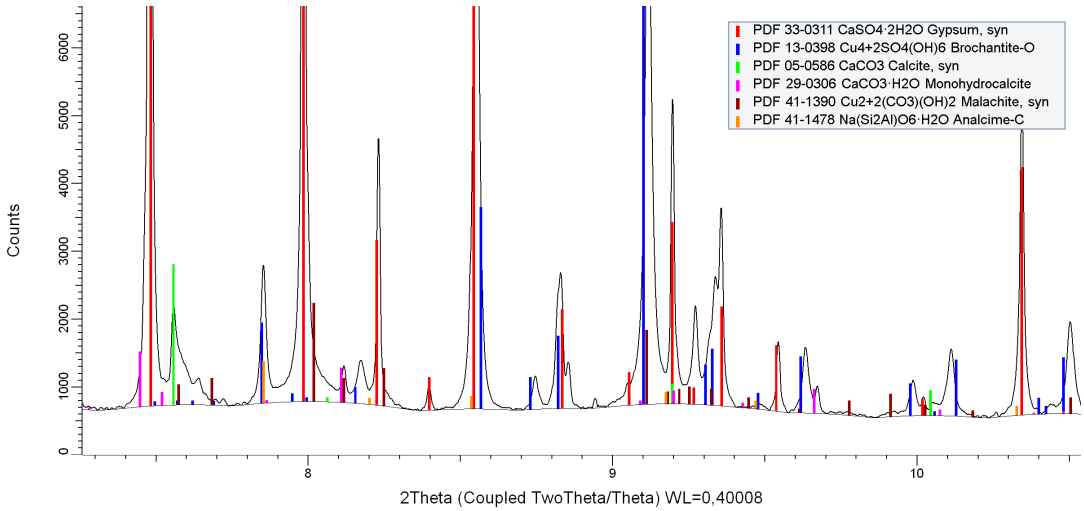

1.8.2 Diffraction patterns Pawley fit

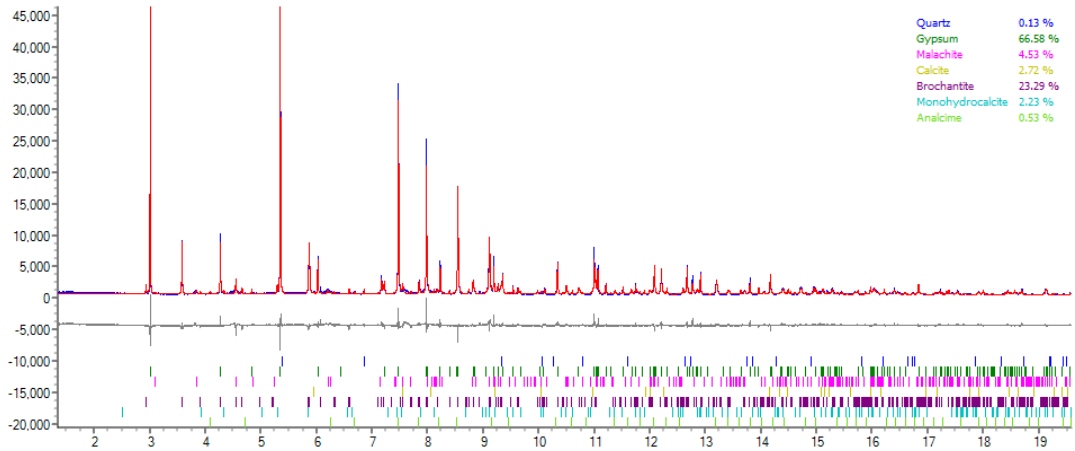

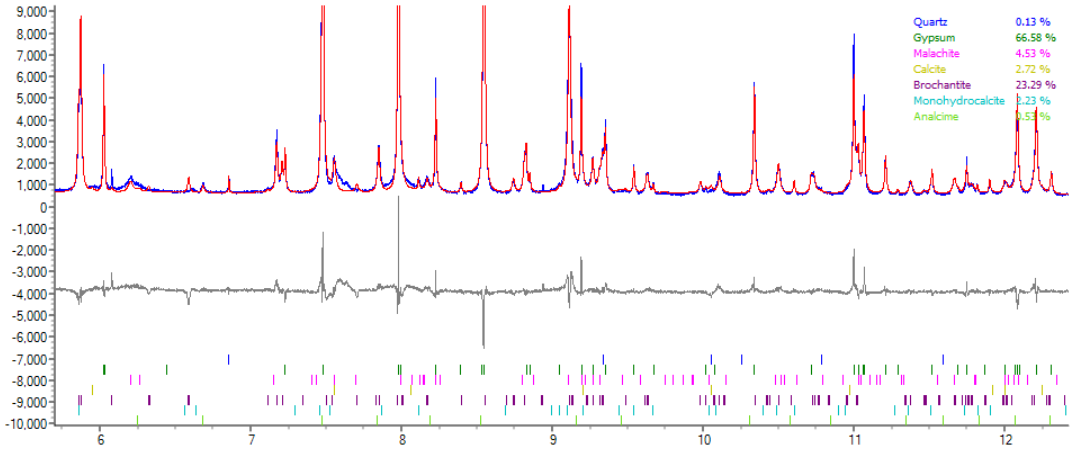

1.8.3 Diffraction patterns 2D and PDF

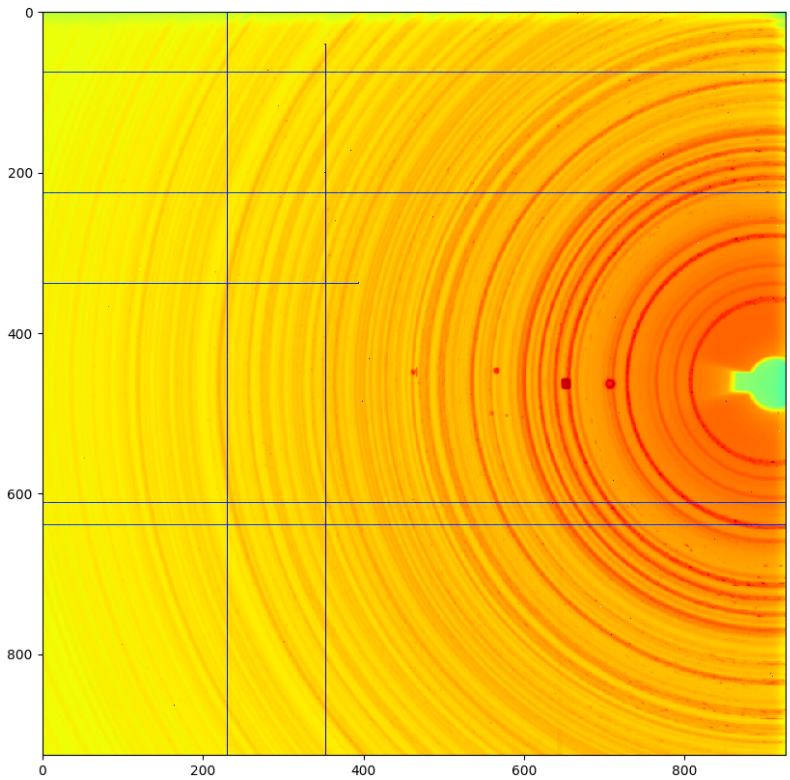

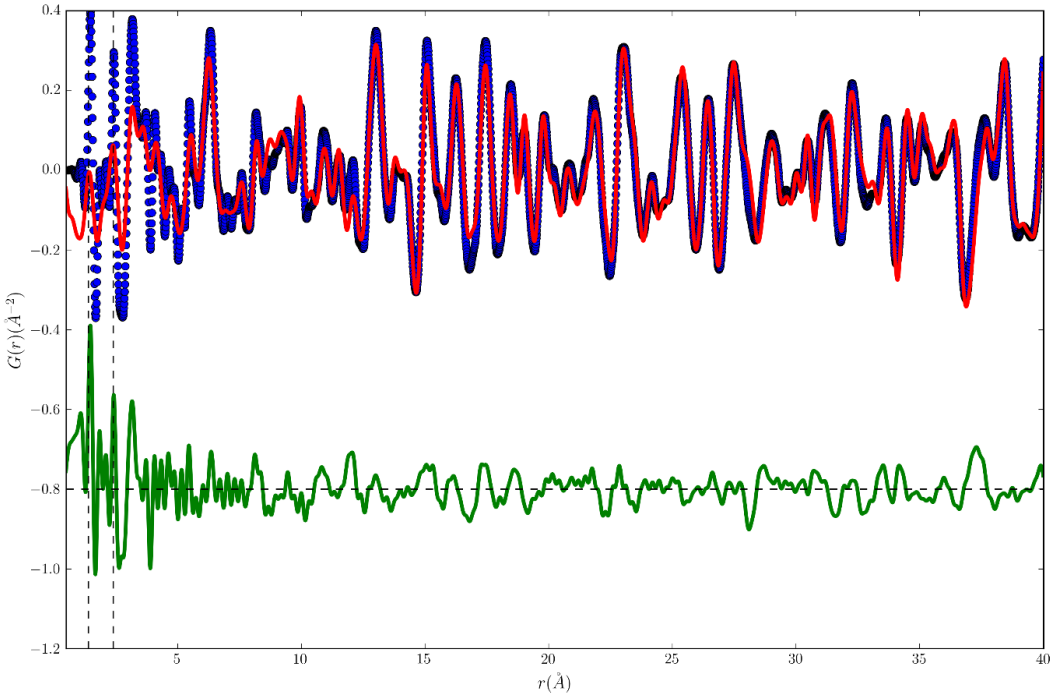
0.4
0.2
0.0
−0.2
−0.4
−0.6
−0.8
−1.0
−1.2
$G(r)(\AA^{-2})$
5
10
15
20
25
30
35
40
$r(\AA)$

1.9 HE08

1.9.1 Diffraction patterns phase identification

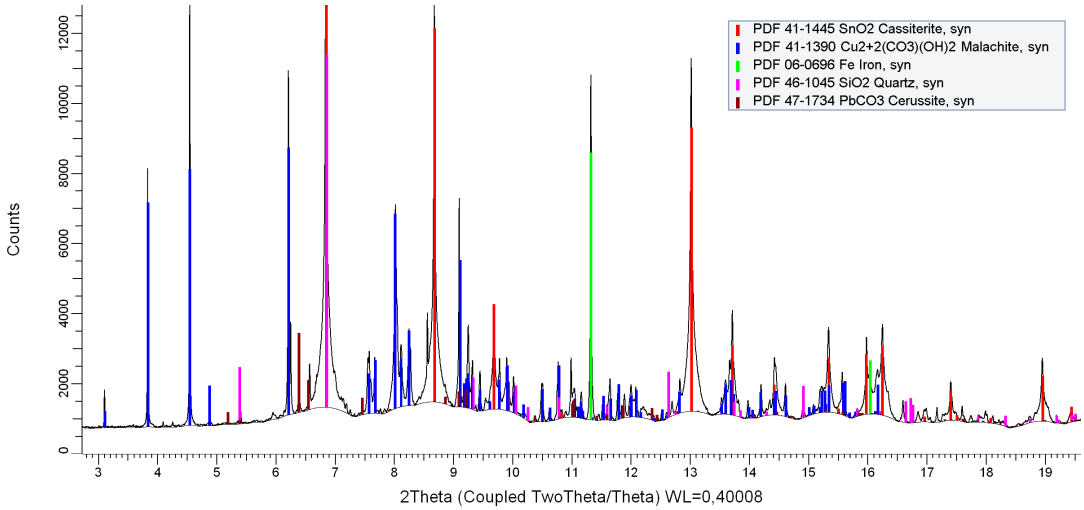

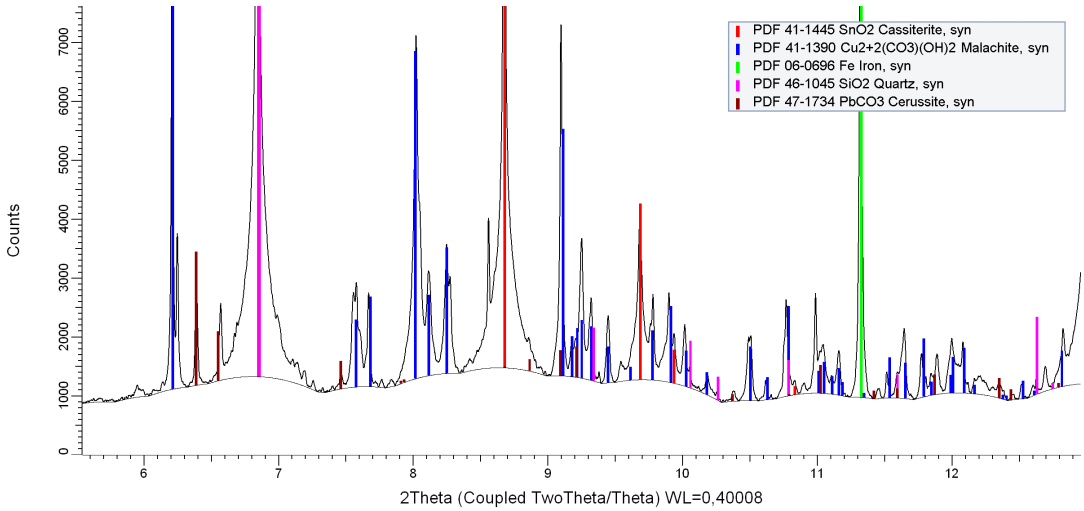

1.9.2 Diffraction patterns Pawley fit

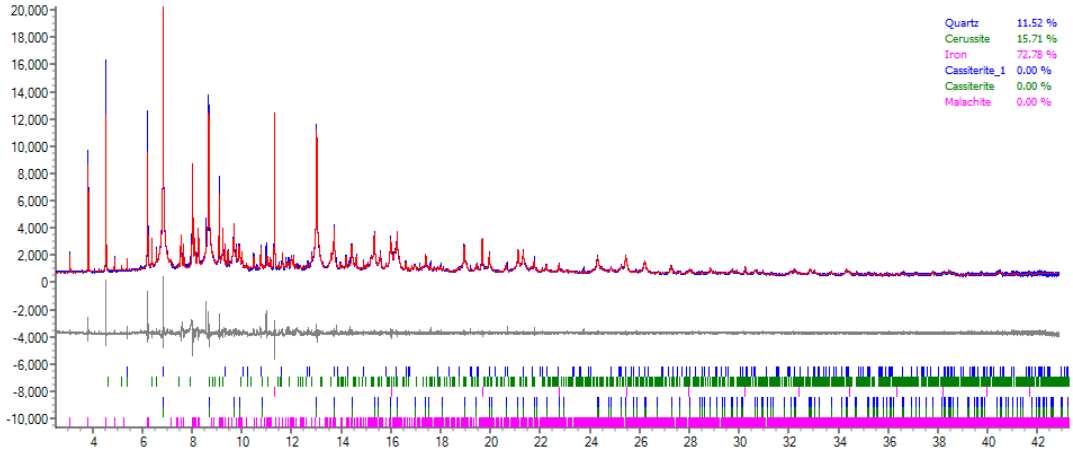

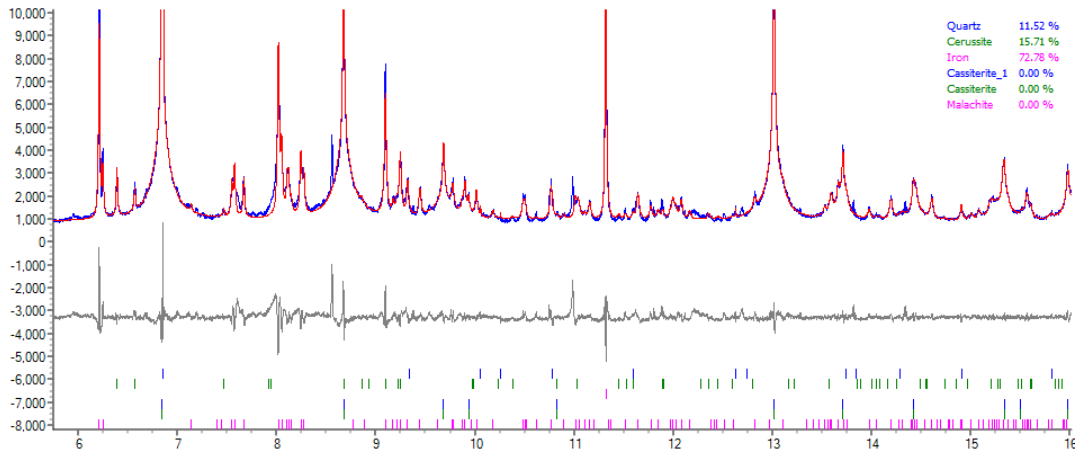

1.9.3 Diffraction patterns 2D and PDF

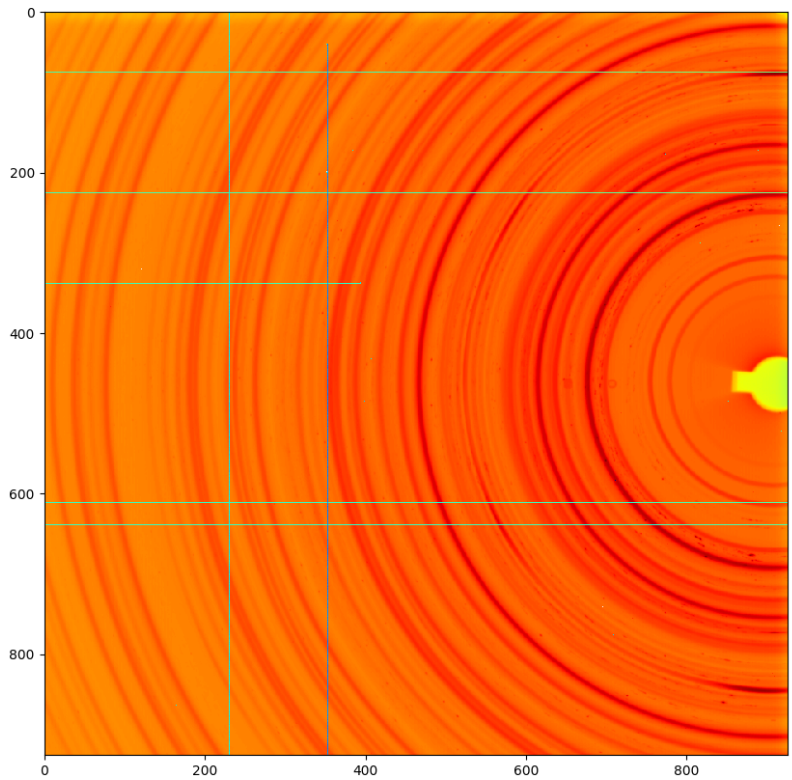

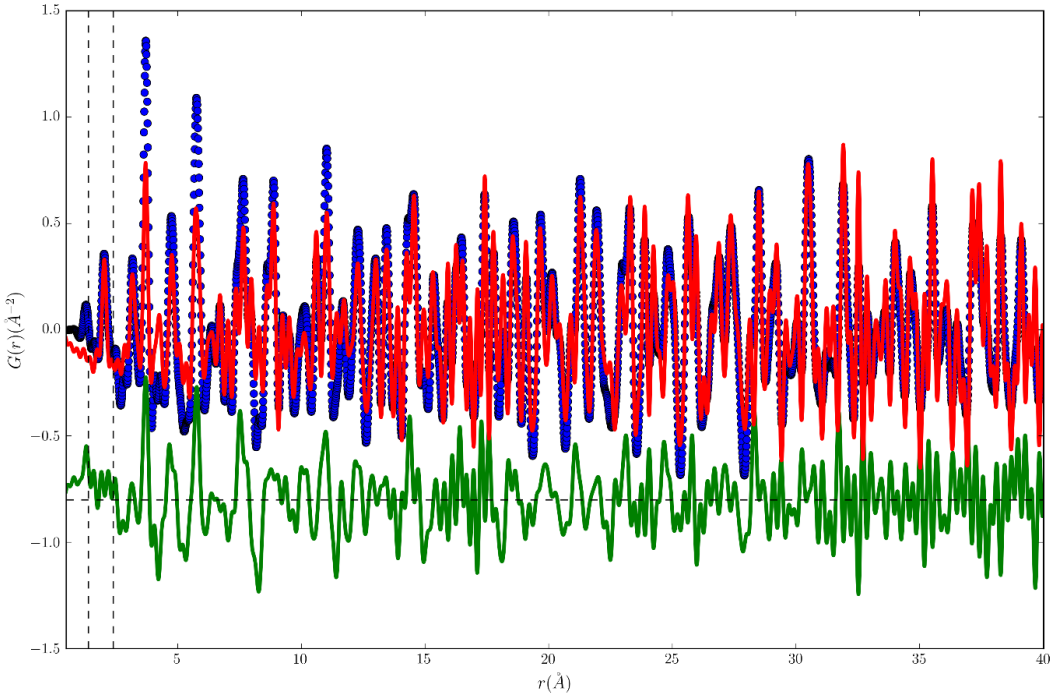
1.5
1.0
0.5
0.0
−0.5
−1.0
−1.5
$G(r)(\AA^{-2})$
5
10
15
20
25
30
35
40
$r(\AA)$

1.10 HE11

1.10.1 Diffraction patterns phase identification

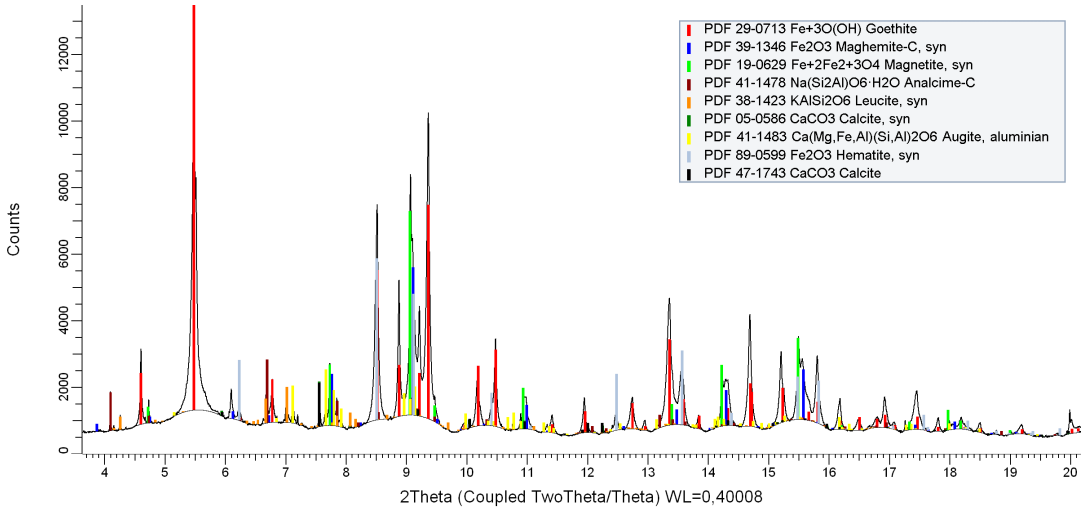

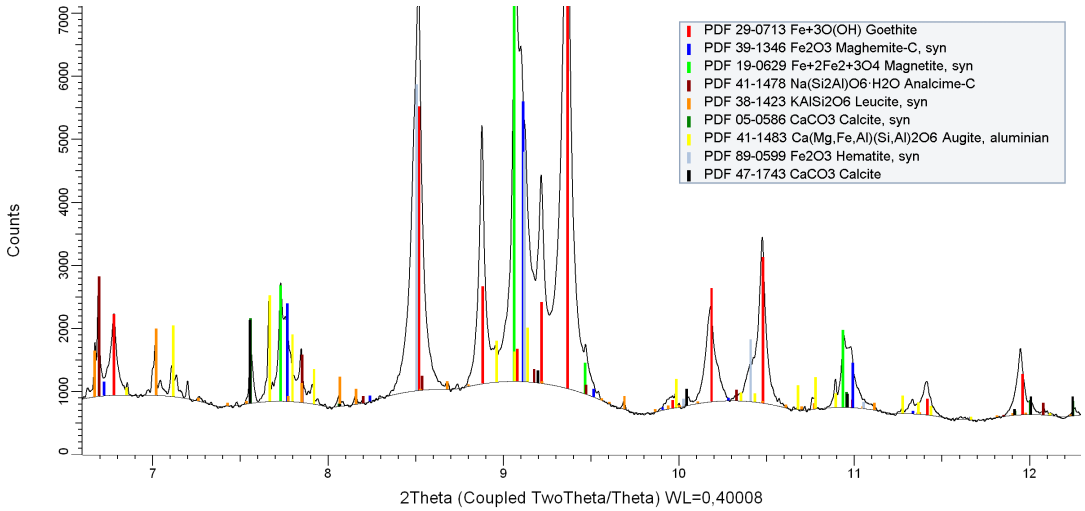

1.10.2 Diffraction patterns Pawley fit

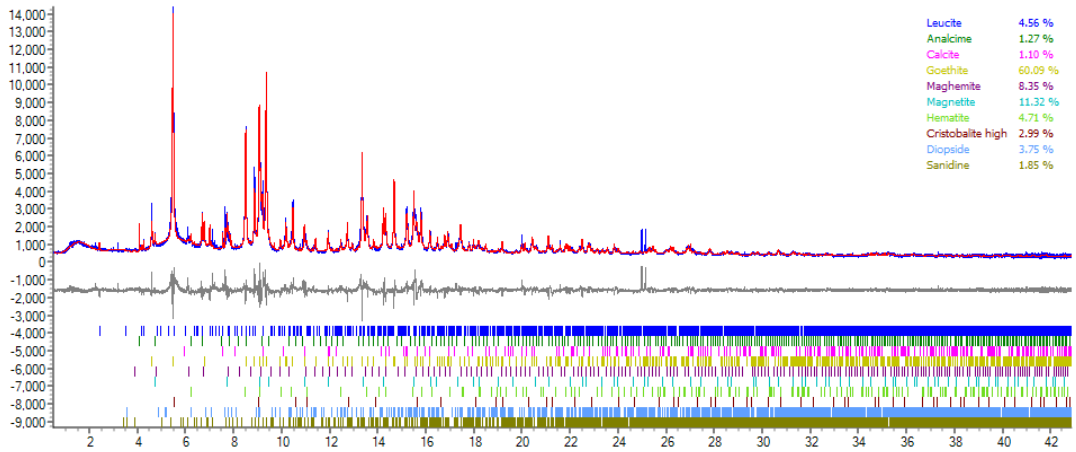

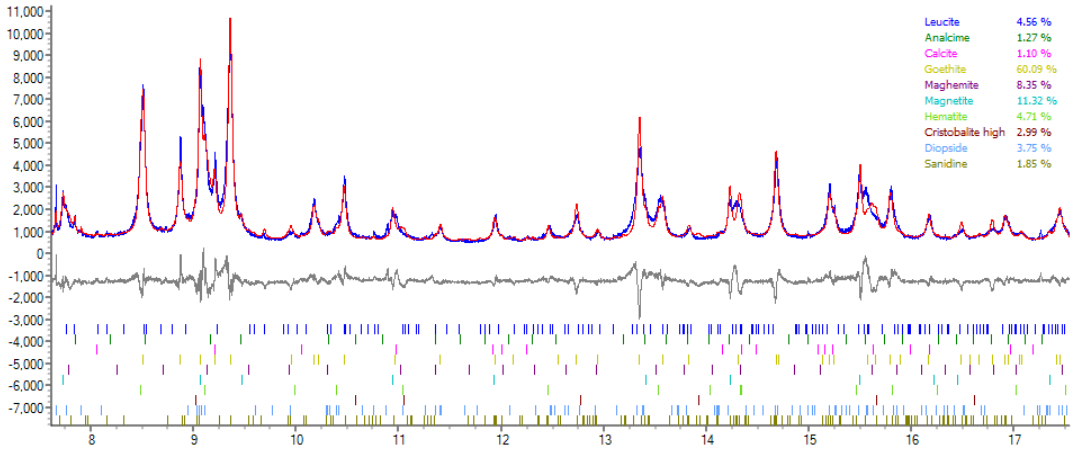

1.10.3 Diffraction patterns 2D and PDF

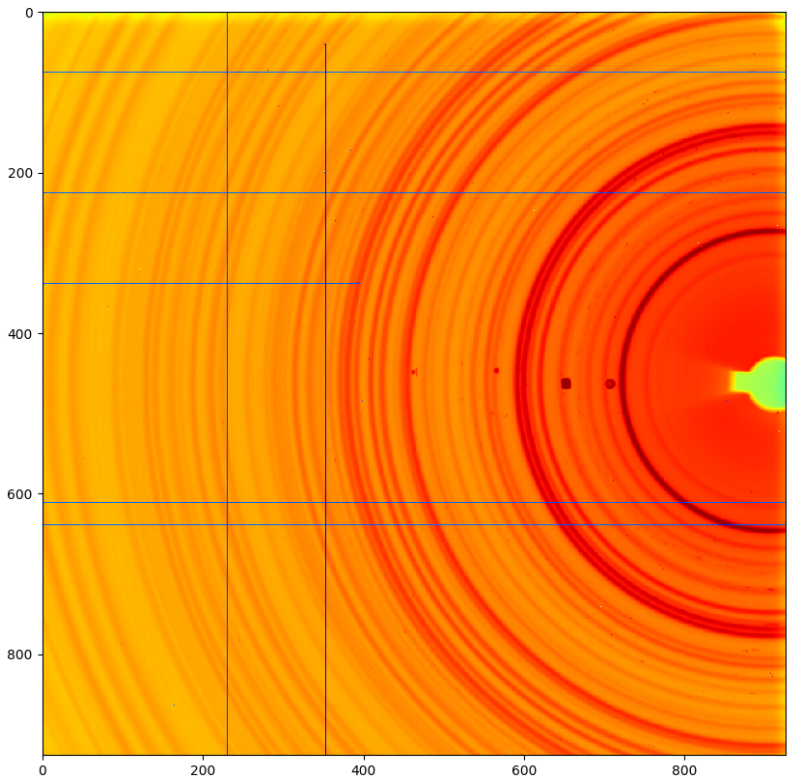

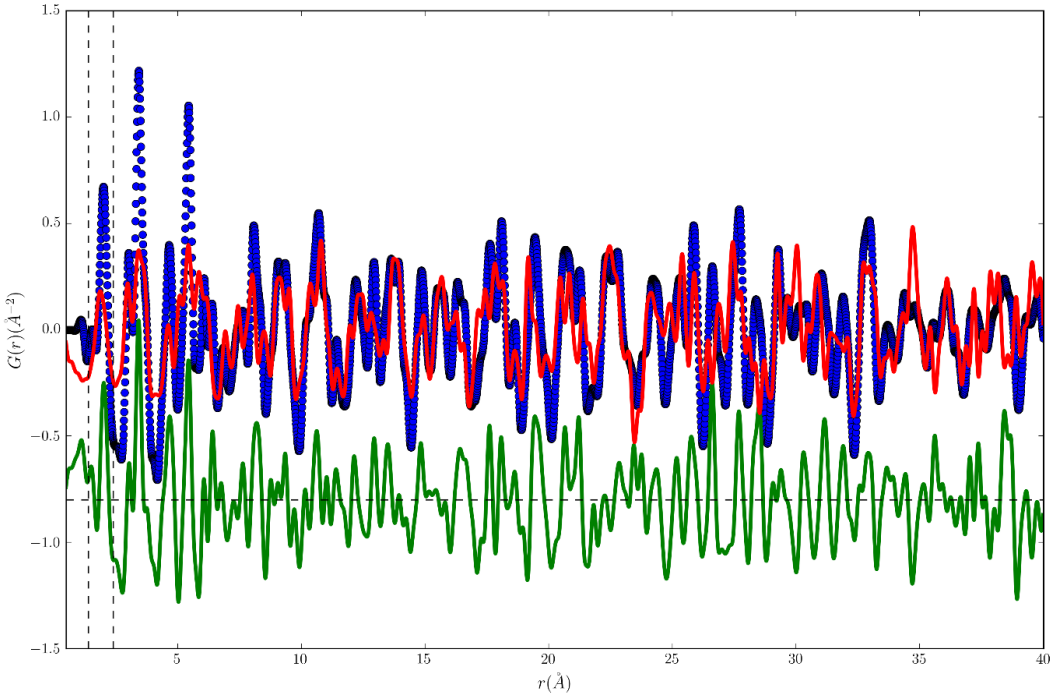
1.5
1.0
0.5
0.0
−0.5
−1.0
−1.5
$G(r)(\AA^{-2})$
5
10
15
20
25
30
35
40
$r(\AA)$

1.11 H75430

1.11.1 Diffraction patterns phase identification

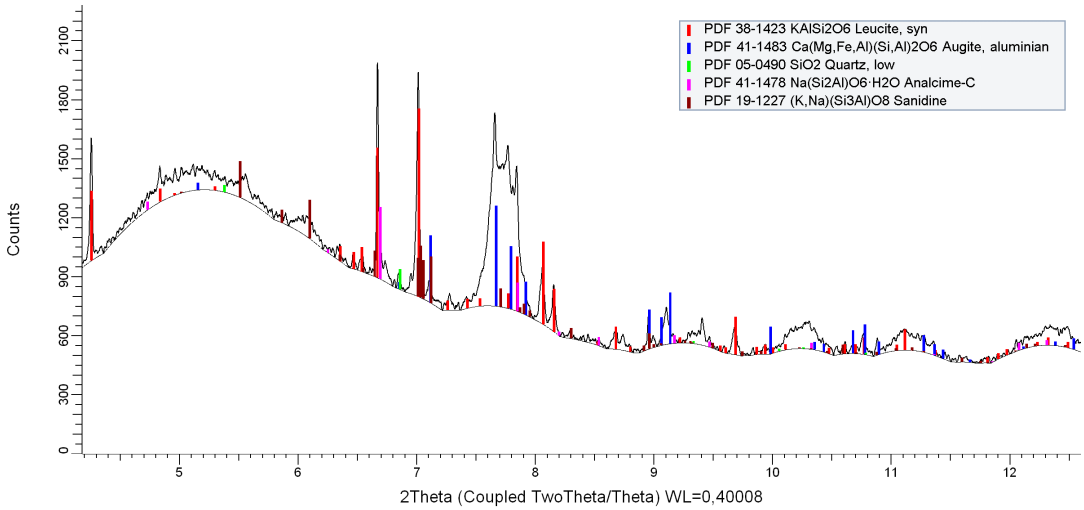

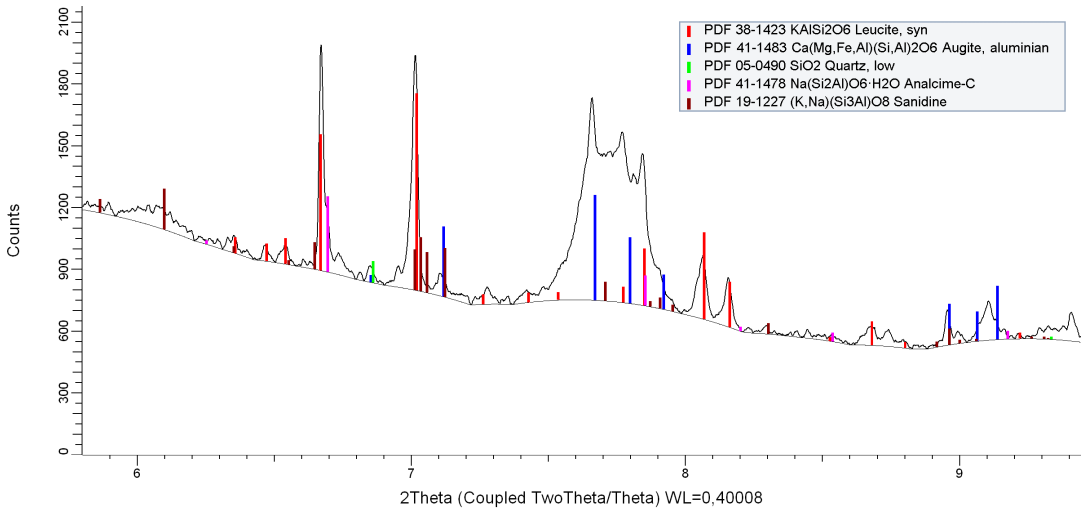

1.11.2 Diffraction patterns Pawley fit

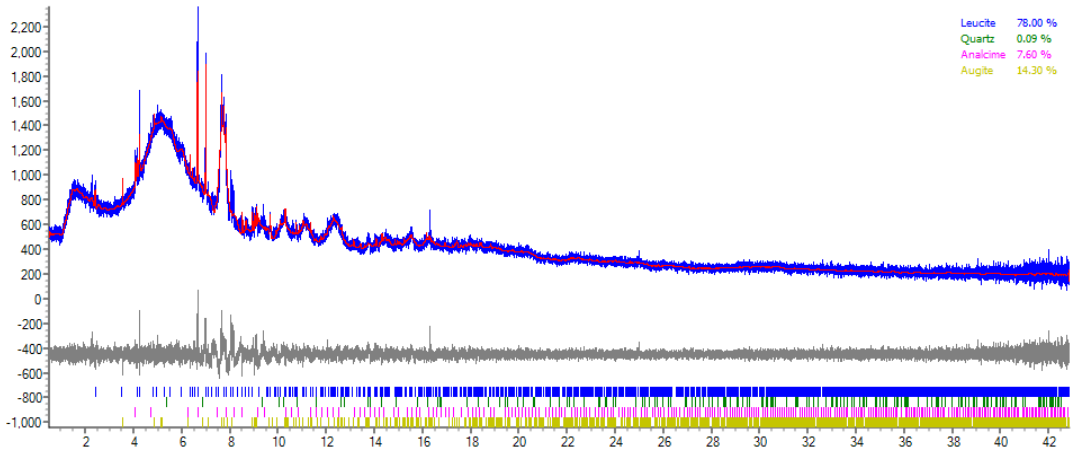

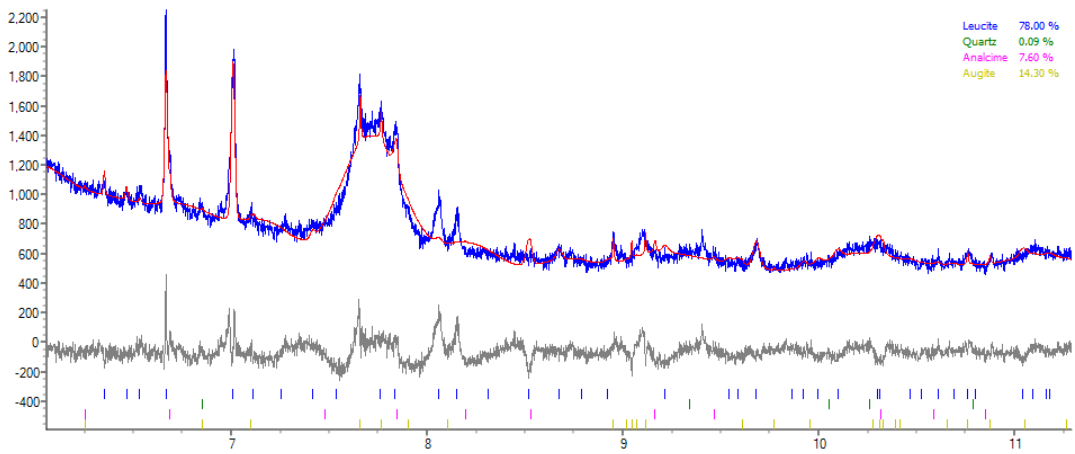

1.11.3 Diffraction patterns 2D and PDF

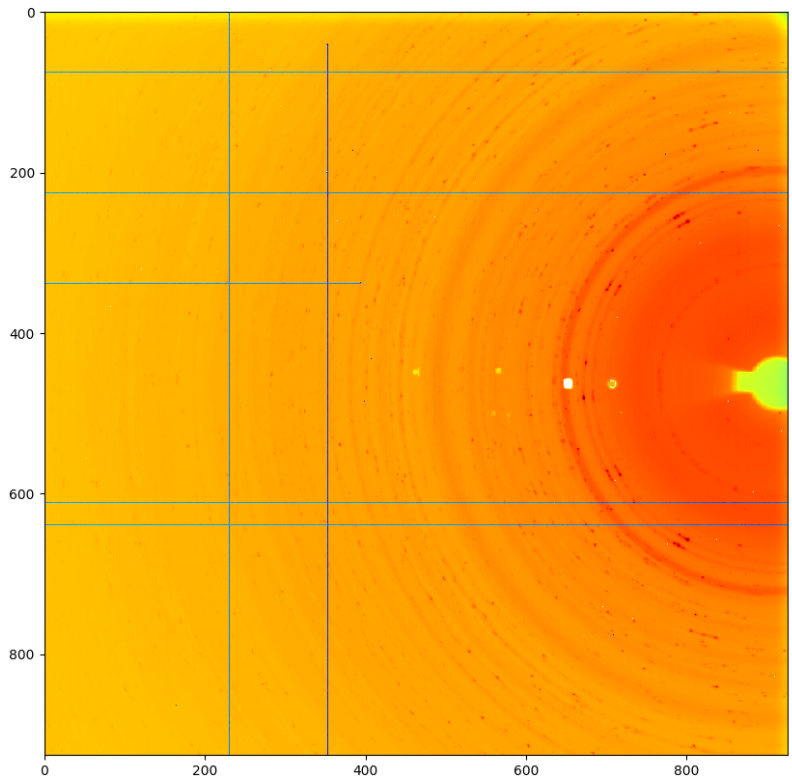

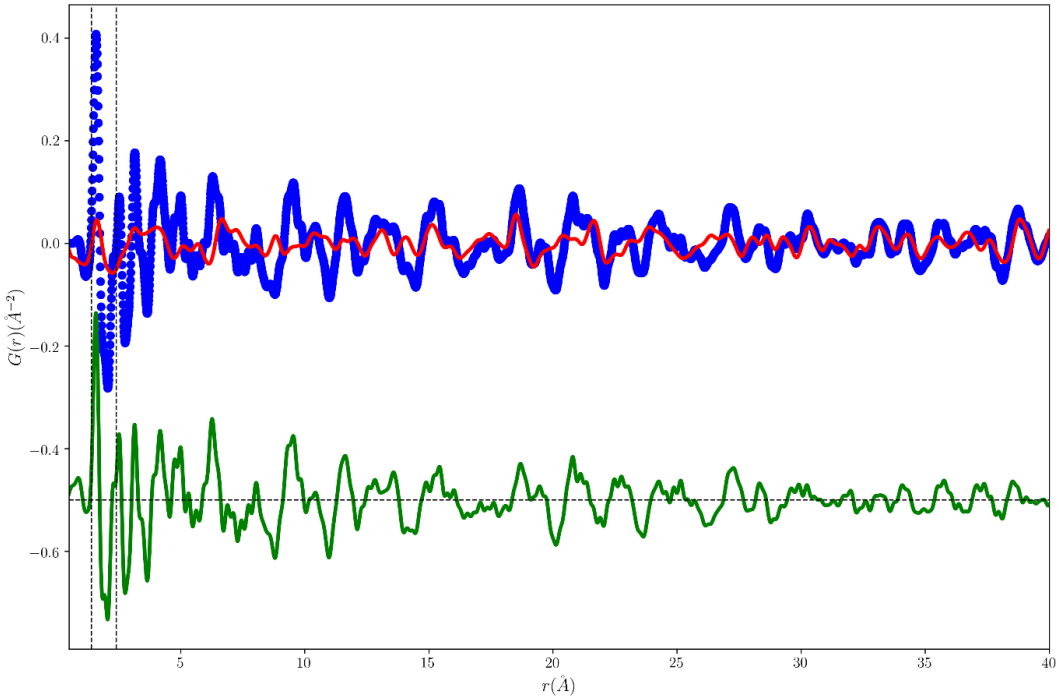
0.4
0.2
0.0
−0.2
−0.4
−0.6
$G(r)(\AA^{-2})$
5
10
15
20
25
30
35
40
$r(\AA)$

1.12 H76238

1.12.1 Diffraction patterns phase identification

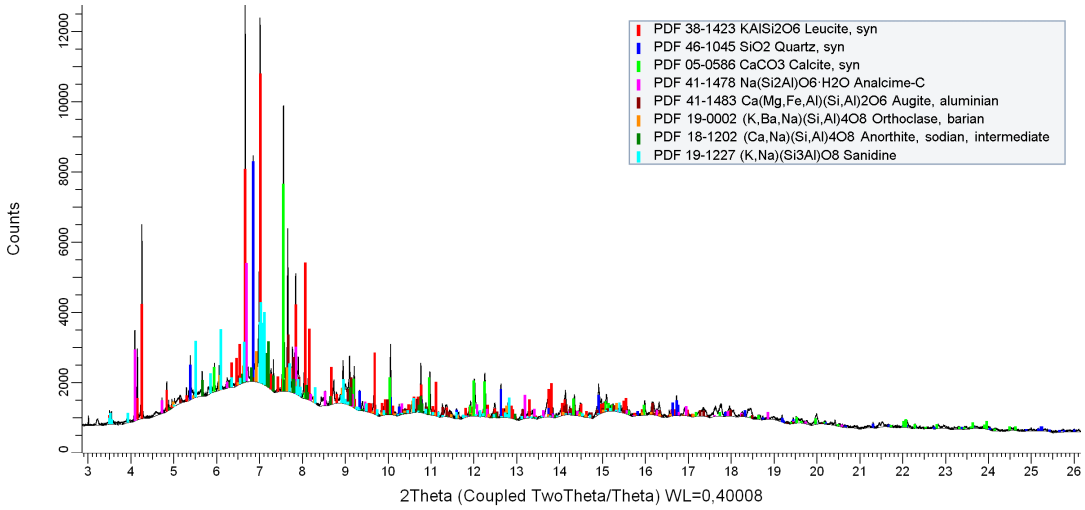

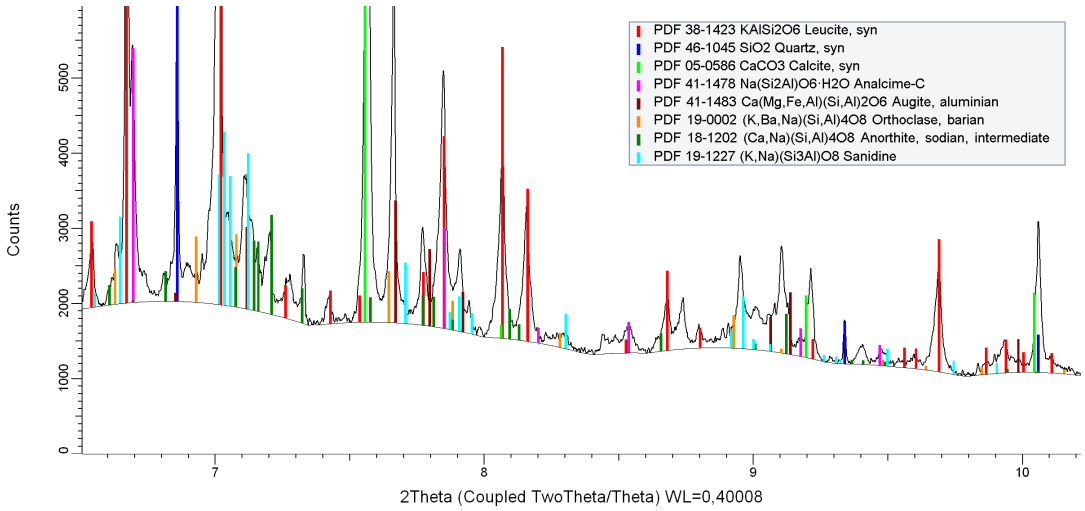

1.12.2 Diffraction patterns Pawley fit

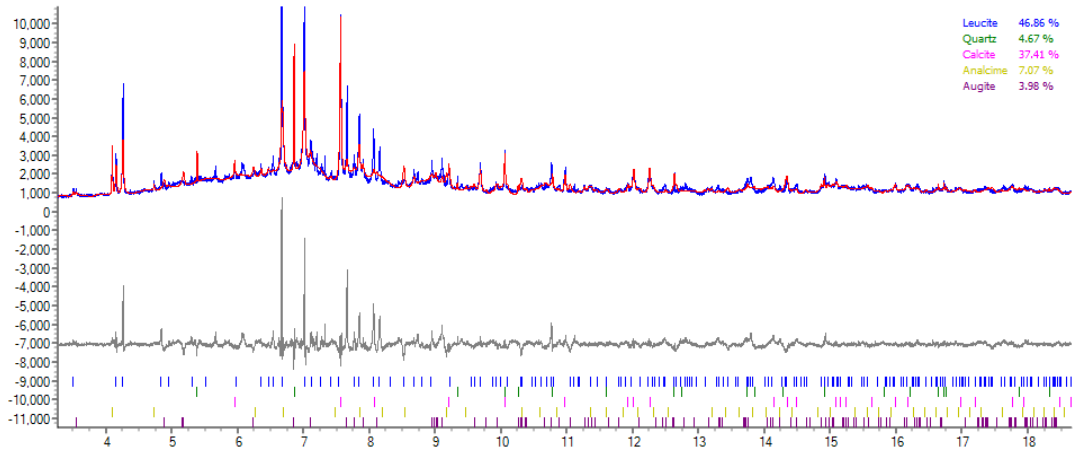

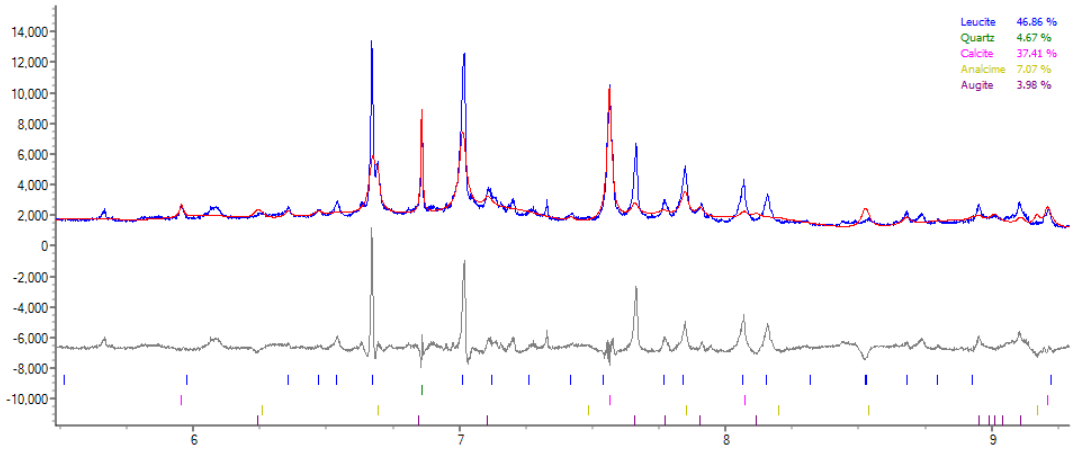

1.12.3 Diffraction patterns 2D and PDF

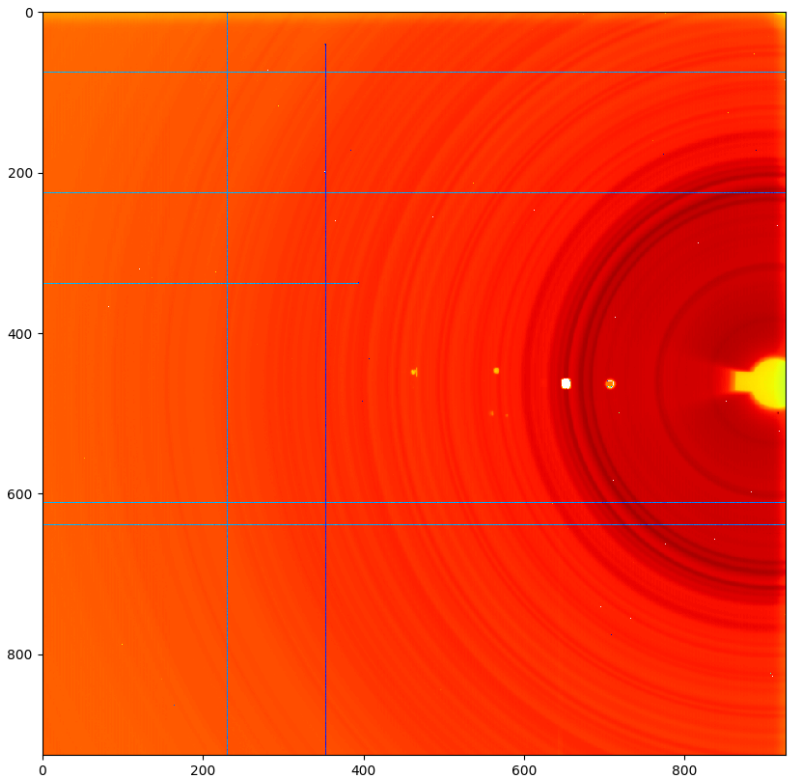

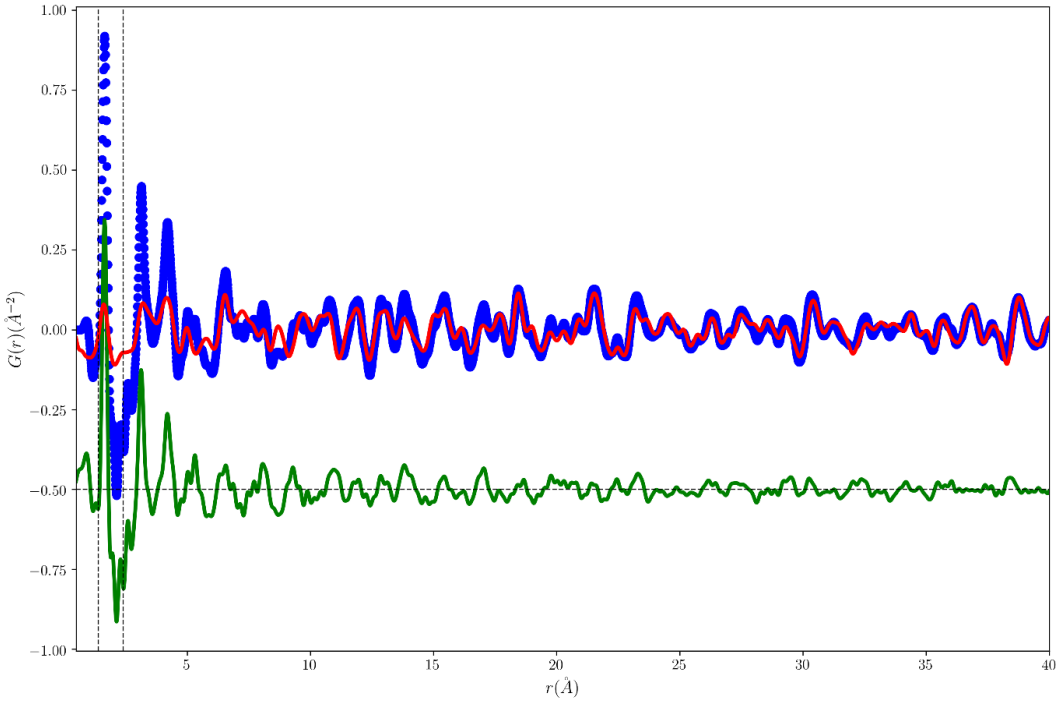
1.00
0.75
0.50
0.25
0.00
−0.25
−0.50
−0.75
−1.00
$G(r)(\AA^{-2})$
5
10
15
20
25
30
35
40
$r(\AA)$

Structural analysis of heterogeneous multi-phased compounds: application to carbon-based black pigments from Antiquity

Résumé

Les inventions de l'encre et du papyrus par les Égyptiens il y a environ 5000 ans ont profondément changé l'humanité en favorisant le développement de l'écriture et la diffusion de l'information. Les informations, partagées jusque-là par un petit groupe de personnes, ont pu être largement diffusées dans toute la Méditerranée antique jusqu'à la Grèce, à Rome et au-delà. La chimie des encres noires utilisées dans l'Antiquité a cependant été peu étudiée jusqu'à présent et notre connaissance de cette invention technologique fondamentale reste donc très incomplète et essentiellement basée sur les informations rapportées dans les textes anciens. Il est généralement admis que l'encre noire utilisée pour l'écriture est à base de carbone et ceci au moins jusqu'au 4ème-5ème siècle après JC. Dans cette thèse, nous tenterons de percer les mystères autour de la nature des pigments noirs à base de carbone utilisés dans l'Antiquité. Nous présenterons les résultats des analyses réalisées sur plusieurs poudres noires de récipients mis au jour sur les sites archéologiques de Pompéi et d'Herculanum, ainsi que sur plusieurs fragments de papyrus de la collection du Musée Champollion, appartenant à plusieurs livres funéraires. Ces échantillons archéologiques sont des matériaux très hétérogènes, avec la présence de phases non-cristallines et cristallines présentant différentes tailles de cristallites. Afin d'étudier ces échantillons, une méthodologie dédiée a été mise en œuvre dans laquelle la microscopie électronique à balayage, la spectroscopie Raman, la fluorescence X et les données de diffraction des rayons X / PDF sont combinées. Nous nous sommes également concentrés sur les études structurales basées sur des techniques impliquant les rayons X synchrotron avec le développement d'outils de traitement de données d'imagerie tomographique. L'identification des différents éléments chimiques, des phases cristallines et des phases désordonnées présentes dans les pigments à base de noir de carbone de l'Antiquité donne de nouvelles perspectives sur les procédés de fabrication développés à l'époque romaine et dans l'Égypte ancienne.

Mots-clés : Pigments noir à base de carbone, Antiquité, matériaux hétérogènes, techniques de rayonnement X synchrotron

Abstract

The joint inventions of ink and papyrus by the Egyptians around 5,000 years ago profoundly changed the intellectual history of mankind by promoting the advent of writing and the dissemination of information. The information, shared until then by a small group of people, was able to be widely disseminated throughout the ancient Mediterranean as far as Greece, Rome, and beyond. The chemistry of the black inks used in Antiquity has however been little studied until now and our knowledge of this fundamental technological invention, therefore, remains very incomplete and essentially based on the information reported in ancient texts. It is generally accepted that the black ink used for writing is carbon-based and this at least until the 4th-5th century AD. In this thesis, we will try to unravel the mysteries around the nature of the carbon-based black pigments used in Antiquity. We will present the results of the analysis carried out on several black powders from containers excavated from Pompei and Herculaneum archeological sites, as well as papyrus fragments from the collection of the Champollion Museum, belonging to several funeral books. These archeological samples are very heterogeneous materials, with the presence of non-crystalline and crystalline phases presenting various crystallite sizes. In order to study these samples, a dedicated methodology was implemented in which scanning electron microscopy, Raman spectroscopy, X-ray fluorescence, and X-ray diffraction data/ PDF are combined. We focused on structural studies based on techniques involving synchrotron X-rays with the development of dedicated tools. The identification of the different chemical elements, crystalline phases, and disordered phases present in the black carbon-based pigments of antiquity gives new insights into the manufacturing processes developed in Roman times and ancient Egypt.

Keywords : Carbon-based pigments, Antiquity, heterogeneous materials, synchrotron X-ray techniques